UNDERSTANDING MECHANISMS FOR C–H BOND ACTIVATION AND HYDROGEN TRANSFER REACTIONS: A THEORETICAL STUDY

A Dissertation

by

BENJAMIN ALAN VASTINE

Submitted to the Office of Graduate Studies of
Texas A&M University
in partial fulfillment of the requirements for the degree of

DOCTOR OF PHILOSOPHY

May 2008

Major Subject: Chemistry

UNDERSTANDING MECHANISMS FOR C–H BOND ACTIVATION AND HYDROGEN TRANSFER REACTIONS: A THEORETICAL STUDY

A Dissertation

by

BENJAMIN ALAN VASTINE

Submitted to the Office of Graduate Studies of
Texas A&M University
in partial fulfillment of the requirements for the degree of

DOCTOR OF PHILOSOPHY

Approved by:

Chair of Committee,	Michael B. Hall
Committee Members,	Simon W. North
	Robert R. Lucchese
	John McIntyre
Head of Department,	David H. Russell

May 2008

Major Subject: Chemistry

ABSTRACT

Understanding Mechanisms for C–H Bond Activation and Hydrogen Transfer Reactions: A Theoretical Study. (May 2008)

Benjamin Alan Vastine, B. S., Virginia Polytechnic Institute and State University

Chair of Advisory Committee: Dr. Michael B. Hall

The results from density functional theory (DFT) studies into C–H bond activation, hydrogen transfer, and alkyne–to–vinylidene isomerization are presented in this work.

The reaction mechanism for the reductive elimination (RE) of methane from [κ^3-$TpPt^{IV}(CH_3)_2H$ (**1**)] (Tp = hydridotris(pyrazolyl)borate) by oxidative addition (OA) of benzene to form [κ^3-$TpPt^{IV}(Ph)_2H$] (**19**) was investigated through DFT calculations. For 31 density functionals, the calculated values for the barriers to methane formation (Ba1) and release (Ba2) from **1** were benchmarked against the experimentally reported values of 26 (Ba1) and 35 (Ba2) kcal•mol^{-1}, respectively. The values for Ba1 and Ba2, calculated at the B3LYP/DZP level of theory, are 24.6 and 34.3 kcal•mol^{-1}, respectively. The best performing functional was BPW91 where the m.a.e. for the calculated values of the two barriers is 0.68 kcal•mol^{-1}.

Classic and newly proposed mechanisms for metal-mediated hydrogen transfer (HT) were analyzed with density functional theory (DFT) and Bader's "Atoms In Molecules" (AIM) analysis. Seven sets of bonding patterns that characterize the

connectivity in metal-mediate HT were found from the analysis of representative models for σ-bond metathesis (σBM), oxidative addition / reductive elimination (OA/RE), and alternative mechanisms.

The mechanism for the formation of the alkynyl, vinylidene complex, $[(P\textit{i}Pr_3)_2Rh(CCPh)(CC(H)(Ph))]$ (**2**), by the addition of two equivalents of phenylacetylene (PA) to $[(\eta^3\text{-}C_3H_5)Rh(P\textit{i}Pr_3)_2]$ (**1**) was studied through DFT calculations. Two experimentally observed intermediates on the reaction coordinate are the η^2-PA, alkynyl complex, $[(P\textit{i}Pr_3)_2Rh(\eta^2\text{-}HCCPh)(CCPh)]$ (**Ia**) and the five-coordinate, pseudo square-pyramidal, Rh^{III}–H complex, $[(P\textit{i}Pr_3)_2Rh(H)(CCPh)_2]$ (**Ib**), and were found to be in equilibrium. The relative energies of **Ia**, **Ib**, and **2** (relative to **1** + 2PA) depend on the phosphine that was used in the calculation; the predicted product is **2** with $P\textit{i}Pr_3$ and PEt_3 but **Ia** with PMe_3, PMe_2Ph, $PMePh_2$, PPh_3, and PH_3. The equilibrium between **Ia** and **Ib** was calculated with PEt_3 and one conformation of $P\textit{i}Pr_3$. We investigated the mechanism for the formation of **2** from **Ia**, and a lower energy pathway where the π-bound PA of **Ia** slips to bind through the σ-C–H bond prior to the formation of **2** through hydrogen migration was found.

DEDICATION

To my parents, Rick and Marcia Vastine.

ACKNOWLEDGEMENTS

I would especially like to thank my graduate research advisor, Dr. Michael B. Hall. I have learned to be a better chemist. Many thanks are in order to the Hall group, especially Lisa Perez, who has always helped me with my research. Alan R. Esker, my undergraduate research advisor also deserves my thanks as he gave me a chance. I could not have accomplished this degree without the faithful support of my parents, Rick and Marcia Vastine. They have provided me with advice, direction, admonishment, and much joy in my life. I have relied on the local support of many people: Kayla and Daric Green, Chris Thomas, Charles Edwin Webster, Chad Beddie, Scott Brothers, Rob Cable, Brian Leonard, Eric Frantz, Jeremy Andreatta, BJ Bench, and Vince Venditto. These friends have provided the friendship required to make it through graduate school. I would like to thank and acknowledge many other friends: Sammy Frame, Ryan Newcomb, Emery Williams, Josh Downing, Jason Downing, Andrew Brunone, Slim, Ben Post, David Oliphant, and Alan Northcutt. All of the above have been there for support and for a few beers. I would like to thank Sandy Young for his ever-present support and spiritual guidance. He is someone who I will always admire. I have rested in the care, compassion, kindness, and love of Farah Dawood. She has been a light in dark places. I principally thank the Author of the "Two Books" for the chance to study both; His Light is a lamp unto my feet.

TABLE OF CONTENTS

CHAPTER Page

Page

LIST OF FIGURES

FIGURE Page

FIGURE Page

FIGURE Page

FIGURE Page

LIST OF TABLES

TABLE Page

CHAPTER I

INTRODUCTION

The activation of carbon–hydrogen (C–H) bonds is important as developments in facilitating the cleavage of this bond would make alkanes a more useful feedstock.[1,2] The C–H bond is difficult to break because of its relatively large bond dissociation energy (BDE = D_0), ~ 100 kcal•mol^{-1};[3] activation of this bond is therefore defined as the facilitation of bond cleavage. Three primary factors related to the strength and inertness of this bond are: (1) the large D_0 value, (2) low proton acidity (high pKa), and (3) a highly non-polar character. Non-metal mediated C–H bond activation typically has been accomplished through high temperature reactions (heterolytic cleavage) and radical pathways (homolytic cleavage).[4,5] Hydride abstraction requires a highly acidic environment[4] while product selectivity is usually lost in the radical pathways.[5] In general, the activation of the C–H bond is usually more facile for a tertiary carbon atom, which is followed by secondary and primary carbon atoms (3º > 2º > 1º).

This dissertation follows the style of the *Journal of the American Chemical Society*.

The problems in C–H activation listed above are ameliorated by using transition metals.[6] Specifically, the *d*-orbitals of the TMs possess the proper symmetry and energies to interact with the C–H bonding and antibonding (C–H*) orbitals.[7] The coordination of the C–H to the metal is a three center, 2-electron interaction where the electron density of this bond is donated into an unoccupied metal *d*-orbital. C–H scission results from back donation of electron density from the TM into the C–H* orbital, and the formation of formal M–C and M–H bonds follows this scission. If the back donation is weak, then the alkane coordinates to the metal through the σ-C–H bond to form a stable "σ-complex".[8] The orbital interactions are shown in Figure 1.1.

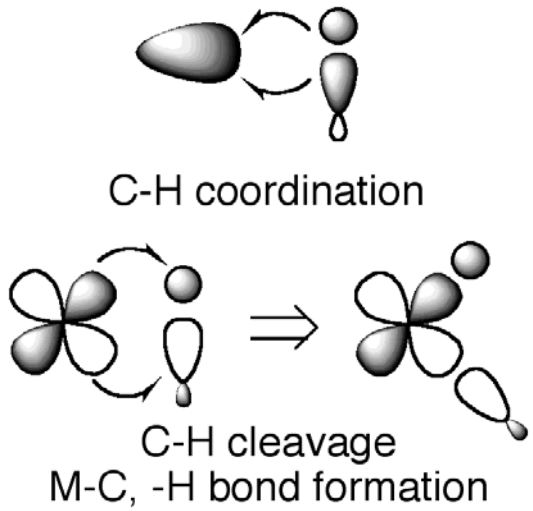

Figure 1.1. The orbital interactions for the coordination of a C–H bond to a metal center and the scission of the C–H bond are described.

Product selectivity is reversed for saturated alkanes as the order of activation is 1° > 2° > 3° in this TM assisted chemistry.[9,10] The activation of aryl C–H bonds is

more accessible,[11] which is shown in the faster H/D exchange[12] rates of these bonds compared to those for saturated alkanes, and in competition studies where the relative rates of activation favor aryl over saturated C–H bonds.

1.1 C–H Bond Activation

The current activity in C–H activation began with H_2 activation, which is physically a close relative to the C–H bond (D_0 of H_2: 104 kcal•mol^{-1}).[3] Halpern and Vaska each reported the activation of H_2 but through different mechanisms. Halpern reported the hydrogenation of $[Cu^{II}(OAc)_2]^{2+}$ to produce the transient species $[Cu^{II}(OAc)(H)]^{+}$ and H^{+}, which implied an "eletrophilic" mechanism for homogeneous H_2 activation.[13] Vaska investigated the addition of H_2 to $[(PPh_3)_2Ir^{I}(Cl)(CO)]$ to form $[(PPh_3)_2Ir^{III}(Cl)(CO)(H)(H)]$, and proposed an "oxidative addition" (OA) mechanism where the formal oxidation state of iridium has increased by two and two formal Ir–H bonds were formed.[14] The intermediate where the H_2 is coordinated to the metal through the σ-bond to form $[M(\eta^2\text{-}H_2)]^{q}$, which is the precursor intermediate to H_2 activation, is now thought to be common between the two mechanisms.[15] Because of the similarity between the H–H and C–H bonds, the attention was turned to activating the latter.

Shilov reported H/D exchange between methane and D_2O catalyzed by $[Pt^{II}Cl_4]^{2-}$, and the electrophilic mechanism was proposed because of the acidic reaction medium.[16] Continuing his work, Shilov studied the oxidation of methane to form methyl chloride and methanol with the same H/D exchange catalyst; however, $[Pt^{IV}Cl_6]^{2-}$ was used as the oxidant in this conversion of methane.[17] This work showed

that the "inert" C–H bond could be selectively activated at mild reaction conditions and form desired products through cross-coupling reaction. The exact mechanism for C–H activation in Shilov chemistry is unclear as electrophilic and oxidative addition / reductive elimination (OA/RE) pathways have been proposed, and the research into this problem and other related aspects of this chemistry have been extensively considered in several books[18] and reviews.[2,19,] We discuss briefly some insights into the mechanism for Shilov chemistry below.

Shilov proposed a scheme of three important steps for alkane activation and functionalization and is shown in Scheme 1.1.[20] Ligand exchange between L' and RH in a tetravalent $[Pt^{II}(L)_3L']$ complex to form $[Pt^{II}(L)_3(R)]$, H^+, and L' is step *i*. Oxidation of this alkyl Pt^{II} complex by a Pt^{IV} oxidant and uptake of X (X = Cl, H_2O) to form a six-coordinate, pseudo-octahedral alkylplatinum complex, $[Pt^{IV}(L)_4(X)(R)]$, is step *ii*. If X is a chloride ion, reductive coupling of RCl produces the alkyl chloride product that was experimentally observed; however, ligand exchange between a chloride ion and H_2O can occur and reductive coupling between R and the H_2O ligand produces the experimentally observed alcohol upon proton elimination (step *iii*). With the RE of the product, the $[Pt^{II}(L)_3L']$ starting material is reformed. The current interest in this chemistry is in understanding the C–H bond activation mechanistic step[21] and replacing the expensive Pt^{IV} oxidant.[22]

Scheme 1.1

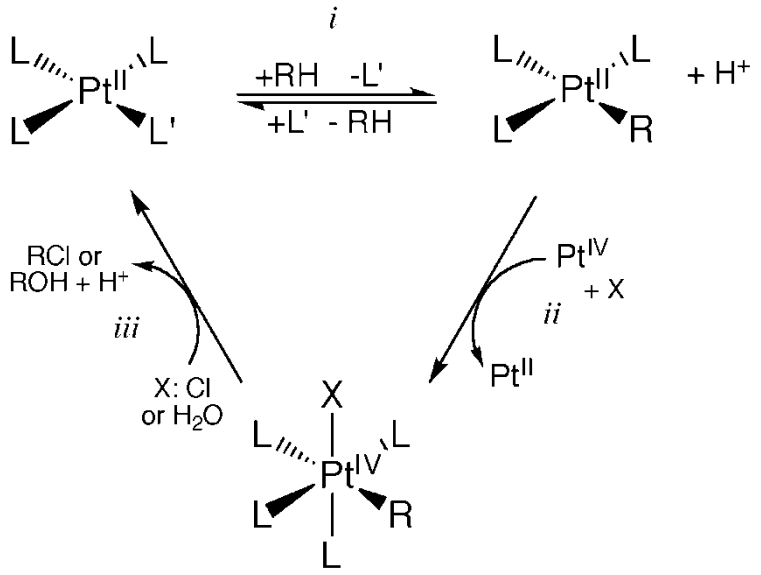

Evidence exists that the mechanism for C–H activation depends on the spectator ligands that are considered. In a computational study, Seigbahn and Crabtree studied the C–H bond activation step catalyzed by $[(Cl_2)[Pt^{II}(OH_2)_2]$ and found that solvent water molecules facilitated hydrogen transfer (HT) between methane and a chloride ligand. The authors could not differentiate between σ-bond metathesis and the OA/RE pathways for C–H decoupling as the relative energies between these two pathways were very similar.[23]

In an elegant study, Wick and Goldberg[24] demonstrated the plausibility of the OA/RE pathway for Shilov chemistry when they reported the formation of a stable Pt^{IV} hydride complex, $[\kappa^3$-Tp*$Pt^{IV}(CH_3)(R)H]$ (R = C_6H_5, C_5H_{11}, C_6H_{11}) where Tp* is the tri-chelating hydridotris(3,5-dimethylpyrazolyl)borate.[25] The starting material, $[\kappa^2$-Tp*$Pt^{II}(CH_3)_2]$, was treated with $B(C_6F_5)_3$ to remove an anionic methyl ligand and

produce a highly reactive unsaturated Pt^{II} species, which then undergoes oxidative addition of a substrate (e.g. C_6H_6, C_5H_{12}, C_6H_{12}) to form a postulated five-coordinate Pt^{IV} intermediate, [κ^2-Tp*$Pt^{IV}(CH_3)(R)H$]. To stabilize this intermediate, the uncoordinated pyrazolyl ring coordinates trans to the hydride ligand to form the final product. This study was the first to observe the heretofore Pt^{IV} hydride product from OA of a C–H bond.

In a related study, Jensen and coworkers offered a detailed investigation into the mechanism of this Shilov-type chemistry where they observed the liberation of two equivalents of methane from [κ^3-Tp*$Pt^{IV}(CH_3)_2H$] (**1'**) by the addition of two equivalents of benzene-d_6 to form the final product [κ^3-Tp*$Pt^{IV}(C_6D_5)_2D$] (**3-*d*$_{11}$**).[26] The enthalpic barriers ($\Delta H^{\ddagger}$) to C–H reductive coupling to form methane (Ba1) and methane liberation from **1'** (Ba2) were measured in the experimental study to be 26 and 35 kcal•mol^{-1}, respectively. The barrier to C–H coupling was measured by observing the rate for H/D scrambling between the methyl and hydride positions, which would imply that a σ-bound methane intermediate complex is found along the potential energy surface (PES) of this reaction; these σ-bound complexes have been proposed to rationalize the inverse isotope effect ($k_H/k_D < 1$) that is often measured in this chemistry.[9,27] The experimental value for Ba2 was obtained from the kinetic experiments for the overall reaction where the observed rate constant is consistent with methane release as the rate-limiting step in the reaction.

These values for Ba1 and Ba2 provided an opportunity to benchmark a variety of density functionals and basis sets for the energy of OA/RE of C–H bond activation

and the binding of a σ-bound complex; the results of this study are reported in Chapter II. The experimental starting material mentioned above (**1'**) was modeled by [κ^3-$TpPt^{IV}(CH_3)_2H$] (Tp = hydridotris(pyrazolyl)borate) (**1**), and good agreement between the calculated and experimental values for the enthalpic barriers were calculated. We also investigated the overall mechanism for the liberation of two equivalents of methane by the addition of two equivalents of benzene and we found that the chemistry for both methane eliminations and benzene additions was very similar.

1.2 Mechanisms for Hydrogen Transfer

The OA/RE mechanism for C–H bond activation discussed above can provide one pathway to HT from one carbon atom to another. Additionally, HT can occur by a direct process without OA/RE, the classic σ-bond metathesis (σBM) reaction. Historically, these have been the two "classic" mechanisms for HT. The reaction profiles for the overall reaction R'–H + M–R → M–R' and R–H are sketched in Scheme 1.2. Only one transition state (TS) is found along the reaction coordinate for HT in the σBM mechanism; whereas, in the OA/RE pathway there are two TSs along this coordinate. In the first TS, the R'–H bond is broken and M–R' and M–H bonds are formed; the result is the formation of an intermediate of a higher formal oxidation state (n + 2). After this intermediate a second TS couples the R–H bond and completes the HT.

Scheme 1.2

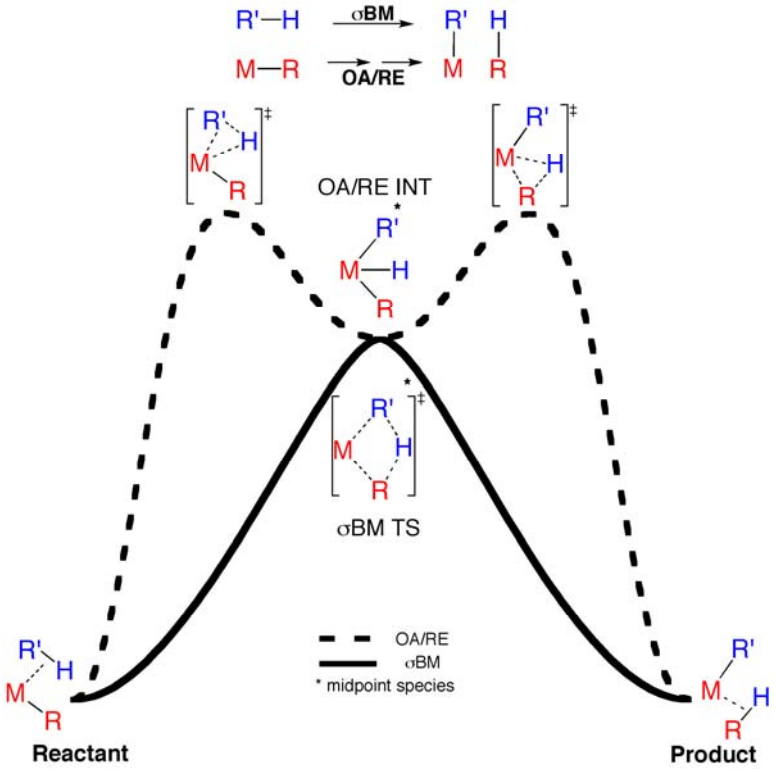

Several groups have reported experimental investigations into the σBM mechanism where group 3 metals were used to study this mechanism in early row transition metal systems. In the experiments by Watson, $^{13}CH_4$ was added to $[Cp_2M(^{12}CH_3)]$ (M = Y, Lu; Cp = η^5-C_5H_5) to produce the final products of $[Cp_2M(^{13}CH_3)]$ and $^{12}CH_4$; strong evidence for C–H bond metathesis by HT between ligands was provided by this labeling experiment.[28] Bercaw studied a similar reaction with the addition of organic substrates to $[Cp^*_2Sc(R)]$ (Cp* = η^5-$C_5(Me)_5$) and measured a moderate enthalpic barrier ($\Delta H^{\ddagger}$) of ~12 kcal•mol^{-1} for HT. The rate for HT was shown to decrease with increasing s-character of the C–H bond.[29] Lastly,

Bruno and coworkers reported the formation of a thoracyclobutane by the release of neopentane from $[Cp_2Th(CH_2C(CH_3)_3)_2]$ where the mechanism for HT proceeds by σBM.[30] The addition of tetramethylsilane and cyclohexane to thoracyclobutane resulted in the formation of a cyclometallic sillyl thallium complex where the HT steps also proceeded by σBM.[31]

Ziegler and coworkers[32] investigated the σBM mechanism in a density functional theory[33] (DFT) study of the addition of H_2 and CH_4 to $[Cp_2ScX]$ (X = H, CH_3). The TSs for HT in these models are characterized by similar geometries and the distances between the scandium center and the transferring hydrogen were ~1.90 Å for the models. This long M–H distance of the σBM TS is considered to be characteristic of the σBM mechanism where the metal and transferring hydrogen do not interact.

The calculated barrier for HT between methyl ligands of ~10 kcal•mol^{-1} was found to be in close agreement with the experimental value (~12 kcal•mol^{-1}); however, several subsequent studies have calculated barriers for similar reactions of ~20 kcal•mol^{-1}.[34] Corrections for hydrogen atom tunneling brought these values down to the experimental one. Further evidence for the important of tunneling is the large experimental kinetic isotopes effect (k_H/k_D) of ~3.[9]

The addition of C–H bonds to metals through the OA mechanism was studied through a series of photoelimination experiments. Green reported that photoelemination of H_2 from $[Cp_2W^{II}H_2]$ in benzene resulted in the formation of the phenyl hydrido tungsten complex, $[Cp_2W^{II}(C_6H_5)H]$.[35] Graham reported a preference for aryl C–H bonds in the addition of organic substrates to $[Cp^*Ir^{I}(CO)]$.[36] Bergman,

reported a preference for primary C–H bonds over secondary ones in studying similar reactions with $[Cp^*Ir^{III}(PMe_3)(H)(H)]$.[37] These studies showed the order of reactivity for organic substrates in OA chemistry (i.e. aryl > 1° > 2° > 3°).

In a subsequent study, Arndtsen and Bergman reported that the related cationic iridium complex, $[Cp^*Ir^{III}(PMe_3)(CH_3)(solv)]^+$, activated C–H bonds at a mild temperature to release methane in what appeared to be a metathesis reaction.[38] The actual mechanism for HT in this system was found to proceed through the OA/RE pathway by a theoretical study by Hall and coworkers where the oxidative cleavage of the C–H bond resulted in a meta-stable bis-alkyl Ir^V hydride species.[39] Analogs of this high valent iridium species were later isolated.[40]

1.3 Mechanisms of Alternative Character

In the recent literature, mechanisms of alternative character have been proposed that lie between the two classic mechanisms that were discussed above; Lin has recently reviewed the current work in this field.[41] Webster and coworkers proposed metal-assisted σ-bond metathesis (MAσBM),[42] Lin and coworkers proposed "oxidatively added transition state" (OATS),[41,43] Oxgaard and Goddard proposed "oxidative hydrogen migration" (OHM),[44] and Perutz and Sabo-Etienne proposed "σ-complex assisted metathesis" (σ-CAM).[45] These alternative mechanisms are characterized by a single TS for HT between R and R', and the geometric parameters of these TSs resemble those of the OA/RE intermediate. In particular, a short M–H distance (~1.5 Å) is often calculated in these TSs.

Our second study is in analyzing the so-called midpoint species that are on the reaction coordinate for HT (Scheme 1.2) with Bader's "Atoms in Molecules" (AIM) analysis.[46] In Chapter III, we present our preliminary findings for the analysis of the bonding patterns of several midpoint species. We first report those patterns for the σBM TS and OA/RE intermediate, which is represented by $[Cp_2Sc(CH_3)_2H]^{‡}$ and $[CpIr(PMe_3)(CH_3)_2H]^{+}$, respectively. These patterns are representative of the two ends of the "spectrum of mechanisms", and we present several models that are characterized by bonding patterns that lie in between these two extremes. In Chapter IV, we present our investigation of a wider range of midpoint species and present in total seven sets of bonding patterns that comprise the spectrum of mechanisms. These patterns were also verified at higher levels of theory to ensure their stability.

1.4 Alkyne-to-Vinylidene Isomerization

The third study in metal assisted C–H bond activation is metal-mediated alkyne to vinylidene isomerization. Schäfer et al. reported the addition of two equivalents of phenylacetylene (PA) to $[(\eta^3\text{-}C_3H_5)Rh(P\textit{i}Pr_3)_2]$ to yield the alkynyl, vinylidene product $[(P\textit{i}Pr_3)_2Rh(CCPh)(CC(H)(Ph))]$, and the mechanism was said to proceed through an OA pathway where a bis-alkynyl rhodium hydride species is an intermediate on the reaction coordinate.[47]

Evidence for a step-wise, oxidative mechanism for this isomerization was obtained when the intermediate $[ClRh(P\textit{i}Pr_3)_2(H)(CCPh)]$ was trapped with pyridine after PA was added to $[ClRh(P\textit{i}Pr_3)_2]$.[48] The vinylidene complex,

[CpRh(P*i*Pr$_3$)(CC(H)(Ph))], was isolated when the intermediate was treated with NaCp and phosphine was lost. Further evidence was collected for the step-wise mechanism when the analogous iridium hydride and vinylidene complexes were isolated.[49]

In a computational study, Wakatsuki and coworkers reported that the lowest energy pathway for this isomerization proceeded through a bimolecular pathway.[50] However, Grotjahn and coworkers reported that H/D cross-over did not occur when [ClRh(P*i*Pr$_2$R^1)$_2$(η^2-alkyne)] (R^1 = Ph, *i*Pr, imidazol-2-yl (Im)) and the deuterated alkyne analog were mixed.[51] In a theoretical study, De Angelis and coworkers reported a free energy barrier to hydrogen migration in the bimolecular pathway that was ~20 kcal•mol^{-1} greater than that of the intramolecular mechanism.[52]

The conclusions of and future directions for this work are presented in Chapter VI. We will now consider some of the basic principles of quantum chemistry, which are elaborated in several excellent books.[53]

1.5 Theoretical Methods

Ab initio and density functional theory are two quantum chemical methods considered in this work. These methods are used to solve the second-order differential time-independent Schrödinger equation (Equation 1), where H is the Hamiltonian operator and ψ is the wave-function that defines the quantum chemical system. *Ab initio* methods construct the Hamiltonian and the wave function from first principles and an example is Hartree–Fock theory. In density functional theory, the wave

function is approximated by a density functional and the energy is derived from the electron density.

$$H\psi = E\psi \qquad [1]$$

Operators are represented with the "hat" above the symbol, and we will drop this notation and for the operators that are included in this report and present them (in general) as *O*.

The Hamiltonian can be dissected between the kinetic (*T*) and potential (*V*) energy terms, and the Hamiltonian can be written in the following form: $H = T + V$. The general construction of the Hamiltonian is shown in Equation 2 where the constant $\hbar$ (h-bar) is Planck's constant (h) divided by 2π; the constants m_e and M_A are the masses of the electron *e* and the nucleus *A*, respectively; *e* is the constant of elementary charge, and Z_M is the atomic number (e.g. H = 1; He = 2, etc).

$$H = -\sum_{i=1}^{N}\frac{\hbar^2}{2m_e}\nabla_i^2 - \sum_{\mathrm{A}=1}^{\mathrm{M}}\frac{\hbar^2}{2M_A}\nabla_A^2 - \sum_{i=1}^{\mathrm{N}}\sum_{A=1}^{\mathrm{M}}\frac{e^2Z_A}{r_{iA}} + \sum_{i=1}^{\mathrm{N}}\sum_{A=1}^{\mathrm{M}}\frac{e^2Z_AZ_B}{r_{AB}} + \sum_{i=1}^{N}\sum_{j>1}^{M}\frac{e^2}{r_{ij}} \qquad [2]$$

The previous formulation of the Hamiltonian can be presented in a more palpable form by setting the constants (i.e. $\hbar$, m_e, e, M_a, Z_x) to unity, which is shown in Equation 3. The energies that are returned when this Hamiltonian is used are in unities of "hartrees", where 1 h. is equal to 27.2 eV.

$$H = -\sum_{i=1}^{N}\frac{\nabla_i^2}{2} - \sum_{\mathrm{A}=1}^{\mathrm{M}}\frac{\nabla_A^2}{2} - \sum_{i=1}^{\mathrm{N}}\sum_{A=1}^{\mathrm{M}}\frac{1}{r_{iA}} + \sum_{i=1}^{\mathrm{N}}\sum_{A=1}^{\mathrm{M}}\frac{1}{r_{AB}} + \sum_{i=1}^{N}\sum_{j>1}^{M}\frac{1}{r_{ij}} \qquad [3]$$

In the Hamiltonian (Equations. 2 and 3), the first two terms are the kinetic energy operators of the electrons and nuclei, respectively. The third term is the attractive potential between the electrons and the nucleus while the fourth term is the repulsive potential between the nuclei in a polyatomic system. Last is the term for the electron correlation energy, which is dependent on the inverse of the distance between the i^{th} and j^{th} electrons (r_{ij}). The Hamiltonian that has been presented here is non-relativistic because relativistic contributions to the energy such as the velocity of particles (inner shell electrons of heavy elements, for example), spin-orbit, magnetic, and spin-spin effects are not included.[54]

The nuclear and electronic motions are decoupled in the Born–Oppenheimer approximation and the electronic energy is solved in an external potential from the fixed nuclei.[55] With this approximation, the Hamiltonian and wave function are functions of the electronic coordinates only and Equation 1 can be rewritten as:

$$H^{elec}\Psi^{elec}(r,R) = E^{eff}(R)\Psi^{elec}(r,R) \quad [4]$$

The kinetic operators for all nuclei are discarded in Equations 2 and 3, and the fourth term is an external potential at fixed nuclear coordinates, V_{NN}, which results in a purely electronic Hamiltonian (H^{elec}, Equation 5). This simplification is reduces the number of terms in the Hamiltonian and the associated error (particularly at the ground state) is minimal.

$$H^{elec} = -\sum_{i=1}^{N}\frac{\nabla_i^2}{2} - \sum_{i=1}^{N}\sum_{j>1}^{M}\frac{1}{r_{iA}} + \sum_{i=1}^{N}\sum_{j>1}^{M}\frac{1}{r_{ij}} + V_{NN} \quad [5]$$

1.5.1 Hartree–Fock Theory

The exact wave function is known for few systems (e.g. hydrogen atom, particle in a box, rigid roter) and must be approximated for polyatomic systems. The wave function must obey the Pauli principle which states that the wave function must be antisymmetric with respect to a change in the spatial location or spin of an electron. Slater proposed an approximate form for the wave function that obeys the Pauli principle by representing it by a determinant, which is shown in Equation 6.

$$\psi_{SD} = \frac{1}{\sqrt{N!}} \begin{pmatrix} \chi_1(1) & \chi_2(1) & \chi_n(1) \\ \chi_1(2) & \chi_2(2) & \chi_n(2) \\ \chi_1(n) & \chi_2(n) & \chi_n(n) \end{pmatrix} \quad [6]$$

The elements of the Slater Determinant, χ_i, are called spin orbitals and these functions are described by the spatial (x,y,z) and the spin coordinates (ξ) of the i^{th} electron: χ_i (x,y,z,ζ) = $\psi_i(\xi)$. The prefactor, $(N!)^{-1/2}$, ensures that the wave function is normalized. The spin operators, $S_z\alpha$ and $S_z\beta$, when applied to the wave function yield the only two possible eigenvalues (ξ) of $\hbar/2\,\alpha$ and $\hbar/2\,\beta$; as a result, there can only be two electrons in each spin orbital by definition.

For normalized wave functions (exact or approximate) that satisfy the boundary conditions, the variational principle states that the variational energy (E_i) is an upper bound to the exact energy, E_0 (i.e. $E_i \geq E_0$). In HF theory, the spin orbitals are used as an approximate wave function and the HF equation (Eq. 7) is derived by minimizing E_i with respect to the spin orbitals.

$$F_i\varphi_i = \varepsilon_i\varphi_i \quad [7]$$

In this equation F_i is the one electron Fock operator, φ_i are the HF molecular orbitals (MO), and ε_i are the HF orbital energies. The Fock operator is shown in Equation 8.

$$F_i = h_i + \sum_i^N [2J_i - K_i] \quad [8]$$

where,

$$h_i = \left\langle \varphi_i \left| -\frac{\nabla_i^2}{2} - \sum \frac{Z_A}{|r_{Ai}|} \right| \varphi_i \right\rangle \quad [9]$$

$$J_{ij} = \langle ij|ij\rangle = \left\langle \varphi_i(1)\varphi_j(2) \left| \frac{1}{r_{ij}} \right| \varphi_i(1)\varphi_j(2) \right\rangle \quad [10]$$

$$K_{ij} = \langle ij|ji\rangle = \left\langle \varphi_i(1)\varphi_j(2) \left| \frac{1}{r_{ij}} \right| \varphi_j(1)\varphi_i(2) \right\rangle \quad [11]$$

The single electron operator, h_i, is comprised of the electron kinetic and electron–nuclear potential energy terms. The repulsive force between the i^{th} and j^{th} electrons is expressed by the $2e^-$ Coulomb integral, J_{ij}, and represents a net destabilization of the energy. The exchange between electrons in these spin orbitals is expressed by the $2e^-$ Exchange integral, K_{ij}, which does not have an analog in classical mechanics, and results in a stabilization of the energy. Upon integration, the HF energy (Eq. 12) is derived and is an upper bound to the exact energy because HF theory is variational (i.e. $E_{HF} \geq E_{elec}$).

$$E_{HF} = 2\sum_{i=1}^{n} H^{core} + \sum_i^n \sum_j^n \left[2J_{ij} - K_{ij}\right] + V_{NN} \quad [12]$$

The expansion of the MOs by a linear combination of atomic orbitals (LCAO) is an accessible way to approximate the wave function in HF theory. The spatial component of the spin orbitals can be expanded in a linear combination of basis functions (Eq. 13), and the set of functions used is called a *basis set*.

$$\varphi = \sum_{i=1} c_{is}\phi_s \qquad [13]$$

Slater type orbitals (STO) are good approximations for the spatial distribution of the oribitals at short and long range, but they are difficult to integrate as they are first order exponentials (exp(-r)). Gaussian type functions, which are second order exponentials ($\exp(-r^2)$) are simpler to integrate but they poorly describe the short and long range behavior of the orbital. The form of the Gaussian type functions are shown in Equation 14, where *N* is the normalization constant, the $x^{lx}y^{ly}z^{lz}$ term determines the angular momentum, and the two coefficients, a_k and α_k, are optimized to give the correct energies for that atoms considered. A series of Gaussian functions can be contracted to mimic the proper behavior of the STO and to decrease the number of functions used in the expansion.

$$\phi_s = Nx^l y^l z^l \sum_{k=1}^{n} a_k e^{-a_k r^2} \qquad [14]$$

Substitution of Equation 14 in the HF equation (Eq. 7) results in:

$$\sum_{s=1}^{n} c_{is}F_i\phi_s = \varepsilon_i \sum_{s=1}^{n} c_{is}\phi_s \qquad [15]$$

The Roothaan–Hall equation (Eq. 16) results from left hand multiplication of Equation 15 by ϕ_r^* and integration. The S_{rs} term is the overlap integral and is either 0 or 1 for orthonormal wave functions; however, for approximate wave functions that are typically non-orthonormal, the overlap integral is usually non-zero.

$$\sum_{s=1}^{n} c_{is}F_{rs} = \varepsilon_i \sum_{s=1}^{n} c_{is}S_{rs}; F_{rs} = \langle \phi_r | F_i | \phi_s \rangle; S_{rs} = \langle \phi_r | \phi_s \rangle \quad [16]$$

A convenient way to solve these single electron equations is simultaneously in matrix form (Eq. 17), which can be generalized in the secular equation (Eq. 18). The roots of the secular equation are the orbital energies, ε_i, and the total HF energy is the sum of these single-electron energies.

$$\begin{pmatrix} F_{11} - \varepsilon S_{11} & F_{12} - \varepsilon S_{12} & F_{1n} - \varepsilon S_{1n} \\ F_{21} - \varepsilon S_{21} & F_{22} - \varepsilon S_{22} & F_{2n} - \varepsilon S_{2n} \\ F_{n1} - \varepsilon S_{n1} & F_{n2} - \varepsilon S_{n2} & F_{nn} - \varepsilon S_{nn} \end{pmatrix} = 0 \quad [17]$$

$$\text{or } |F_{rs} - \varepsilon_i S_{rs}| = 0 \quad [18]$$

However, since these equations are non-linear, the preferred way of solving for the energies is through matrix methods. The Roothaan–Hall equations can be written in matrix form (Eq. 19) where **F**, **C**, **S,** and $\boldsymbol{\varepsilon}$ are square matrices whose elements are the F_{rs}, c_{is}, S_{rs}, and $\delta_{is}\varepsilon_i$ terms, respectively.

$$\mathbf{FC} = \mathbf{SC}\boldsymbol{\varepsilon} \quad [19]$$

The basis set must be made orthogonal to solve the Roothaan–Hall equations (Eq. 19), which requires matrix **C** to be transformed. The transformation matrix must be constructed, **X**, and satisfy: $\mathbf{X}^{\mathbf{T}}\mathbf{S}\mathbf{X} = \mathbf{1}$. A new coefficient matrix can be constructed, **C'**, once **X** is known where: $\mathbf{C'} = \mathbf{X}^{-1}\mathbf{C}$ or $\mathbf{C} = \mathbf{X}\mathbf{C'}$. This new definition for **C** is inserted into the l.h.s of Equation 19 to form: $\mathbf{F}\mathbf{X}\mathbf{C'} = \mathbf{S}\mathbf{X}\mathbf{C'}\boldsymbol{\varepsilon}$. Left hand multiplication of this new expression with $\mathbf{X}^{\mathbf{T}}$ results in $\mathbf{X}^{\mathbf{T}}\mathbf{F}\mathbf{X}\mathbf{C'} = \mathbf{X}^{\mathbf{T}}\mathbf{S}\mathbf{X}\mathbf{C'}\boldsymbol{\varepsilon}$. The first three matrices of the l.h.s. are combined to form the new Fock matrix, **F'**, while the first three matrices on the r.h.s. equal unity. We can write the reformed Roothaan–Hall matrices as $\mathbf{F'C'} = \mathbf{C'}\boldsymbol{\varepsilon}$. The first step in the iterative procedure is to diagonalize **F'** to obtain **C'**. The new values for **C'** on the l.h.s. are inserted into **C'** of the r.h.s. and these cycles continue until the change in the elements of **C'** satisfies imposed convergence criteria. This iterative process is called the "self-consistent field" (SCF) procedure as the orbitals are optimized relative to previous potential field.

HF theory does not consider electron correlation and there have been a variety of "post SCF" solutions that have been proposed to correct the E_{HF} energy (e.g. perturbation theory, couple-cluster theory, configuration interaction, etc.). One tractable way of calculating the energy of a polyatomic system that includes the exchange and correlation energies is density functional theory.

1.5.2 Density Functional Theory

In density functional theory (DFT), the energy of a system is determined from the electron density ($\rho(\mathbf{r})$) of the system. Briefly, a functional, $F[f]$, is a rule where the

argument is a function and a number is associated with the function *f*. Hohenberg and Kohn introduced the "existence theorem", which shows that there is a direct point for point relationship between the total energy and the electron density of a given system.[56] Because of the existence theorem, the time-independent Schrodinger equation can be written as:

$$H\psi = E_{DFT}[\rho]\psi \qquad [20]$$

The expression for the energy from the DFT method is shown in Equation 21, where T_{ni}, V_{ne}, and V_{ee} are the electron kinetic, electron-nuclear potential, electron–electron, energies, respectively and ΔT, and ΔV_{ee} are the corrections to the kinetic and electron-electron energies, respectively.

$$E_{DFT}[\rho(r)] = T_{ni}[\rho(r)] + V_{ne}[\rho(r)] + V_{ee}[\rho(r)] + \Delta T[\rho(r)] + \Delta V_{ee}[\rho(r)] \qquad [21]$$

If atomic orbitals, ϕ_i, are used as in HF theory, the E_{DFT} expression is as follows:

$$E_{DFT}[\rho(r)] = \sum_{i}^{N}\left(\left\langle\phi_i\left|-\frac{\nabla_i^2}{2}\right|\phi_i\right\rangle - \left\langle\phi_i\left|\sum_{k}^{nuc}\frac{Z_k}{|r_i - r_k|}\right|\phi_i\right\rangle\right) + \sum_{i}^{N}\left\langle\phi_i\left|\frac{1}{2}\int\frac{\rho(r')}{|r_i - r'|}\right|\phi_i\right\rangle + E_{XC}[\rho(r)] \qquad [22]$$

The first three integrals, which are the electron kinetic energy, electron-nuclei potential energy, and electron self-interaction energy terms, can be solved, but the ΔT and ΔV_{ee} terms are combined in the term called $E_{XC}[\rho(\boldsymbol{r})]$, which is the exchange-correlation

energy. It is this term that is unknown and has been the primary focus of DFT development.

As in HF theory, the DFT equations can be expressed in matrix form and solved with the self-consistent approach, which was demonstrated by Kohn and Sham.[57] The matrix elements, K_{rs}, are analogous to the F_{rs} matrix elements and are shown in Equation 23.

$$K_{rs} = \left\langle \phi_r \left| \sum_{i=1}^{N} -\frac{\nabla_i^2}{2} - \sum_{A=1}^{A} \frac{Z_A}{|r_{Ai}|} + \int \frac{\rho(r')}{|r-r'|} \partial r' + V_{XC} \right| \phi_r \right\rangle \qquad [23]$$

A popular density functional that approximates the exchange and correlation energies is B3LYP, which is a combination of the Becke3 (B3) exchange[58] and Lee–Yang–Parr (LYP) correlation[59] functionals, respectively. The expression for the B3LYP energy (Eq. 24) is the sum the local spin-density approximation exchange, HF (or exact) exchange, gradient corrected B88 exchange,[60] LYP correlation, and Vosko–Wilk–Nusair correlation[61] energies, respectively.

$$E_{XC}^{B3LYP} = (1-a_0)E_X^{LDA} + a_0 E_X^{HF} + a_k \Delta E_X^{B88} + a_C E_C^{LYP} + (1-a_C)E_C^{VWM} \qquad [24]$$

The constants in this functional are a_0, a_x, and a_C, and have values of 0.20, 0.72, and 0.81, respectively. Since exact exchange is admixed into B3LYP this functional is in the "hybrid" category of density functionals.

1.5.3 Bader's "Atoms in Molecules" Analysis

In Bader's analysis, the charge density ($\rho(\mathbf{r})$) of a given molecule, which is a physical observable, is analyzed for critical points (CP) in the density. The location of a CP is denoted by the position vector, $\mathbf{r}_c$, and at these points the first derivative of the density vanishes ($\nabla(\rho(\mathbf{r}_c) = 0$); therefore, these points can be minima, maxima, or saddle points in the density. The charge density of a molecule is three-dimensional and so there are three curvatures at a CP; the number of curvatures is called the rank (ω) of the CP. Through the Hessian matrix ($\mathbf{A}(\mathbf{r}_c)$ Eq. 25), which is a (3x3) array of the second derivatives of coordinates with respect to the density ($\delta^2\rho/\delta q^2$), the curvatures at a given CP are determined.

$$\boldsymbol{A}(\boldsymbol{r}_c) = \begin{pmatrix} \frac{\partial^2\rho}{\partial x^2} & \frac{\partial^2\rho}{\partial x\partial y} & \frac{\partial^2\rho}{\partial x\partial z} \\ \frac{\partial^2\rho}{\partial y\partial x} & \frac{\partial^2\rho}{\partial y^2} & \frac{\partial^2\rho}{\partial y\partial z} \\ \frac{\partial^2\rho}{\partial z\partial x} & \frac{\partial^2\rho}{\partial z\partial y} & \frac{\partial^2\rho}{\partial z^2} \end{pmatrix} \qquad [25]$$

Upon the diagonalization of the Hessian matrix ($\mathbf{\Lambda}$ Eq. 26), the off diagonal elements vanish and the trace elements (eigenvalues), of which there are three, identify the character of these CPs. The sum of the signs of these eigenvalues ($\lambda_1+\lambda_2+\lambda_3$) is the signature ($\sigma$) of the CP; as such, the CPs are marked by the rank and signature as (ω, σ).

$$\mathbf{\Lambda} = \begin{pmatrix} \frac{\partial^2 \rho}{\partial x^2} & 0 & 0 \\ 0 & \frac{\partial^2 \rho}{\partial y^2} & 0 \\ 0 & 0 & \frac{\partial^2 \rho}{\partial z^2} \end{pmatrix} = \begin{pmatrix} \lambda_1 & 0 & 0 \\ 0 & \lambda_2 & 0 \\ 0 & 0 & \lambda_3 \end{pmatrix} \quad [26]$$

For example, the result of this analysis at atomic centers gives three eigenvalues that are negative in character; therefore, atoms have a rank 3 for the curvatures and have a signature of –3 for the sum of the signs of the eigenvalues. The CPs at atomic centers are therefore labeled as (3, –3). There are three other possibilities for the signatures of rank 3 CPs, which include:

- (3, –1): two negative eigenvalues; one positive
- (3, +1): one negative eigenvalue; two positive
- (3, +3): all three eigenvalues positive

The (3, –1) CP is called a bond critical point (BCP) because it connects two independent trajectories in the gradient field of the density that originate at two adjacent atoms. Likewise, the (3, +1) CP is termed a ring critical point (RCP) because these CPs are located inside the ring of atoms that are linked together by a series of BCPs. Accordingly, if this ring motif is extended in a third dimension then a cage critical point, which is denoted (3, +3), is located in the density.

CHAPTER II

CARBON–HYDROGEN BOND ACTIVATION IN HYDRIDOTRIS(PYRAZOLYL)BORATE PLATINUM(IV) COMPLEXES: COMPARISON OF DENSITY FUNCTIONALS, BASIS SETS, AND BONDING PATTERNS*

2.1 Introduction

The goal of facile conversion of saturated hydrocarbons into desirable organic materials motivates C–H bond activation research, and platinum is an important metal for these reactions.[62] Garnett and Hodges[63] were the first to report platinum mediated C–H bond activation and they observed H/D exchange between deuterated water and aromatic substrates catalyzed by Pt^{II} salts in an acidic solution. Shilov and coworkers[2,16,18] investigated the catalytic oxidation of methane to methanol and chloromethane by [$PtCl_4^{2-}$] and [$PtCl_6^{4-}$] salts in acidic aqueous solution. The research into mechanistic aspects related to the Shilov chemistry is chronicled in two reviews,[19b,19c] which include a discussion of the formation of five-coordinate, coordinatively unsaturated Pt^{IV} complexes and their purported role in the reductive elimination (RE) step.

The isolation of five-coordinate Pt^{IV} complexes is important because they are believed to be intermediates in platinum mediated oxidative addition (OA) and RE chemistry. The first isolated five-coordinate Pt^{IV} alkyl complex[64] was implicated in C–C bond forming RE chemistry,[65] and Goldberg and coworkers[66] proposed five-coordinate, coordinatively unsaturated Pt^{IV} complexes as intermediates in C–H and C–C RE coupling reactions. Templeton and coworkers[67] isolated three different five-coordinate, Pt^{IV} complexes that were stabilized by silanes, and proposed several five-coordinate, Pt^{IV} complexes as intermediates.[68]

In a theoretical study of Shilov chemistry, Siegbahn and Crabtree[23] argued that a σBM mechanism is preferred over OA/RE mechanism; however, the possibility of the oxidative pathway could not be eliminated because of the similar energetics to that of metathesis. They also stated that the solvent was integral to the reaction. Bartlett et al. reported two studies of RE C–H coupling that used Pt^{II} and Pt^{IV} model complexes,[69] and both reports arrived at the same conclusion. For Pt^{II} complexes, direct elimination of methane was found to be favored energetically over phosphine loss prior to RE C–H coupling, but ligand loss prior to C–H coupling was preferred for the Pt^{IV} complexes.

Jensen et al.[26] reported the RE of methane and OA of benzene-d_6 to form [κ^3-$Tp^{3,5-Me}Pt^{IV}(C_6D_5)_2D$] from [$\kappa^3$-$Tp^{3,5-Me}Pt^{IV}(CH_3)_2H$] (**1'**), where $Tp^{3,5-Me}$ (or Tp*) is the hydridotris(3,5-dimethylpyrazolyl)borate ligand (Scheme 2.1).[25] From the kinetic studies, enthalpic barriers to methane formation (barrier 1 – Ba1) and methane release (barrier 2 – Ba2) from **1'** were measured and reported. The proposed mechanistic step for Ba1 is C–H coupling between a methyl ligand and the hydride of **1'**, and for Ba2,

methane elimination from **1'**. The authors concluded that this elimination precedes benzene addition, which is consistent with a dissociative mechanism. Another recent report also concluded that the dissociative mechanism is the preferred pathway for methane elimination from Pt^{IV} complexes.[70] Suggestions have been made that the Tp* ring *trans* to the hydride could de-chelate, bind in a κ^2- interaction to the platinum center, and provide an open coordination site. Zarić and Hall reported that loss of one degree of coordination of the Tp ligand ($\kappa^3 \rightarrow \kappa^2$) occurred prior to methane activation in a TpRh(CO) complex.[71]

Scheme 2.1

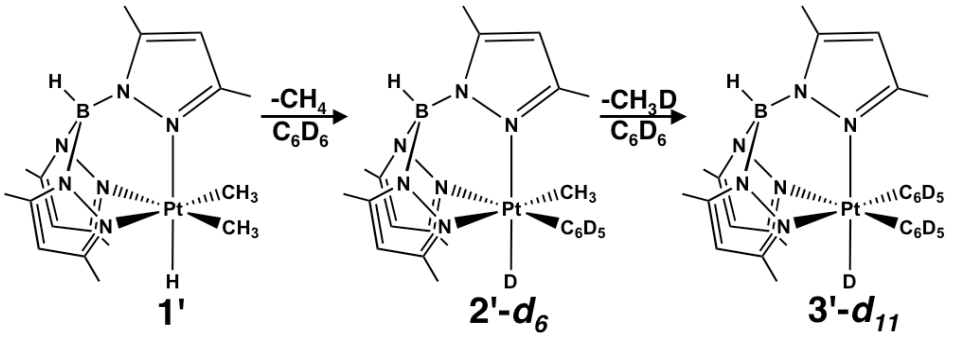

Here, the results of a DFT[33] study on the reaction in Scheme 2.1 are presented. Specifically, 31 density functionals and a variety of basis sets are benchmarked against the experimental values of Ba1 and Ba2 that were reported by Jensen et al. For some of the reported results, the experimental Tp* ligand (**1'**, etc) is replaced with the parent Tp ligand (**1**, etc). The basic mechanism for the reaction studied is presented in section

2.2.1 and possible alternative pathways for the mechanism of C–H coupling and methane release are examined in section 2.2.2. The bonding schemes of several complexes are presented in section 2.2.3; studies in benchmarking DFT and various basis sets against the experimental values for Ba1 and Ba2 are presented in section 2.2.4.

2.2 Results and Discussion

2.2.1 Mechanism

In the following section, specific steps of the mechanism from the dimethyl reactant (**1**) to the methyl–phenyl intermediate (**10**) are studied. The mechanism and relative energies of the two barriers and the specific coordination modes of benzene in the methyl–benzene complexes (**6** and **8**) are presented and discussed. Then, the analogous reaction pathway for the release of the second methane and coordination of the second benzene to form the final diphenyl product (**19**) is presented.

Procedure: All calculations were performed by using the Gaussian 03 suite of programs.[72] Each complex reported in this section was fully optimized at the B3LYP/BS1 level of theory, and the analytical frequencies were calculated at this same level of theory for each complex to determine if the force constants were real (intermediate) or if one was imaginary (transition state). All optimizations were accomplished with the default convergence criteria and each complex was optimized in C_1 symmetry. The B3LYP hybrid density functional is comprised of the Becke3 exchange[58] functional and the Lee, Yang, and Parr correlation[59] functional. The basis set (BS1) that was used in the optimization and frequency calculations is as follows:

platinum was assigned the Hay and Wadt small core Los Alamos National Laboratory effective core potential[73] (ECP = LANL2) and valence double-ζ (341/341/21 = DZ) basis set (BS) as modified by Couty and Hall[74] (ECP/BS = LANL2mDZ); each nitrogen, boron, and the carbon and hydrogen atoms bound to the platinum were assigned Dunning's correlation consistent polarized valence double-ζ (cc-pVDZ) basis set;[75] all other atoms were assigned Dunning's full double-ζ D95 basis set.[76] Details for the density functionals and basis sets benchmarking studies will be given later. Unless noted otherwise, all energies are in kcal•mol^{-1} and relative to **1**. Most values discussed in the text are enthalpies ($\Delta H^{\circ/\ddagger}$) in the gas phase at standard conditions (298K, 1 atm). The electronic energies (ΔE_{elec}), electronic energies with zero point corrections (ΔE_0), and free energies ($\Delta G^{\circ/\ddagger}$) are reported in tables. Three-dimensional molecular geometric representations were constructed with JIMP 2.[77]

Table 2.1. Relative B3LYP/BS1 energies for complexes **1** through **10**.

complex	energies			
	ΔE_{elec}	ΔE_0	$\Delta H^{\circ/\ddagger}$	$\Delta G^{\circ/\ddagger}$
1[a]	0	0	0	0
2-TS[a]	24.15	24.14	24.33	23.70
3[a]	20.82	20.82	21.43	19.49
4-TS[a]	32.28	32.28	33.76	26.90
5[a,b]	32.56	32.56	33.76	20.64
6[b]	14.46	14.46	15.76	15.42
7-TS[b]	20.58	20.58	21.68	21.52
8[b]	19.20	19.20	20.67	19.33
9-TS[b]	20.06	20.06	20.92	22.40
10[b]	–4.55	–4.55	–3.60	–2.15

a:+ C_6H_6. *b*:+ CH_4 Energy values are given in kcal•mol^{-1} and are relative to **1**.

[κ^3-TpPt^{IV}(CH$_3$)$_2$H] (1) + C$_6$H$_6$ to [κ^3-TpPt^{IV}(CH$_3$)(C$_6$H$_5$)H] (10) + CH$_4$: The B3LYP/BS1 reaction energy profile for reductive elimination (C–H bond formation), methane release, benzene coordination, and oxidative addition of benzene is displayed in Figure 2.1. The orientations of the ligand atom positions in the complexes, as referenced in the text, are defined in Figure 2.2. The relative energy values (**1** + benzene = 0) for species **1** through **10** are tabulated in Table 2.1. The B3LYP/BS1 optimized geometries of complexes along the potential energy surface (PES), with relevant bond distances (Å), are shown in Figure 2.3.

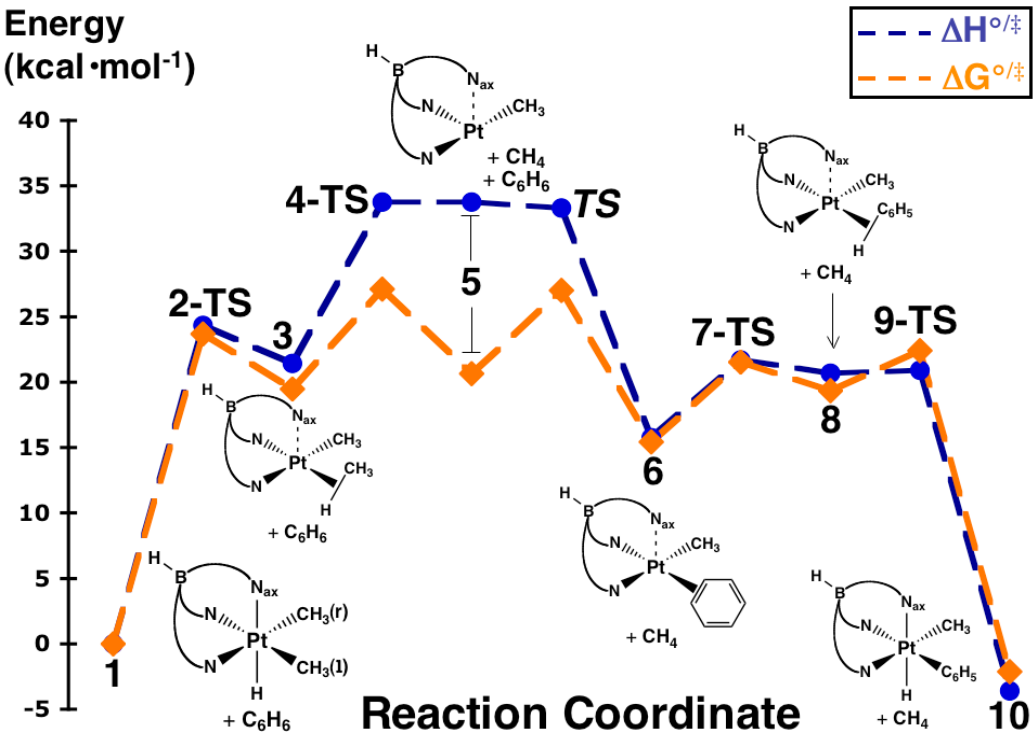

Figure 2.1. The B3LYP/BS1 relative enthalpies (blue) and free energies (orange) for complexes **1** through **10** (kcal•mol^{-1}). The complex designations correspond to the structures listed in Figure 2.3 and Table 2.1. The TS that connects **5** and **6** (***TS***) *was not calculated* and is only a qualitative representation.

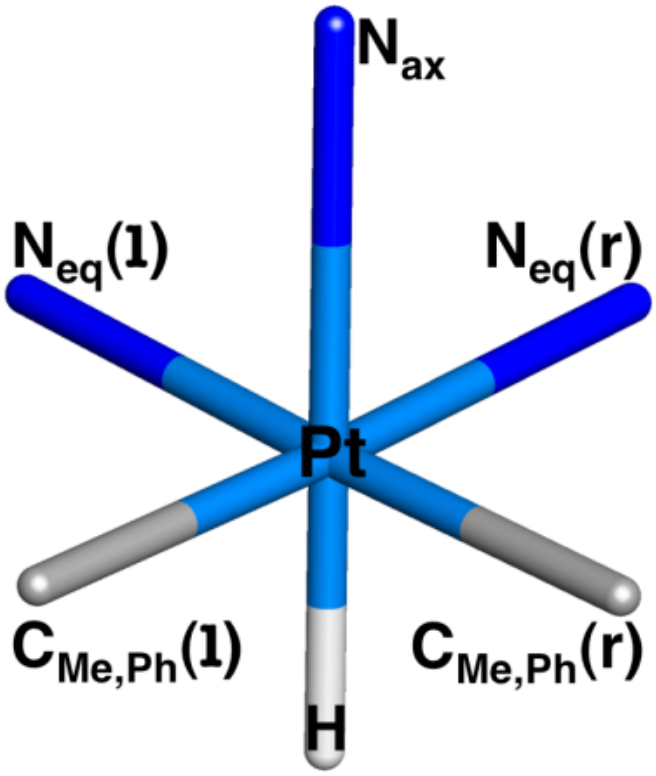

Figure 2.2. A generalized model that illustrates the orientations of the atoms within the ligands. These assignments are referenced in the text.

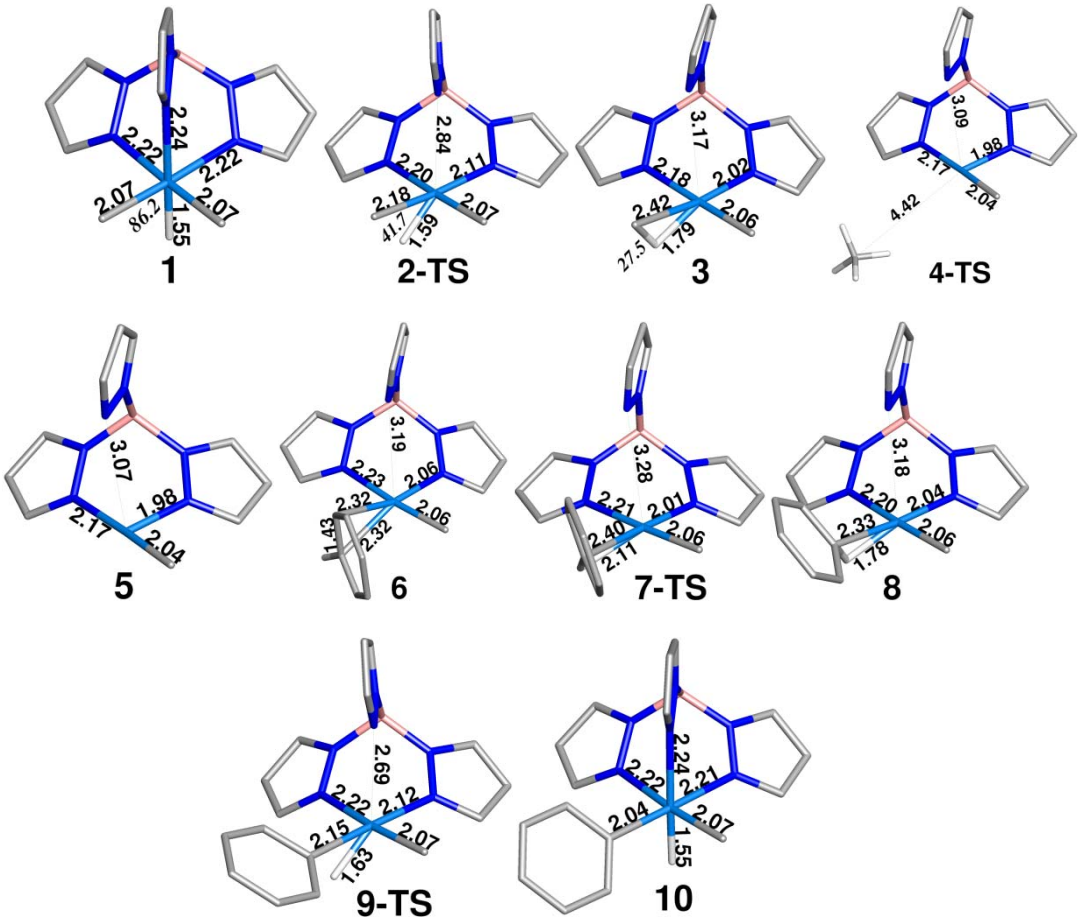

Figure 2.3. The optimized geometries for complexes **1** through **10**. Relevant bond lengths are included in the representations, and are given in angstroms. The C_{Me}(l)–Pt–H angles (degrees) are the numbers in italics. All non-essential hydrogen atoms have been removed for clarity.

C–H coupling through reductive elimination of methane (Ba1): In reactant **1**, the stronger trans influence of the hydride is noticeable in the slightly longer Pt–N_{ax} bond. The transition state for the C–H coupling mode (**2-TS**) has an enthalpic barrier of 24.3 kcal•mol^{-1} and can be characterized as a late transition state in which the C_{Me}(l)–Pt–H angle has decreased by more than half its original value. This transition state leads to the formation of the relatively unstable intermediate **3** where the Pt–C_{Me}(l) bond has lengthened by 0.35 Å, and the C–H bond is 1.17 Å. During this process the Pt–N_{ax} progressively lengthens and **3** is essentially a four-coordinate square planar complex as expected for a d^8 metal (Pt^{II}). The Pt–N_{eq}(r), which is trans to the weakly bound CH_4 molecule, has shortened by 0.2 Å.

Methane loss from 3 (Ba2): When the weakly bound CH_4 ligand of **3** is released the Pt–N_{eq}(r) bond shortens to its minimum length (1.98 Å). The unimolecular dissociation transition state (**4-TS**) for this process is characterized by an enthalpic difference of 33.8 kcal•mol^{-1} (relative to **1**) and results in a coordinatively unsaturated (three-coordinate), $16e^-$ Pt^{II} (d^8) species (**5**) where the Pt–N_{ax} distance shortens slightly from that of **3**. This intermediate, **5**, is nearly isenthalpic with **4-TS**, and this result is explained below. The Pt–C_{Me}(r) and –N_{eq}(l) bond lengths are unaffected by methane release.

Common assumptions for the dissociation of a neutral dative ligand from a transition-metal complex that does not rearrange following a dissociation are as follows: (1) that entropy does not contribute until after the transition state is passed and (2) no enthalpic barrier exists for the recoordination.[42b,78] With this assumption the free energy

barrier ($\Delta G^{\ddagger}$) equals the enthalpic barrier ($\Delta H^{\ddagger}$). In Figure 2.4, the relative enthalpies and free energies versus length of the Pt–C_{Me}(l) coordinate starting from **3** are plotted for six points; the enthalpy curve plateaus at 4.42 Å and a value of 34 kcal•mol^{-1}, while the free energy curve plateaus at a length of 3.62 Å and a value of 26 kcal•mol^{-1}. The dissociation transition state, **4-TS**, is chosen to be located at 4.42 Å because both curves have plateaued by this point, and **4-TS** is isenthalpic with the relative enthalpy difference between **1** and **5**. Our primary purpose here is to consider the enthalpic barrier to methane release and we have shown that the enthalpic difference between the separated products and the starting material is a good approximation for the experimental enthalpic barrier; therefore, *Ba2 is defined as the calculated relative enthalpic difference between **1** and **5** (+ free methane).* The relative free energy difference does not increase at the same rate as the enthalpy so there is a contribution of the entropy to the transition state. The difference between the common assumption and the free energy difference calculated for **4-TS** is 4.9 kcal•mol^{-1}, ~38% of the total entropy for the dissociation to **5** (+ free methane).

Barriers 1 and 2: The experimental and calculated barriers (Ba1 and Ba2) are compared in Figure 2.5 where the energies are reported for Tp (**1** = 0.0) and for Tp* (**1'** = 0.0) in square brackets, and we observe agreement within two units of experimental uncertainty between the calculated and experimental value for both barriers; however, both calculated values are slightly less than the experimental value. For methane release from **1'**, the B3LYP/BS1 value for Ba1 is similar to that of **1**; however, the value for Ba2 is eight kcal•mol^{-1} less than experiment. The Pt–N_{ax} distance of **5'** (2.15 Å) is 0.92 Å

shorter than that of **5** (3.07 Å), and the result is the stabilization of the coordinatively unsaturated intermediate.

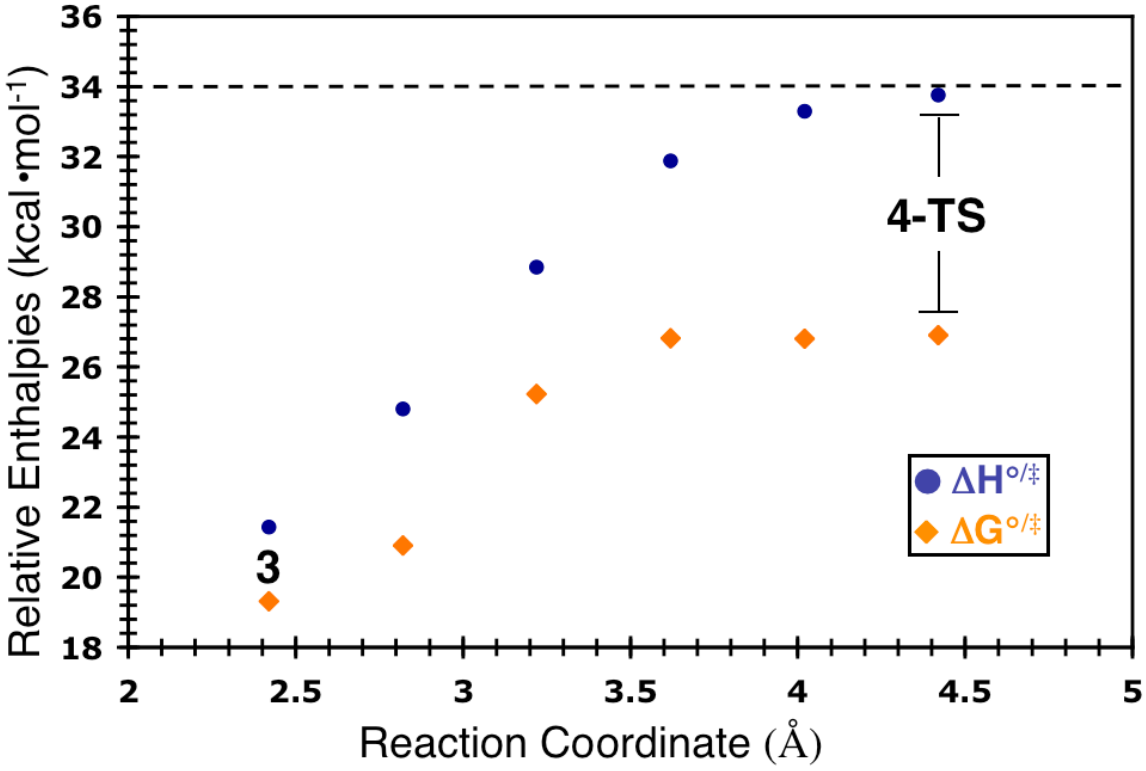

Figure 2.4. Relative enthalpy and free energy values for six select points along the Pt–$C_{\sigma\text{-Me}}$(l) coordinate. The dashed line represents the calculated enthalpic value for Ba2 (**4-TS**).

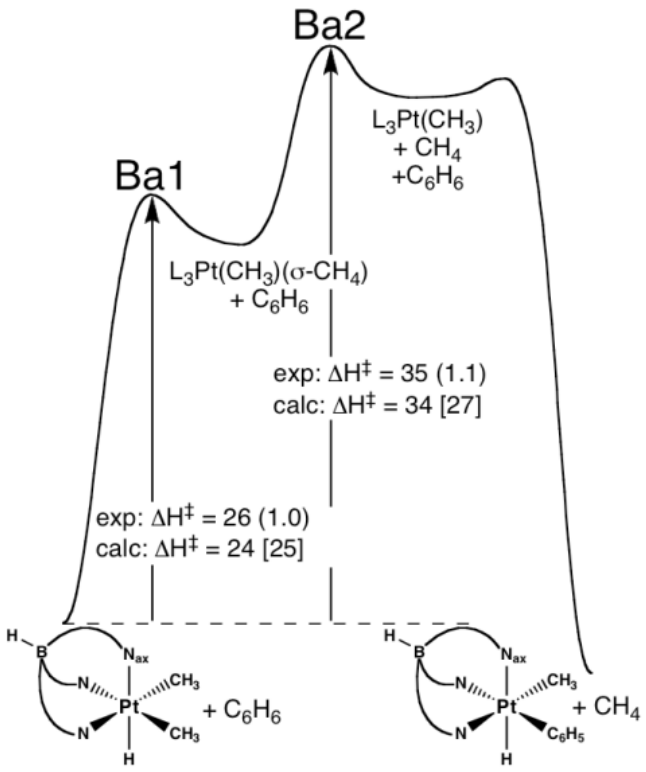

Figure 2.5. Comparison of the experimental and B3LYP/BS1 values for Ba1 and Ba2 (kcal•mol^{-1}). The Tp ligand is denoted as "L_3". The values in square brackets are the calculated values relative to **1'**.

Benzene coordination and OA to form [κ^3-TpPt^{IV}(CH$_3$)(C$_6$H$_5$)H] (10): The transition state for benzene coordinating to **5** (***TS*** – Figure 2.1) was not located on the B3LYP/BS1 PES, and its value was assumed to be similar to **4-TS**. There are two coordination modes for benzene to **5** that are in agreement with experimental observations:[79] (1) an η^2-benzene bound through two carbons (π bond) forming complex **6**, and (2) a σ-bound complex forming an η^2-benzene bound through a C–H bond (**8**). Species **6** is more stable than **8** by 4.91 kcal•mol^{-1}, and they are connected through **7-TS** with a barrier of 5.92 kcal•mol^{-1} (relative to **6**). Benzene acts as a π-donor/acceptor in **6**

as the calculated carbon–carbon bond length of the two carbons π-bound to the platinum center (1.43 Å) is slightly longer than that calculated for the carbon–carbon bond length of free benzene (1.40 Å). The Pt–N_{eq}(r) bond length is slightly longer in **6**, which, coupled with the relative enthalpy difference, supports the view that benzene is a donor in the π-bound form. Reinartz et al.[67] reported geometric parameters of an isolated η^2 benzene complex that is analogous to **6**, and the calculated parameters of **6** agree well with their complex; the experimentally determined Pt–C, Pt–N_{eq}(r), and C–C bond lengths are shorter compared to those in **6** by 0.08, 0.07, and 0.02 Å, respectively. The geometries of **6** and **8** are pseudo square planar (four-coordinate) at platinum and the Pt–N_{ax} distance is long for both. The facile OA splitting of the σ-C–H bond occurs (**9-TS**) to form the pseudo-octahedral complex, **10**. Overall, the exchange of phenyl for methyl is slightly exothermic.

From [κ^3-TpPt^{IV}(CH_3)(C_6H_5)H] (10) to [κ^3-TpPt^{IV}(C_6H_5)$_2$H] (19): The B3LYP/BS1 reaction profile for the elimination of the second methane and addition of the second benzene (**10** to **19**) is shown in Figure 2.6 and is analogous to Figure 2.1. The molecular geometries for complexes **11** through **19** are analogous to the complexes involved in the first methane elimination and benzene addition events, and these representations are included in Figure A-1. Calculated relative energies for complexes **10** through **19** are reported in Table 2.2. The calculated bond lengths of **19** are in agreement with the bond lengths found in the crystal structure, and this result is shown in Figure 2.7. The overall reaction is calculated to be exothermic and exergonic by 4.36 and 1.26 kcal•mol^{-1}, respectively. To compare the two methane release events, the

analogues of Ba1 and Ba2, in this second replacement, are one and three kcal•mol^{-1} less than the B3LYP/BS1 values of Ba1 and Ba2 for the first replacement. The analogous barriers are defined as **11-TS** and **14** and are both relative to **10**. As with the addition of the first benzene, the transition state for benzene addition to **14** (***TS)*** was not located; however, ***TS*** is qualitative and included in Figure 6.

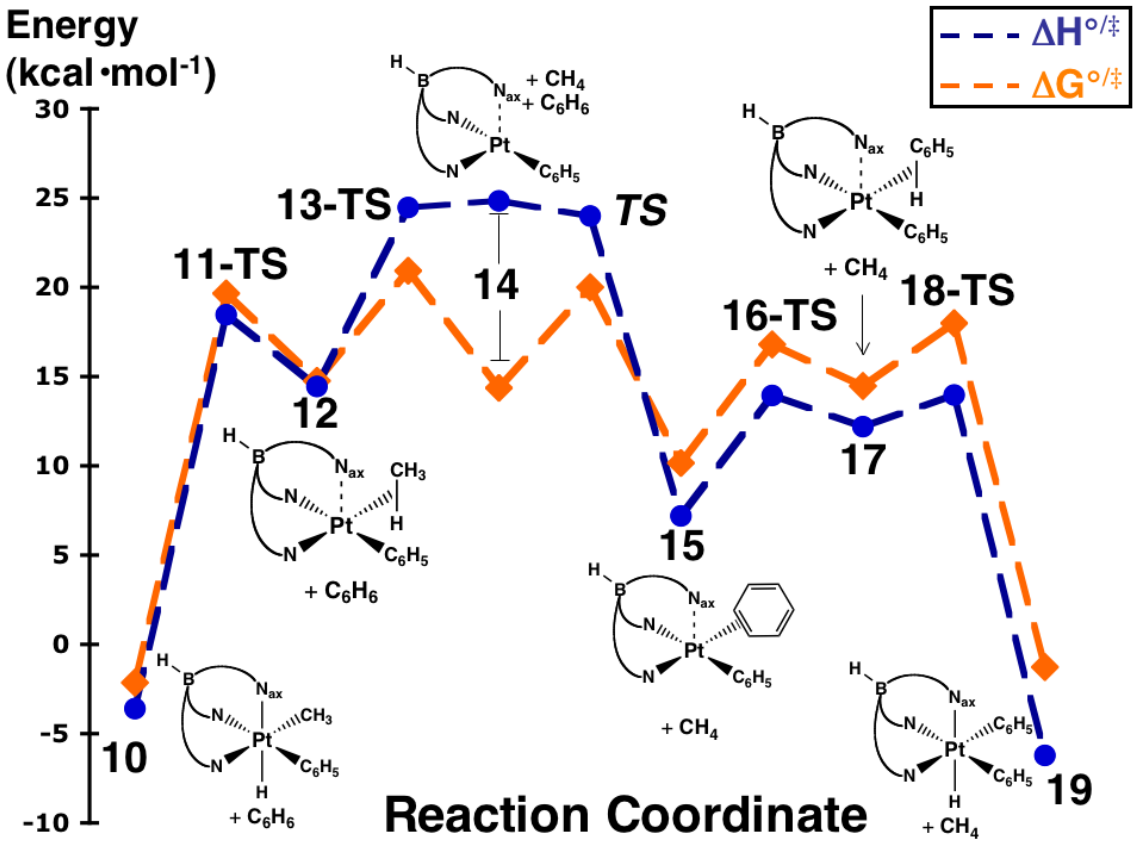

Figure 2.6. The B3LYP/BS1 calculated relative enthalpies (blue) and free energies (orange) in kcal•mol^{-1} for **10** to **19** (values relative to **1**). The species included in the Figure are representative of those listed in Figure A-1 and Table 2.2. The TS that connects **14** and **15** (***TS***) *was not calculated* and is only a qualitative representation.

Table 2.2. Relative B3LYP/BS1 energies for complexes **10** through **19**.

complex	energies			
	ΔE_{elec}	ΔE_0	$\Delta H^{\circ/\ddagger}$	$\Delta G^{\circ/\ddagger}$
10[a]	-4.55	-4.55	-3.60	-2.15
11-TS[a]	18.47	19.73	19.73	19.66
12[a]	14.45	16.14	16.14	14.75
13-TS[a]	24.48	27.00	27.00	20.92
14[a,b]	24.85	26.49	27.09	14.36
15[b]	7.20	9.64	9.64	10.15
16-TS[b]	13.95	16.12	16.12	16.80
17[b]	12.20	14.69	14.69	14.48
18-TS[b]	13.96	16.04	16.04	18.00
19[b]	-6.21	-4.36	-4.36	-1.26

a:+ C_6H_6 *b*:+ CH_4 Energies are reported in kcal•mol^{-1} and relative to **1**.

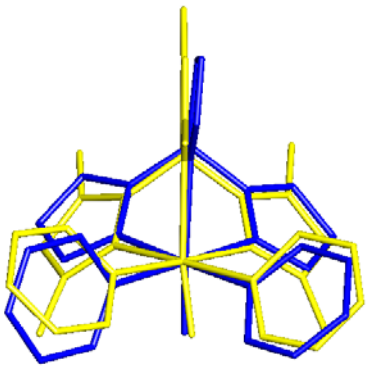

Figure 2.7. The crystal structure for [κ^3-Tp*Pt^{IV}(Ph)$_2$H] (yellow) and the B3LYP/BS1 equilibrium geometry for [κ^3-TpPt^{IV}(Ph)$_2$H] (blue) are overlaid. Bond lengths and angles are in general agreement between the two structures.

2.2.2 Alternative Pathways

In this section, alternative pathways are explored for the C–H coupling and methane release. The possibility of an associative mechanism is examined where benzene coordinates prior to methane release. Two possible orientations of a pyrazolyl (pz) ring are also examined: (1) ring *rotation* about a B–N bond resulting in a side-on interaction of a pz ring with platinum and (2) *inversion* of the boron so that a pz ring is

completely removed from the ligand sphere. Last, the possible formation of a dimer is examined. The relative energies are tabulated for the *rotation* and *inversion* pathways in Table 2.3, and these pathways are shown in Figure 2.8.

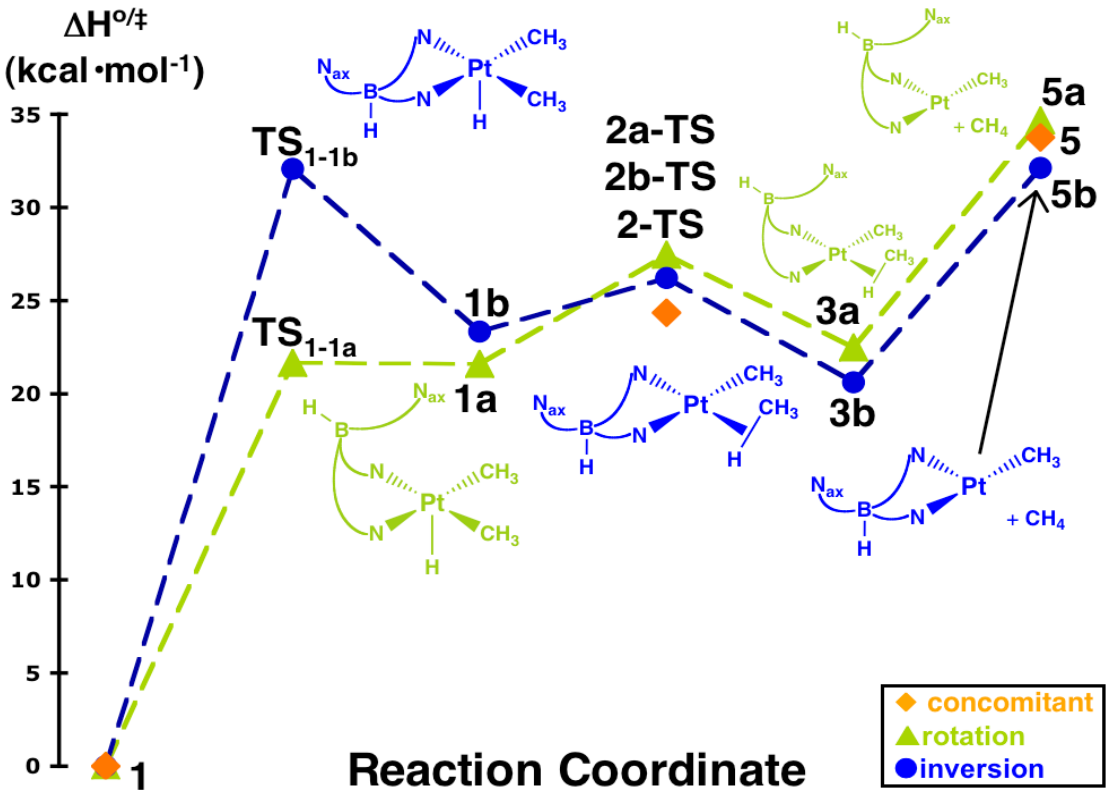

Figure 2.8. A comparison between the enthalpic PES for the concomitant (orange diamonds), *inversion* (blue dots), and *rotation* (green triangles) pathways leading to C–H bond formation (RE) and methane release. The energies, relative to **1**, are in kcal•mol^{-1}.

In Figure 2.9, representative geometries are presented for complexes on the *rotation* and *inversion* pathways; and the difference is shown between the binding modes of the Tp ligand. The complexes along the *rotation* and *inversion* pathways not shown in Figure 2.9 are shown in Figure A-2. All structures were calculated at the B3LYP/BS1 level of theory as in section 1.

Table 2.3. Relative B3LYP/BS1 energies (kcal•mol^{-1}) for *rotation* and *inversion* mechanisms.

complex	energies			
	ΔE_{elec}	ΔE_0	$\Delta H^{\circ/\ddagger}$	$\Delta G^{\circ/\ddagger}$
1[a]	0	0	0	0
TS$_{1\text{-}1a}$[a]	21.77	21.77	21.65	21.93
1a	21.28	21.28	21.60	20.92
2a-TS[a]	27.23	27.23	27.46	26.37
3a[a]	21.88	21.88	22.48	20.66
5a[a,b]	33.47	33.47	34.67	21.41
TS$_{1\text{-}1b}$[a]	32.16	32.16	32.06	31.27
1b[a]	22.82	22.82	23.32	21.78
2b-TS[a]	26.00	26.00	26.20	25.33
3b[a]	19.98	19.98	20.60	18.86
5b[a,b]	30.94	31.54	32.13	19.17

a: +C_6H_6 *b*: +CH_4 Energies are reported in kcal•mol^{-1} and relative to **1**.

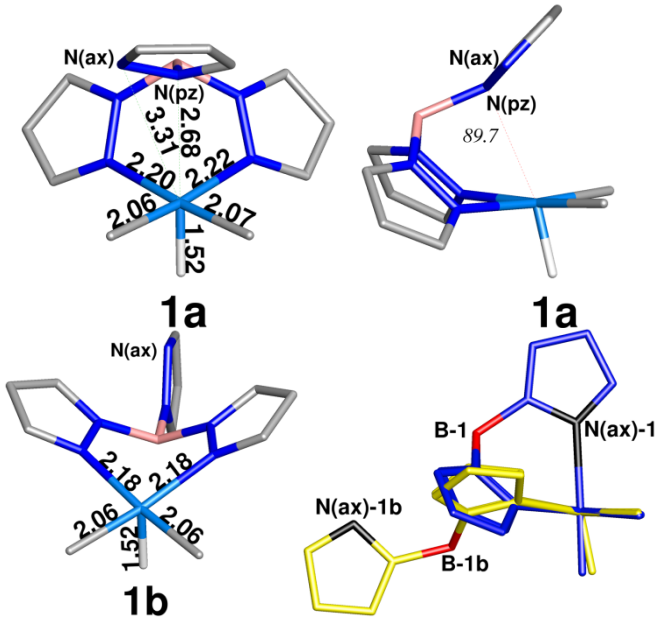

Figure 2.9. The B3LYP/BS1 optimized geometries for [κ^2-, κ'-TpPt^{IV}(CH$_3$)$_2$H] (**1a**), [κ^2-TpPt^{IV}(CH$_3$)$_2$H] (**1b**), and the comparison between the starting material (**1**-blue) and the inverted form (**1b**-yellow). Bond lengths are reported in angstroms.

Though the experimental work by Jensen et al. supported a dissociative mechanism for methane loss, evidence for an associative mechanism for methane loss was reported by Johansson and Tilset where increased concentrations of solvent acetonitrile changed the ratio of CH_4/CH_3D released from protonated Pt^{II} complexes.[80] Therefore, several models were designed to investigate the possible associative mechanism where benzene and methane are both bound simultaneously to the platinum center; the benzene and methane are π- and σ- bound to the platinum center, respectively. All attempts to locate a transition state geometry for an associative complex were unsuccessful, and our data support the dissociative mechanism (Figure 2).

The next alternative pathway (*rotation*) is described by rotation of the pz ring *axial* to the hydride about the B–N_{pz} bond (N_{pz} is the nitrogen of the *axial* pz ring bonded to the boron), and formation of a complex where two pz rings are coordinated as usual and the third pz ring has "slipped" to form a κ^2-, κ'-Tp complex (**1a**). The barrier to pz ring rotation is 21.7 kcal•mol^{-1} (**TS_{1-1a}**). The N_{pz} has a small amount of four-coordinate character as the B–N_{pz}–Pt angle is 89.7º (Figure 2.9) and the Pt–N_{pz} distance is 2.69 Å, which is ~0.5 Å longer than the Pt–N_{ax} distance in **1**. The barrier to C–H coupling (**2a-TS**) is slightly greater than that of the *concomitant* pathway in Figure 2.1 (*rotation*: 27.5 vs. *con*: 24.1 kcal•mol^{-1}), and a pseudo-square planar (four-coordinate) complex (**3a**) results from C–H coupling. As with the *concomitant* pathway, the 16e$^-$, coordinatively unsaturated Pt^{II} (d^8) complex that results from methane loss (**5a**) is stabilized by an increase in the interaction of pz ring that was trans to the hydride, but is now trans to the vacant coordination site.

In the *inversion* pathway, the *axial* pz ring is removed from the ligand sphere by inversion of the boron geometry, which results in a κ^2-Tp ligand. The barrier to inversion (**TS_{1-1b}**) is 32.1 kcal•mol^{-1}, which is the highest initial barrier of any of these pathways. A five-coordinate Pt^{IV} species (**1b**) is formed where the *axial* pz ring is outside of the coordination sphere, and the boron is shown to reside below the *equatorial* pz rings (Figure 2.9). The C–H bond coupling transition state (**2b-TS**) is 26.6 kcal•mol^{-1} (relative to **1**), which is slightly greater than the *concomitant* pathway. A weakly bound methane complex is formed (**3b**) and loss of methane from this complex results in a

three-coordinate, Pt^{II} complex. This pathway has the lowest value for Ba2 of the three pathways at 32.1 kcal•mol^{-1}.

Summary of the two alternative pathways: Facile C–H activation of benzene by $[\kappa^2\text{-}[Ph_2B(pz)_2]Pt^{II}(Me)_2]^+$ was reported by Thomas and Peters;[81] however, the *inversion* pathway is disfavored because the initial barrier (**$TS_{1–1b}$**) is higher in energy. Both barriers along the *rotation* pathway are similar to those of the *concomitant* pathway. The calculated values for Ba1 and Ba2 are not significantly altered when the interaction between the *axial* pz ring and the platinum is changed (*rotation*) or removed (*inversion*). A difference of 10.4 kcal•mol^{-1} is measured between the initial barriers to the *inversion* and *rotation* pathways ($\Delta\Delta H°$: **$TS_{1–1b}$** – **$TS_{1–1a}$**); this difference is slightly greater than the difference of 6.4 kcal•mol^{-1} that was reported by Webster and Hall for the same barriers in the isomerization chemistry of $TpRh(CO)_2$.[82]

In a mixture of $[TpRu(PMe_3)_2OH]$ and 1-methylpyrazole in C_6D_6, H/D exchange was reported by Gunnoe and coworkers at the four position of each pz ring, and this mechanism likely proceeds through a pathway where the pz ring coordinates to the ruthenium in a side-on interaction.[83] This experimental observation supports a competitive route via the *rotation* pathway. The *rotation* and *concomitant* pathways compete in the elimination of methane because of these similar relative energies.

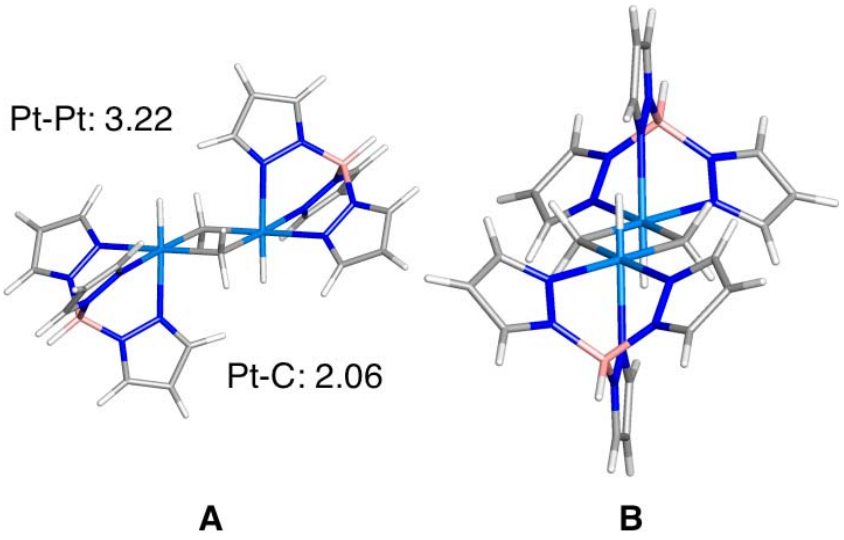

Figure 2.10. Two different views of the dimer complex. The view in **A** is down the bridging carbon-carbon atoms, while the view in **B** is down the Pt–Pt axis of the molecule. The opposing geometry of the Tp ligands is represented clearly in **A**.

Possible formation of a $[TpPt]_2$ dimer: A dimer was not observed in the kinetic studies of C–H coupling and methane release, but other studies have reported the formation and isolation of bridged binuclear complexes.[84] A common structural characteristic of the binuclear structures observed experimentally is opposing ligand geometries as seen in the calculated structure, Figure 2.10. Species **5** has an open coordination site available for dimer formation with a second molecule of **5**. In the optimized geometry of the calculated dimer, the two TpPt moieties are joined by a 4-center, $8e^-$ bridge. In addition to reformation of the Pt–H bond, the Tp ligand returns to a trisdentate interaction with the platinum. Dimer formation from **1** ($2\bullet$**1** → dimer + $2\bullet CH_4$) is exergonic (–4.5 kcal•mol^{-1}) and endothermic (2.4 kcal•mol^{-1}); because of its instability, the dimer was not studied further.

2.2.3 Bonding Analysis

To investigate the bonding interactions that are involved in this chemistry, the B3LYP/BS1 electron densities of complexes **1**, **2-TS**, **3**, **5**, and **1a** were investigated with Bader's "Atoms in Molecules" (AIM) analysis.[46] Specific bond critical point (BCP) densities that are relevant to the C–H coupling and methane release chemistry are tabulated in Table 2.4. AIM2000 was used to calculate the BCP's.[85]

The electron density of **1** was analyzed with AIM and six (3, –1) BCPs were found between the platinum and the atoms listed in Table 2.4. The Pt–N_{ax} bond CP has the least density, which results from the stronger trans influence of the hydride. The BCP densities typically follow an inverse trend with respect to bond lengths; for example, the Pt–N_{eq}(r) BCP density increases with C–H coupling and methane release and the bond length shortens for this process. The Pt–C_{Me}(r) and –N_{eq}(l) bond densities are shown to be insensitive to the C–H coupling chemistry, and this correlates with geometric observations. Interestingly, a Pt–C_{Me}(l) BCP was not located in the density of **2-TS** and **3**; thus, the bond is manifested solely by a CP between the platinum and the hydrogen. For **1a** (one pz rotated), a BCP was located along the Pt–N_{pz} coordinate with a density of 0.030405 e•bohr^{-3}, which is significantly less than the Pt–N_{ax} BCP density value of **1**. The decrease in BCP density is consistent with an increase in bond lengths, but the multiple CP's that are characteristic of a ligand π-bound to a metal (i.e. η^5-C_5H_5) are not observed for this rotated pz ring.

Table 2.4. Bond critical point (CP) densities for bonds involved in C–H coupling and methane release.

bond: Pt-X	(3, –1) bond CP density (ρ(r) / e•bohr^{-3})				
	1	**2-TS**	**3**	**5**	**1a**
N_{ax}	0.0727040408	0.0241899527	0.0139997372	0.0167954419	NA
N_{eq}(l)	0.0757628782	0.0791088190	0.0811165097	0.0825009156	0.0795292241
N_{eq}(r)	0.0756648650	0.0979133965	0.1203747575	0.1334978956	0.0765416921
C_{Me}(l)	0.1329266488	NF[b]	NF	NA	0.1348946156
C_{Me}(r)	0.1330781962	0.1329927831	0.1337466884	0.1403112418	0.1336717972
H	0.1741331362	0.1485854220	0.0831396505	NA	0.1816352613
N_{pz}	NA[a]	NA	NA	NA	0.0304053343

a: NF = Not Found *b*: NA = Not Applicable.

2.2.4 Density Functional and Basis Set Benchmarking

Benchmarking studies of density functionals and basis sets are presented in this section. Thirty-one functionals were benchmarked for the barriers. Basis set saturation was also studied and the trends are presented. The procedure that was used for these studies is explained prior to each benchmarking study. The mean average error (m.a.e.) is reported for each study.

Functionals: For all but two of the functionals, the optimized geometry and analytical frequencies of **1**, **2-TS**, **5**, and methane were calculated at the functional/BS1 level of theory. Intermediates and transitions states were verified as having zero and one imaginary mode, respectively, as determined by frequency calculations. To calculate the barrier value at each level of theory, the functional/BSX//functional/BS1 (X = 2, 3) energies of **1**, **2-TS**, **5** and methane were added to the function/BS1 correction to the enthalpy for each complex. For BS2 and BS3 basis sets, only the cc-pVDZ basis set of BS1 was replaced with cc-pVTZ and cc-pVQZ in BS2 and BS3, respectively, but the other basis sets remained as assigned in BS1. *All subsequent calculated values for the*

two barriers are presented at the functional/BS3 level of theory. The procedure for the B2-PLYP[86] and mPW2-PLYP[87] functionals was slightly modified because of computational costs; the B2-PLYP/BSX// and mPW2-PLYP/BSX//B3LYP/BS1 (X = 1, 2, 3) energies of **1**, **2-TS**, **3**, **5**, and methane were added to the second order correction and the B3LYP/BS1 correction to the enthalpy for each molecule to obtain the corrected enthalpy. The second-order perturbative correction was scaled by 0.27 and 0.25 for the B2-PLYP and mPW2-PLYP functionals, respectively.[88]

Pure density functionals, in which exact exchange is not incorporated, included in this study are BLYP,[60,59] BPW91,[60,89] BP86,[60,90] G96LYP,[91,59] G96PW91,[91,89] HCTH,[92] mPWPW91,[93] and PBE.[94] Hybrid density functionals (HDFT), which include a percentage of Hartree–Fock (exact) exchange, included in this study are the B3LYP,[58,59] B3PW91,[58,89] B3P86,[58,90] B97-1,[92] mPW1PW91 (mPW0),[89,93] PBE1PBE (PBE0),[94] MPW1K,[95] BH&HLYP,[96,59] and MPWLYP1M.[97] Two newly developed hybrid functionals that include contributions from unoccupied virtual orbitals via perturbation theory are included in this report: B2-PLYP and mPW2-PLYP. Meta functionals (MDFT), which include the orbital kinetic energy component, included in this study are BB95,[60,98] mPWB95,[83,93,98] mPWKCIS,[89,93,99] PBEKCIS,[94,99] TPSS,[100] and VSXC.[101] Hybrid meta functionals (HMDFT), which includes exact exchange into meta functionals, employed in this study are B1B95,[98] MPWKCIS1K,[102] BB1K,[103] MPWB1K,[104] MPW1B95,[104] and TPSSh.[105]

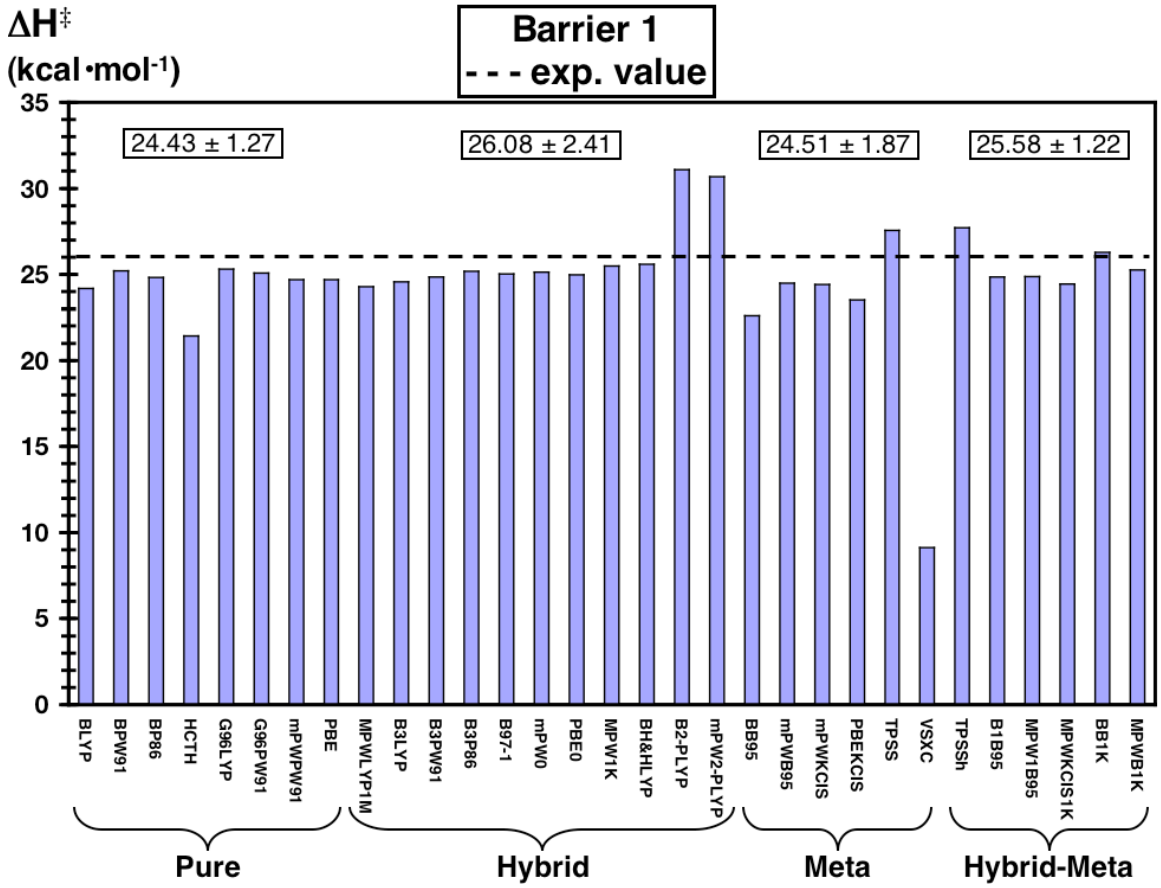

Figure 2.11. The calculated value for Ba1 for each functional. The dashed line represents the experimental value. In the boxes, the average values with standard deviations are presented for each group. The VSXC functional failed the Q-test (C.I. 90%) that was applied to the meta group and was not included in the statistics.

Barrier 1: The values of Ba1, calculated with all the functionals previously mentioned, are shown in Figure 2.11. A value for Ba1 within five kcal•mol^{-1} of experiment, which is the typical margin of error for DFT in calculating barrier heights, was calculated for all but three of the functionals tested. However, a value within one kcal•mol^{-1} of experiment, which is the definition for "chemical accuracy" of a calculation, was calculated with the BPW91, G96LYP, G96PW91, B3P86, B97-1,

mPW0, MPW1K, BH&HLYP, BB1K, and MPWB1K functionals. The error in these calculations is systematically below the experimental value; only the TPSS, TPSSh, BB1K, B2-PLYP, and mPW2-PLYP functionals calculated a value greater than the experimental value. Generally, the accuracy of the calculation does increase when exact exchange is included in the functional; for example, the MPW1K, BB1K, and MPWB1K return values that are more accurate than the mPWPW91, BB95, and mPWB95 parent functionals. The average value and standard deviation was calculated for each DFT category, and these numbers are included in Figure 2.11. A particularly poor value for Ba1 was calculated with the VSXC functional because the VSXC/BS1 optimized geometry of **2-TS** is similar to the structure of **2a-TS** where the *axial* pz ring has rotated to form the side-on interaction. For Ba1, a value of 24.3 kcal•mol^{-1} was calculated by using the HF method (HF/BS3 level of theory), and following the same procedure for this calculation as was performed with the density functionals.

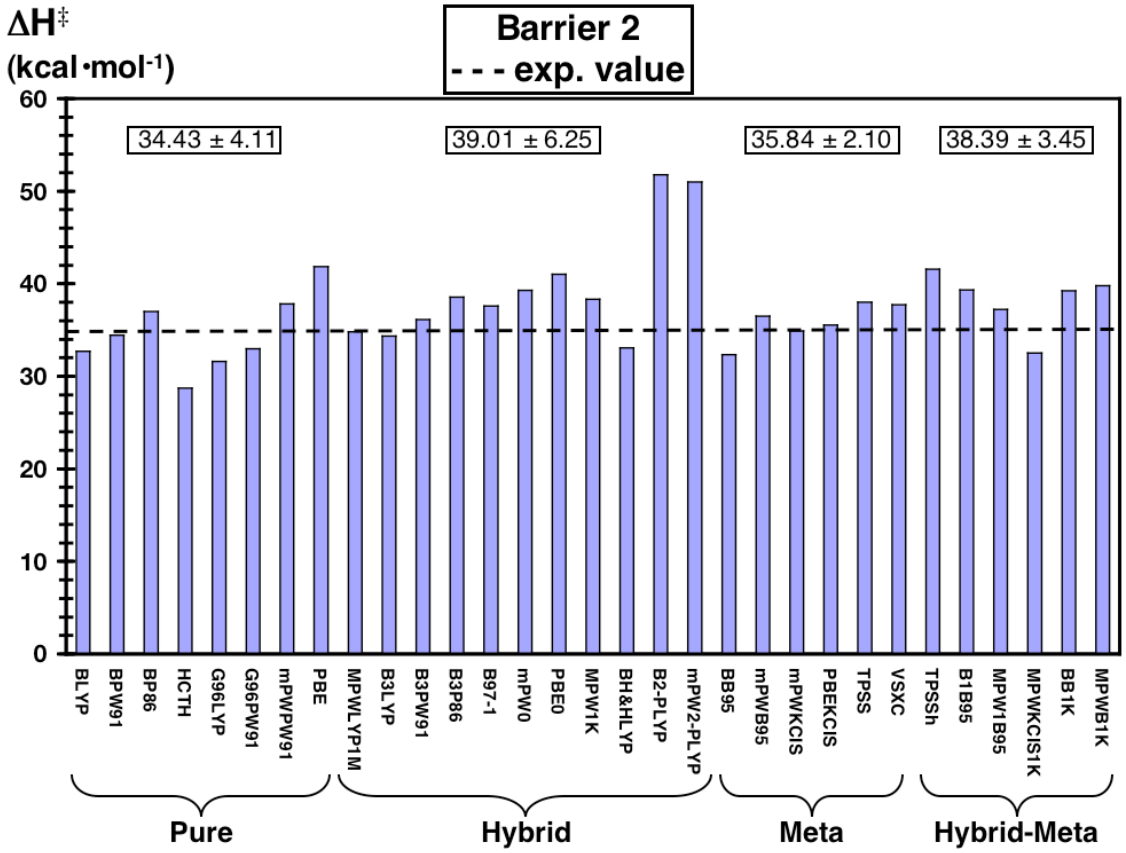

Figure 2.12. The calculated value of Ba2 for each functional. The dashed line represents the experimental value. The numbers in the boxes are the average values with standard deviations for each DFT category.

Barrier 2: In Figure 2.12, the calculated value of Ba2 is presented for each functional and for the average values for each functional group. A value for Ba2 within five kcal•mol^{-1} was calculated for all but four of the functionals tested; however, a value within chemical accuracy was calculated for only the BPW91, MPWLYP1M, B3LYP, mPWKCIS, and PBEKCIS functionals. The accuracy and precision in calculating Ba2 is poorer for each functional category; the meta category is the most accurate and precise group. For Ba2, the calculated value does increase when exact exchange is included in

the functional, but the accuracy generally decreases; for example, the meta group has a smaller average value and a lower deviation than the hybrid-meta group. At the HF/BS3 level of theory, a value of 11.2 kcal•mol^{-1} was calculated for Ba2.

Statistical Analysis: The m.a.e. for the functionals tested are listed in Table 2.5, and these values were determined for the results calculated at the functional/BS3 level of theory. From this error analysis, the best performing pure, hybrid, meta, and hybrid-meta density functionals are BPW91, MPWLYP1M, mPWKCIS, and MPW1B95, respectively; and the best overall performer is the BPW91 functional.

Table 2.5. The m.a.e. for the functionals tested in this report.

pure		hybrid		meta		hybrid-meta	
functional	m.a.e.	functional	m.a.e.	functional	m.a.e.	functional	m.a.e.
BLYP	2.05	MPWLYP1M	*0.95*	BB95	3.04	TPSSh	4.15
BPW91	***0.68***	B3LYP	1.05	mPWB95	1.52	B1B95	2.74
BP86	1.58	B3PW91	1.15	mPWKCIS	*0.84*	MPW1B95	*1.68*
G96LYP	5.44	B3P86	2.18	PBEKCIS	1.51	MPWKCIS1K	2.03
G96PW91	1.48	B97-1	1.77	TPSS	2.28	BB1K	5.46
HCTH	2.04	mPW0	2.58	VSXC	9.81	MPWB1K	2.76
mPWPW91	2.06	PBE0	3.52				
PBE	4.07	MPW1K	1.93				
		BH&HLYP	1.17				
		B2-PLYP	10.92				
		mPW2-PLYP	10.33				

Summary of density functional benchmarking studies: Overall, the accuracy of the calculations is greater for Ba1 than for Ba2; the errors in the individual calculation of **5** and methane are summed, which decreases the accuracy of the calculations of Ba2. In previous studies, more accurate values for barriers were calculated with functionals

where greater amounts of exact exchange were admixed into the functionals,[106] and this trend is supported with the data for Ba1. For example, the calculated value for Ba1 with the BLYP, B3LYP, and BH&HLYP functionals approaches the experimental value as the amount of exact exchange admixed into the functional increases. For both barriers, the average value increases when exact exchange is incorporated into the functionals; however, the deviation generally increases (Figures 11 and 12). To measure the effect of changing between common exchange and correlation functionals, the LYP, PW91, and P86 correlation functionals were paired with the B88 and B3 exchange functionals; and the general trend is that greater values (Ba1 and Ba2) were calculated in the order of LYP < PW91 < P86. The functionals with the B3 exchange functional calculated values that were greater than the corresponding functional with the B88 exchange functional. The only functional that calculated a value within one kcal•mol^{-1} for both barriers was BPW91. The B2-PLYP and mPW2-PLYP functionals, which include contributions from the virtual orbitals, are unsuitable for calculating these barrier heights as the value were much too high and diverged from experiment with basis set saturation.

Recently, Truhlar et al. performed a DFT benchmarking study[97] with a test set comprised predominantly of metal-containing compounds, and the G96LYP and MPWLYP1M functionals were shown to be suitable for these systems. In our study, accurate values for Ba1 and Ba2 were returned with the G96LYP and MPWLYP1M functionals, respectively. Quintal et al.[107] reported a benchmarking study of various functionals and found the kinetic functionals optimized for barrier heights (i.e. MPW1K) unsuitable for barriers of late row transition metal reactions; in our study, these kinetic

functionals performed well for Ba1 but not Ba2. The enthalpic values for Ba1 and Ba2 are tabulated for each functional in Table A-1 at the BS1, BS2, and BS3 levels of theory.

Basis set study: Only the first barrier (Ba1) was considered for the ECP/BS and all electron basis set benchmarking studies and only the B3LYP functional was used in the large basis set study. Twelve ECP/BSs were examined to measure the effect on the value of Ba1. The same procedure that was used to test the functionals was used here but only the ECP/BS was replaced for each test. The geometries of **1** and **2-TS** were fully optimized with each ECP/BS (with the all-electron basis sets of BS1 for the first row elements) and single-point (SP) calculations were run on these optimized geometries with the ECP/BS and the all-electron basis sets of BS3 for the first row elements. These SCF energies were then added to the B3LYP/BS1 corrections to the enthalpy for **1** and **2-TS** to obtain the relative enthalpy difference. Four ECPs were used in this study for the inner $60e^-$ of platinum and they are the Hay and Wadt LANL2,[73] the Stuttgart relativistic small core (RSC) 1997[108] ECP, the averaged relativistic (AREP) ECP of Ross et al.,[109] and the relativistic compact effective potential (RCEP) of Stevens et al. (SBKJC).[110] The basis sets coupled with the ECPs are the Hay and Wadt valence double-ζ BS[111] (HW-VDZ); the LANL2mDZ BS of Couty and Hall as previously mentioned; the valence double-ζ SBKJC BS of Steven et al.;[110] the Stuttgart/Dresden triple-ζ SDD BS; the split valence (SV), triple-ζ with one (TZVP) and two (TZVPP) polarization functions, and quadruple-ζ with one polarization function (QZVP) of Weigend and Ahlrichs.[112]

In Table 2.6, the results of benchmark studies are shown for the platinum ECP/BSs considered in this study. For each BS used in this study, the addition of a polarization function resulted in an increased valued calculated for Ba1. The modification of Couty and Hall to the HW-VDZ BS improved the value by nearly two kcal•mol^{-1}, while de-contracting the d shell to form a triple-ζ quality BS returned a similar value to that of the LANL2mDZ. Similar values for Ba1 were calculated with the TZVP and TZVPP BS; however, the values that were calculated with the SV and QZVP BS are the lowest in this study. Of all the ECP/BS that were assigned to platinum, the SV and QZVP BS are poorest for calculating the value of this barrier.

Table 2.6. The results in calculating Ba1 for various ECP/BS that were assigned to platinum.

no.	Pt: outermost 18e$^-$	ECP for Pt: inner 60e$^-$	$\Delta H^{\ddagger}$ Ba1 kcal•mol^{-1}
1	CRENBL	AREP ECP	25.22
2	SBKJC	SBKJC ECP	23.90
3	HW-VDZ (341/321/21)	LANL2 ECP	22.88
4	mLANL2DZ (341/341/21)		24.58
5	LANL2DZ(f) (341/341/21/1)		25.79
6	LANL2TZ (341/341/111)		24.95
7	SDD	Stuttgart RSC 1997 ECP	23.80
8	SDD(2f)		24.14
9	SV		21.80
10	TZVP		23.65
11	TZVPP		23.89
12	QZVP		20.38

All other atoms were assigned the basis sets of BS3

To benchmark the all-electron basis sets for the first row elements, platinum was assigned the ECP/BS of BS1 and the first row atoms were assigned the same basis sets from the list of Pople's n-Gaussian[113] (STO-nG, n=3,6) basis sets; Pople-style split

valence[114] from 3-21G to 6-311++G**; Dunning's full double-ζ basis set (DZ), double-ζ plus polarization basis set (DZP),[115] and split valence double-ζ plus polarization (SVP) basis set;[116] Ahlrich's valence double- and triple-ζ basis sets (VDZ, VTZ).[117] To measure basis set saturation, the large basis sets of the complete basis set atomic pair natural orbital (CBS-APNO) method of Petersson and coworkers were used,[118] and these basis sets are denoted CBS1 and CBS2.[119] To obtain the calculated value for Ba1, the SCF energies from these SP calculations were added to the B3LYP/BS1 correction to the enthalpy.

The results are shown in Figure 2.13 for the all-electron basis set benchmarking study. The most important factor for calculating accurate barrier values is the addition of polarization functions to the basis set, and this trend is seen for each family of basis sets. Diffuse functions, applied either to non-hydrogen atoms (+) or to all atoms (++), did not significantly alter the calculated value compared to the same basis sets without the diffuse functions. Increasing the size of the basis sets from double- to triple-zeta did not significantly alter the calculated value for the barrier. Basis set saturation was reached at the CBS1 level of theory as the addition of two f polarization functions to CBS1, producing CBS2, did not alter the calculated value of Ba1. The energies for each basis set are included in Table A-2.

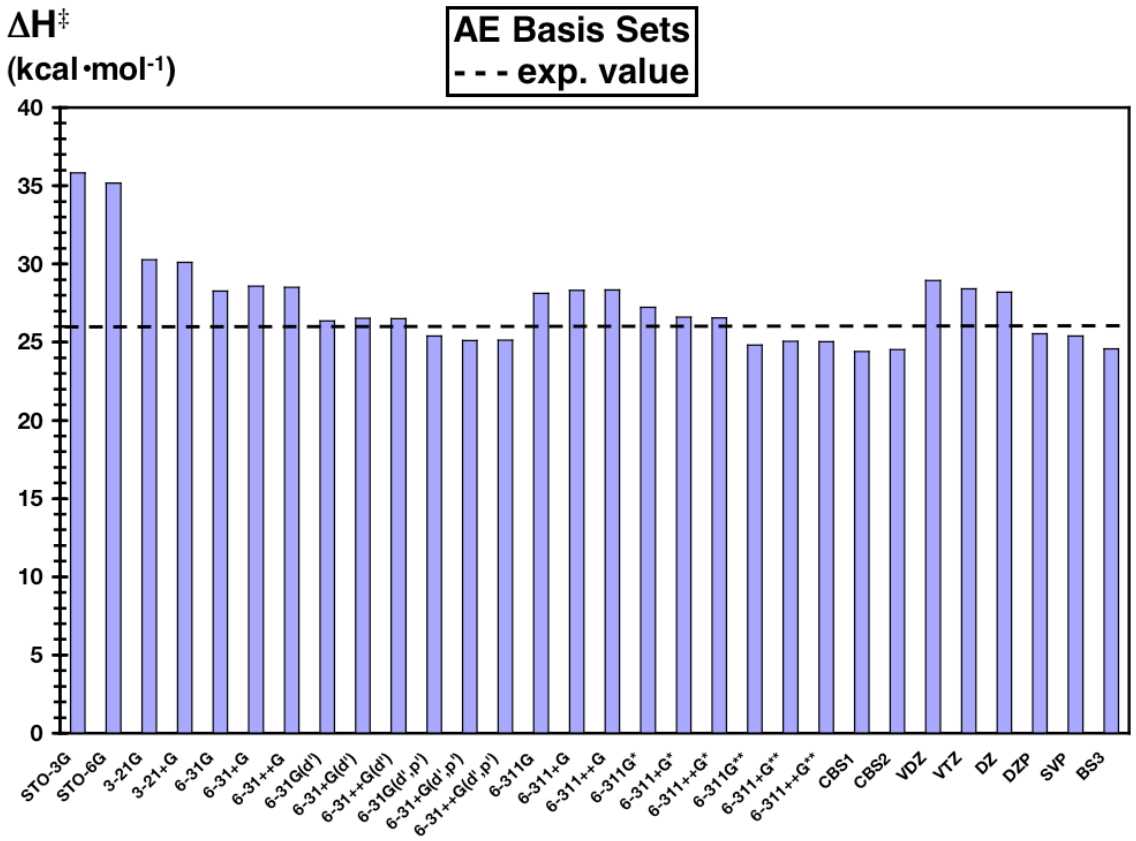

Figure 2.13. The effect of the basis set on the value of Ba1. The B3LYP/BS1 geometries were used in this study and all non-platinum elements were assigned the basis set listed. The experimental value of Ba1 is represented by the dashed line.

Basis sets and functionals: The trends in basis set saturation (BSS) are shown in Figure 2.14. For most of the functionals tested, the BSS trend is unexpected because the value calculated at the cc-pVTZ (BS2) level of theory is less than that of both the cc-pVDZ (BS1) and cc-pVQZ (BS3) levels of theory, and the data presented for the BLYP, PBE, and B3LYP functionals are representative for most of the functionals. However, there are exceptions; an expected BSS trend is observed for BB95 (Ba1 & Ba2) where the calculated value decreases with the increase in basis set size, while the BSS trend for

the TPSSh values increase and diverge from the experimental value (Ba2 only). The B2-PLYP and mPW2-PLYP functionals exhibit a similar trend as with TPSSh but for both barriers. For example, the values for Ba1 and Ba2, calculated with the B2-PLYP functional, increase from 27.7 to 31.1 and from 42.8 to 51.7 kcal•mol^{-1} for the BS1, BS2, and BS3 levels of theory, respectively.

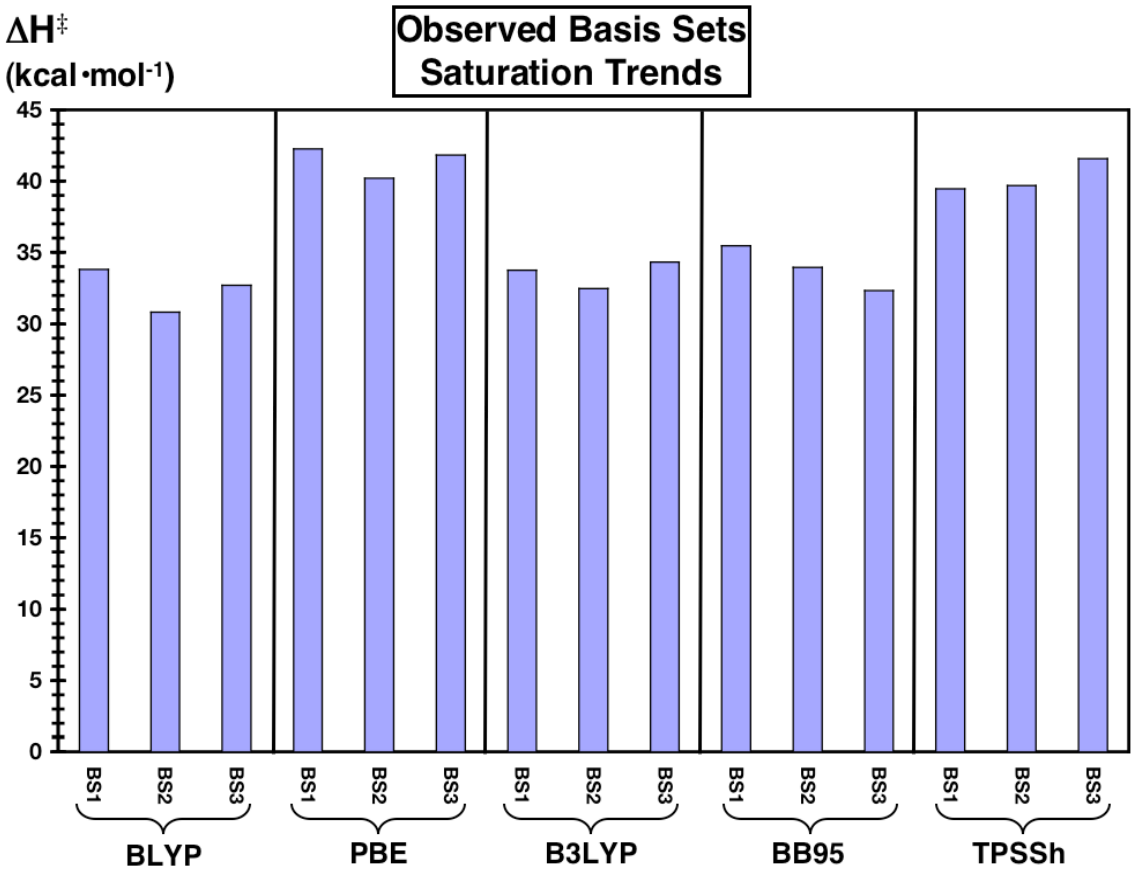

Figure 2.14. The three basis set saturation trends observed in this work. The trend represented by BLYP, PBE, and B3LYP are representative for most of the functionals tested. The exceptions are discussed in the text.

2.3 Conclusions

We presented the reaction mechanism for the conversion of **1** into **19**, where the important mechanistic barriers to C–H coupling and methane release were analyzed. Against the experimental values of these barriers, 31 density functionals were benchmarked and, within the definition of "chemical accuracy", 11 were found to be accurate for calculating the C–H coupling barrier while only 5 were accurate for calculating the value of Ba2. In general, more accurate values for Ba1 were calculated with the functionals with higher values of exact exchange (~40%) admixed into the functional, but those functionals did not perform well for calculating the dissociation barrier. Many of the common ECP/BS combinations available for platinum were found to be suitable for calculating reaction barriers; and polarization functions, added to each all electron basis set, were shown to be a requirement. In this study, DFT was shown to be a suitable method for electron correlation, as it greatly outperformed Hartree-Fock theory in calculating these two barriers.

CHAPTER III

CARBON-HYDROGEN BOND ACTIVATION: TWO, THREE OR MORE MECHANISMS?*

3.1 Introduction

Carbon–hydrogen bond activation, a critically important step in a variety of reactions, has received considerable attention.[1,15,19b] For the special case of hydrogen transfer (HT) between R'–H and M–R, there are two well-established mechanisms (Scheme 3.1): (a) σ-bond metathesis (σBM)[28–32] and (b) oxidative addition / reductive elimination (OA/RE).[6,11,35–40] Historically, the midpoint in the reaction coordinate for σBM has been characterized as a single four-centered transition state (TS) with a small R'–M–R angle and a nonbonding M–H distance, while the midpoint for the OA/RE mechanism has been characterized as an intermediate with a higher formal oxidation state (n+2), a large R'–M–R angle, and a M–H bond.

---

*Reproduced with permission from Vastine, B. A.; Hall, M. B. *J. Am. Chem. Soc.* **2007**, *129*, 12068 – 12069. Copyright 2007 American Chemical Society.

Recently, several groups have suggested alternative mechanisms that appear to be in between these extremes. We termed our alternative mechanism metal-assisted σ-bond metathesis (MAσBM),[42] Lin and coworkers termed theirs oxidatively added transition state (OATS),[41,43] Oxgaard et al. termed theirs oxidative hydrogen migration (OHM),[44,120] and Perutz et al. termed theirs σ-complex assisted metathesis (σ-CAM).[45] The identification of these different mechanisms has typically been only through comparison of computed geometric parameters.

Scheme 3.1

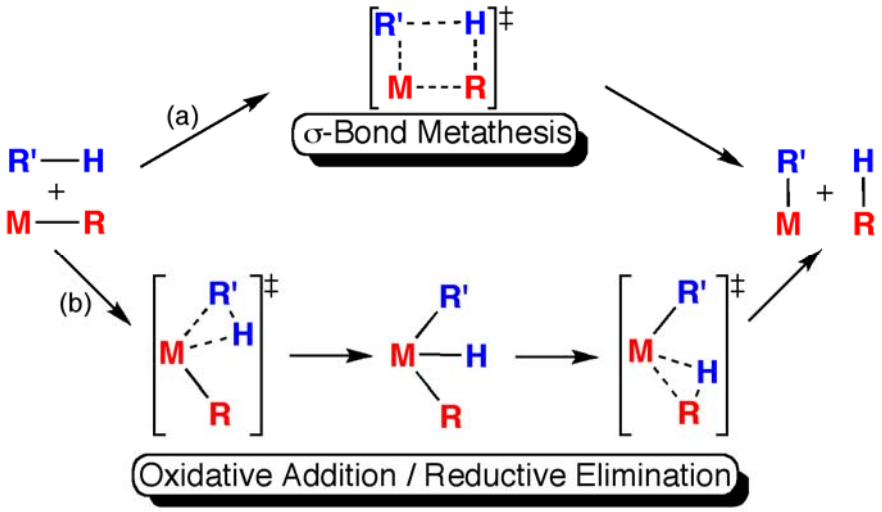

Here, we analyze the reaction coordinate midpoint (intermediates or TSs) of these mechanisms with Bader's "Atoms in Molecules" (AIM) analysis.[46] The midpoints of the alternative mechanisms are all TSs that directly connect reactant and product.

Through this analysis, we show that mechanisms can be unambiguously differentiated on the basis of their AIM bonding patterns.

3.2 Procedure

All optimized geometries and analytical frequencies were calculated in Gaussian 03[72] at the B3LYP/DZP[58,59,121] level of theory. The character (intermediates vs. TSs) of the species was identified through the frequency calculations. AIM2000[85] was used to analyze the electron density, its gradient field, and its Laplacian; bond (B) and ring (R) critical points (CP) in the gradient field were located through this analysis. A BCP is essential for a direct interaction between atoms, and is symbolized by a red dot in the AIM representations. A RCP is symbolized by a yellow dot. All 3D molecular and AIM representations were made with JIMP 2 visualization software.[77] The dashed lines that connect critical points in the following figures are approximate bond paths.

3.3 Results and Discussion

The σBM and OA/RE mechanisms, the two "classic" mechanisms for HT, have been theoretically investigated by methane addition to $[Cp_2ScCH_3]$ (Cp = η^5-C_5H_5) and to $[Cp^*Ir(PMe_3)(C'H_3)]^+$ (Cp* = η^5-$C_5(CH_3)_5$), respectively, as models closely related to the experimental systems.[6,28–32,38,39] Figure 3.1 shows the optimized geometric parameters, which agree well with published data, and CPs of the σBM TS, $[Cp_2Sc(CH_3)_2H]^‡$ (**1**), the OA/RE intermediate, $[Cp^*Ir(PMe_3)(CH_3)(C'H_3)H]^+$ (**2**), and the OA/RE TS, $[[Cp^*Ir(PMe_3)(CH_4)(C'H_3)]^+]^‡$ (**3**). Geometrically, **1** has a long Sc–H

distance and a small C–Sc–C angle whereas **2** has a short Ir–H distance and a large C–Ir–C' angle. In the AIM analysis, **1** is characterized by two Sc–C BCPs, two C–H BCPs, and a RCP at the center of the four-centered TS, while **2** is characterized by Ir–C, Ir–C', and Ir–H BCPs. As expected for this intermediate (**2**), no interactions between the hydride and pendent methyl ligands like those in **1** are found. The TS for OA/RE, **3**, is responsible for C–H cleavage leading to formation of **2**. At the TS's optimized geometry, BCPs are found for the "breaking" C–H bond and "forming" Ir–H bond, but not for the "forming" Ir–C bond.

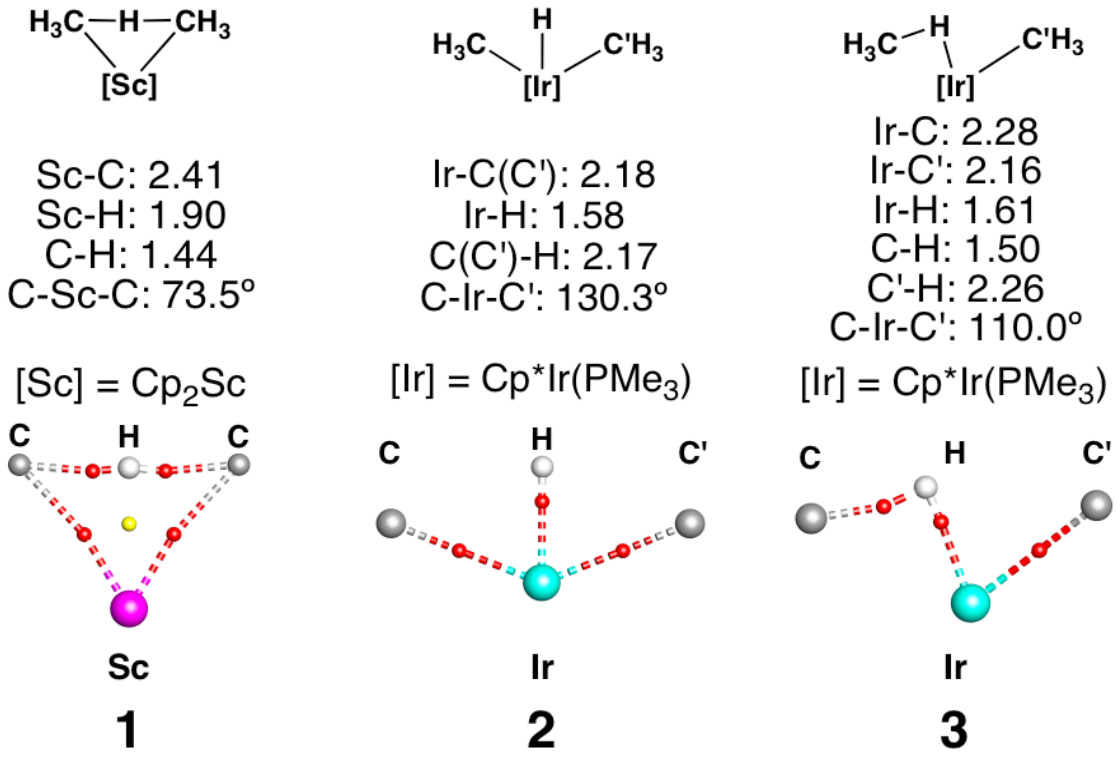

Figure 3.1. B3LYP/DZP optimized geometric parameters and AIM critical points for **1**, **2**, and **3**. Distances are given in angstroms.

Among the systems proposed to proceed by one of the new mechanisms is the asymmetric HT that occurs between C^{sp3} and C^{sp2} atoms in the Ir^{V}, seven–coordinate TS $[(acac)_2Ir(C_2{}^{sp3}H_4Ph)(C_6{}^{sp2}H_5)H]^{‡}$ (**4**) in the reaction of the alkane with $[(acac)_2IrPh]$.[44,120] Geometrically, TS **4** has an Ir–H bond length comparable to **2**; the C^{sp3}– and C^{sp2}–H interactions of 1.68 and 1.93 Å, respectively, are shorter than those of **2** but longer than those of **1**, and the C–Ir–C angle is intermediate to those of **1** and **2**. In the AIM analysis, **4** is characterized by Ir–C^{sp3}, Ir–C^{sp2}, Ir–H, and C^{sp3}–H BCPs with a RCP inside the Ir–C^{sp3}–H coordinates. Interestingly, in this TS, the transferring hydrogen is shown to interact with the metal center and only one of the pendent ligands. The geometric parameters and AIM representation of **4** are shown in Figure 3.2.

In order to understand **4** more thoroughly, we examined analogous reactions which proceed through symmetric HT between and C^{sp3} and C^{sp2} atoms in $[(acac)_2Ir(Me)_2H]$ (**5**) and $[(acac)_2Ir(Ph)_2H]^{‡}$ (**6**), respectively (Figure 3.2). HT between two methyl ligands proceeds through **5**, which is a C_2 symmetric, Ir^{V}, seven–coordinate intermediate, while a similar reaction between two phenyl ligands proceeds through **6**, which is a C_2 symmetric, seven–coordinate TS. In both **5** and **6**, the Ir–C and Ir–H distances are similar to those in **2** and **4**, but the C–M–C angles are smaller than the angle of **2** and comparable to that of **4**. Interestingly, **5** and **6** are characterized by Ir–C and Ir–H BCPs only; even in TS **6**, no C–H interactions were found. Note that in **4** the C–H BCP not found in **5** or **6** is close to the RCP; the coalescence of the two CPs would result in their annihilation, and then **4** would resemble intermediate **5** or TS **6**.

Table 3.1. Geometric parameters for osmium and platinum complexes.

	$[(acac)_2Os(X)_2H]^-$		$[(acac)_2Pt(X)_2H]^+$	
	Me (**7**)	Ph (**8**)	Me (**9**)	Ph (**10**)
M-H	1.58	1.59	1.63	1.92
M-C	2.15	2.11	2.17	2.13
C-H	1.99	1.91	1.56	1.42
C-M-C∠	124.5	120.3	91.6	81.6
	Intermediate	Intermediate	TS	TS

Distances in angstroms, angles in degrees.

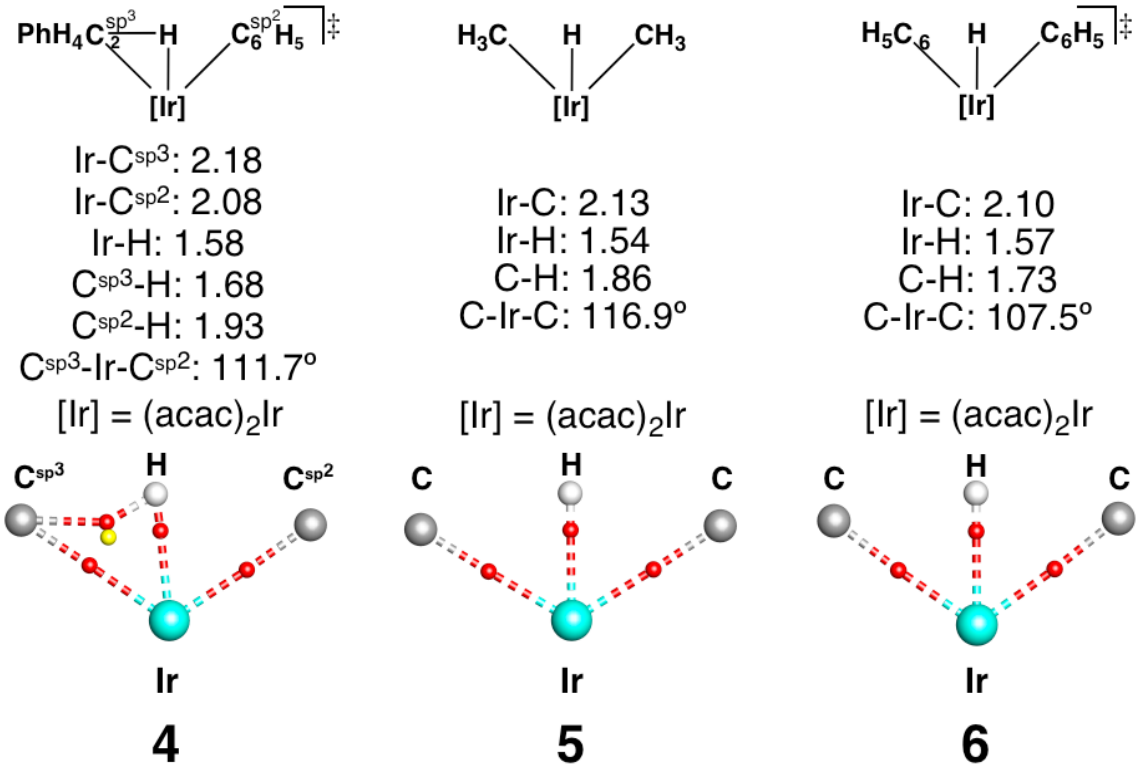

Figure 3.2. B3LYP/DZP optimized geometric parameters and AIM critical points for **4**, **5**, and **6**. Distances are given in angstroms.

To explore the full range of possible mechanisms for HT, the iridium center of **5** and **6** was replaced to produce the isoelectronic osmium and platinum species ($[(acac)_2Os(X)_2H]^-$ X = Me (**7**), Ph (**8**); $[(acac)_2Pt(X)_2H]^+$ X = Me (**9**), Ph (**10**)). The

optimized geometric parameters are found in Table 1. For osmium, both **7** and **8** are intermediates with M–H distances similar to the other intermediates studied, but larger C–M–C angles and longer C–H distances. On the other hand, both platinum species are TSs with longer M–H distances and smaller C–M–C angles. Compared to **9**, the smaller C–Pt–C angle in **10** is accompanied by a longer Pt–H distance. In the AIM analysis, the osmium intermediates (**7, 8**) are characterized by the same CPs as the other intermediates (**2**, **5**); however, the two platinum TSs are characterized differently. For **9**, two Pt–C, two C–H, and one Pt–H BCPs were found with one RCP inside of each Pt–H–C coordinates. TS **9** is unique because the transferring hydrogen is shown to interact with both pendent ligands and the metal center (shown as **B** in Figure 3.3). TS **10** is characterized by the same CPs as **1**, as the Pt–H distance is too great for an interaction (shown as **A** in Figure 3.3).

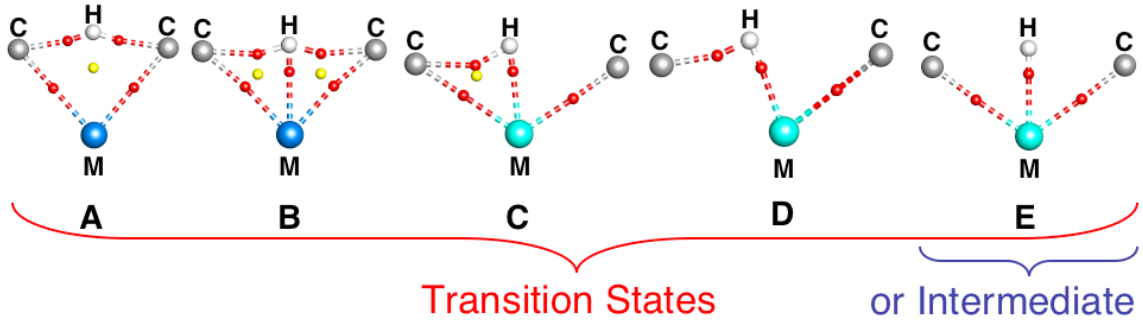

Figure 3.3. Spectrum of mechanisms for metal mediated hydrogen transfer.

3.4 Conclusions

This study provides a spectrum of mechanisms for metal-mediated HT that can be resolved by AIM analysis. The resolution of this spectrum is shown in Figure 3 with suggested assignments of: **A** = σBM (**1**, **10)**; **B** = MAσBM (**9**); **C** = OATS/σ-CAM (**4**); **D** = OA/RE TS (**3**); and **E** = OHM TS or OA/RE intermediate (**2**, **5**, **6**, **7**, and **8**).

CHAPTER IV

UNDERSTANDING THE SCOPE OF METAL-ASSISTED HYDROGEN TRANSFER: A BADER'S ANALYSIS AND DENSITY FUNCTIONAL THEORY INVESTIGATION

4.1 Introduction

The activation of the carbon–hydrogen (C–H) bond is an area of high interest in chemical research.[1,2,15,19b] Transition metals (TM) are especially suited for use in the facile activation of these bonds because the metal d orbitals possess the proper energies and symmetries that match the C–H bonding and antibonding (C–H*) orbitals.[7] When coordinating to the metal, the filled C–H bond donates electron density to an available d orbital, and back donation of electron density from the metal to the C–H* orbital results in C–H bond scission. Upon activation, the hydrogen can be transferred to a pendant ligand.

The general reaction profiles for the two "classic" mechanisms for hydrogen transfer (HT), σ-bond metathesis (σBM)[28–32] and oxidative addition / reductive elimination (OA/RE),[35–40] are sketched in Scheme 4.1. For σBM, only one transition state (TS) is found along the reaction coordinate that joins the reactant and product and is the midpoint along this reaction coordinate. However, the midpoint along the OA/RE pathway is an intermediate (INT) and two TSs are along the reaction coordinate. In the

first TS, the R'–H bond is broken and M–R' and M–H bonds are formed; the resulting INT is in a higher formal oxidation state (n + 2). A second TS forms the R–H bond and completes the HT. Geometrically, the σBM TS is characterized by a four-centered geometry with a long M–H distance (~2.0 Å) and a small R–M–R' angle (~90°); conversely, the geometry of the oxidized INT is characterized by a short M–H distance (~1.5 Å) and a large R–M–R' angle (~130°).

Scheme 4.1

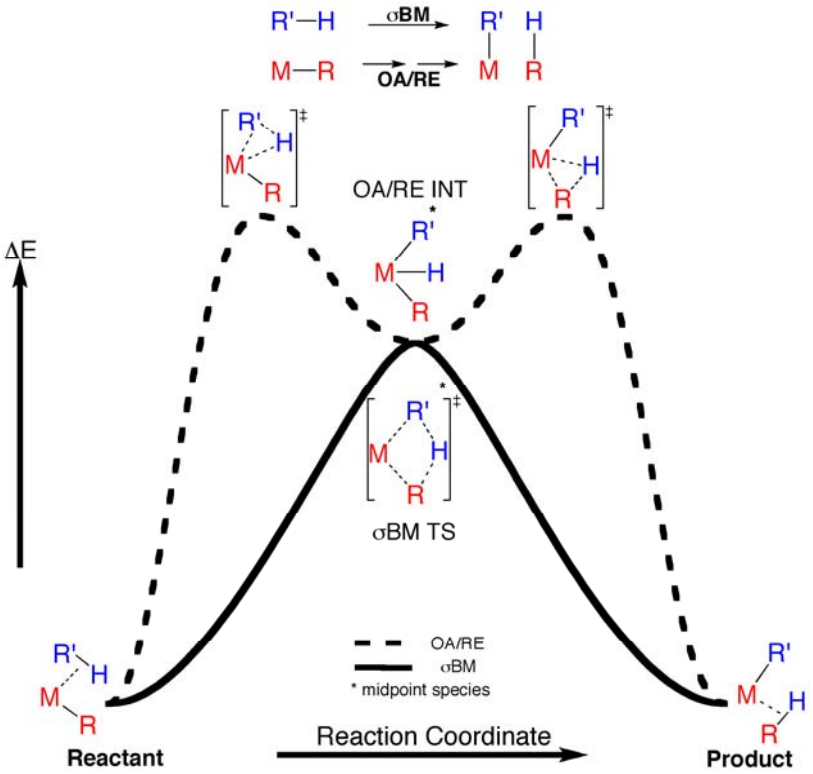

Alternatives to the two classic mechanisms have been proposed. Webster and coworkers investigated the borylation of alkanes and arenes by $LM(CO)_nBR_2$ (M = Fe, n = 1; M = W, n = 2; L: Cp = η^5-C_5H_5; R = OCH_2) and found that HT proceeded through a single TS for C–H and B–H coupling / decoupling, which would imply a σBM type mechanism.[42] However, the short calculated M–H distances (~1.5 Å) and orbitals localized along these coordinates suggest an interaction between the metal the transferring hydrogen. Therefore, the researchers proposed the metal–assisted σBM (MAσBM) mechanism.

Lin and coworkers proposed the "oxidatively added transition state" (OATS) mechanism in studying the mechanisms for borylation of alkane and arene and H/D exchanged.[41,43] The TSs for HT were characterized by short M–H distances, and electron density was localized along the M–H coordinates. These results indicate that the metal and transferring hydrogen interact during HT.

Oxgaard and coworkers investigated the mechanism for the arylation of olefin catalyzed by iridium[122] and ruthenium[123] systems and proposed the "oxidative hydrogen migration" (OHM) mechanism.[44,120,124] These systems were characterized by one TS for HT that geometrically resembled seven-coordinate, M^V (M = Ir, Ru) species. The M–H distances were short (~1.5 Å), and the distances between the alkyl and aryl ligands and the transferring hydrogen were considered too long for C–H interactions.

Finally, Perutz and Sabo–Etienne proposed the σ-complex assisted metathesis (σ-CAM) mechanism, and several examples were given including several systems mentioned above.[45] This mechanism includes HT and R–R' cross-coupling steps. The

close proximity of the metal and the transferring hydrogen in the TS for HT and R–R' coupling result from the dynamic rearrangements of σ-bound[8] ligands.

In several recent reports, the bonding patterns of non-equilibrium species have been characterized by using Bader's "Atoms in Molecules" (AIM) analysis.[46] We proposed a spectrum of mechanisms in studying the bonding patterns of representative models for the σBM, OA/RE, and alternative mechanisms.[125] Cundari et al. studied the 1,2-addition of C–H bonds to d^6 metal complexes and the TS for HT was characterized by bonding patterns similar to those of the σBM TS.[126] These studies presented a range of bonding patterns that describe the connectivity in HT.

Here, we analyze model complexes to identify the full range of bonding patterns for HT. Non-midpoint species on the OA/RE coordinate are examined to identify the changes in connectivity in this step-wise pathway. The influences of the spectator ligands on the bonding patterns are also considered. We identify seven sets of bonding patterns in total, five of which lie in between those that are characteristic of the σBM TS and the OA/RE INT. Last we examine the effects of basis sets and density functionals on the bonding patterns.

4.1.1 Theory of Bader's "Atoms in Molecules" Analysis

In Bader's analysis, the charge density ($\rho(\mathbf{r})$) of a given molecule, which is a physical observable, is analyzed for critical points (CP) in the density. The location of a CP is denoted by the position vector, $\mathbf{r}_c$, and at these points the first derivative of the density vanishes ($\nabla\rho(\mathbf{r}_c) = 0$); therefore, these points can be minima, maxima, or saddle

points in the density. The charge density of a molecule is three-dimensional, so there are three curvatures at a CP, which is the rank (ω) of the CP. Through analysis of the Hessian matrix ($\mathbf{A}(\mathbf{r}_c)$ eq. 1), which is a (3x3) matrix of the second derivatives of coordinates with respect to the density ($\delta^2\rho/\delta q^2$), the curvatures at a given CP are determined.

$$\boldsymbol{A}(\boldsymbol{r}_c) = \begin{pmatrix} \frac{\partial^2\rho}{\partial x^2} & \frac{\partial^2\rho}{\partial x\partial y} & \frac{\partial^2\rho}{\partial x\partial z} \\ \frac{\partial^2\rho}{\partial y\partial x} & \frac{\partial^2\rho}{\partial y^2} & \frac{\partial^2\rho}{\partial y\partial z} \\ \frac{\partial^2\rho}{\partial z\partial x} & \frac{\partial^2\rho}{\partial z\partial y} & \frac{\partial^2\rho}{\partial z^2} \end{pmatrix} \quad (1)$$

Diagonalization of the Hessian matrix ($\mathbf{\Lambda}$ eq. 2) yields three eigenvalues ($\lambda_1+\lambda_2+\lambda_3$) whose sum of signs is the signature (σ) of the CP; as such, the CPs are marked by the rank and signature as (ω, σ).

$$\mathbf{\Lambda} = \begin{pmatrix} \frac{\partial^2\rho}{\partial x^2} & 0 & 0 \\ 0 & \frac{\partial^2\rho}{\partial y^2} & 0 \\ 0 & 0 & \frac{\partial^2\rho}{\partial z^2} \end{pmatrix} = \begin{pmatrix} \lambda_1 & 0 & 0 \\ 0 & \lambda_2 & 0 \\ 0 & 0 & \lambda_3 \end{pmatrix} \quad (2)$$

For example, the result of this analysis at atomic centers gives three eigenvalues that are negative in character; therefore, atoms have a rank 3 for the curvatures and have a signature of –3 for the sum of the signs of the eigenvalues. The CPs at atomic centers

are therefore labeled as (3, –3). There are three other possibilities for the signatures of rank 3 CPs, which include:

- (3, –1): two negative eigenvalues; one positive
- (3, +1): one negative eigenvalue; two positive
- (3, +3): all three eigenvalues positive

The (3, –1) CP is called a bond critical point (BCP) because it connects two independent trajectories in the gradient field of the density that originate at two adjacent atoms. Likewise, the (3, +1) CP is termed a ring critical point (RCP) because these CPs are located inside the ring of atoms that are linked together by a series of BCPs. Accordingly, if this ring motif is extended in a third dimension then a cage critical point, which is denoted (3, +3), is located in the density.

4.2 Computational Method

All density functional theory[33] (DFT) calculations were performed with the Gaussian03 suite of programs.[72] Unless otherwise noted, geometries were optimized at the B3LYP/DZP level of theory, and the basis set is described below. The analytic frequencies were calculated for all species; intermediates are characterized by real frequencies and TSs by one imaginary frequency. The B3LYP density functional is comprised of the Becke3 exchange[58] and Lee–Yang–Parr correlation[59] functionals, respectively. All 3D geometric and bonding pattern representations were constructed with JIMP2 visualization software.[77] The electron densities of these species were analyzed with the implementation of Bader's analysis in AIM2000.[85] In the following

representations, B and RCPs are marked by red and yellow dots, respectively. The bond paths are approximate and represented by dashed lines.

In the DZP basis set, the TM was assigned the Los Alamos National Laboratory 2 (LANL2) effective core potential (ECP) of Hay and Wadt[73] for the core electrons and the (341/341/n1) (Sc $\rightarrow$ Cu: n = 4; Y $\rightarrow$ Ag: n = 3; La $\rightarrow$ Au: n = 2) double-ζ basis set as modified by Couty and Hall[74] (mDZ) for the electrons considered explicitly. One f polarization function was added to this basis set. The first and second row atoms that interact directly with the TM were assigned the correlation consisted double-ζ basis set (cc-pVDZ) of Dunning.[75] Those atoms that do not interact with the metal were assigned the full double-ζ D95 basis set of Dunning.[76] For only **1**, **2**, and **3**, the cc-pVDZ basis sets were augmented with diffuse functions in the optimization and frequency calculations. These assignments are listed explicitly for each species in Appendix C. For those species optimized at the TPSS/TZP level of theory, the basis set (TZP) is as follows: Iridium was assigned the Stuttgart Relativistic Small Core (RSC) 1997 ECP[108] (SDD) for the inner 60 electrons and the (311111/22111/411) basis set for the 17 explicit electrons; all atoms that touch the metal were assigned the cc-pVTZ basis set;[75] the remaining carbon and hydrogen atoms were assigned the D95 basis set.[76]

In the AIM analyses, the ECP/BS that was assigned to the metal was replaced with the Well Tempered basis set (WTBS) to reintroduce the core electrons and create an all electron model.[127] For **1**, **2**, and **3**, the diffuse functions that were added to the cc-pVDZ basis sets were not used. All other assignments of the DZP basis set remained the

same. In the following representations, BCPs and RCPs are marked by red and yellow dots, respectively. The bond paths are approximate and represented by dashed lines.

An analysis of this procedure and the robustness of the CP results was made for the scandium model (**1**) where the basis sets are as follows: Pople's STO-nG (n = 3,6),[113] 3-21G,[128] 6-31G with and without an f-polarization function;[129] Huzinaga's WTBS;[127] Ahlrich's pVDZ,[117] TZV,[130] VDZ,[117] VTZ,[130] and TZVPP;[131] Peterson's cc-pVDZ, aug-cc-pVDZ, cc-pVDZ-DK, cc-pVTZ, and cc-pVQZ,[132] Wachters+f,[133] and Bauschlicher's ANO.[134] The density functionals that were used in the same section are as follows: exchange: Becke88 (B),[60] Becke3 (B3),[58] Becke Half&Half (BH&H),[96] modified Perdew–Wang 91 (mPW);[89,93] correlation: Lee–Yang–Parr (LYP),[59] Perdew–Yang 91 (PW91),[89] Becke95 (B95);[98] exchange/correlation: Perdew–Burke–Ernzerhof (PBE),[94] Tao–Perdew–Staroverov–Scuseria (TPSS);[100] stand-alone: MPWLYP1M.[97] The hybrid versions of the mPWPW91 (MPW0)[89,93] and PBE (PBE0)[94] functionals were also used in this analysis.

4.3 Results and Discussion

4.3.1 The Two "Classic" Mechanisms: σBM and OA/RE

The "classic" σBM and OA/RE mechanisms have been theoretically investigated by methane addition to $[Cp_2ScCH_3]$ (Cp = η^5-C_5H_5) and to $[Cp^*Ir(PMe_3)(C'H_3)]^+$, respectively, as models closely related to the experimental systems.[28–30,35–40,125] The characteristic bonding patterns for the four-centered geometry of the σBM TSs, $[Cp_2M(CH_3)_2H]^‡$ (M = Sc (**1**), Y (**2**) , La (**3**)), are presented in Figure 4.1. BCPs are

located along both M–C and C–H coordinates and a RCP inside the M–C–C–H coordinates. In Table 4.1 the optimized geometric parameters and density values for the CPs are reported for **1**, **2**, and **3**. Geometrically, the M–C and M–H distances increase; the C–H distances remain essentially unchanged; the M–H distances increase; and the C–M–C angles increase as the metal is replaced. The bonding patterns of **1**, **2**, and **3** are qualitatively the same; however, the values of the M–C, C–H BCPs and RCPs densities decrease, remain unchanged, and decrease down the period, respectively.

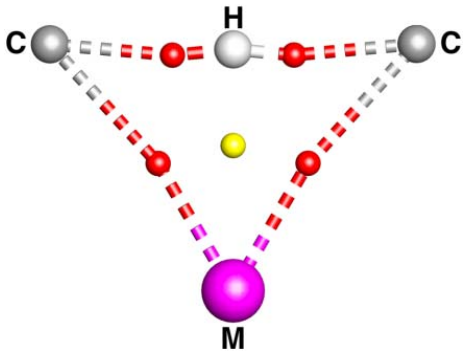

Figure 4.1. Characteristic bonding patterns of **1**, **2**, and **3**. Red dots are BCPs and the yellow dot is a RCP.

Table 4.1. Metric and AIM data for **1**, **2**, and **3**.

M	M–C		C–H				
	r[a]	ρ(r)[b] BCP	r[a]	ρ(r)[b] BCP	r[a] (M–H)	ρ(r)[b] RCP	C–M–C$\angle$[c]
Sc (**1**)	2.41	0.049	1.44	0.128	1.90	0.046	73.5
Y (**2**)	2.54	0.047	1.45	0.125	2.05	0.043	69.7
La (**3**)	2.73	0.038	1.44	0.128	2.23	0.035	64.6

a: distances in angstroms; *b*: densities in (e/bohr^3); *c*: angles in degrees.

To study the OA/RE mechanism, the σ-complexes, TSs, and oxidized INTs along the reaction coordinates for methane addition to $[CpIrPH_3(C'H_3)]^+$ and $[(acac)_2Ir(C'H_3)]$ (acac = acetylacetonate) were studied. The geometric parameters and bonding patterns of $[CpIrPH_3(CH_4)(C'H_3)]^+$ (**4**), $[[CpIrPH_3(CH_3)(C'H_3)H]^+]^‡$ (**5**), and $[CpIrPH_3(CH_3)(C'H_3)H]^+$ (**6**) are presented in Figure 4.2. Likewise, the results of similar analyses for $[(acac)_2Ir(CH_4)(C'H_3)]$ (**7**), $[(acac)_2Ir(CH_3)(C'H_3)H]^‡$ (**8**), and $[(acac)_2Ir(CH_3)(C'H_3)H]$ (**9**) are shown in Figure 4.3. At the B3LYP/DZP level of theory, we were unable to locate analogs of **4** with the Cp* and PMe_3 ligands. However, the analogs $[CpIrPMe_3(CH_4)(C'H_3)]$ and $[Cp^*IrPH_3(CH_4)(C'H_3)]$ were located at the TPSS/TZP level of theory, but the analog $[Cp^*IrPMe_3(CH_4)(C'H_3)]$ was not located at this higher level. As a result, we considered the Cp/PH_3 species in our analysis.

CH_4 + $[CpIrPH_3(C'H_3)]$: As anticipated for a σ-complex, the Ir–C and Ir–H distances in **4** are very long. The calculated C–H bond distance is similar to that of free methane, which indicates that the metal exhibits little influence on this parameter. BCPs were found along the Ir–C, Ir–H, and C–H coordinates. The σ-interaction is manifested solely in the Ir–H bonding interaction, which is consistent with previously reported results for methane weakly coordinated to a metal.[135]

In the TS for C–H bond cleavage (**5**), the C–H bond lengthens, the Ir–C and Ir–H distances shorten, and the Ir–C' bond length lengthens slightly. The largest geometric changes are in the Ir–C and C–H bonds as one prepares to form while the other prepares to break. The C–Ir–C' angle is much wider in this TS than in the precursor σ-complex.

Species **5** is characterized by the same bonding patterns of **4**; the Ir–C and C–H bonds are formed and broken, respectively, after the TS is passed.

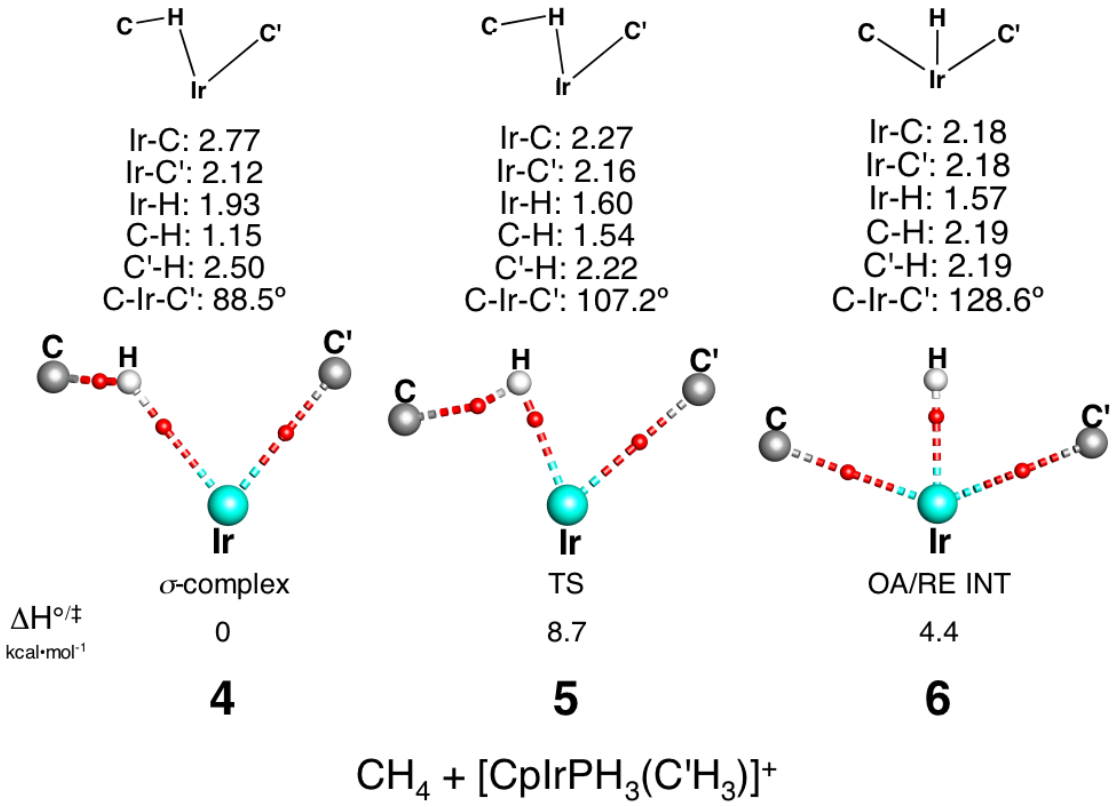

Figure 4.2. Optimized geometric parameters and bonding patterns of **4**, **5**, and **6**. The distances listed are in angstroms and the angles in degrees.

The geometric parameters of **6** are consistent with an Ir^{V} species. The Ir–C, Ir–C', Ir–H distances of 2.18, 2.18, and 1.54 Å, respectively, are similar to those of formal Ir–C and –H bonds, respectively, and the C–Ir–C' is wide at ~117°. BCPs were found along the Ir–C and Ir–H coordinates which is consistent with previously reported results for oxidized intermediates.[125]

Relative to **4**, the enthalpic barrier for C–H bond cleavage ($\Delta H^{\ddagger}_{5-4}$) is 8.7 kcal•mol^{-1}, and the formation of the intermediate ($\Delta H°_{6-4}$) is slightly endothermic at 4.4 kcal•mol^{-1}. The thermodynamic value for the formation of **6** agrees well with the value reported previously, but the enthalpic barrier to C–H bond cleavage is lower by ~3 kcal•mol^{-1} with this basis.[39a]

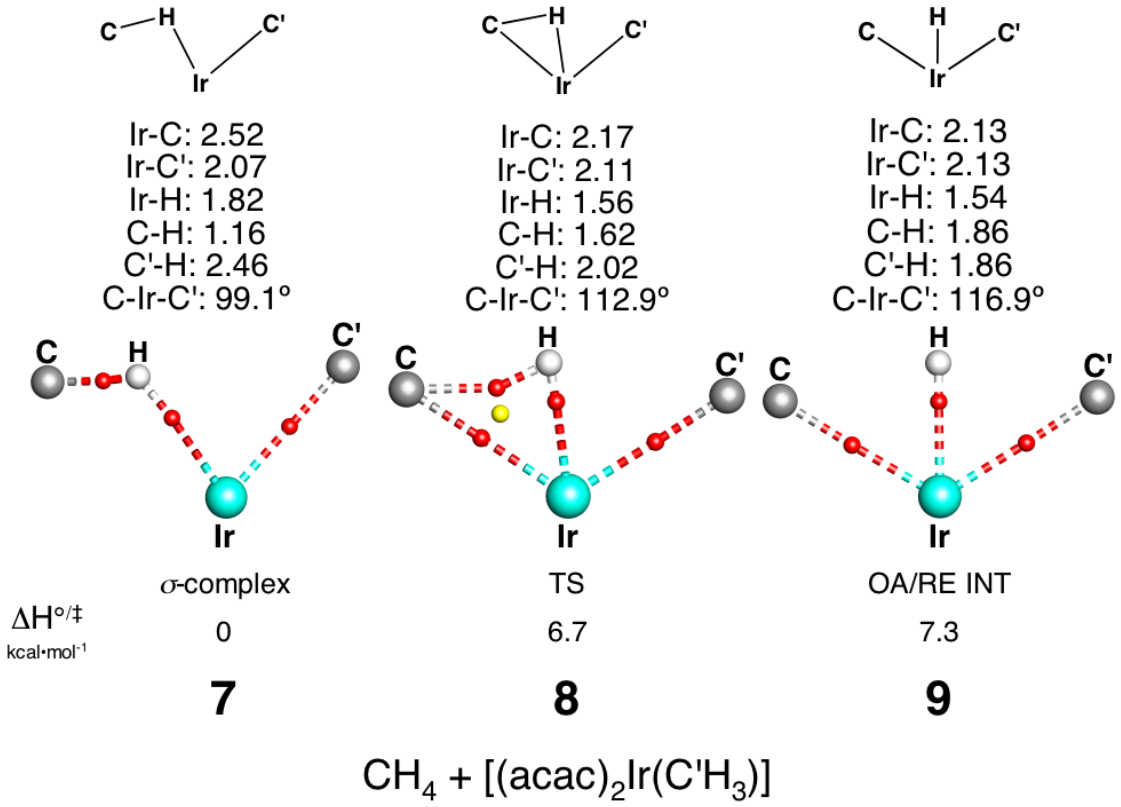

Figure 4.3. Optimized geometric parameters and bonding patterns of **7**, **8**, and **9**. The distances listed are in angstroms and the angles in degrees.

CH_4 + $[(acac)_2Ir(C'H_3)]$: In **7**, methane is weakly bound to the iridium center through the σ-C–H bond. The calculated C–H bond length is also similar to that of free methane, which would indicate little influence from the metal on this geometric parameter. Compared to **4**, the analogous Ir–C and Ir–H distances are shorter by ~0.2 and ~0.1 Å, respectively, which would indicate that the acac ligand exhibits a weaker trans influence than the Cp ligand. In the AIM analysis, **7** is characterized by Ir–C', Ir–H, and C–H BCPs, and the interaction of the σ-bound methane to the iridium center is manifested solely through the Ir–H interaction.

Relative to the values in **7**, the Ir–C and Ir–H distances decrease by ~0.3 Å and the C–H distance increases by ~0.5 Å in **8**. A BCP is located along the Ir–C coordinate, which is consistent with the shorter length. BCPs are also located along the Ir–C', Ir–H, and C–H coordinates, and a RCP is found inside the Ir–C–H coordinates. The activation of the C–H bond occurs earlier along the reaction coordinate in the bis-acac system, which is displayed in the shorter Ir–C and longer C–H distances and presence of Ir–C BCP in **8**.

Last, the geometric parameters and bonding patterns of **9** are presented. The bond distances, intra-ligand distances, and C–Ir–C angle are consistent with an Ir^V intermediate, and BCPs are located along the Ir–C and Ir–H coordinates. The weaker trans influence of the acac ligands results in shorter Ir–C and Ir–H distances in **9** (relative to **6**).

The relative enthalpies of **8** and **9** are 6.7 and 7.3 kcal•mol^{-1}, respectively. However, relative to **7**, the SCF energies are 8.5 and 8.1 kcal•mol^{-1}, respectively, but the

corresponding zero-point energies are 7.4 and 7.7 kcal•mol^{-1}. Together, these energies show that the potential energy surface at **9** is characterized as a shallow minimum, and the lower relative enthalpy for **8** results from this zero-point effect.

We have presented the bonding patterns that are characteristic of the σBM and OA/RE mechanism, and in the case of the later mechanism we have shown how these patterns change along the reaction coordinate. We now describe the bonding patterns that can be found in between these two classic cases.

4.3.2 Bonding Patterns for Models of Alternative Character

Previously, we identified the characteristic bonding patterns for the midpoint species along the σBM and OA/RE pathways. We also considered several representative models for alternative mechanisms and identified bonding patterns with differing degrees of connectivity.[125] Here, we consider all possible degrees of connectivity by presenting in general form the bonding patterns for metal-mediated (M) HT between R and R'. These sets of bonding patterns (**A** $\rightarrow$ **G**) are shown in Figure 4.4.

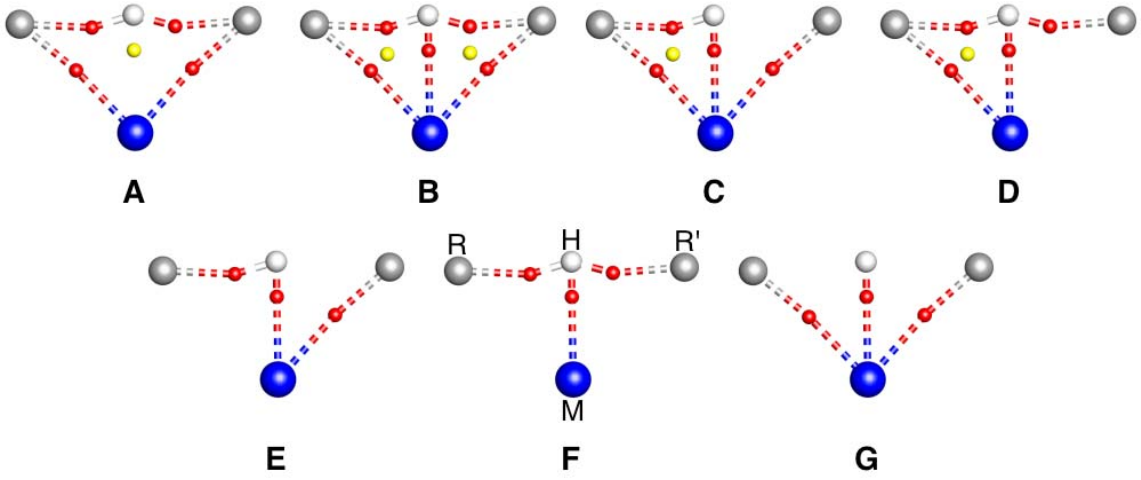

Figure 4.4. All possible degrees of connectivity for a four-centered geometry. These patterns are for HT between R and R' supported by a metal, M.

The first set of bonding patterns, **A**, is characterized by M–R, M–R', R–H, and R'–H BCPs with a RCP inside the coordinates of the four atoms; the metal supports only the pendent ligands and the hydrogen interacts only with the pendent ligands. With the addition of a BCP along the M–H coordinate to the analogous BCPs identified in set **A**, two RCPs inside the M–R–H and M–R'–H coordinates are found and together characterize the bonding patterns of set **B**. In this set, which has the highest possible degree of connectivity, the metal supports the pendent ligands and the transferring hydrogen.

We can rationalize the next two sets of bonding patterns (**C**, **D**) in considering the coalescence of one BCP with one RCP of set **B**. Bader described the points in the density where a BCP and RCP coalesce and annihilate as the "catastrophe point of the conflict type".[46] For example, the coalescence of the R'–H BCP with the corresponding RCP results in the annihilation of the BCP along the R'–H coordinates, which is shown

in set **C**. Conversely, the coalescence of the M–R' BCP with the corresponding RCP results in the annihilation of the CP along M–R' coordinates, which is shown in set **D**. In set **C**, the metal again supports the pendent ligands and the transferring hydrogen. The interaction between the transferring hydrogen and one pendent ligand is lost. However, in set **D**, the metal supports only one pendent ligand and the transferring hydrogen while the interactions between the pendent ligands and the transferring hydrogen are retained.

The remaining three sets of bonding patterns can be rationalized by the coalescence of each RCP with a BCP from set **B**. The respective coalescence of the M–R–H and M–R'–H RCPs with the M–R and R'–H BCPs results in set **E** where the metal interacts with only one pendent ligand (excluding the transferring hydrogen) and the transferring hydrogen interacts with only one pendent ligand (excluding the metal). Next, the coalescence of the M–R–H and M–R'–H RCPs with the respective M–R and –R' BCPs annihilates the BCPs along the M–R and M–R' coordinates, which is shown in set **F**. Here, the metal supports only the transferring hydrogen, which retains R–H and R'–H interactions. Last, the coalescence of the M–R–H and M–R'–H RCPs with the R–H and R'–H BCPs results in set **G**, which is typical of an intermediate. The metal is shown to interact with only the pendent ligands, which is consistent with the understood bonding in intermediates.

To verify that these sets exist (**A** → **G**), we analyzed the bonding patterns of the midpoint species of three reactions: (**R1**) C_6H_6 + [$(acac)_2M(C_2H_4Ph)(Ph)H$] (M = Fe^- (**10**), Co (**11**), Ni^+ (**12**), Ru^- (**13**), Rh (**14**), Pd^+ (**15**), Os^- (**16**), Ir (**17**), Pt^+ (**18**)), (**R2**) C_6H_6 + [$TpM(CO)(C_2H_4Ph)(Ph)H$] (M = Mn^- (**19**), Fe (**20**), Co^+ (**21**), Tc^- (**22**), Ru (**23**),

Rh^+ (**24**), Re^- (**25**), Os (**26**), Ir^+ (**27**)), and (**R3**) CH_4 + [CpM(CO)($B(OCH_2)_2$] (M = Mn^- (**28**), Fe (**29**), Co^+ (**30**), Tc^- (**31**), Ru (**32**), Rh^+ (**33**), Re^- (**34**), Os (**35**), Ir^+ (**36**). The relative energies for all systems are included for each reaction in the respective section. Those systems that proceed by a σBM-like pathway where one TS connects reactant (R) and product (P) are labeled under "Pathway 1". The energy barrier (R → TS) in this pathway is between the reactant and the TS for HT. The systems that proceed by the OA/RE pathway are labeled under "Pathway 2". The energy barrier (R → TS) in this pathway is between the reactant and the TS that results in the oxidized intermediate. The reactants and products are described in the respective sections for each model reaction. For the first two reactions, the carbon atoms of the phenyl and ethylbenzene ligands are labeled C^{sp2} and C^{sp3}, respectively.

R1: The relative energies (kcal•mol^{-1}) for the first, second, and third row analogs of this reaction are reported in Table 4.2. Unless noted otherwise, the reactants are the σ-bound benzene complexes, [$(acac)_2$M(σ-C_6H_6)(C_2H_4Ph)], and the energies are relative to these species. The products are either the σ-bound ethylbenzene complexes, [$(acac)_2$M (C_6H_5)(σ-C_2H_4Ph)] (Pathway 1) or the oxidized intermediates, [$(acac)_2$M(C_2H_4Ph)(C_6H_5)H] (Pathway 2).

Table 4.2. Relative energies (kcal•mol^{-1}) for C_6H_6 + $[(acac)_2M(C_2H_4Ph)]$.

metal	pathway	R → TS				R → P			
		ΔE_0	ΔE_{elec}	$\Delta H^{\ddagger}$	$\Delta G^{\ddagger}$	ΔE_0	ΔE_{elec}	$\Delta H°$	$\Delta G°$
Fe^-	1	7.91	8.46	7.87	21.08	–5.90	–5.86	–5.86	–5.51
Co	1	16.27	16.74	16.15	30.02	–1.31	0.12	–0.47	9.05
Ni^+	1	37.40	38.06	37.47	50.39	28.75	30.25	29.66	38.08
Ru^-	1	3.89	3.69	3.69	4.69	–8.01	–7.82	–7.82	–8.01
Rh	1	13.93	13.62	13.62	14.67	–3.43	–3.35	–3.35	–3.51
Pd^+	1	21.03	20.65	20.65	21.94	8.28	8.50	8.50	6.53
Os^-	2	NF	NF	NF	NF	–26.47	–25.86	–26.46	–12.80
Ir	1	5.47	5.37	5.37	5.04	–3.33	–3.22	–3.22	–3.58
Pt^+	1	19.01	18.77	18.77	19.44	5.74	5.89	5.89	5.29

The optimized geometric parameters and bonding patterns of **10**, **11**, and **12** are shown in Figure 4.5. In the geometric analysis, the M–C^{sp2} distances are similar between the three species. The M–C^{sp3} distance increases by ~0.15 Å from the similar values of **10** and **11** to the value of **12**. The M–C^{sp2} and C^{sp2}–H distances oscillate, the M–H distances increase, and the C^{sp3}–H distances and C^{sp3}–M–C^{sp2} angles decrease in value. Species **10** and **12** are characterized by the same bonding patterns; M–C^{sp2}, M–H, C^{sp3}–H and C^{sp2}–H BCPs are located along these respective coordinates. A RCP is also located inside each M–C^{sp2}–H triangle for **10** and **12**. However, **11** is characterized by Co–H, C^{sp3}–H, and C^{sp2}–H BCPs in spite having the shortest M–C^{sp2} distance. To check this anomaly, cobalt was assigned the cc-pVDZ basis set and the Co–C^{sp2} BCP was located at this level in the basis. The corresponding Co–C^{sp2}–H RCP was also located. For these first row species, the metal interacts more with the benzene in transferring the hydrogen to the pendent ethylbenzene ligand.

The energy barriers to HT increase as the metal is replaced. For iron, the reactants are $[(acac)_2Fe(C_2H_4Ph)]$ and free benzene, which results in the large free

energy barrier. The barrier for the cobalt system increases by ~8 kcal•mol^{-1} and the product is isenthalpic with the reactant. In the nickel system, the enthalpic barrier to HT is large at 37.5 kcal•mol^{-1}; the barrier to HT increases as the metal is replaced. The energies are relative to the five-coordinate nickel complex, [(acac)$_2$Ni(C$_2$H$_4$Ph)], and free benzene.

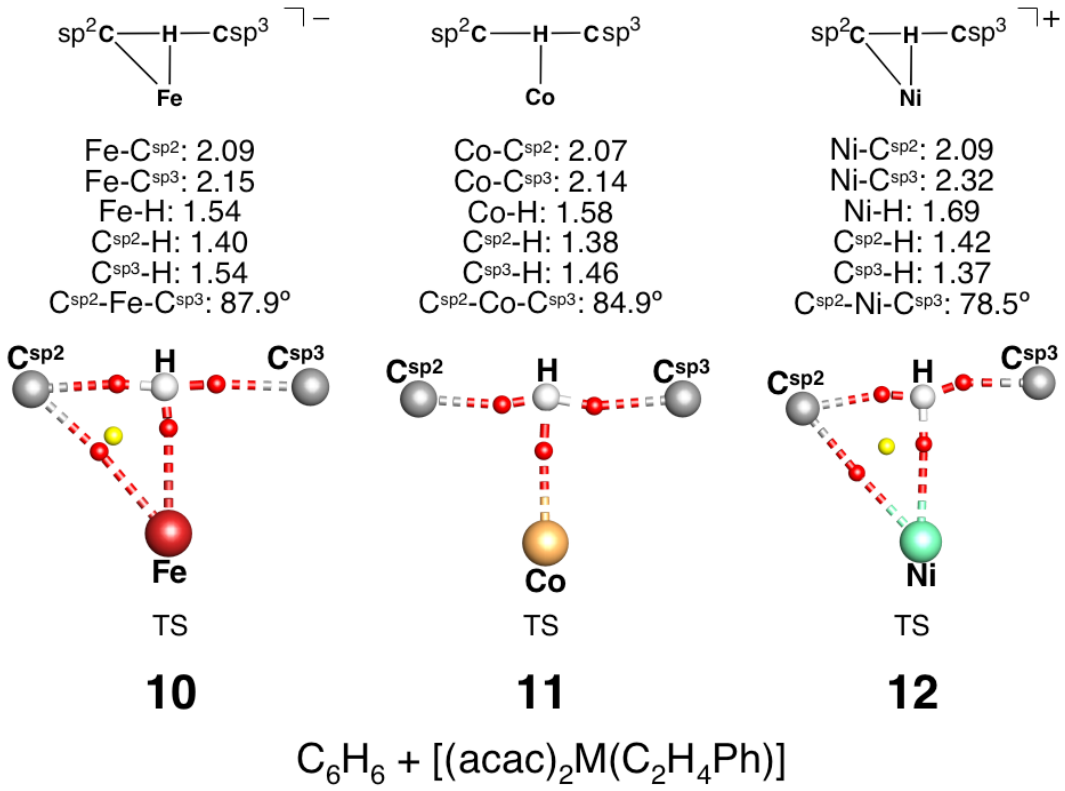

Figure 4.5. Optimized geometric parameters and bonding patterns of **10**, **11** and **12**. The distances listed are in angstroms and the angles in degrees.

For **13**, **14**, and **15**, the M–C^{sp2}, M–C^{sp3}, and M–H parameters increase while the C^{sp3}–H, C^{sp2}–H, and C^{sp3}–M–C^{sp2} parameters decrease as the metal is replaced. In the

bonding analysis, **13** is characterized by Ru–C^{sp2}, Ru–C^{sp3}, Ru–H, and C^{sp3}–H BCPs; a RCP is also located inside the Ru–C^{sp3}–H coordinates. In **14**, the M–C^{sp3} BCP disappears and a C^{sp2}–H BCP appears, which parallels the lengthening and shortening of the respective bonds. A RCP is also found in this species but inside the Rh–H–C^{sp2} coordinates. Species **15** is characterized by full connectivity as Pd–C^{sp2}, Pd–C^{sp3}, Pd–H, C^{sp2}–H, and C^{sp3}–H BCPs are located; RCPs are located inside the Pd–C^{sp2}–H and Pd–C^{sp3}–H coordinates, respectively. The geometric coordinates and bonding patterns of these species are shown in Figure 4.6.

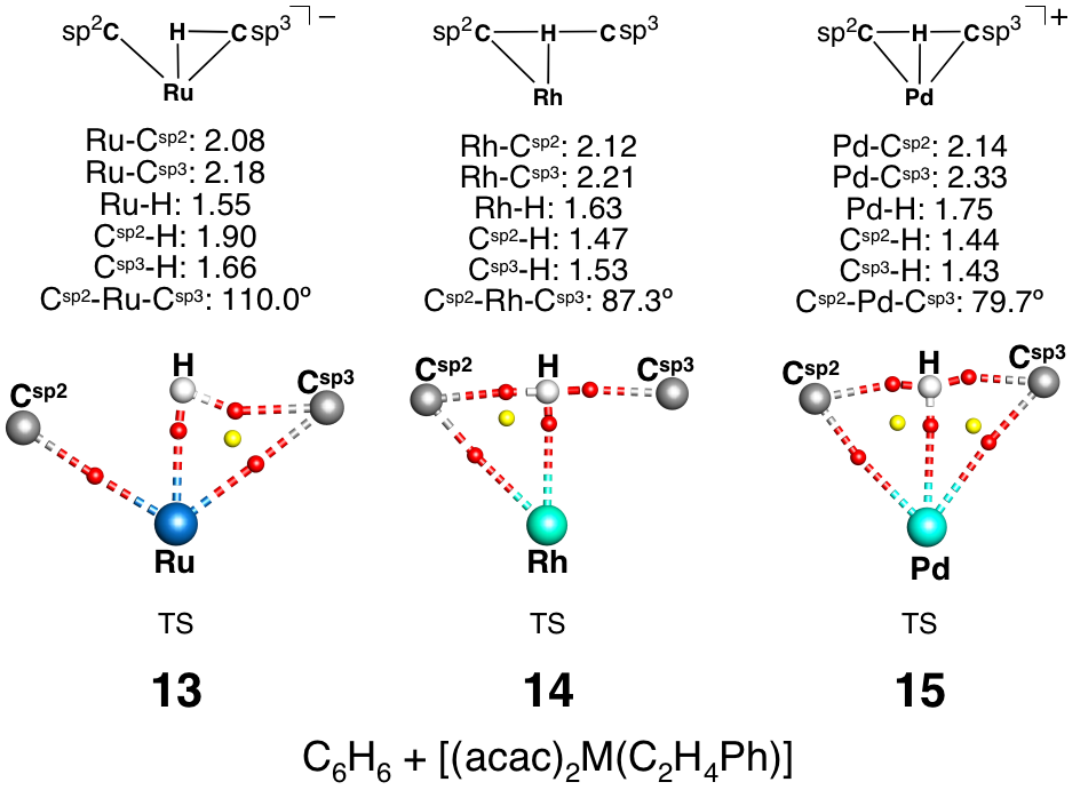

Figure 4.6. Optimized geometric parameters and bonding patterns of **13**, **14** and **15**. The distances listed are in angstroms and the angles in degrees.

The barrier for HT is small (3.7 kcal•mol^{-1}) in the ruthenium system, and the formation of the σ-bound ethylbenzene complex is exothermic by 7.8 kcal•mol^{-1}. The barrier is greater by ~10 kcal•mol^{-1} in the rhodium system, but the reaction is exothermic by 3.4 kcal•mol^{-1}. The barrier is high in the palladium system (20.7 kcal•mol^{-1}) and product formation is endothermic by 8.5 kcal•mol^{-1}.

For the third row models (**16**, **17**, **18**), the M–C^{sp2} distances are once again similar between the three systems, and the M–C^{sp3} distances are the only coordinates that lengthen as the metal is replaced. The M–H distances oscillate while the C^{sp2}–H and C^{sp3}–H distances and C^{sp2}–M–C^{sp3} angles decrease as the metal is replaced. In the bonding analysis, **16** is characterized by metal–ligand BCPs as anticipated for an intermediate. For **17**, BCPs are located along the Ir–C^{sp2}, Ir–C^{sp3}, Ir–H, and C^{sp3}–H coordinates; a RCP is found inside the Ir–C^{sp3}–H coordinates. Like the palladium congener, **18** is characterized by full connectivity; BCPs are located along the Pt–C^{sp2}, Pt–C^{sp3}, Pt–H, C^{sp2}–H, and C^{sp3}–H coordinates, and RCPs are located inside the Pt–C^{sp2}–H and Pt–C^{sp3}–H coordinates, respectively. These results are shown in Figure 4.7.

Similar trends in the relative energies are calculated for the third row analogs. A small barrier to the formation of **16** is calculated and the formation of this species is highly exothermic (26.5 kcal•mol^{-1}); all attempts to locate the TS in the osmium system failed. The barrier in the iridium system is also small (5.4 kcal•mol^{-1}) and the reaction is exothermic by 3.2 kcal•mol^{-1}. Like the palladium system, the barrier for HT is large in the platinum system (18.8 kcal•mol^{-1}), and the product formation is endothermic (5.9 kcal•mol^{-1}).

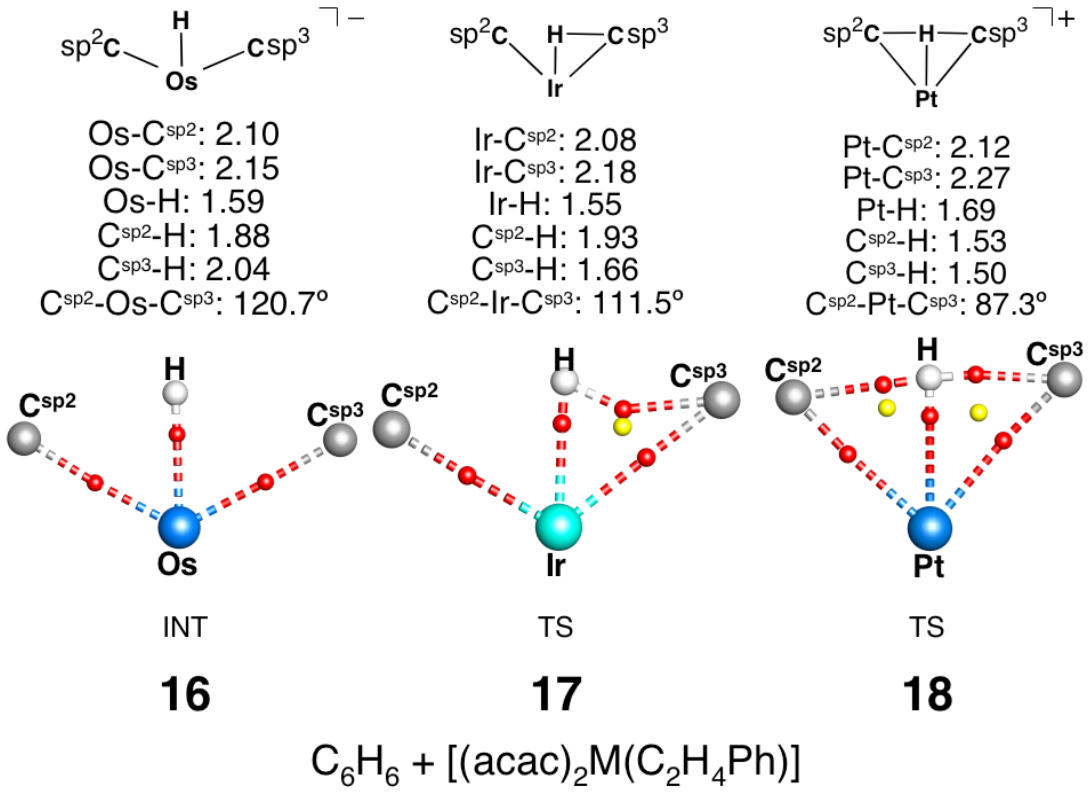

Figure 4.7. Optimized geometric parameters and bonding patterns of **16**, **17** and **18**. The distances listed are in angstroms and the angles in degrees.

In descending down the group 8 metals, the M–C^{sp3} bond is formed prior to the breaking of the C^{sp2}–H and C^{sp3}–H bonds. For group 9, the M–C^{sp3} bond is formed in the iridium species, but the C^{sp3}–H bond is not broken. Likewise, for group 10, the M–C^{sp3} bond is formed in the palladium and platinum congeners.

R2: Similar analyses were accomplished for the first TM row (**19**, **20**, **21**), second TM row (**22**, **23**, **24**), and third TM row (**25**, **26**, **27**) metals of the reaction: C_6H_6 + [TpM(CO)(C_2H_4Ph)(Ph)H]. The relative energies (kcal•mol^{-1}) for the first, second,

and third row analogs for this system are reported in Table 4.3. The reactants, TSs, and products for these systems are defined the same way as in the previous system.

Table 4.3. Relative energies (kcal•mol^{-1}) for C_6H_6 + [TpM(CO)(C_2H_4Ph)].

metal	pathway	R → TS				R → P			
		ΔE_0	ΔE_{elec}	$\Delta H^{\ddagger}$	$\Delta G^{\ddagger}$	ΔE_0	ΔE_{elec}	$\Delta H°$	$\Delta G°$
Mn^-	1	8.26	7.77	7.77	9.80	–10.21	–9.88	–9.88	–11.07
Fe	1	14.71	14.45	14.45	16.82	–6.26	–5.72	–5.72	–6.74
Co^+	1	14.76	14.26	14.26	16.03	–0.89	–0.77	–0.77	–1.42
Tc^-	2	NF	NF	NF	NF	–0.12	–0.10	–0.10	–0.37
Ru	1	11.71	11.42	11.42	12.53	–7.14	–6.97	–6.97	–7.98
Rh^+	1	18.74	18.36	18.36	19.64	–0.17	–0.06	–0.06	–0.70
Re^-	2	NF	NF	NF	NF	NF	NF	NF	NF
Os	2	0.51	0.20	0.20	0.93	0.58	0.52	0.52	0.79
Ir^+	1	12.92	12.69	12.69	13.73	–3.69	–3.59	–3.59	–3.91

In the geometric analysis of the first row species, the M–C^{sp2} and C^{sp2}–M–C^{sp3} parameters oscillate as the metal is replaced. The M–C^{sp3} and C^{sp2}–H distances decrease from their values in **19** to identical distances in **20** and **21**, respectively. The M–H distance increases while the C^{sp3}–H distances decrease as the metal is replaced. In the bonding analysis, **19** is characterized by Mn–C^{sp3}, Mn–H, C^{sp2}–H, and C^{sp3}–H BCPs with a RCP located inside the Mn–C^{sp3}–H coordinates. Species **20** and **21** are characterized by the same bonding patterns; only M–H, C^{sp2}–H, and C^{sp3}–H BCPs were located. The results of these analyses for these species are presented in Figure 4.8.

Once again, the energy barrier to HT increases as the metal is replaced; however, the values of the iron and cobalt systems are similar. The product is more exothermic in the manganese system and becomes isenthalpic with the reactant in the cobalt system.

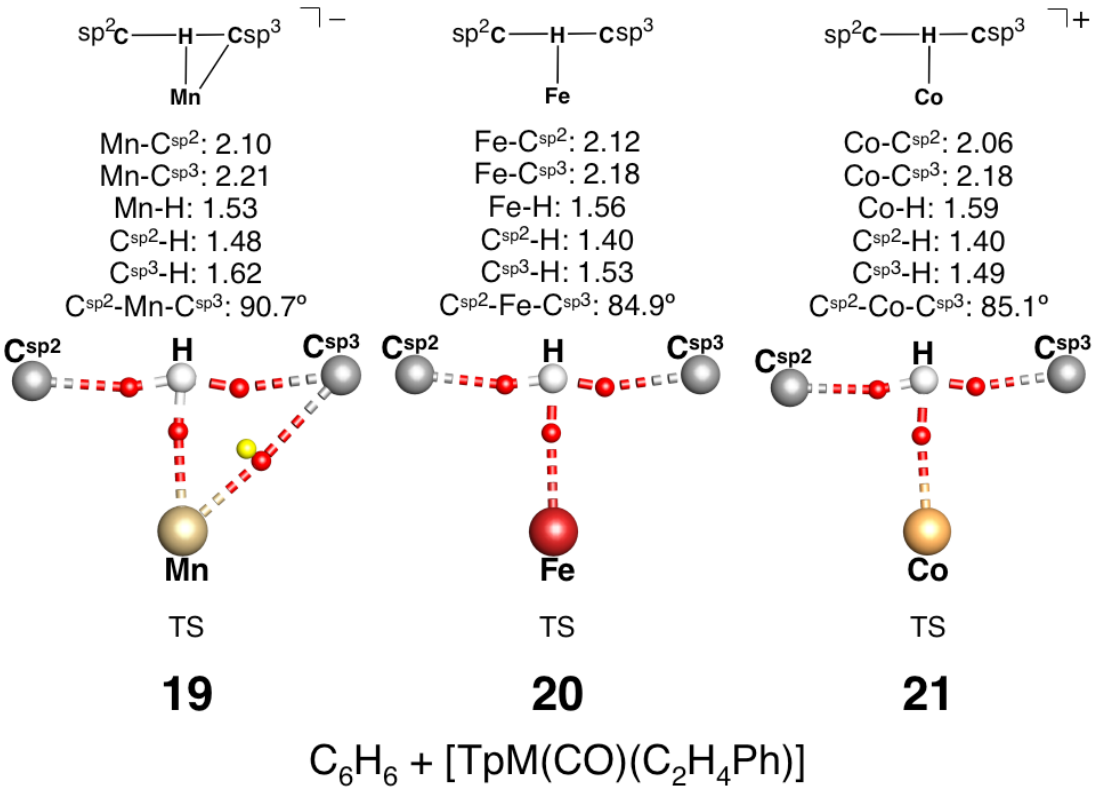

Figure 4.8. Optimized geometric parameters and bonding patterns of **19**, **20** and **21**. The distances listed are in angstroms and the angles in degrees.

For **22**, **23**, and **24**, the M–C^{sp3} and M–H distances oscillate and the C^{sp3}–H, C^{sp2}–H distances and C^{sp3}–M–C^{sp2} angles decrease as the metal is replaced. The M–C^{sp3} distances are the only parameters that increase. In the bonding analysis, BCPs are only found along the Tc–C^{sp3}, Tc–C^{sp2}, and Tc–H coordinates in **22** as characteristic of an intermediate. Species **23** is characterized by full connectivity; Ru–C^{sp2}, Ru–C^{sp3}, Ru–H, C^{sp2}–H, and C^{sp3}–H BCPs were found along these coordinates. RCPs were found inside the Ru–C^{sp2}–H and Ru–C^{sp3}–H coordinates, respectively. The Rh–C^{sp3} BCP is lost in species **24**, but BCPs are located along the Rh–C^{sp2}, Rh–H, C^{sp2}–H, and C^{sp3}–H

coordinates. A RCP is found inside the Rh–C^{sp2}–H coordinates, but the RCP inside the Rh–C^{sp3}–H coordinates is lost. The optimized geometric parameters and bonding patterns of these species are shown in Figure 4.9.

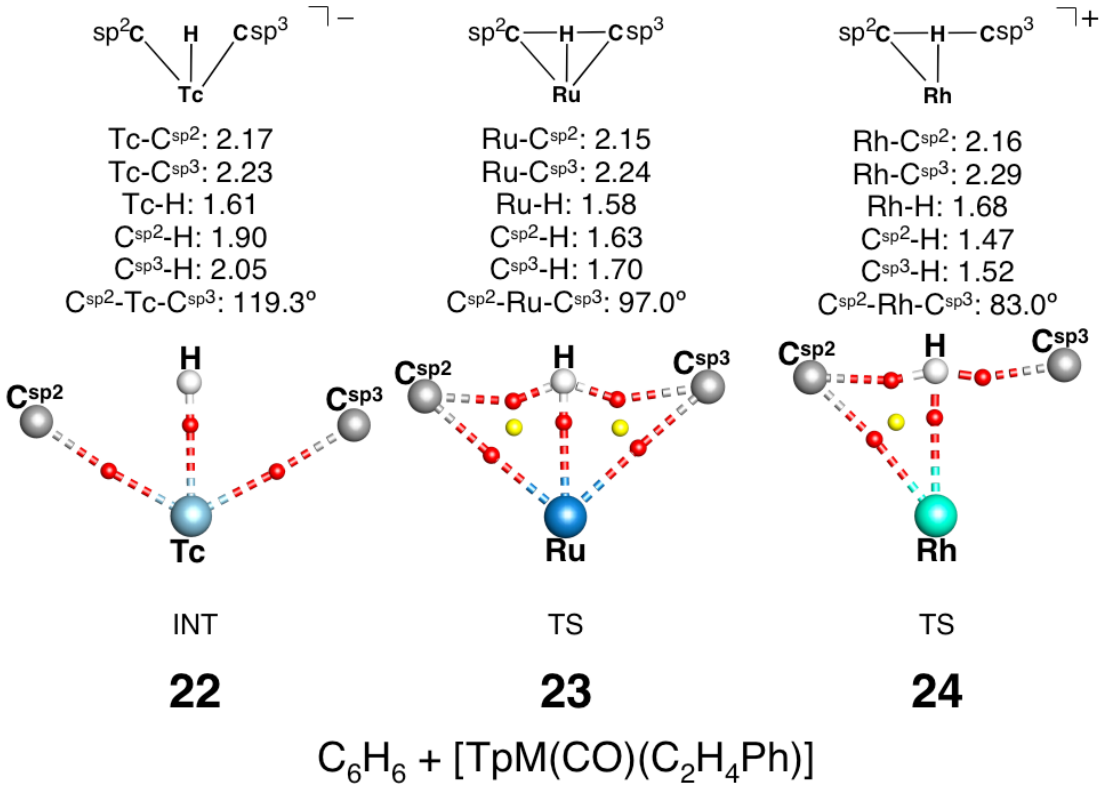

Figure 4.9. Optimized geometric parameters and bonding patterns of **22**, **23** and **24**. The distances listed are in angstroms and the angles in degrees.

The general increase in energy of the barrier is not seen for the second row analogs as the technetium system proceeds by a different pathway than the ruthenium and rhodium systems. For the former system, the oxidized intermediate is isenthalpic with the reactant, but all attempts to locate the TS for oxidative C–H bond cleavage

failed. For the latter two systems, the energy barrier increases between the metals and product formation is less exothermic.

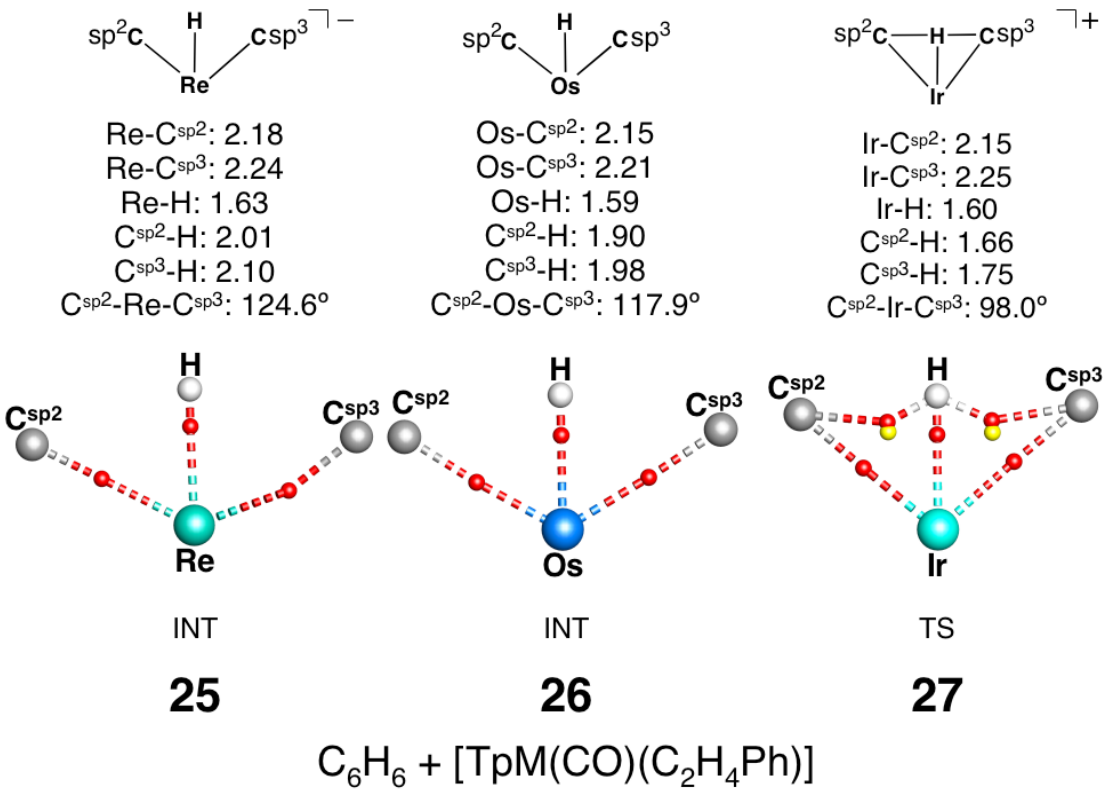

Figure 4.10. Optimized geometric parameters and bonding patterns of **25**, **26**, and **27**. The distances listed are in angstroms and the angles in degrees.

In the geometric analyses of **25**, **26**, and **27**, the M–C^{sp2} distance decreases by 0.03 from the value in **25** to the identical values in **26** and **27**. The M–C^{sp3} and M–H distances oscillate between the three species. The last three parameters, the C^{sp2}–H distance, the C^{sp3}–H distance, and the C^{sp2}–M–C^{sp3} angle, decrease as the metal is replaced. In the bonding analyses of these species, M–C^{sp2}, M–C^{sp3}, and M–H BCPs are

located in **25** and **26**. Species **27** is characterized by full connectivity; BCPs were located along the Ir–C^{sp2}, Ir–C^{sp3}, Ir–H, C^{sp2}–H, and C^{sp3}–H coordinates, and RCPs are located inside the Ir–C^{sp3}–H and Ir–C^{sp2}–H coordinates, respectively. The results for these complexes are shown in Figure 4.10.

The σ-bound benzene reactant and the TS for oxidative C–H bond cleavage were not located in the rhenium system; all attempts to optimize these species resulted in the oxidized intermediate. For osmium, the barrier to oxidative C–H bond cleavage is lower than product formation; the relative SCF energies for the TS and product are 1.8 and 1.0 kcal•mol^{-1}, respectively. The lower value for the barrier results is the result of a zero-point effect. The barrier to HT is moderate in the iridium system at 12.7 kcal•mol^{-1}, and product formation is exothermic by 3.6 kcal•mol^{-1}.

For the group 7 metals, the C^{sp2}–H and C^{sp3}–H bonds are broken and the M–C^{sp2} bond is formed in switching between manganese and technetium. For group 8, the M–C^{sp2} and M–C^{sp3} bonds are formed prior to breaking the C^{sp2}–H and C^{sp3}–H bonds. Last, for group 9, the M–C^{sp2} bond is formed prior to forming the M–C^{sp3} bond.

The group 8 and 9 metals are common between the **R1** and **R2**. The bis-acac system is characterized by higher degrees of connectivity for the first row metals, but the second and third row metal Tp/CO species exhibit higher degrees of connectivity than the bis-acac analogs.

R3: Here, we analyze the midpoint species along the reaction coordinate for **R3**: CH_4 + [CpM(CO)($B(OCH_2)_2$]. The relative energies for these systems are presented in

Table 4.4. All of these systems proceed by Pathway 1; the reactants and products are the σ-bound methane and σ-bound borane complexes, respectively.

Table 4.4. Relative energies (kcal•mol^{-1}) for CH_4 + [CpM(CO)(B(OCH$_2$)$_2$)].

metal	pathway	R → TS				R → P			
		ΔE_0	ΔE_{elec}	$\Delta H^{\ddagger}$	$\Delta G^{\ddagger}$	ΔE_0	ΔE_{elec}	$\Delta H°$	$\Delta G°$
Mn^-	1	4.18	3.30	3.30	5.97	–8.79	–9.85	–9.85	–6.38
Fe	1	8.23	7.48	7.48	9.58	1.04	0.28	0.28	2.66
Co^+	1	13.17	12.38	12.38	14.56	6.42	5.77	5.77	7.47
Tc^-	1	2.10	1.39	1.39	3.41	–14.16	–15.09	–15.09	–12.14
Ru	1	7.11	6.40	6.40	8.44	–0.97	–1.75	–1.75	0.57
Rh^+	1	15.03	14.47	14.47	17.14	8.34	7.59	7.59	9.84
Re^-	1	–0.56	–1.17	–1.17	0.37	–23.30	–24.07	–24.07	–21.67
Os	1	0.45	–0.08	–0.08	1.44	–12.65	–13.42	–13.42	–10.64
Ir^+	1	5.37	4.74	4.74	6.65	–0.55	–1.23	–1.23	0.92

The optimized geometric parameters and bonding patterns of the first TM row species, **28**, **29**, and **30**, are shown in Figure 4.11. The M–B distance is identical in **28** and **29**, but lengthens slightly in **30**. Conversely, The M–H distance decreases from **28** to an identical value in **29** and **30**. The M–C, B–H, and B–M–C parameters decrease as the metal is replaced; only the C–H distance shortens in this series. In the bonding analysis, BCPs are found along the M–B, M–H, and C–H coordinates in **28**. The analogous BCPs are located in **29** along with a B–H BCP and a RCP inside the M–B–H coordinates. The location of the B–H BCP parallels the shortening of this bond. In **30**, the M–B BCP is lost, which parallels the lengthening of this bond; only M–H, C–H, and B–H BCPs were located.

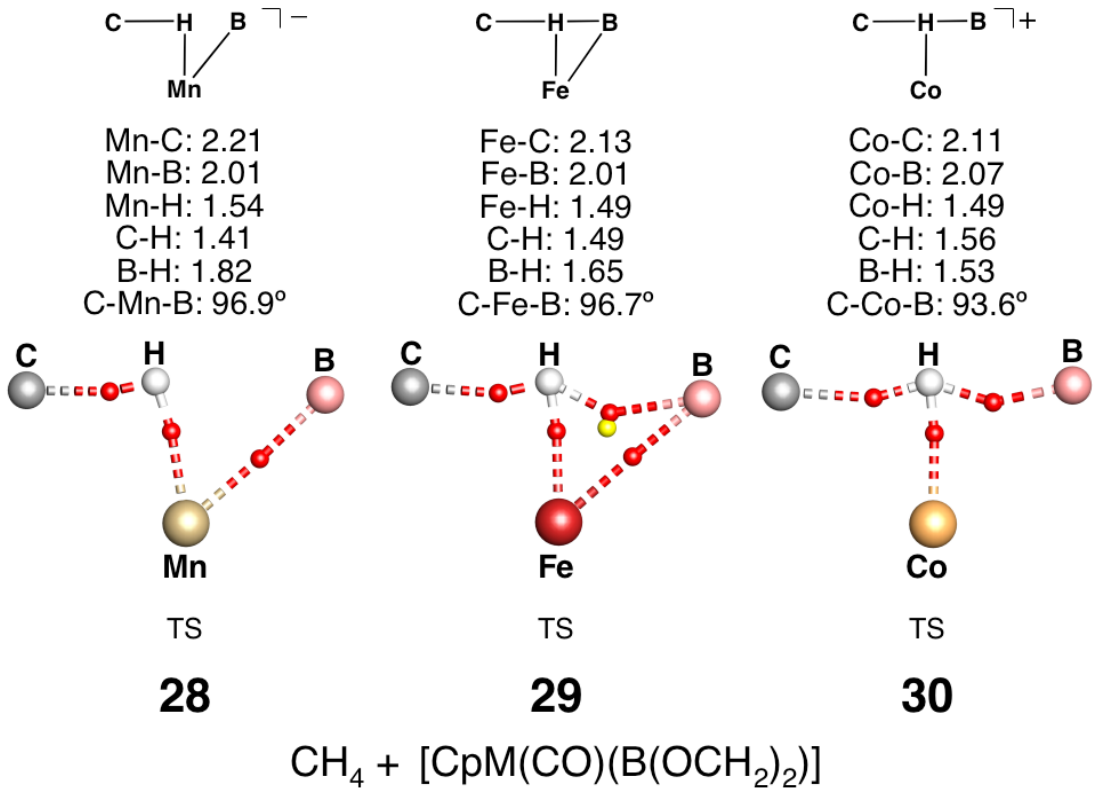

Figure 4.11. Optimized geometric parameters and bonding patterns of **28**, **29**, and **30**. The distances listed are in angstroms and the angles in degrees.

The results of similar analyses of the second row analogs (**31**, **32**, **33**) are shown in Figure 4.12. In these species, the M–B and B–M–C parameters oscillate; the M–C, M–H and B–H distances decrease; and the C–H distance increases as the metal is replaced across the row. Species **31** and **32** exhibit the same bonding patterns; M–B, M–H, and C–H BCPs were located in these species. A M–C BCP was located along this coordinate in **33**, which is also exhibits the shortest M–C distance. The M–B, M–H, and C–H BCPs were retained, and a RCP was located inside the Rh–C–H coordinates.

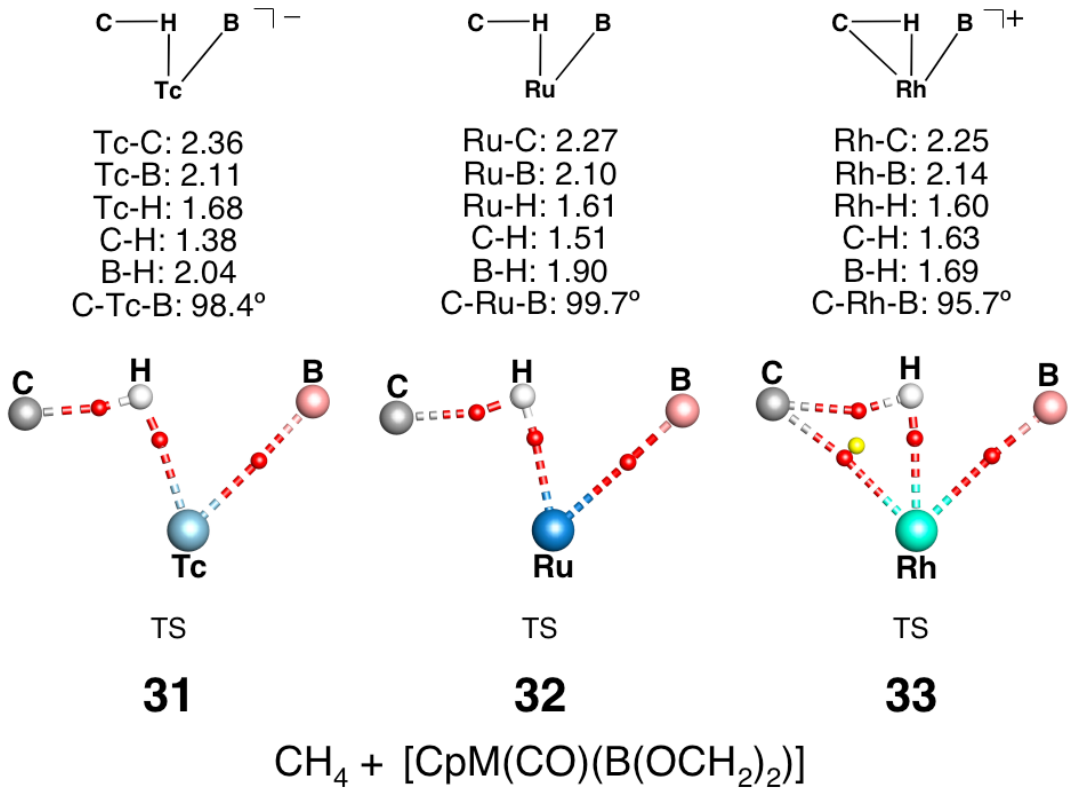

Figure 4.12. Optimized geometric parameters and bonding patterns of **31**, **32**, and **33**. The distances are reported in angstroms and angles in degrees.

The third row analogs (**34**, **35**, **36** – Figure 4.13) exhibit the same geometric trends for the first five parameters listed as the second row analogs: The M–B and B–M–C parameters oscillate; the M–C, M–H and B–H distances decrease; and the C–H distance increases between these species. The C–M–B angles, however, increase as the metal is replaced. These species exhibit the same bonding patterns as their second row analogs; M–B, M–H, and C–H BCPs were located in **34** and **35**. In **36**, Ir–C, Ir–B, Ir–H and C–H BCPs were located, and a RCP was located inside the Ir–C–H coordinates.

The rhenium and osmium systems are characterized by negative energy barriers. The $\Delta E^{\ddagger}_{SCF}$ values for these two systems are 0.6 and 1.8 kcal•mol^{-1}, respectively, while the ΔE_0 energies are –0.6 and 0.5 kcal•mol^{-1}, respectively. Together, these relative energies indicate that the negative energy barrier values result from zero-point effects. The formation of the σ-bound borane products are exothermic by 24.1 and 13.4 kcal•mol^{-1} for the rhenium and osmium systems, respectively. For the iridium system, the barrier to HT is small at 4.7 kcal•mol^{-1}, and the formation of the σ-bound borane complex is exothermic by 1.2 kcal•mol^{-1}.

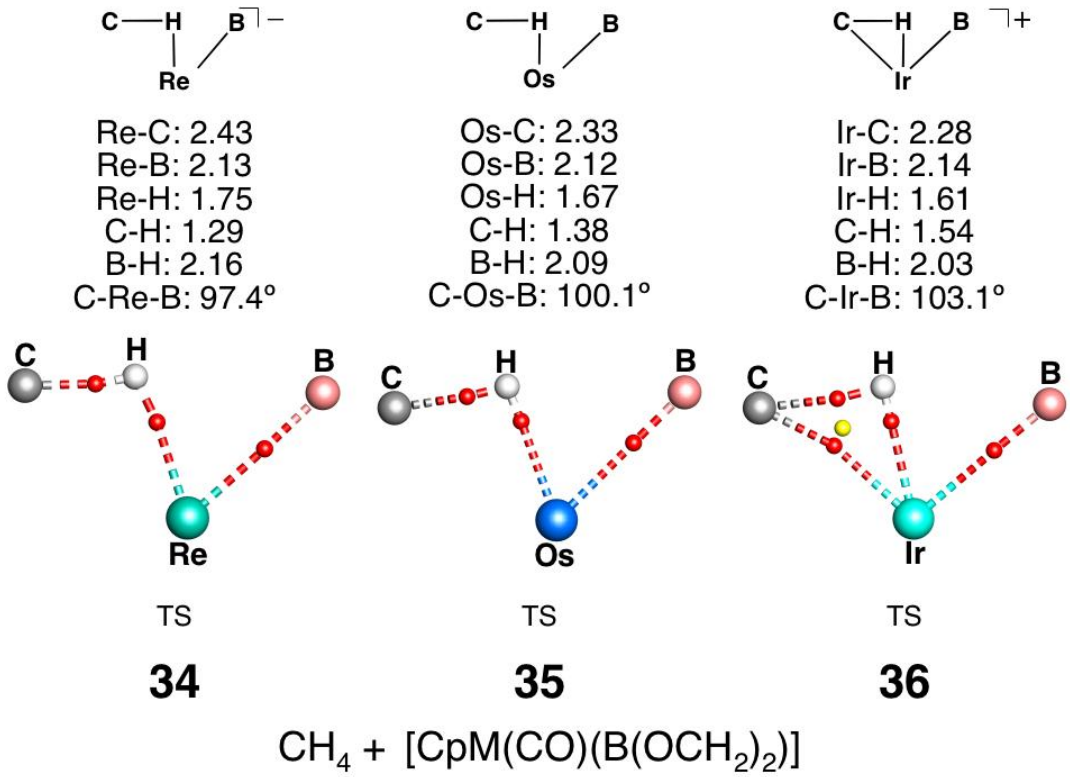

Figure 4.13. Optimized geometric parameters and bonding patterns of **34**, **35**, and **36**. The distances are reported in angstroms and angles in degrees.

Effects of Spectator Ligand on Bonding Patterns: The effect of spectator ligand on the bonding patterns were considered by studying the reaction: CH_4 + [$LM(PH_3)H'$] (M = Fe, Ru, Os). The ligands (L) considered for this study are Cp, Tp, a tris-carbene ligand[136] ($HB(NHC)_3$) that is similar to Tp, and a tris-phosphine ligand[137] ($HB(PMe_2CH_2)_3$ = HBP_3). The results for [$LFe(PH_3)(CH_3)(H)(H')$] (L = Cp (**37**), Tp (**37a**), $HB(NHC)_3$ (**37b**), HBP_3 (**37c**)) are presented in Figure 4.14. The results for the ruthenium analogs, [$LRu(PH_3)(CH_3)(H)(H')$] (L = Cp (**38**), Tp (**38a**), $HB(NHC)_3$ (**38b**), HBP_3 (**38c**)), are presented in Figure 4.15. Likewise, the results for the osmium analogs, [$LOs(PH_3)(CH_3)(H)(H')$] (L = Cp (**39**), Tp (**39a**), $HB(NHC)_3$ (**39b**), HBP_3 (**39c**)) are shown in Figure 4.16.

In the geometric analyses of the iron species, the Fe–C, Fe–H, distance lengthens as the ligand is replaced. The Fe–H', C–H, and H–H' distances oscillate between the species. Likewise, the C–Fe–H' angle decreases as the ligand is replaced. In the bonding analysis, **37** is characterized by Fe–H, Fe–H', C–H, and H–H' BCPs; a RCP is found inside the Fe–H–H' coordinates. However, the H–H' and Fe– H–H' RCP coalesce and the BCP is lost along the Fe–H' coordinate in **37a**. Species **37b** and **37c** exhibit the same bonding patterns as the Tp analog. The loss of the BCP along the Fe–H' coordinate parallels the increasing bond distance from **37** to **37c**.

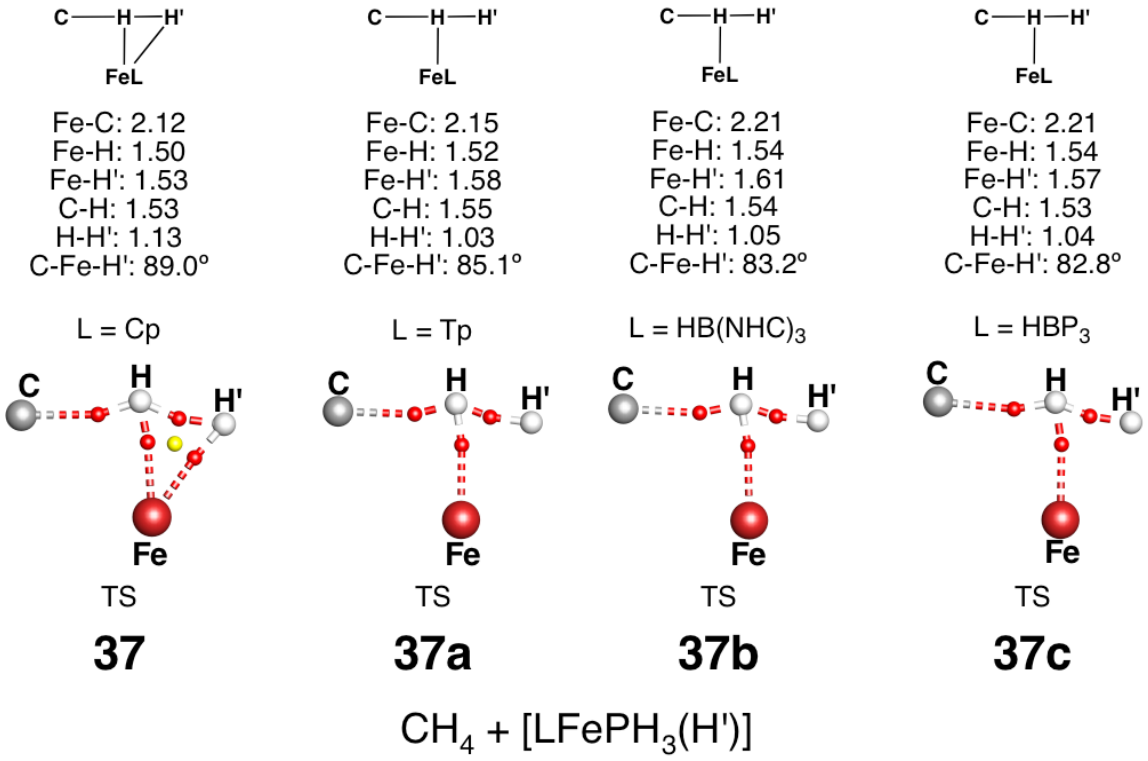

Figure 4.14. Optimized geometric parameters and bonding patterns for **37** (L = Cp), **37a** (L = Tp), **37b** (L = $HB(NHC)_3$), and **37c** (L = HBP_3). The distances listed are in angstroms and the angles in degrees.

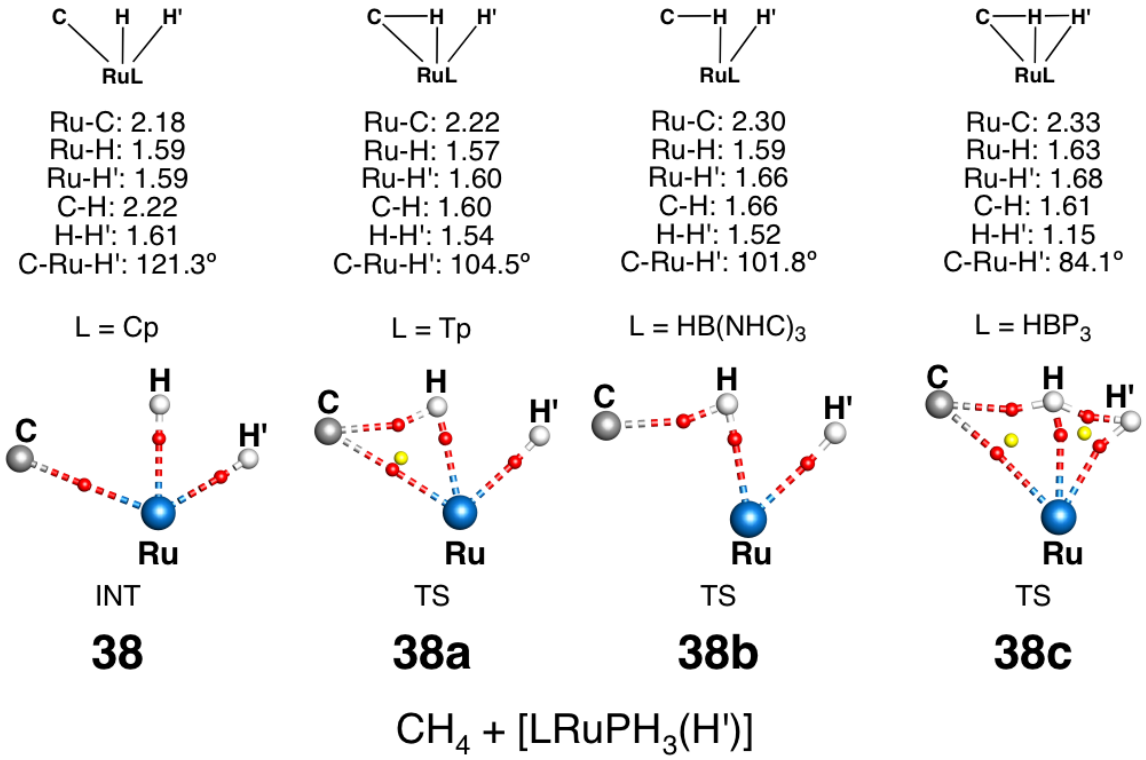

Figure 4.15. Optimized geometric parameters and bonding patterns for **38** (L = Cp), **38a** (L = Tp), **38b** (L = $HB(NHC)_3$), and **38c** (L = HBP_3). The distances listed are in angstroms and the angles in degrees.

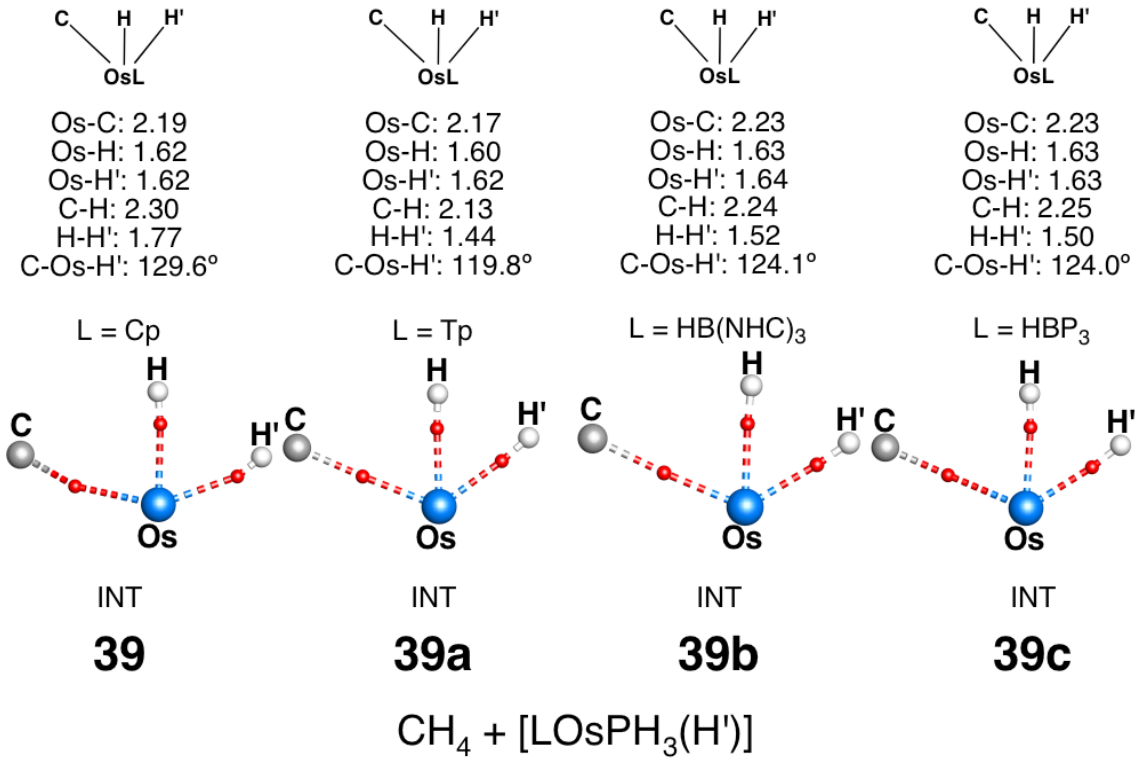

Figure 4.16. Optimized geometric parameters and bonding patterns for **39** (L = Cp), **39a** (L = Tp), **39b** (L = $HB(NHC)_3$), and **39c** (L = HBP_3). The distances listed are in angstroms and the angles in degrees.

In the geometric analyses of the ruthenium analogs, the Ru–C and Ru–H' distances lengthen as the ligand is replaced. The Ru–H and C–H distances oscillate while the H–H' and C–Ru–H parameters decrease between the species. Interestingly, the ruthenium Cp analog, **38** is an intermediate and BCPs are located along the Ru–C, Ru–H, and Ru–H' coordinates. Species **38a** is characterized by Ru–C, Ru–H, Ru–H' BCPs, and a RCP is found inside the Ru–C–H coordinates. The Ru–C BCP and RCP of **38a** coalesce and the the BCP along the Ru–C coordinate is lost in **38b**. The Ru–H, Ru–H', and C–H BCPs are retained. Despite having a longer Ru–C bond than in **38b**, a BCP is

located along this coordinate in **38c**. Species **38c** is characterized by full connectivity as Ru–C, –H, –H', C–H, and H–H' BCPs were found along with RCPs inside the Ru–C–H and Ru–H–H' coordinates.

In the osmium analogs, all of the geometric parameters oscillate as the ligand is replaced. Each species is an intermediate, and Os–C, Os–H, and Os–H' BCPs are located for these species. The character of the midpoint species, geometric parameters, and bonding patterns are insensitive to the change in ligand.

The influence of the spectator ligand on the bonding patters is limited. Species **37** exhibits a higher degree of connectivity than **37a**, **37b**, and **37c** where the former are characterized by the same bonding patterns. However, the four ruthenium species exhibit different bonding patterns. Consistent with an intermediate, **38** is characterized by only metal–ligand BCPs; however, **38c** exhibits full connectivity. The degrees of connectivity of **38a** and **38b** are in between the Cp and HBP_3 analogs. The character and bonding patterns of the osmium species are insensitive to the spectator ligand.

4.3.3 Stability of Bonding Patterns

To verify the stability of these bonding patterns, we examined seven models that individually displayed one of these sets of bonding patterns and assigned a higher level basis set to the metal center. The basis sets that were assigned to the non-metal atoms for the previous Bader's analyses were unchanged. Sets **A**, **D**, **E**, and **F** were verified up to the quadruple-ζ level by assigning the cc-pVQZ basis set to the scandium, nickel, manganese, and iron centers of **1**, **12**, **28**, and **37a**, respectively. Sets **B** and **C** were

verified at the triple-ζ level by assigning the TZVPP basis set to the palladium and ruthenium centers of **15** and **38a**, respectively. Set **G** was verified with **9**, and the last four primitives of the last shell of each angular momentum were split from each shell in WTBS to form a quadruple-ζ basis set in the valence. All seven sets have been identified and verified to higher levels in the basis.

4.3.4 Analysis of Basis Set and Density Functional Effects

Here, we investigate the basis set and density functional (DF) effects on the CPs of **1**, where a single previously optimized geometry was used. A variety of basis sets and DFs were considered in this analysis. Finally, **1** was individually optimized with four different basis sets assigned to scandium (the basis sets for the carbon and hydrogen atoms of section 1 remained the same) and the gradient fields were analyzed and compared.

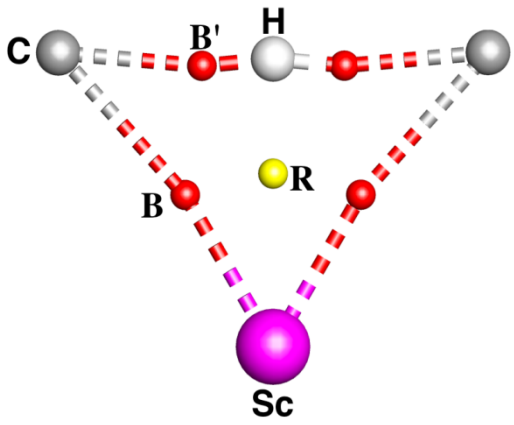

Figure 4.17. Atomic and CP definitions for the following analyses of **1**.

Basis Sets: For this investigation, the B3LYP/DZP coordinates of **1** and the B3LYP DF were used. The basis sets assigned to the carbon and hydrogen atoms in the previous analysis remain the same. The basis sets assigned to the scandium with the corresponding density and metric values for the Sc–C (**B**), C–H (**B'**), and ring (**R**) CPs of **1** are listed in Table 4.5. In Figure 4.17, the CPs and atoms designations are defined and will be used throughout this section.

Table 4.5. Density and metric data for the **B**, **B'** and **R** CPs of **1** for the basis sets listed.

basis set	CP ρ(e/bohr^3)			metric data (Å)			Sc–**B**–C
	B	**B'**	**R**	**B**	**R**	**B–R**	∠(°)
STO-3G	0.04812	0.13143	NA	NA	NA	NA	163.3
STO-6G	0.04789	0.13134	0.04643	1.114	1.019	0.556	163.8
WTBS	0.04981	0.12846	0.04607	1.158	1.136	0.605	168.2
3-21G	0.05104	0.12770	0.04763	1.159	1.144	0.622	167.7
6-31G	0.04991	0.12842	0.04677	1.161	1.138	0.597	167.4
6-31G*	0.05081	0.12845	0.04724	1.164	1.139	0.598	167.5
pVDZ	0.05039	0.12831	0.04674	1.158	1.136	0.605	168.0
TZV	0.05099	0.12828	0.04750	1.155	1.135	0.599	167.7
VDZ	0.05015	0.12835	0.04642	1.160	1.137	0.605	168.2
VTZ	0.05132	0.12840	0.04779	1.157	1.135	0.600	167.8
Wachters+f	0.05270	0.12847	0.04782	1.159	1.137	0.612	168.8
cc-pVDZ	0.05204	0.12831	0.04783	1.159	1.135	0.605	168.1
aug-cc-pVDZ	0.05213	0.12850	0.04776	1.159	1.136	0.607	168.3
cc-pVDZ-DK	0.05221	0.12853	0.04777	1.160	1.137	0.608	168.4
cc-pVTZ	0.05205	0.12836	0.04810	1.160	1.137	0.603	167.9
cc-pVQZ	0.05286	0.12822	0.04821	1.157	1.136	0.606	168.3
ANO	0.05269	0.12826	0.04794	1.159	1.136	0.609	168.5

The values of the density at **B** calculated with the fully contracted basis sets are slightly smaller than those calculated with the split valence, double-ζ, triple-ζ, and quadruple-ζ basis sets. The values of **B** and **B'** increase to ~0.052 and ~0.128 (e/bohr^3), respectively, with the change in basis. The density value of **R** increases slightly.

Geometrically, the distances between the **B** and **R** to scandium are insensitive to the basis set. Likewise, the distance between the **B** and **R** remains ~0.6 Å. For the Sc–**B**–C angles, a value of ~168° is reported for all but the STO-nG (n = 3,6) basis sets, which return a value smaller by ~5°.

The characteristic RCP that is found inside the four-center coordinates of **1** was not located in the gradient field in the STO-3G basis; instead, a BCP was located along the Sc–H coordinates with two RCPs nearly overlapping this BCP on both sides. Because of this discrepancy in bonding patterns for this small basis, we do not report the values for the RCP density and the geometric parameters at this level.

Basis set effects are more prominent for the densities of the CPs than for the relative locations of the CPs in the density. However the STO-nG (n = 3,6) basis sets performed poorly in describing both the value of the density at these CPs and their relative locations. While the values of the density at the CPs are slightly smaller at the WTBS level, the relative coordinates of the CPs are similar for this basis set to those of the larger basis sets.

Density Functionals: In Table 4.6, we report the metric and density values of the three CPs of **1** that were calculated with twelve DFs. We used the B3LYP/DZP optimized coordinates of **1** and assigned the cc-pVDZ basis sets to the scandium, carbon, and transferring hydrogen atoms while the methyl and Cp hydrogen atoms were assigned the D95 basis set. This level of basis was chosen as it was shown in the previous table to return accurate values for these CPs so any effect of the density functional will be readily seen.

The change in exchange and correlation functionals exhibits little effect on these values in comparing the data of the first four functionals. The radial distance of **B** (from the scandium coordinates) shortens when exact exchange is admixed into the DF, this distance continues to shorten as more exact exchange is included. Conversely, the radial distance of **B'** (from the carbon coordinates) increases as more exact exchange is admixed into the functional; the corresponding parameter for **R** remains essentially unchanged. The values of the density at these CPs are insensitive to the DF that was considered. Last we tested two meta density functionals (BB95, TPSS) and a hybrid density functional (MPWLYP1M) and observe minor differences between the values calculated with these functionals.

Table 4.6. Density and metric data for **B**, **B'** and **R** of **1** for the density functionals listed.

functional	CP ρ(e/bohr^3)			metric data (Å)			Sc–**B**–C
	B	**B'**	**R**	Sc–**B**	C–**B'**	Sc–**R**	∠(°)
BLYP	0.05146	0.12771	0.04803	1.164	0.958	1.137	167.9
BPW91	0.05206	0.12697	0.04846	1.164	0.961	1.138	167.8
mPWPW91	0.05200	0.12691	0.04844	1.164	0.961	1.138	167.7
PBE	0.05211	0.12671	0.04855	1.164	0.962	1.139	167.7
B3LYP	0.05204	0.12831	0.04783	1.159	0.966	1.135	168.1
B3PW91	0.05251	0.12768	0.04817	1.159	0.968	1.136	168.0
MPW0	0.05262	0.12777	0.04814	1.158	0.970	1.136	168.0
PBE0	0.05271	0.12760	0.04823	1.158	0.970	1.136	167.9
BH&HLYP	0.05252	0.12944	0.04741	1.152	0.977	1.133	168.2
BB95	0.05137	0.12634	0.04806	1.164	0.959	1.138	167.9
TPSS	0.05172	0.12768	0.04798	1.162	0.960	1.137	168.0
MPWLYP1M	0.05162	0.12803	0.04781	1.162	0.960	1.137	168.3

Full Optimization: Species **1** was individually optimized with four different basis sets assigned to the scandium (WTBS, Wachters+f, cc-pVDZ, and LANL2mDZ) and the electron densities of these optimized geometries were analyzed with Bader's

analysis. The basis sets assigned to the carbon and hydrogen atoms of DZP remained the same for these optimizations. The optimized geometric parameters are presented in Table 4.7.

Interestingly, the optimized geometric parameters of **1** are similar between these four basis sets. The C–H distance that was calculated at the WTBS level is slightly smaller than the other three values, and this distance corresponds to the slightly smaller C–Sc–C angle at this same level.

Table 4.7. Optimized geometric parameters for **1** optimized with four basis sets assigned to scandium.

basis set	metric data			
	r(Sc–C) (Å)	r(Sc–H) (Å)	r(C–H) (Å)	C–Sc–C ∠ (°)
WTBS	2.409	1.891	1.438	73.3
Wachters+f	2.408	1.899	1.441	73.5
cc–pVDZ	2.408	1.897	1.440	73.4
LANL2mDZ(f)	2.409	1.896	1.441	73.5

The corresponding metric data and density values for the CPs for these four geometries of **1** are reported in Table 4.8. Minimal differences between the density values and radial distances of these CPs are observed. The distance of **R** from the scandium center calculated at the Wachters+f level is ~0.1 Å longer than those calculated at the other levels, and the Sc–**B**–C angle is two degrees smaller at this same level in the basis. Interestingly, the values returned with WTBS assigned to scandium are similar to those values calculated at higher levels of theory when the molecule was optimized with this basis set.

Table 4.8. Metric data of the CPs and corresponding densities for **1** optimized with each basis set listed.

basis set	**B**		**B'**		**R**		Sc–**B**–C
	r^a (Å)	ρ (e/bohr^3)	r^b(Å)	ρ (e/bohr^3)	r^a (Å)	ρ (e/bohr^3)	$\angle$ (°)
WTBS	1.157	0.05012	0.965	0.12905	1.134	0.04653	168.0
Wachters+f	1.159	0.05313	0.964	0.12578	1.144	0.04611	166.0
cc–pVDZ	1.159	0.05210	0.965	0.12853	1.136	0.04768	168.4
LANL2mDZ(f)	1.157	0.05010	0.964	0.12912	1.134	0.04653	168.0

a: relative to scandium coordinates; *b*: relative to carbon coordinates

4.4 Conclusions

We have identified all seven sets of bonding patterns by analyzing midpoint species along the reaction coordinates of the reactions described above. On the sole basis of geometric parameters of these TM species, the bonding patterns cannot be determined *a priori.* Bader's analysis has been shown to be helpful in characterizing the bonding patterns of these model complexes. The transferring hydrogen does not interact with the metal center in the "classic" σBM mechanism (e.g. **1**, **2**, **3**). For the other "classic" mechanism, OA/RE, the hydrogen can interact in the TS (e.g. **8**) and forms a formal bond in the oxidized intermediate (e.g. **6**, **9**). Differing degrees of connectivity have been identified in TSs for HT; thus connectivity varies in these reactions. In general, those metal center that have d electrons available to participate in HT interact with the transferring hydrogen during this reaction.

CHAPTER V

DENSITY FUNCTIONAL THEORY INVESTIGATION INTO THE MECHANISM FOR η^2-ALKYNE TO VINYLIDENE ISOMERIZATION BY THE ADDITION OF PHENYLACETYLENE TO $[(\eta^3\text{-}C_3H_5)Rh(P\textit{i}Pr_3)_2]$

5.1 Introduction

Hydrocarbons can provide "ubiquitous functionality" by developing techniques for facile carbon–hydrogen (C–H) bond activation.[1] Facile activation of this bond can occur at transition metals (TM),[2] and selectively has been demonstrated with TM systems.[35–37] For example, the C–H bond is the isomerization of an alkyne to the corresponding vinylidene (HCCX → :CC(H)(X)), which in the gas phase is very endothermic,[138] can be easily accomplished at a TM center.

Antonova and coworkers synthesized the vinylidene complex $[CpMn(CO)_2(CC(H)(Ph))]$ by photolyzing $[CpMn(CO)_3]$ in alkyne.[139] The mechanism for vinylidene formation was unclear, but an η^2-alkyne complex, $[CpMn(CO)_2(\eta^2\text{-}HCCPh)]$, was detected by IR spectroscopy and considered to be the precursor species to the final vinylidene product.

The Hoffmann[140] and De Angelis[141] groups studied the mechanism for vinylidene formation from $[CpMn(CO)_2(\eta^2\text{-}HCCH)]$. In the lowest energy pathway, the η^2-alkyne

slipped to bind through the σ-C–H bond to form [CpMn(CO)$_2$(σ-HCCH)]. Hydrogen migration to the β carbon followed and the vinylidene product was formed. This mechanism is called *1–2 shift*, which is the consensus on the mechanism for a d^6 metal center (i.e. [CpMn(CO)$_2$]).

Werner and coworkers considered an oxidative pathway from the d^8 metal complex, [ClRh(P*i*Pr$_3$)$_2$(η^2-HCCH)], and the product, [C_5H_5Rh(P*i*Pr$_3$)(CCH_2)], was isolated upon ligand exchange and phosphine loss.[142] The same reaction was run with HCCPh and the η^2-alkyne complex [C_5H_5Rh(P*i*Pr$_3$)(η^2-HCCPh)], the alkynyl rhodium hydride complex [C_5H_5Rh(H)(P*i*Pr$_3$)(CCPh)], and the vinylidene complex [C_5H_5Rh(P*i*Pr$_3$)(CC(H)(Ph))] were isolated.[48] Analogous alkynyl hydride complexes of rhodium[48] and iridium[49] were isolated, which implied that the mechanism proceeded through an oxidative pathway.

Scheme 5.1

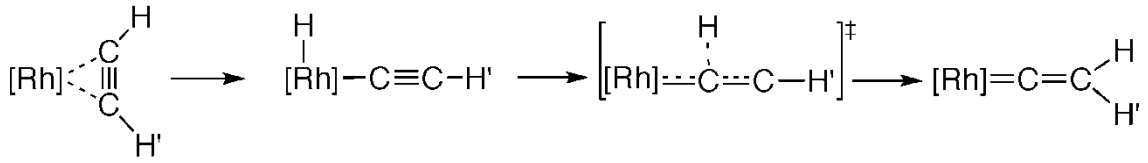

Wakatsuki et al. theoretically studied the oxidative pathway from the reactant, [ClRh(PH_3)$_2$(η^2-HCCH')], and found that this pathway proceeded in two steps (Scheme 5.1).[50] Oxidative cleavage of acetylene from the reactant to form the five-coordinate, alkynyl rhodium hydride intermediate, [ClRh(PH_3)$_2$(H)(CCH')], was the first step. The

vinylidene product, [ClRh(PH_3)$_2$(CC(H)(H'))], resulted from hydrogen migration from the rhodium to the β carbon, which is the second step. A single TS between the alkynyl rhodium hydride intermediate and the final vinylidene product was found that was characterized by an inverted "T–shaped" geometry. This pathway was called *1–3 shift*. However, the barrier for hydrogen migration in the intramolecular pathway was high, and a bimolecular mechanism was investigated and found to be lower in energy than the former.

Grotjahn and coworkers reported that H/D cross over was not observed when the complexes [ClRh(P*i*Pr$_2$R^1)$_2$(η^2-HCC*i*Pr)] (R^1 = Ph, *i*Pr, imidazol-2-yl) and the deuterated alkyne analogs were mixed.[51] The bimolecular pathway was therefore shown to be implausible for this isomerization. In further work, the researchers confirmed the *1–3 shift* mechanism.[143] De Angelis et al. recently investigated this chemistry from the starting material (SM) [ClRh(P*i*Pr$_3$)$_2$(η^2-HCCH)] and found that the enthalpic barriers to hydrogen migration in the intra and bimolecular pathways were similar, but the free energy barrier of the intramolecular pathway was ~20 kcal•mol^{-1} less than that of the bimolecular pathway.[52]

Scheme 5.2

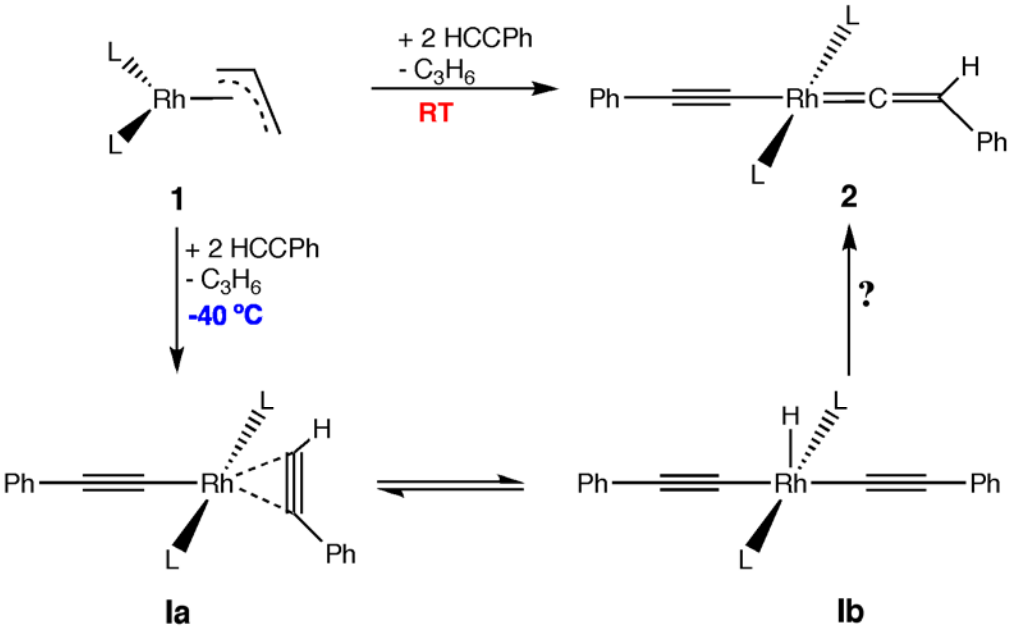

Important experimental observations:
- At RT, addition of 2 HCCPh to **1** resulted in **2**.
- At -40 °C, the same reaction resulted in formation (and isolation) of **Ia**.
- Via ^{1}H NMR, **Ia** and **Ib** were observed to be in equilibrium.
- With excess pyridine in solution, **Ib**(pyr.) was isolated.

L = P*i*Pr$_3$

In further studying this isomerization, Werner and coworkers added two equivalents of phenylacetylene (PA) to [(η^3-C_3H_5)Rh(P*i*Pr$_3$)$_2$] (**1**) to form the alkynyl, vinylidene rhodium product, **2**, (Scheme 5.2).[47] At room temperature (RT), the reaction proceeded to form the alkynyl, vinylidene complex **2**; however, at –40 ºC, the reaction proceeded to form the π-bound PA, alkynyl complex, **Ia**. In solution, **Ia** was observed (via ^{1}H NMR) to be in equilibrium with **Ib**, the bis-alkynyl Rh^{III}–H complex. Complex **Ib** was trapped by running the reaction in excess pyridine where a pyridine molecule coordinated trans to the hydride to form **Ib**(pyr). The experimentalist concluded that **Ia** and **Ib** are intermediates on the reaction pathway that results in the formation of **2**.

Here we present our density functional theory (DFT) study of the mechanism for the formation and of **2**. We consider the effect of the phosphine on the relative energies (Section 5.3.1), the reaction mechanism to form **Ia** (Section 5.3.2), and finally the various pathways for the alkyne to vinylidene isomerization (**Ia** to **2** - Section 5.3.3). The lowest energy pathway for the formation of **2** is compared to the pathway for this isomerization from [ClRh(P*i*Pr$_3$)$_2$(η^2-HCCPh)] (**Ia-Cl**).

5.2 Computational Method

All DFT calculations reported here were performed with the Gaussian 03 suite of programs.[72] Each complex reported in this section was optimized at the B3LYP/BS1 level of theory, and the analytical frequencies were calculated at this same level of theory for each complex to determine if the force constants were real (intermediate) or if one was imaginary (TS). The default convergence criteria were used for all optimizations. The B3LYP density functional is a combination of the Becke3 exchange[58] and Lee–Yang–Parr correlation[59] functionals. Basis set 1 (BS1) is defined as follows: Rhodium was assigned the small core Los Alamos National Laboratory 2 (LANL2) effective core potential of Hay and Wadt[73] and the valence double-ζ (341/341/31) basis set as modified by Couty and Hall[74] (ECP/BS = LANL2mDZ); the phosphorus, C_α, C_β, C_γ, C_1', C_1", C_2', C_2", H', and H" atoms were assigned the correlation consistent polarized valence double-ζ (cc-pVDZ) basis sets of Dunning;[75] the remaining carbon and hydrogen atoms were assigned the full double-ζ (D95) basis sets of Dunning.[76] For the B3LYP/BS1 optimized intermediates and TSs, frequency

calculations were performed at this same level of theory where the zero point correction and corrections to the electronic energy, enthalpy, and free energy were obtained.

For the barriers for allyl rearrangement that were refined at a higher level in the basis (**$TS_{1–3}$**, **TS'**), the basis set used (BSr) consists of the Stuttgart relativistic small core (RSC) 1997[108] ECP and the triple-ζ basis set.[144] The phosphorus, C_α, C_β, and C_γ atoms were assigned the correlation consistent polarized valence triple-ζ (cc-pVTZ) basis sets of Dunning,[75] and the remaining carbon and hydrogen atoms retained the original assignments of the D95 basis sets. The B3LYP/BSr//B3LYP/BS1 energies were added to the B3LYP/BS1 corrections to the enthalpy and free energy to obtain the thermodynamic values for these barriers.

The values discussed in the text are primarily enthalpies ($\Delta H^{\circ/\ddagger}$) and free energies ($\Delta G^{\circ/\ddagger}$) in the gas phase at standard conditions (298K, 1 atm). The electronic energies (ΔE_{elec}), electronic energies with zero point corrections (ΔE_0), enthalpies ($\Delta H^{\circ/\ddagger}$), and free energies ($\Delta G^{\circ/\ddagger}$) are reported in tables. All 3D representations of the optimized molecular geometries were constructed with JIMP 2.[77]

5.3 Results and Discussion

5.3.1. Effect of Phosphine Ligand on Relative Energies

The relative energies of **Ia**, **Ib**, and **2** (all relative to **1** + 2PA) were calculated with a variety of phosphines and the results are presented in Table 5.1. Three arrangements of P*i*Pr$_3$ are examined and illustrated in Figure 5.1. For "chase", the primary carbon atoms of the individual propyl units reside above and below the Rh–C–H

plane, and rotation about the pseudo–C_3 axis will turn each propyl unit into the other. For "umbrella", the hydrogen atoms of each secondary carbon are pointed toward the center of the phosphine. For the crystal structure arrangement, two of the propyl units are symmetric while the other is rotated 180° about the Rh–C bond relative to the other propyl units. These former two forms are higher in energy than the latter by 11.7 and 18.4 kcal•mol^{-1}, respectively.

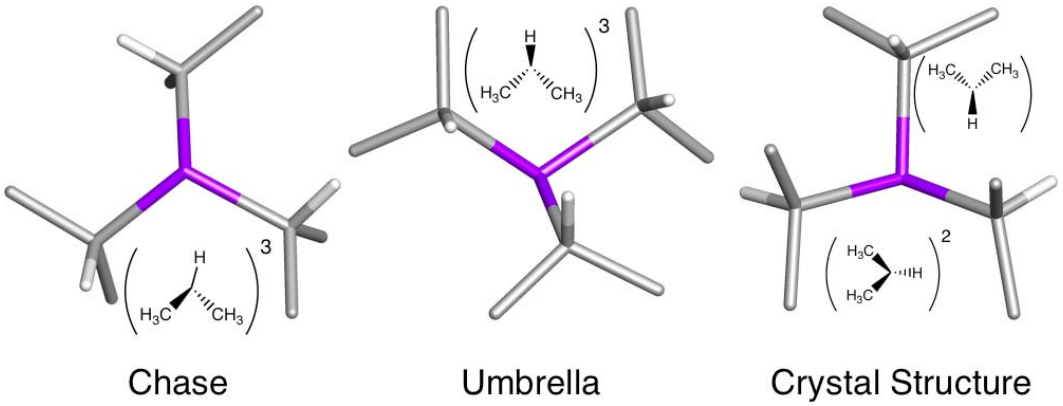

Figure 5.1. The three arrangements of the P*i*Pr$_3$ ligand that are used in this study. The methyl hydrogen atoms have been removed for clarity.

Table 5.1. Relative energies of **Ia**, **Ib**, and **2**. Energies are relative to **1** + 2PA. Energies are reported in kcal•mol^{-1}.

	1		**2**		**Ia**		**Ib**	
	$\Delta H°$	$\Delta G°$	$\Delta H°$	$\Delta G°$	$\Delta H°$	$\Delta G°$	$\Delta H°$	$\Delta G°$
P*i*Pr$_3$[a]			-25.41	-15.54	-23.76	-12.99	-21.81	-13.49
P*i*Pr$_3$[b]			-27.67	-17.33	-24.17	-13.92	-25.32	-17.41
P*i*Pr$_3$[c]			-25.60	-18.10	-22.43	-12.51	-22.79	-16.60
PEt_3			-17.57	-7.98	-17.08	-6.33	-14.61	-5.69
PMe_3			-17.01	-8.29	-18.46	-8.59	-13.25	-4.94
PMe_2Ph	0	0	-13.17	-3.79	-14.70	-5.85	-10.26	-0.71
$PMePh_2$			-12.45	-2.23	-14.46	-3.36	-7.89	2.68
PPh_3			-15.30	-7.80	-17.65	-8.51	-10.47	1.38
PH_3			-6.93	3.70	-10.51	0.36	2.03	9.85
PCl_3			11.57	23.29	2.94	12.06	27.04	36.17
PF_3			12.39	21.75	5.34	12.92	28.93	38.48

a: "chase" arrangement; *b*: "umbrella" arrangement; *c*: crystal structure alignment

The experimental observations are matched with the "chase" P*i*Pr$_3$ ligands as **2** is the predicted product and **Ia** and **Ib** are calculated to be in equilibrium ($\Delta G°_{\mathbf{Ib–Ia}}$ = 0.5 kcal•mol^{-1}) at the B3LYP/BS1 level of theory. However, for the latter two arrangements, **Ib** is exergonic by ~3.5 kcal•mol^{-1} (relative to **Ia**). Species **2** was the predicted product for P*i*Pr$_3$ and PEt_3 while **Ia** was the predicted product with PMe_3 to PH_3. The reaction was endothermic with PF_3 and PCl_3. We used the crystal structure form of P*i*Pr$_3$ in our study of the mechanism (sections 2 and 3) because **2** was predicted to be the product with this ligand. Even PEt_3 does not show the strong enthalpic stabilization of **2** over **Ia** that is shown for P*i*Pr$_3$.

Theoretical and experimental evidence exists for this sensitivity to the phosphine used. De Angelis and coworkers reported that the η^2-alkyne and alkynyl rhodium hydride complexes, [ClRh(PR$_3$)$_2$(η^2-HCCH)] and [ClRh(PR$_3$)$_2$(H)(CCH)], are isoenergetic when R = *i*Pr but the latter is ~9 kcal•mol^{-1} greater in energy relative to the

former when R = H. Werner and coworkers reported that the synthesis of η^2-alkyne [$CpRhPR_3$] complexes was unsuccessful with PMe_3 but successful P*i*Pr_3.[145]

*5.3.2. The Mechanism for the Formation of **Ia***

In this section, we present our calculated mechanism for the addition of two equivalents of PhCCH (PA) to **1** to form the intermediate, **Ia**. The formation of this intermediate follows the isomerization of **1**, the binding and activation of the first equivalent of PA (PA'), the elimination of propene, and finally the binding of the second equivalent of PA (PA''). The *sp* carbon atoms of PA' are labeled C_1', C_2', and the hydrogen that is transferred is labeled H'. The relative enthalpies and free energies for the intermediates and TSs on this pathway are presented in Table 5.2. The enthalpies and free energies are presented as relative to **1** (+ 2PA) in the first set and relative to the intermediate that precedes the following TS and next intermediate in the second set. For example, the numbers reported for both $\mathbf{TS_{4a–5a}}$ and **5a** in the second set are relative to **4a**.

Isomerization of the reactant. Two plausible mechanisms for the isomerization of **1** are considered (Scheme 5.3). Complex **1** is a pseudo square–planar, four-coordinate η^3-allyl Rh^I complex with C_α–Rh–C_γ and P–Rh–P angles of 66.7º and 109.4º, respectively. Complex **3** is a pseudo T–shaped, three-coordinate, η^1-allyl Rh^I complex with a P–Rh–P angle of 165.1º and the allyl has slipped to bind η^1 to the rhodium. The carbon backbone of the allyl is aligned with the C_α–H_α bond (dihedral angle between H_α–C_α–C_β–C_γ is ~0º). Complexes **1** and **3** are joined by $\mathbf{TS_{1–3}}$ where, in the animation

of the imaginary mode, the widening of the P–Rh–P angle is *concomitant* with allyl slippage to bind η^1. At the B3LYP/BS1 level of theory, the enthalpic and free energy barriers to this isomerization are 23.8 and 21.0 kcal•mol^{-1}, respectively. The optimized geometries of **1** and **3** at this level of theory are shown along with select angles and bond lengths in Figure 5.2.

Table 5.2. The relative energies for the intermediates and TSs of section 2. Energies are reported in kcal•mol^{-1}.

	set 1: relative to **1**[a]		set 2: relative to prior intermediate[b]	
species	$\Delta H^{\circ/\ddagger}$	$\Delta G^{\circ/\ddagger}$	$\Delta H^{\circ/\ddagger}$	$\Delta G^{\circ/\ddagger}$
1[c]	0	0	0	0
TS$_{1-3}$[c]	23.79	21.01	23.79	21.01
3[c]	19.49	14.46	19.49	14.46
4a[d]	11.94	23.55	–7.55	9.08
4b	13.19	23.69	–6.30	9.23
TS$_{4a-5a}$[d]	24.67	34.82	12.26	12.50
TS$_{4b-5b}$[d]	24.22	34.07	11.03	10.38
5a[d]	15.39	24.38	3.45	0.83
5b[d]	13.15	22.06	-0.04	–1.63
TS$_{5a-6a}$[d]	16.89	26.09	1.50	1.72
TS$_{5b-6b}$[d]	14.42	22.83	1.27	0.77
6a[d]	7.25	17.19	–8.14	–7.18
6b[d]	7.21	15.70	–5.95	–6.36
TS$_{6a-8}$[d]	11.98	21.59	4.73	4.40
TS$_{6b-7b}$[d]	10.91	19.44	3.70	3.74
7a[d]	NA	NA	NA	NA
7b[d]	–2.98	1.16	–10.19	–14.55
8[e]	–5.86	–13.27	---	---
9[f]	–12.85	–2.44	---	---
Ia[g]	–22.43	–12.51	---	---

a: relative to **1** + 2PA; *b*:IM and TS is relative to preceding IM; *c*: +2PA; *d*: + PA; *e*: +PA, C_3H_6; *f*: +PA; *g*: +C_3H_6

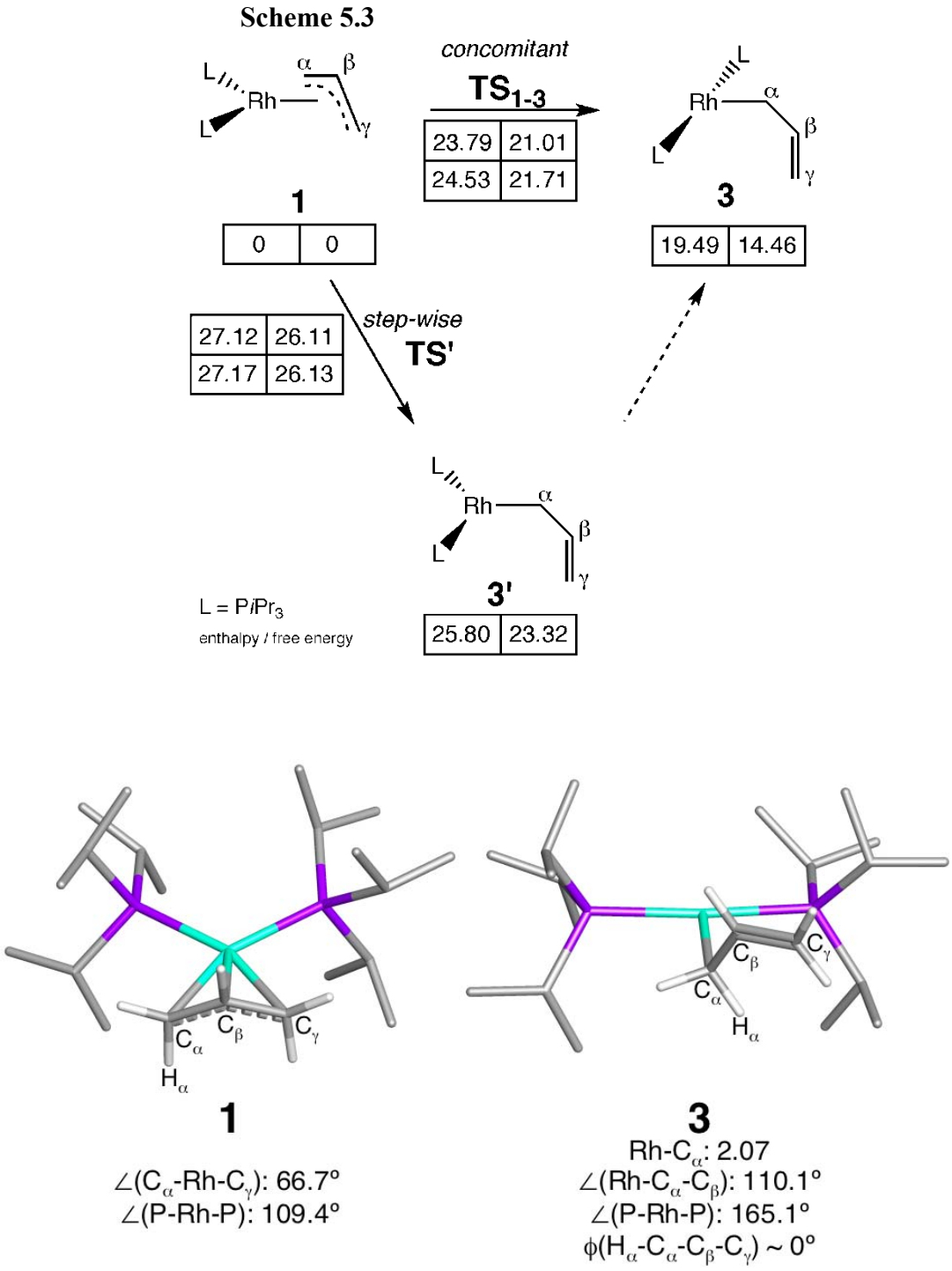

Figure 5.2. B3LYP/BS1 optimized geometries of **1** and **3** and select optimized parameters. Distances listed are in angstroms and angles in degrees. Non-essential hydrogen atoms have been removed for clarity.

A *step-wise* mechanism for this isomerization was investigated, but it proceeds through a higher energy intermediate (**3'**). Mechanistically, the allyl slips to η^1 prior to a change in the P–Rh–P angle, which is nearly identical to that of **1** (110.7º). A transition state (**TS'**) was located that connects **1** to **3'** where, in the animation of the imaginary mode, the allyl slips to bind η^1 without a significant change in the P–Rh–P angle. At the B3LYP/BS1 level of theory, the enthalpic and free energy barriers of this *step-wise* pathway (**TS'**) are 27.2 and 26.1 kcal•mol^{-1}, respectively, which are 3.3 and 5.1 kcal•mol^{-1} greater than those of the *concomitant* pathway.

The enthalpic and free energy barriers of $\mathbf{TS_{1–3}}$ and **TS'** were refined at the higher level of theory (B3LYP/BSr) and reported in the second row of the 2x2 boxes in Scheme 5.3. The enthalpic and free energy barriers for the *concomitant* pathway are slightly higher at this level of theory, but the values for the *step-wise* pathway are nearly identical. As a result, the enthalpic and free energy barriers of **TS'** at this higher level of theory are greater than $\mathbf{TS_{1–3}}$ by 2.6 and 4.4 kcal•mol^{-1}, respectively; therefore, the *step-wise* pathway was not pursued further.

The binding of PA' to **3** follows the isomerization a **1** and may assist it in ways not examined here. In Scheme 5.4, the reaction is illustrated to the formation of **Ia**. The relative enthalpies and free energies (relative to **1**) are reported in kcal•mol^{-1} and included in the scheme.

Binding of PA'. Isomer **4a** is a pseudo square–planar, Rh^I complex where the η^1-allyl is aligned *syn* to the phenyl ring of the alkyne, while complex **4b** is a rotormer of **4a** where the allyl has rotated ~180º around the Rh–C_α bond to align *anti* to the PA' ligand. The optimized geometries of both rotormers are shown in Figure 5.3 and important geometric parameters are also listed. This rotation causes few changes in most of the geometric parameters; however, the Rh–C_α–C_β angle of **4b** is ~17° wider than **4a**. Relative to **4a**, complex **4b** is slightly less stable. The trans influence of PA' in the π-binding mode is seen in the length of the Rh–C_α bond (relative to the bond length of **3**), which lengthens by ~0.1 Å with the coordination of PA. The π-binding of PA' stabilized **3** by ~7 kcal•mol^{-1} ($\Delta H°_{\mathbf{4a(b)–3}}$) but is endergonic by ~9 kcal•mol^{-1}. In the π-binding of an alkyne to a metal center, the C–X bonds pendent to the triple bond are typically bent, and this phenomenon was calculated for both isomers of **4** as the H'–C_1'–C_2' and C_1'–C_2'–C_{Ph} angles are included in Figure 5.3.

Scheme 5.4

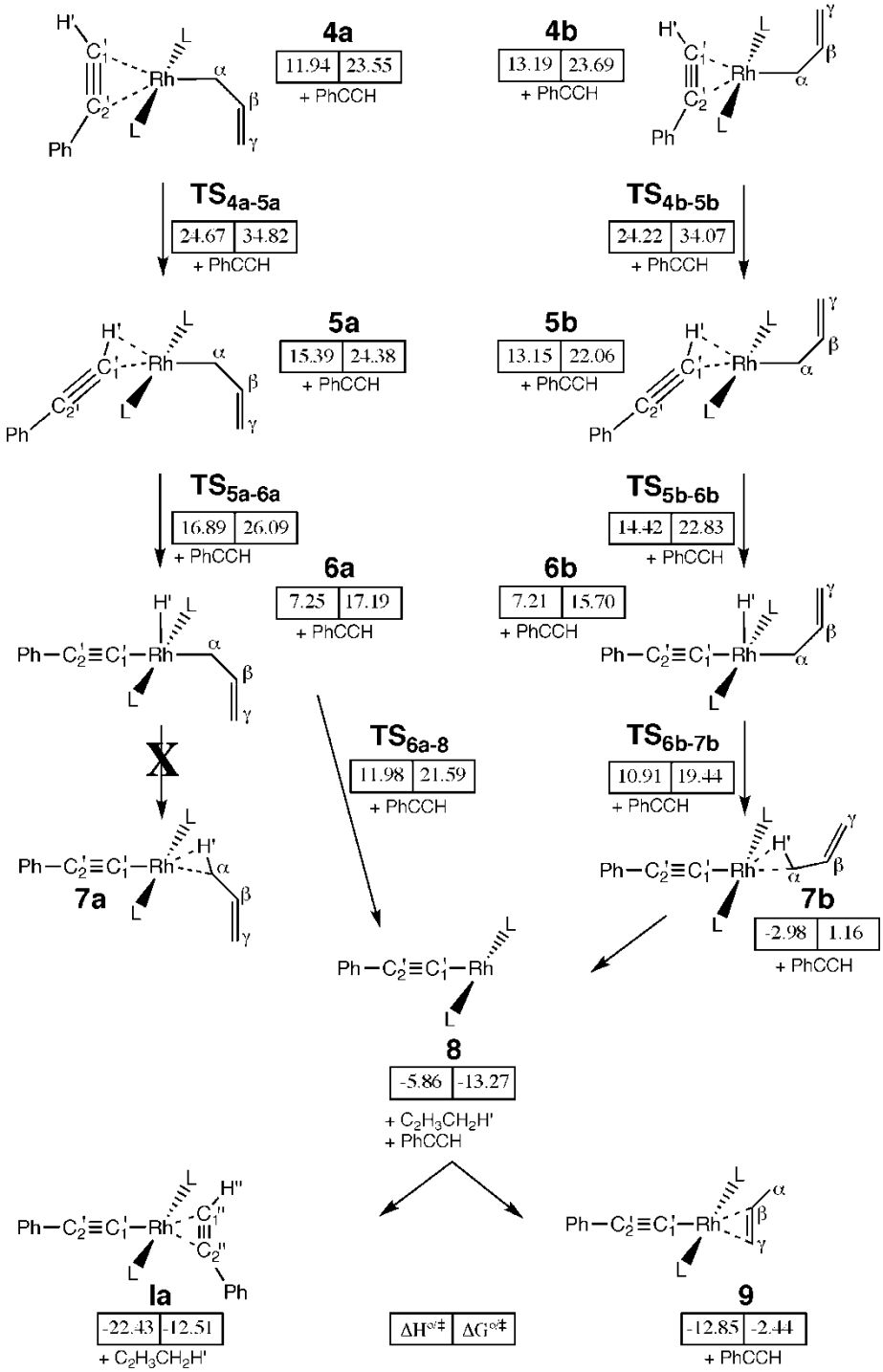
4a
11.94 23.55
+ PhCCH
4b
13.19 23.69
+ PhCCH
TS4a-5a
24.67 34.82
+ PhCCH
TS4b-5b
24.22 34.07
+ PhCCH
5a
15.39 24.38
+ PhCCH
5b
13.15 22.06
+ PhCCH
TS5a-6a
16.89 26.09
+ PhCCH
TS5b-6b
14.42 22.83
+ PhCCH
6a
7.25 17.19
+ PhCCH
6b
7.21 15.70
+ PhCCH
TS6a-8
11.98 21.59
+ PhCCH
TS6b-7b
10.91 19.44
+ PhCCH
7a
7b
-2.98 1.16
+ PhCCH
8
-5.86 -13.27
+ C2H3CH2H'
+ PhCCH
Ia
-22.43 -12.51
+ C2H3CH2H'
ΔH°‡ ΔG°‡
9
-12.85 -2.44
+ PhCCH

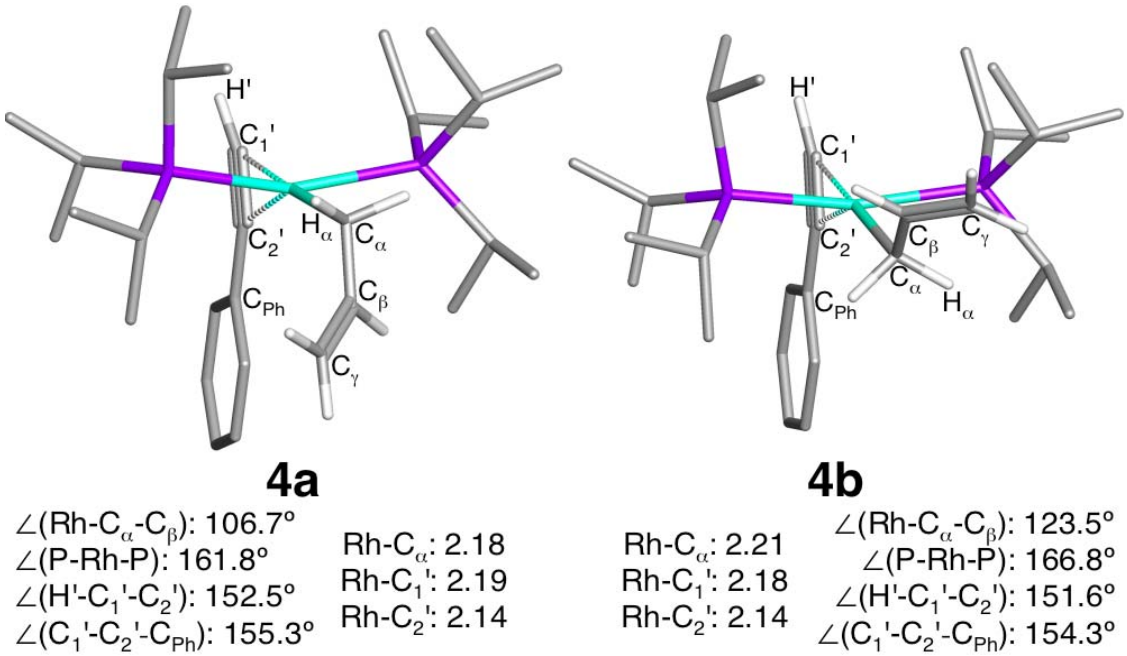

Figure 5.3. B3LYP/BS1 optimized geometries of **4a** and **4b** and select optimized parameters. Distances listed are in angstroms and angles in degrees. Non-essential hydrogen atoms have been removed for clarity.

The isomerization from the π- to σ- binding mode of PA'. The optimized geometries of the σ-bound PA', η^1-allyl complexes, **5a(b)**, are shown in Figure 5.4. These complexes *presumably* result from alkyne slippage to bind through the σ-C–H bond. The enthalpic difference (ΔH^o: **5x** – **4x**) for the **a** isomers is greater than that for the nearly isenthalpic **b** isomers; however, the free energy difference (ΔG^o: **5x** – **4x**) between both sets is small. The geometric parameters listed in Figure 5.4 are very similar between the **a** and **b** isomers of **5**; however, in **5a**, the P–Rh–P angle is more strained at 163.6° whereas the same angle is **5b** is 179.1°. With the coordination of PA' in the σ-binding mode, the Rh–C_α bond length shortens slightly to 2.16 Å, which would

indicate that the trans influence for this binding mode is slightly less than that of the π-binding mode. The difference in the Rh–C_α–C_β angle that was large for the isomers of **4** has decreased significantly to 3º for the isomers of **5**. In the **4** isomers, the phenyl ring is in the plane defined by the C_1', C_2', and Rh atoms; however, in the σ-binding mode of **5**, the phenyl ring has rotated roughly 90º to be orthogonal to the previously defined plane.

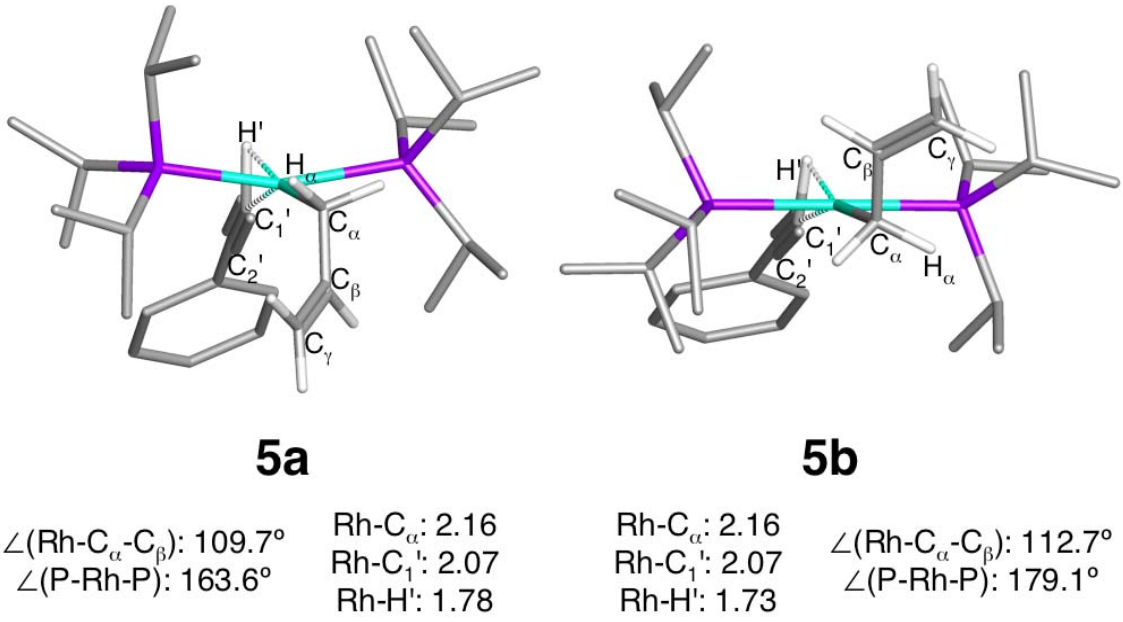

Figure 5.4. B3LYP/BS1 optimized geometries of **5a** and **5b** and select optimized parameters. Distances listed are in angstroms and angles in degrees. Non-essential hydrogen atoms have been removed for clarity.

Relative to **4x**, the enthalpic and free energy barriers of the transition states (**$TS_{4x–5x}$**) for the isomerization of the π-bound PA' to the σ-binding mode are greater than 10 kcal•mol^{-1}. Relative to **1**, the free energy barriers are quite high (~35 kcal•

mol^{-1}). Although one might expect that there would be a large steric influence on the barriers, calculations with PMe_3 and acetylene (relative to PMe_3 analog of **4x**) show even higher enthalpic and free energy barriers of ~15 kcal•mol^{-1}.

The enthalpic barrier to isomerization between the two binding modes of PA is calculated to be higher than the enthalpic barrier for the loss of PA. One possibility for this mechanism is that the incoming PA can bind *either* in the π- *or* σ-binding mode, and the PA' ligand can freely de-coordinate and bind in either mode without proceeding through $\mathbf{TS_{4x–5x}}$. Thus, the reaction coordinate can proceed from **3** to **5x** where the subsequent OA splitting of the C_1'–H' bond is accessible from the σ-coordination mode.

Oxidative cleavage of the C_1'–H' bond. The five-coordinate alkynyl rhodium hydride complexes, **6x**, that result from oxidative cleavage of the C_1'–H' bond are shown in Figure 5.5. These complexes are characterized by Rh–C_α distances (2.19 Å) that are similar to those of the isomers of **4**, which would indicate that the trans influence of the PA' ligand in the η^2 and η^1 binding modes is similar. The Rh–H' bond lengths of **6x** (1.51 Å) are typical for a metal–hydride bond. The difference in the Rh–C_α–C_β angle is large as the angle of **6b** is ~11º wider than the analogous angle of **6a**. Relative to their respective isomers of **5**, the enthalpic and free energy barriers ($\mathbf{TS_{5x–6x}}$) to C_1'–H' activation are quite small. Formation of these rhodium alkynyl species through OA is an important step in this overall reaction.

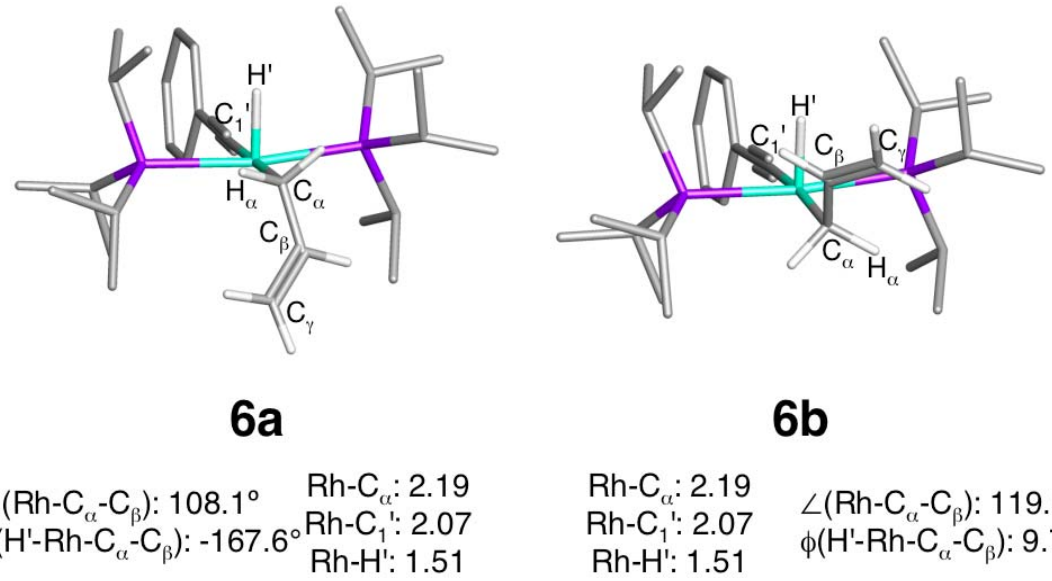

Figure 5.5. B3LYP/BS1 optimized geometries of **6a** and **6b** and select optimized parameters. Distances listed are in angstroms and angles in degrees. Non-essential hydrogen atoms have been removed for clarity.

Reductive coupling of the C_α–H'bond. Propene is formed with reductive coupling of the C_α–H' bond, and relative to the respective isomers of **6** the barriers (**$TS_{6a(b)–8/7b}$**) to this coupling are small. The difference in the Rh–C_α–C_β angle between **$TS_{6a–8}$** and **$TS_{6b–7b}$** is 35º, and this narrow angle in **$TS_{6a–8}$** positions the allyl nearly trans to the hydride coordination site whereas the wide angle in **$TS_{6b–7b}$** effectively removes the allyl backbone from the ligand sphere. The optimized geometric parameters of these two TS's are shown in Figure 5.6.

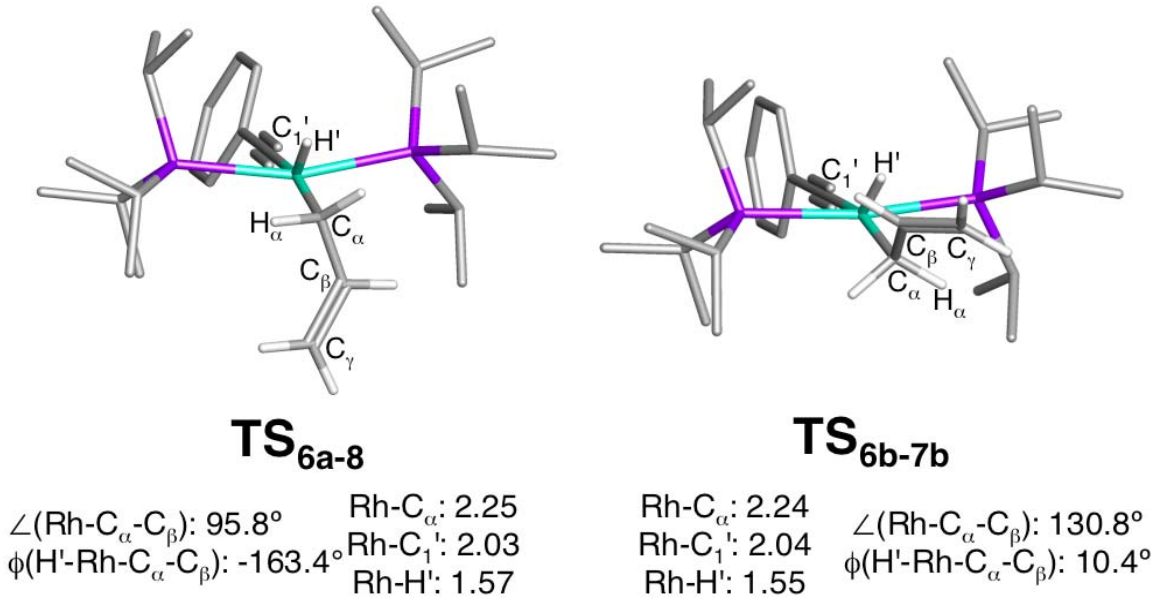

Figure 5.6. B3LYP/BS1 optimized geometries of $\mathbf{TS_{6a–8}}$ and $\mathbf{TS_{6b–7b}}$ and select optimized parameters. Distances listed are in angstroms and angles in degrees. Non-essential hydrogen atoms have been removed for clarity.

Direct elimination of propene from **6a** results in the three-coordinate Rh^I intermediate, **8**, and is exothermic and exergonic by 5.9 and 13.3 kcal•mol^{-1}, respectively (relative to **1** + PA, C_3H_6). With this liberation of propene, the Rh–C_1' bond distance in **8** shortens to 1.91 Å. Because the allyl is removed from the ligand sphere in the "**b**" isomers, propene can bind to the rhodium through the σ-C_α–H' bond to form the pseudo four-coordinate Rh^I complex, **7b**. The corresponding isomer, **7a**, was not located on the B3LYP/BS1 potential energy surface (PES). The pseudo four-coordinate Rh^I complex, **7b**, is a higher energy intermediate than **8** as it is exothermic and endergonic (relative to **1**+2PA) by 3.0 and 1.2 kcal•mol^{-1}, but **7b** easily loses propene to form **8**.

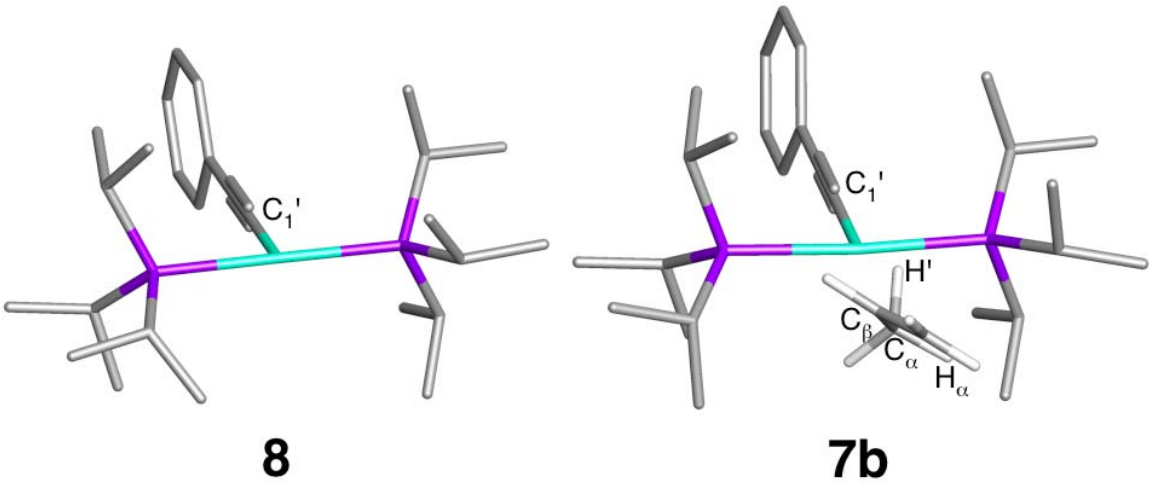

Figure 5.7. B3LYP/BS1 optimized geometries of **8** and **7b** and select optimized parameters. Distances listed are in angstroms and angles in degrees. Non-essential hydrogen atoms have been removed for clarity.

The formation of Ia. With the formation of **8**, propene can re-coordinate and π-bind to the rhodium to form **9** or the second equivalent of phenylacetylene (PA") can π-bind to the rhodium to form **Ia**. The optimized geometries of these two complexes are shown in Figure 5.8. The π-binding of PA" is preferred energetically over the analogous binding of propene by ~10 kcal•mol^{-1}. In terms of free energy, **Ia** is nearly isoenergetic with **8** while **9** is endergonic by ~10 kcal•mol^{-1}. Although **9** is plausible, the overall energetic preference for **Ia** indicates that **9** is not a contributor to the mechanism.

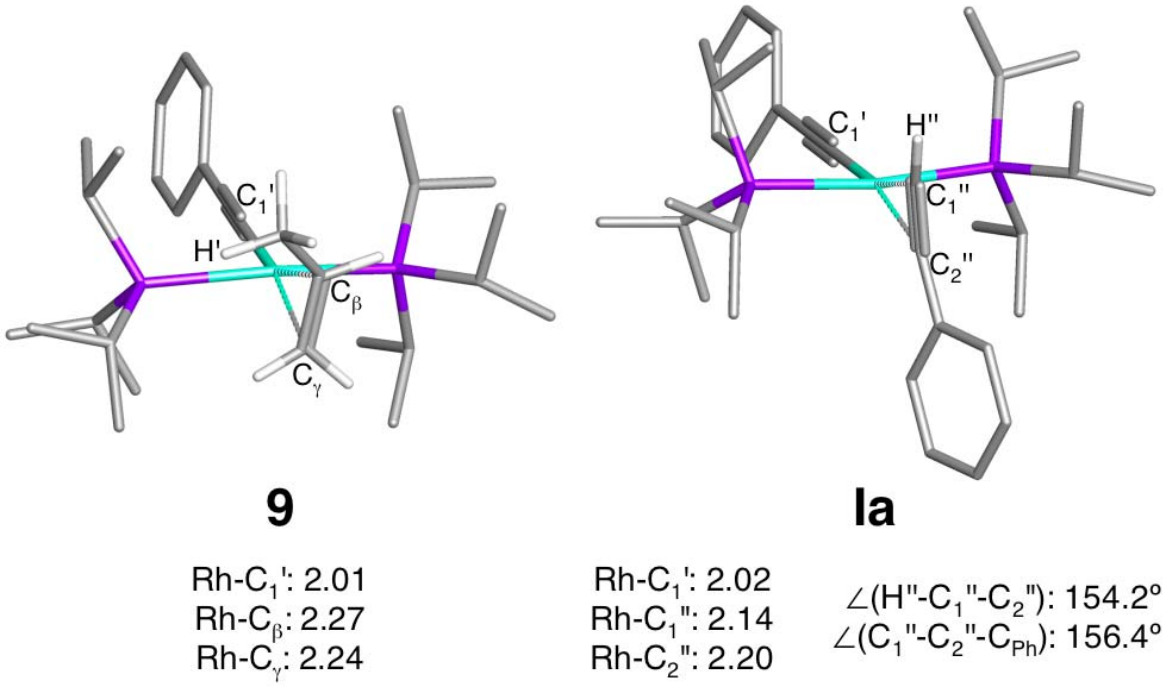

Figure 5.8. B3LYP/BS1 optimized geometries of **9** and **Ia** and select optimized parameters. Distances listed are in angstroms and angles in degrees. Non-essential hydrogen atoms have been removed for clarity.

Experimental evidence exists for the existence of a π-bound alkene, alkynyl complex that is analogous to **9**. The researchers showed that a 1:1 mixture of various alkynes and ethylene with the benzyl analog of **1** resulted in the isolation of a π-bound ethylene, alkynyl intermediate; the step-wise addition of a second equivalent of alkyne to the intermediate lead to the alkynyl, vinylidene product that is analogous to **2**. These results show that the mechanism proceeds to the π-bound alkyne complex when the reaction is run in excess alkyne.

5.3.3. Phenylacetylene–to–Vinylidene Isomerization

Here, we consider three possible pathways for the formation of **2** from **Ia**, which are shown in Figure 5.9. We investigate the mechanistic steps along these pathways and report the relative enthalpies and free energies in Table 5.3. The cobalt and iridium congeners of these species are also reported in the table. For PA", the *sp* carbon atoms are labeled C_1", C_2", and the hydrogen that is transferred is labeled H".

Table 5.3. Relative enthalpies and free energies of the species along the three pathways for alkyne–to–vinylidene isomerization. The cobalt and iridium congeners are included. Energies are relative to **Ia** (and congeners) and are reported in kcal•mol^{-1}.

		Rh		Co[a]		Ir[a]	
pathway	species	$\Delta H^{\circ/\ddagger}$	$\Delta G^{\circ/\ddagger}$	$\Delta H^{\circ/\ddagger}$	$\Delta G^{\circ/\ddagger}$	$\Delta H^{\circ/\ddagger}$	$\Delta G^{\circ/\ddagger}$
	Ia	0	0	0	0	0	0
1	**$TS_{Ia–10}$**	44.93	45.33	45.02	45.17	46.78	46.97
	10	32.13	30.14	NF	NF	30.69	31.21
	$TS_{Ia–11}$	12.94	12.12	18.33	17.13	24.14	22.83
2	**11**	4.71	1.68	2.68	1.67	5.88	2.84
	$TS_{11–2}$	24.64	25.54	25.29	23.95	24.70	28.83
	$TS_{11–Ib}$	5.44	2.07	5.82	5.84	1.03	0.13
3	**Ib**	-0.36	-4.09	-3.34	-5.69	-9.79	-13.12
	$TS_{Ib–12}$	35.39	34.54	31.50	32.43	34.72	34.35
	12	32.46	30.11	29.27	28.18	35.02	34.32
	2	-3.16	-5.59	-6.37	-7.60	-12.27	-15.33

a: the complexes are the Co and Ir congeners of the listed species. NF: not found

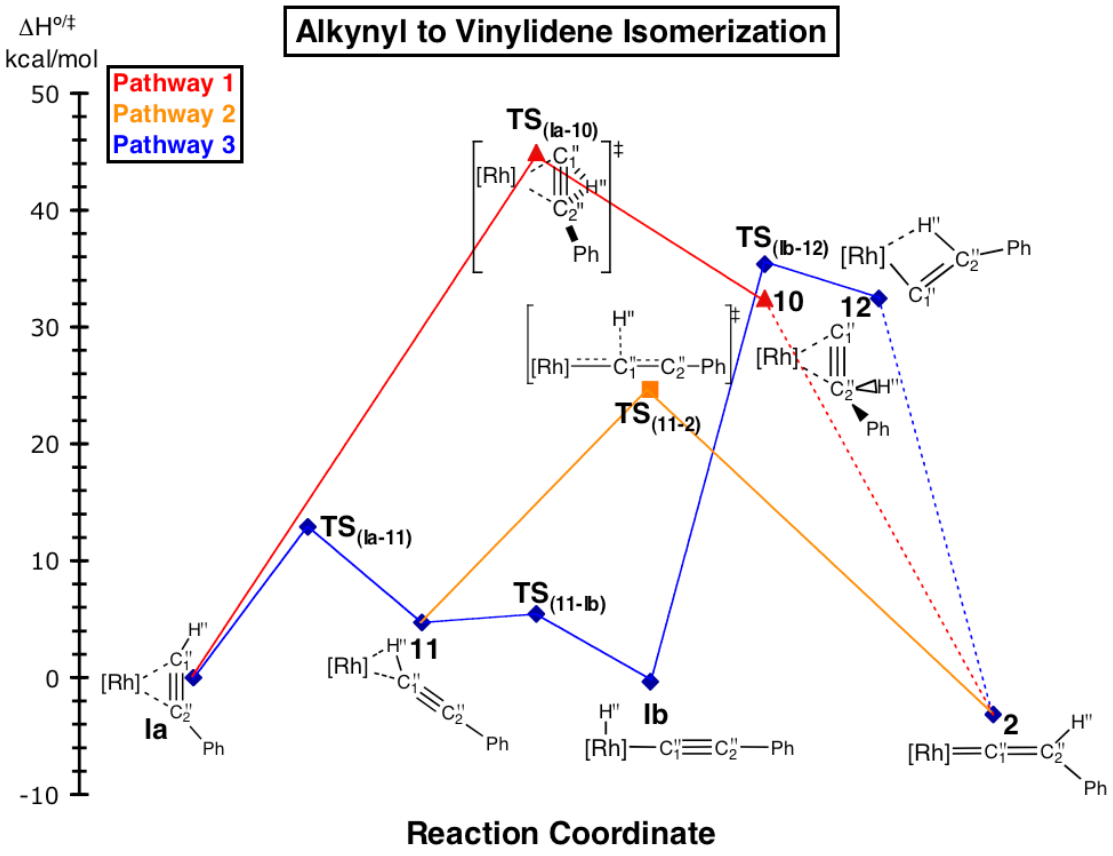

Figure 5.9. The three pathways for hydrogen transfer in the alkyne–to–vinylidene isomerization. Energies are relative to **Ia** and reported in kcal•mol^{-1}.

The result of hydrogen migration is the vinylidene product, **2**, where the optimized geometry is shown in Figure 5.10. The Rh–C_1" bond length is short at 1.85 Å, which indicates that the vinylidene is tightly bound to the rhodium. Interestingly, the vinylidene is bent slightly as the Rh–C_1"–C_2" angle is 173º. Relative to **Ia**, the formation of **2** is exothermic and exergonic by 3.2 and 5.6 kcal•mol^{-1}, respectively.

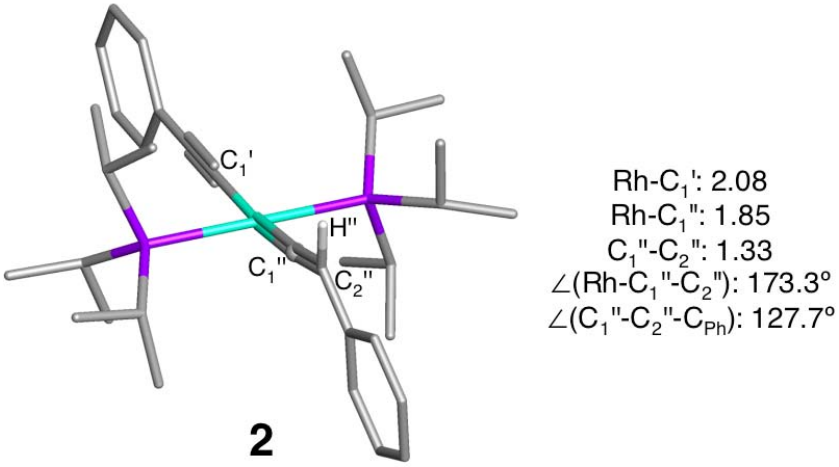

Figure 5.10. B3LYP/BS1 optimized geometry of **2** and select optimized parameters. Distances listed are in angstroms and angles in degrees. Non-essential hydrogen atoms have been removed for clarity**.**

Pathway 1: In the first pathway (red curve), H" migrates to C_2" without a change in the geometry of the η^2-alkyne. In $\mathbf{TS_{Ia–10}}$, the migrating hydrogen is located orthogonal to the Rh–C_1"–C_2" plane and the Rh–C_1', Rh–C_1", and Rh–C_2" distances are similar to those of **Ia**. The enthalpic barrier in this pathway is large at ~45 kcal•mol^{-1}. Species **10** results from this TS and the vinylidene is pseudo π-bound to the rhodium in this unstable intermediate. The trans influence of the reacting PA" ligand does not change with H" migration; similar Rh–C_1' bond lengths are calculated for **Ia**, $\mathbf{TS_{Ia–10}}$, and **10**. This pathway is eliminated because the barrier to hydrogen transfer is very high; as a result, the TS that connects **10** to **2** was not pursued. However, the coordinates of the π-bound vinylidene were perturbed slightly and the optimization of these coordinates did result in the formation of **2**. The B3LYP/BS1 optimized geometries of $\mathbf{TS_{Ia–10}}$ and **10** are shown in Figure D-1.

Pathway 2: In this pathway, the σ-C_1"–H" bond interacts with the rhodium, which facilitates H" migration from C_1" to C_2". In the initial step, which is endothermic and endergonic by 4.7 and 1.7 kcal•mol^{-1}, respectively, the π-bound PA" ligand of **Ia** slips to bind to the rhodium through the σ-C_1"–H" bond (**11**). Relative to **Ia**, the enthalpic and free energy barriers for this isomerization (**TS$_{Ia–11}$**) are 12.9 and 12.1 kcal•mol^{-1}, respectively. The Rh–C_1' bond shortens slightly in **TS$_{Ia–11}$** before returning to a similar value in **11**. Likewise, the Rh–C_1" bond shortens with isomerization while the C_1"–H" bond lengthens. In this binding mode, the phenyl ring of PA" rotates to align parallel to the Rh–P axes. The optimized geometries of **TS$_{Ia–11}$** and **11** are shown in Figure 5.11.

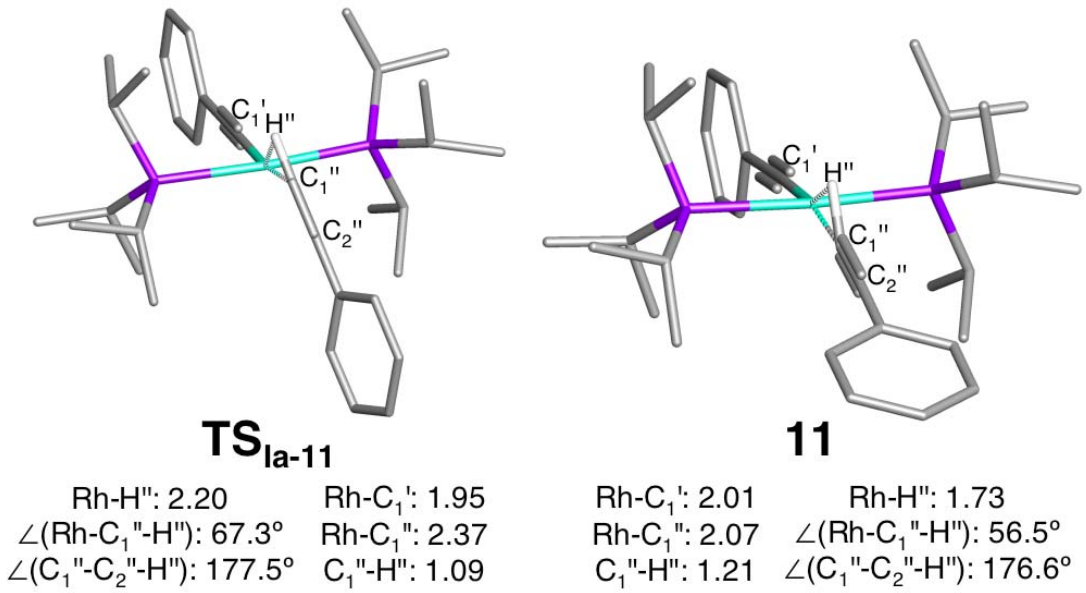

Figure 5.11. B3LYP/BS1 optimized geometry and select optimized parameters of **TS$_{Ia–11}$** and **11**. Distances listed are in angstroms and angles in degrees. Non-essential hydrogen atoms have been removed for clarity.

Species **11** is connected to **2** by $\mathbf{TS_{11-2}}$, which is characterized by a local pseudo T-shaped geometry. With H" migration, the Rh–C_1' bond lengthens while the Rh–C_1" bond shortens. The alkynyl moiety is nearly linear as the C_1"– C_2"–H" angle is ~178°, and the phenyl ring is also aligned parallel with the Rh–P axes. Relative to **11**, the enthalpic and free energy barriers of this TS are 19.9 and 23.9 kcal•mol^{-1}, respectively.

We verified that $\mathbf{TS_{11-2}}$ connects **11** and **2** by following the intrinsic reaction coordinate (IRC) in both directions from $\mathbf{TS_{11-2}}$.[146] The geometric parameters of the last optimization step for migration to the rhodium are similar to those of **11**; the Rh–H" and Rh–C_1" distances are 1.73 and 2.04 Å, respectively, and the value of the Rh–C_1"–H" angle is 57.8º. A full optimization of the coordinates from the last step in the IRC resulted in **11**. In following the vector for migration to C_2", the C_1"–C_2"–H" angle widens to 86.2°, which is ~33° wider than the value in $\mathbf{TS_{11-2}}$. Likewise, the C_1"–C_2"–C_{Ph} angle begins to bend. The IRC optimization terminates here as the phenyl ring begins to rotate to its position in **2**. The optimized geometries of $\mathbf{TS_{11-2}}$ and the species that result in **11** (**A**) and **2** (**B**) are shown in Figure 5.12.

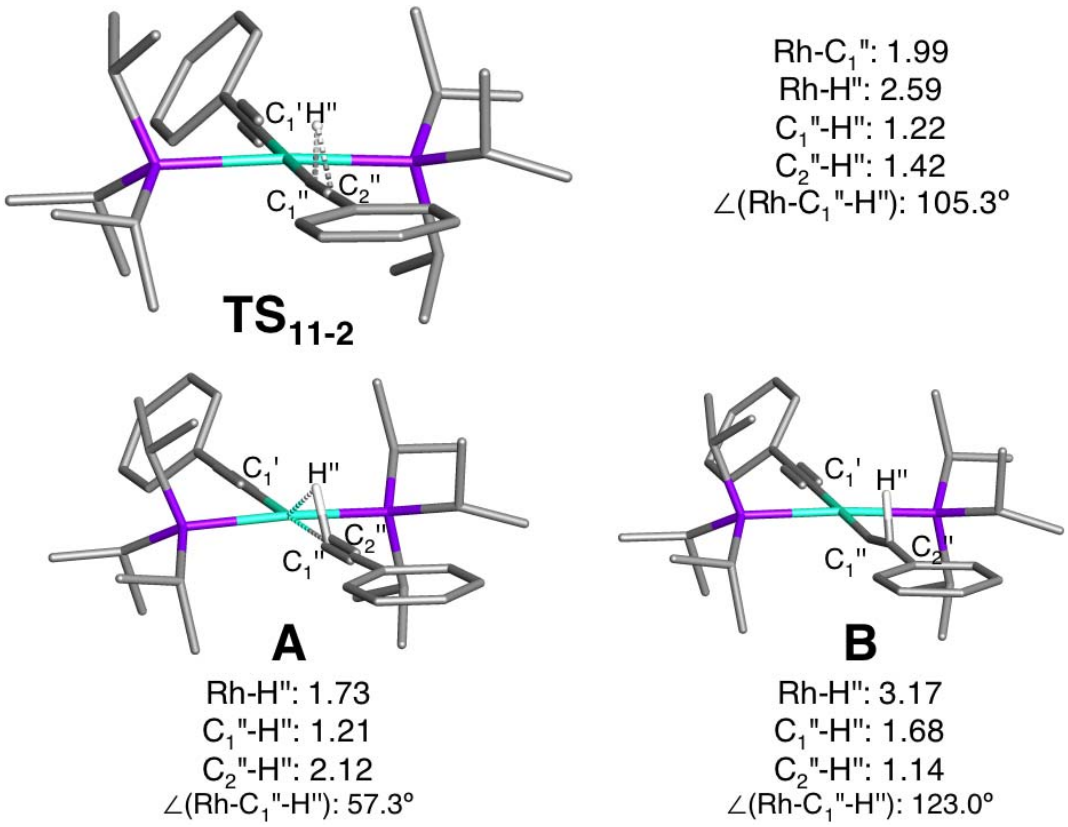

Figure 5.12. Optimized coordinates of $\mathbf{TS_{11-2}}$ and the two species from the IRC calculation. **A** is the result of hydrogen migration towards rhodium and **B** is hydrogen migration towards C_2". Distances listed are in angstroms and angles in degrees.

Pathway 3: The initial mechanistic step for Pathway 3 is the same as in the previous pathway (**Ia** → **11**). However, the experimentally observed bis-alkynyl rhodium hydride complex, **Ib**, results from the oxidative cleavage of the σ-C_1"–H" bond ($\mathbf{TS_{11-Ib}}$). Species **Ib** is isoenthalpic with **Ia**, as discussed above, and is characterized by typical Rh–C and Rh–H bond lengths. Relative to **11**, the enthalpic and free energy barriers to oxidative cleavage of the C_1"–H" ($\mathbf{TS_{11-Ib}}$) are small at 0.7 and 0.4 kcal•mol^{-1}, respectively. The optimized geometries of $\mathbf{TS_{11-Ib}}$ and **Ib** are shown in Figure 5.13.

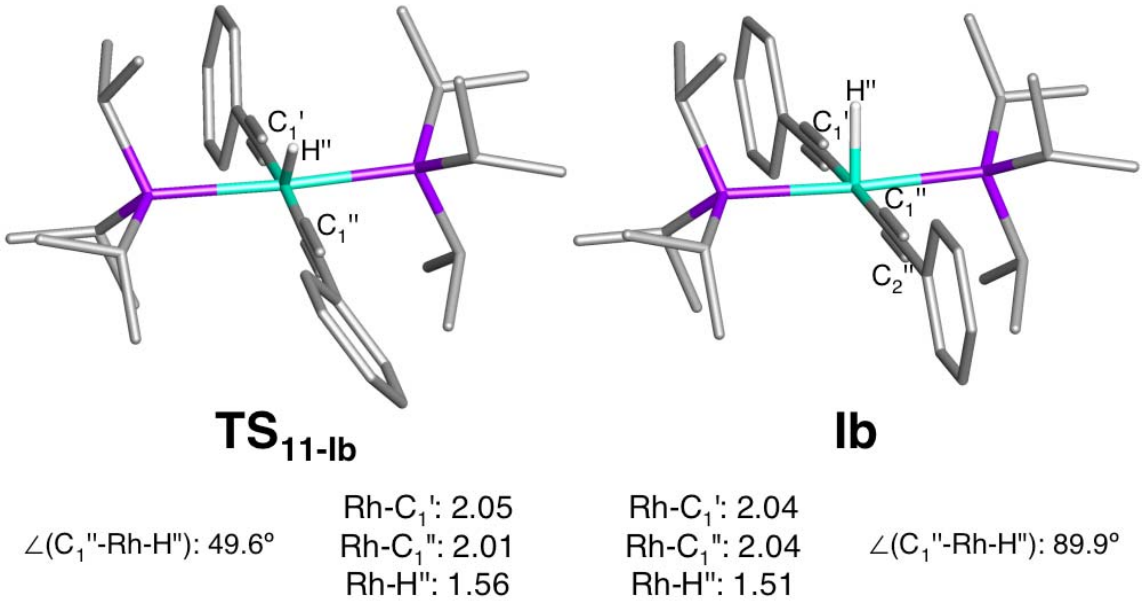

Figure 5.13. B3LYP/BS1 optimized geometries and select optimized parameters of **TS_{11-Ib}** and **Ib**. Distances listed are in angstroms and angles in degrees. Non-essential hydrogen atoms have been removed for clarity.

Hydrogen is transferred directly from **Ib** to C_2" through **TS_{Ib-12}**, which is uphill by 35.4 kcal•mol^{-1}. An unstable intermediate results where the vinylidene ligand is weakly bound to the rhodium through the C_2"–H" bond (**12**). Since the barrier to this coupling is large (**TS_{Ib-12}**), the TS between **12** and **2** was not pursued. However, the coordinates of the vinylidene ligand were perturbed and optimization resulted in **2**. The optimized geometries of **TS_{Ib-12}** and **12** are shown in Figure D-2.

Cobalt and Iridium Analogs: The cobalt and iridium analogs of **TS_{Ia-10}** are also very high at 45.0 and 46.8 kcal•mol^{-1}, respectively. As observed in the rhodium system, the relative free energy barriers are nearly identical to the relative enthalpic barriers.

The only congener of **10** that was found was in the iridium system, which is 30.7 kcal•mol^{-1} greater in energy than the iridium congener of **Ia**.

Interestingly, the barrier for the isomerization from the π–bound alkyne complex to the σ-binding mode (**TS$_{Ia–11}$**) is larger for the cobalt and iridium systems by 5.4 and 11.2 kcal•mol^{-1}, respectively. Beyond this discrepancy, the remaining relative energies along these pathways are very similar between the three systems. In particular, the cobalt and iridium analogs of **TS$_{11–2}$** are also ~25 kcal•mol^{-1} greater than **Ia**. The preference for Pathway 2 does not change with a change in the metal center.

The cobalt and iridium congeners of **Ib** are relatively more stable than the corresponding congeners of **Ia**, whereas with rhodium **Ia** and **Ib** are calculated to be nearly isoenthalpic. Because of the stability of the iridium congener of **Ib**, the barrier to C_2"–H" coupling is greater than for rhodium and cobalt and the unstable intermediate (**12**) is also much higher in energy. However, in replacing the metal center, the overall relative energies of Pathway 3 are similar and this pathway is also eliminated for the cobalt and iridium systems.

Chloride Analogs: The mechanism for vinylidene formation was calculated where the ligand trans to the forming vinylidene was a chloride ion.[147] The η^2-alkyne complex, TS for C–H bond cleavage, alkynyl rhodium hydride complex, TS for hydrogen migration, and vinylidene product are **Ia-Cl**, **TS1**, **Ib-Cl**, **TS2**, and **2-Cl**, respectively, which are analogs of **Ia**, **TS$_{Ia–11}$**, **Ib**, **TS$_{11–2}$**, and **2**, respectively. However, the analog to **11** was not located. The optimized geometries of these species are shown

in Figure 5.14, and the relative enthalpies and free energies of these species are presented in Table 5.4.

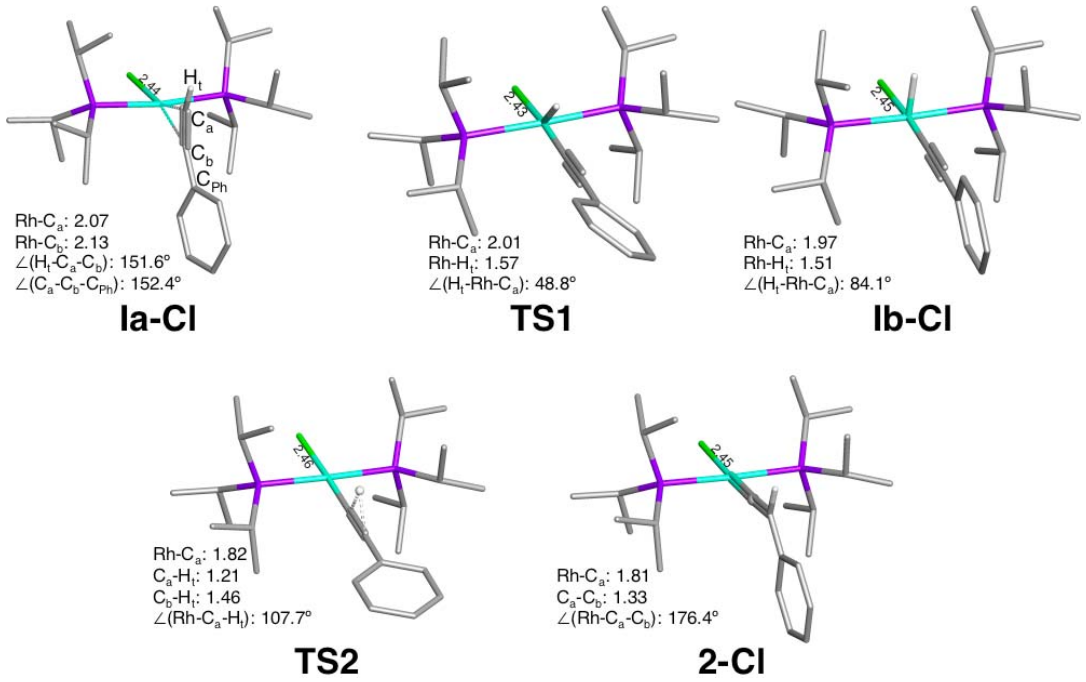

Figure 5.14. Optimized geometries (B3LYP/BS1) of **Ia-Cl**, **TS1**, **Ib-Cl**, **TS2**, and **2-Cl**. Select optimized bond lengths are included and are in angstroms. Non-essential hydrogen atoms have been removed for clarity.

Table 5.4. Relative enthalpies and free energies of the analogs of chlorine. Energies are relative to **Ia-Cl** and in kcal•mol^{-1}.

species	relative energies	
	$\Delta H^{\circ/\ddagger}$	$\Delta G^{\circ/\ddagger}$
Ia-Cl	0	0
TS1	5.22	2.97
Ib-Cl	0.01	–5.16
TS2	25.42	19.50
2-Cl	–6.67	–9.64

Geometrically, these species are very similar to their bis-alkynyl analogs. The H_t–C_a–C_b and C_a–C_b–C_{Ph} angles in **Ia-Cl** are similar to the analogous angles in **Ia**; however, the Rh–C_a and Rh–C_b distances are shorter than those in **Ia**. Species **TS1** exhibits a slightly shorter Rh–H_t distance compared to the analogous distance in $\mathbf{TS_{11–Ib}}$, and the H_t–Rh–C_a angle (48.8°) is slightly smaller. In **Ib-Cl**, the Rh–H_t distance is identical to that of **Ib**, and the Rh–C_a bond distance is once again slightly shorter. For **TS2**, the geometric parameters are very similar to those of $\mathbf{TS_{11–2}}$, and the relative orientation of the phenyl ring is the same between the two analogs. Likewise, the geometric parameters between **2-Cl** and **2** are also very similar, and the phenyl ring is aligned orthogonal to the Rh–P axes. The Rh–Cl distance is insensitive to this isomerization.

The relative energies for most of these species are similar to the analogous energies of the bis-alkynyl system. The barrier to oxidative cleavage is once again small (**TS1**), and **Ia-Cl** is nearly isothermic with **Ib-Cl**; however, the latter is exergonic by 4 kcal•mol^{-1}. In particular, the enthalpic barrier of **TS2** is similar to that of $\mathbf{TS_{11–2}}$, but the free energy barrier is ~6 kcal•mol^{-1} lower in the former. The formation of **2-Cl** is more exothermic and exergonic than **2** by ~3 and ~4 kcal•mol^{-1}, respectively.

Mechanistically, this pathway is similar to Pathway 2, but the σ-bound PA analog was not located. Instead, the first TS (**TS1**) results in oxidative cleavage of the C–H bond and the formation of **Ib-Cl**. Hydrogen migration (**TS2**) from **Ib-Cl** results in the vinylidene complex, **2-Cl**. We verified that **TS2** connects **Ib-Cl** and **2-Cl** through IRC calculations. Several geometries from the IRC calculations in following the vector

towards **Ib-Cl** were individually optimized and all resulted in **Ib-Cl**. Pathway 2 (blue) is compared with this pathway (green) in Figure 5.15. The pathway for the formation of **Ib** is included in the figure (dashed blue curve). The influence of the spectator ligand on the mechanism is displayed; with a chloride ligand trans to the isomerizing alkyne, the TS for alkyne isomerization ($\mathbf{TS_{Ia–11}}$), the σ-bound phenylacetylene intermediate (**11**), and the TS for oxidative C–H cleavage ($\mathbf{TS_{11–Ib}}$) "coalesce" into a single TS (**TS1**). However, with phenylacetylide ligand, the σ-binding mode of phenylacetylene is stabilized.

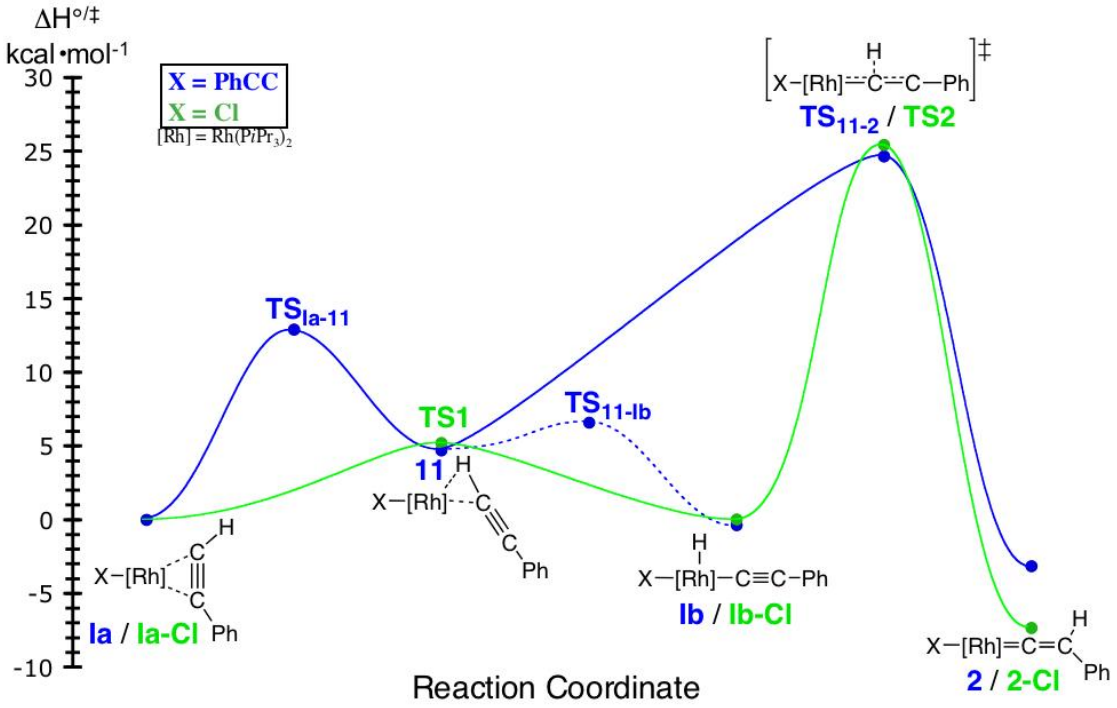

Figure 5.15. The bis-alkynyl (blue) and chloride (green) potential energy surfaces for alkyne–to–vinylidene isomerization. The formation of **Ib** is included (dashed line). Only the energies at the blue and green dots were calculated; the surfaces represented by the curves are approximate.

5.4 Conclusions

The relative energies of **Ia**, **Ib**, and **2** are sensitive to the phosphine ligand; **2** is the product for weaker π-acids and **Ia** is preferred with stronger π-acids. Species **Ib** is more exergonic than **Ia** for only the P*i*Pr$_3$ ligands; the preference switches to **Ia** for the other phosphines considered. The formation of propene is facile, and steric interactions promote the direct elimination of propene. While the π-binding of propene is tenable, the π-binding of PA is preferred energetically.

Three pathways were considered for the formation of the vinylidene product for the bis-alkynyl system. Pathway 2 is preferred for the formation of **2** as the lowest energy barrier is found on this pathway. The σ-bound PA species, **11**, is the precursor species to hydrogen migration; the formation of **Ib** is facile but Ib likely reverts to **11** before forming **2**. This mechanism is slightly different than the common *1–3 shift* mechanism where the precursor species is the alkynyl rhodium hydride species, and our calculations with the chloride species agree with the latter mechanism.

CHAPTER VI

CONCLUSIONS

Density functional theory is an extremely popular quantum chemical method as studies of large chemical systems are tractable. We applied DFT to study C–H bond activation, hydrogen transfer, and hydrogen migration and have presented the results in this work. Density functional theory can resolve the differences in the character of the reaction coordinate for alkyne–to–vinylidene isomerization. Two model systems were studied for this chemistry and the reactions were shown to proceed by mechanism that differ slightly, which was elucidated by using DFT. Bader's "Atoms in Molecules" analysis is a useful tool for describing the bonding patterns in a molecule. The local connectivity of equilibrium and non-equilibrium models for hydrogen transfer has been characterized with this method, and a wide range of connectivity has been presented.

Analogous Tp and Cp complexes have been synthesized and compared.[148] The influence of these ligands on the electron density can be studied with Bader's analysis. We reported the bonding patterns for the Tp and Cp analogs between the group 8 complexes of $[LM(CH_3)(H)(H')]$ (L = Tp, Cp; M = Fe, Ru, Os). These comparative studies can include the newly synthesized tris-phosphine and tris-carbene tripodal ligands. Second, the Tp ligand in $[\kappa^3\text{-TpPt}(CH_3)_2H]$ can also be replaced with these ligands and the influence on the barriers to C–H coupling and methane release can be measured.

Cross-coupling reactions have been proposed to proceed by the OATS and σ-CAM mechanisms, and the bonding patterns of the TS for R–R' coupling can be characterized by AIM analysis. The local connectivity for cross-coupling transition states is unclear and should be investigated. These studies can elucidate the differences between HT and cross-coupling and the influence of spectator ligands on these chemistries.

Last, the mechanism for the alkyne–to–vinylidene isomerization has been considered with several ligands. Phosphine ligands of low π-acidity are known to stabilize the metal-hydride and vinylidene isomers (relative to the η^2-alkyne species). Analogous complexes with N-heterocyclic carbene (NHC) ligands, which are entirely σ-donating in character, should be examined. The mechanism for this isomerization would be sensitive to the stabilizations of the species by these ligands.

REFERENCES

[1] Godula, K.; Sames, D. *Science* **2006**, *312*, 67–72.

[2] Shilov, A. E.; Shul'pin, G. B. *Chem. Rev.* **1997**, *97*, 2879–2932.

[3] Masterton, W. L.; Hurley, C. N. *Chemistry: Principles and Reactions*, 3rd ed.; Saunders College Publishing: New York, 1997; p. 225.

[4] Olah, G. A.; Surya Prakash, G. K.; Sommer, J. Superacids, Wiley & Sons: New York, 1985.

[5] Jones Jr., M. Radical Reactions. In *Organic Chemistry*; W. W. Norton and Company: New York, 1997; Chapter 10, pp 417–464.

[6] Crabtree, R. H. *Chem. Rev.* **1985**, *85*, 245–269.

[7] Sakaki, S. Theoretical Studies of C–H σ-bond Activation and Related Reactions by Transition-Metal Complexes. In *Theoretical Aspects of Transition Metal Catalysis*; Frenking, G., Ed.; Topics in Organometallic Chemistry; Springer: New York, 2005; Vol 12, pp 3–4.

[8] (a) Crabtree, R. H. *Angew. Chem., Int. Ed. Engl.* **1993**, *32*, 789–805.
(b) Hall, C.; Perutz, R. N. *Chem. Rev.* **1996**, *96*, 3125–3146.

[9] Buchanan, J. M.; Stryker, J. M.; Bergman, R. G. *J. Am. Chem. Soc.* **1986**, *108*, 1537–1550.

[10] Crabtree, R. H. The Homogeneous Activation of H–H and X–H Bonds by Metals. In *Selective Hydrocarbon Activation: Principles and Progress*; Davies, J. A.; Watson, P. L.; Liebman, J. F.; Greenberg, A., Eds.; VCH: New York, 1990; pp 2–6.

[11] Bergman, R. G. *Science* **1984**, *223*, 902–908.

[12] (a) Atzrodt, J.; Derdau, V.; Fey, T.; Zimmermann, J. *Angew. Chem., Int. Ed. Engl.* **2007**, *46*, 7744–7765.
(b) Jones, W. D. *Acc. Chem. Res.* **2003**, *36*, 140–146.

[13] (a) Halpern, J.; Dakers, R. G. *J. Chem. Phys.* **1954**, *22*, 1272–1273.
(b) Halpern, J.; Peters, E. *J. Chem. Phys.* **1955**, *23*, 605.

(c) Halpern, J.; Peters, E. *J. Phys. Chem.* **1955**, *59*, 793–796.

[14] Vaska, L.; Diluzio, J. W. *J. Am. Chem. Soc.* **1962**, *84*, 679–680.

[15] *Activation and Functionalization of C–H Bonds*; Goldberg, K. I.; Goldman, A. S. Eds.; Oxford University Press, Washington DC, 2004; pp 1–440.

[16] Gol'dshleger, N. F.; Tyabin, M. B.; Shilov, A. E.; Shteinman, A. A. *Russ. J. Phys. Chem.* **1969**, *43*, 1222–1223 (English translation).

[17] Gol'dshleger, N. F.; Es'kova, V. V.; Shilov, A. E.; Shteinman, A. A. *Zhurnal Fizicheskoi Khimii* **1972**, *46*, 1353.

[18] (a) Shilov, A. E. *Activation of Saturated Hydrocarbons by Transition Metal Complexes*; D. Riedel: Dordrecht, The Netherlands, 1984; pp 1–203.
(b) Shilov, A. E.; Shul'pin, G. B. *Activation and Catalytic Reactions of Saturated Hydrocarbons in the Presence of Metal Complexes*; Kluwer, Dordrecht, The Netherlands, 2000; pp 1–534.

[19] (a) Labinger, J. A.; Bercaw, J. E. *Nature* **2002**, *417*, 507–514.
(b) Lersch, M.; Tilset, M. *Chem. Rev.* **2005**, *105*, 2471–2526.
(c) Stahl, S. S.; Labinger, J. A.; Bercaw, J. E. *Angew. Chem., Int. Ed. Engl.* **1998**, *37*, 2180–2192.

[20] Kushch, L. A.; Lavrushko, V. V.; Misharin, Y. S.; Moravsky, A. P.; Shilov, A. E. *Nouv. J. Chim.* **1983**, *7*, 729–733.

[21] Stahl, S. S.; Labinger, J. A.; Bercaw, J. E. *J. Am. Chem. Soc.* **1996**, *118*, 5961–5976.

[22] (a) Periana, R. A.; Taube, D. J.; Gamble, S.; Taube, H.; Satoh, T.; Fujii, H. *Science* **1998**, *280*, 560–564.
(b) Vedernikov, A. N.; Fettinger, J. C.; Mohr, F. *J. Am. Chem. Soc.* **2004**, *126*, 11160–11161.

[23] Siegbahn, P. E. M.; Crabtree, R. H. *J. Am. Chem. Soc.* **1996**, *118*, 4442–4450.

[24] Wick, D. D.; Goldberg, K. I. *J. Am. Chem. Soc.* **1997**, *119*, 10235–10236.

[25] Trofimenko, S. *Chem. Rev.* **1993**, *93*, 943–980.

[26] Jensen, M. P.; Wick, D. D.; Reinartz, S.; White, P. S.; Templeton, J. L.; Goldberg, K. I. *J. Am. Chem. Soc.* **2003**, *125*, 8614–8624.

[27] (a) Periana, R. A.; Bergman, R. G. *J. Am. Chem. Soc.* **1986**, *108*, 7332–7346.
(b) Bullock, R. M.; Headford, C. E. L.; Hennessy, K. M.; Kegley, S. E.; Norton, J. R. *J. Am. Chem. Soc.* **1989**, *111*, 3897–3908.
(c) Parkin, G.; Bercaw, J. E. *Organometallics* **1989**, *8*, 1172–1179.

[28] (a) Watson, P. L. *J. Am. Chem. Soc.* **1983**, *105*, 6491–6493.
(b) Watson, P. L.; Parshall, G. W. *Acc. Chem. Res.* **1985**, *18*, 51–56.

[29] Thompson, M. E.; Baxter, S. M.; Bulls, A. R.; Burger, B. J.; Nolan, M. C.; Santarsiero, B. D.; Schaefer, W. P.; Bercaw, J. E. *J. Am. Chem. Soc.* **1987**, *109*, 203–219.

[30] Bruno, J. W.; Marks, T. J.; Day, V. W. *J. Am. Chem. Soc.* **1982**, *104*, 7357–7360.

[31] (a) Frederick, C. M.; Marks, T. J. *J. Am. Chem. Soc.* **1984**, *106*, 2214–2216.
(b) Frederick, C. M.; Marks, T. J. *J. Am. Chem. Soc.* **1986**, *108*, 425–437.

[32] (a) Ziegler, T.; Folga, E.; Berces, A. *J. Am. Chem. Soc.* **1993**, *115*, 636–646.
(b) Folga, E.; Ziegler, T. *Can. J. Chem.* **1992**, *70*, 333–342.

[33] Parr, R. G. *Density Functional Theory of Atoms and Molecules*; Oxford University Press: New York, 1989; pp 1–333.

[34] (a) Sherer, E. C.; Cramer, C. J. *Organometallics* **2003**, *22*, 1682–1689.
(b) Maron, L.; Perrin, L.; Eisenstein, O. *J. Chem. Soc., Dalton Trans.* **2002**, 534–539.

[35] Green, M. L. H.; Knowles, P. J. *J. Chem. Soc., Chem. Comm.* **1970**, 1677.

[36] Hoyano, J. K.; Graham, W. A. G. *J. Am. Chem. Soc.* **1982**, *104*, 3723–3725.

[37] Janowicz, A. H.; Bergman, R. G. *J. Am. Chem. Soc.* **1982**, *104*, 352–354.

[38] Arndsten, B. A.; Bergman, R. G. *Science* **1995**, *270*, 1970–1973.

[39] (a) Strout, D. L.; Zarić, S.; Niu, S.; Hall, M. B. *J. Am. Chem. Soc.* **1996**, *118*, 6068–6069.
(b) Niu, S.; Hall, M. B. *J. Am. Chem. Soc.* **1998**, *120*, 6169–6170.
(c) Niu, S.; Hall, M. B. *Chem. Rev.* **2000**, *100*, 353–406.

[40] Klei, S. R.; Tilley, T. D.; Berman, R. G. *J. Am. Chem. Soc.* **2000**, *122*, 1816–1817.

[41] Lin, Z. *Coord. Chem. Rev.* **2007**, *251*, 2280–2291.

[42] (a) Webster, C. E.; Fan, Y.; Hall, M. B.; Kunz, D.; Hartwig, J. F. *J. Am. Chem. Soc.* **2003**, *125*, 858–859.
(b) Hartwig, J. F.; Cook, K. S.; Hapke, M.; Incarvito, C. D.; Fan, Y.; Webster, C. E.; Hall, M. B. *J. Am. Chem. Soc.* **2005**, *127*, 2538–2552.

[43] (a) Lam, W. H.; Lin, Z. *Organometallics* **2003**, *22*, 473–480.
(b) Ng, S. M.; Lam, W. H.; Mak, C. C.; Tsang, C. W.; Jia, G.; Lin, Z. *Organometallics* **2003**, *22*, 641–651.
(c) Lam, W. H.; Jia, G.; Lin, Z.; Lau, C. P.; Eisenstein, O. *Chem. Eur. J.* **2003**, *9*, 2775–2782.

[44] Oxgaard, J.; Muller, R. P.; Goddard III, W. A.; Periana, R. A. *J. Am. Chem. Soc.* **2004**, *126*, 352–363.

[45] Perutz, R. N.; Sabo-Etienne, S. *Angew. Chem., Int. Ed. Engl.* **2007**, *46*, 2578–2592.

[46] Bader, R. F. W. *Atoms in Molecules, A Quantum Theory*; Oxford University Press: Ithaca, New York, 1990; pp 1–438.

[47] Schäfer, M.; Wolf, J.; Werner, H. *Organometallics* **2004**, *23*, 5713–5728.

[48] Werner, H.; Wolf, J.; Garcia Alonso, F. J.; Ziegler, M. L.; Serhadli, O. *J. Organomet. Chem.* **1987**, *336*, 397–411.

[49] Garcia Alonso, F. J.; Höhn, A.; Wolf, J.; Otto, H.; Werner, H. *Angew. Chem., Int. Ed. Engl.* **1985**, *24*, 406–407.

[50] Wakatsuki, Y.; Koga, N.; Werner, H.; Morokuma, K. *J. Am. Chem. Soc.* **1997**, *119*, 360–366.

[51] Grotjahn, D. B.; Zeng, X.; Cooksy, A. L. *J. Am. Chem. Soc.* **2006**, *128*, 2798–2799.

[52] De Angelis, F.; Sgamellotti, A.; Re, N. *Organometallics*, **2007**, *26*, 5285–5288.

[53] (a) Piela, L. *Ideas of Quantum Chemistry*; Elsevier: Amsterdam, 2007.
(b) Leach, A. R. *Molecular Modeling: Principles and Applications*, 2nd ed.; Prentice Hall: New York; 2001.
(c) Cramer, C. J. *Essentials of Computational Chemistry: Theories and Models*; Wiley & Sons: New York; 2002.
(d) Lewars, E. *Computational Chemistry: Introduction to the Theory and Applications of Molecular and Quantum Mechanics*; Kluwer Academic Publishers: Boston, 2003.

(e) Hehre, W. J.; Radom, L.; Schleyer, P. v. R.; Pople, J. A. *Ab Initio Molecular Orbital Theory*; Wiley & Sons: New York, 1986.
(f) Levine, I. N. *Quantum Chemistry*, 5th ed.; Prentice Hall: New York, 2000.

[54] Dyall, K. G.; Fægri Jr., K. *Introduction to Relativistic Quantum Chemistry*; Oxford University Press, New York, 2007.

[55] Born, M.; Oppenheimer, J. R. *Ann. Physik.* **1927**, *84*, 457.

[56] Hohenberg, P.; Kohn, W. *Phys. Rev.* **1964**, *136*, B864–B871.

[57] Kohn, W.; Sham, L. J. *J. Phys. Rev.* **1965**, *140*, A1133–A1138.

[58] Becke, A. D. *J. Chem. Phys.* **1993**, *98*, 5648–5652.

[59] Lee, C.; Yang, W.; Parr, R. G. *Phys. Rev. B: Condens. Mater. Phys.* **1988**, *37*, 785–789.

[60] Becke, A. D. *Phys. Rev. A* **1988**, *38*, 3098.

[61] Vosko, S. H.; Wilk, L.; Nusair, M. *Can. J. Phys.* **1980**, *58*, 1200–1211.

[62] (a) Williams, T. J.; Labinger, J. A.; Bercaw, J. E. *Organometallics* **2007**, *26*, 281–287.
(b) Zhang, F.; Kirby, C. W.; Hairsine, D. W.; Jennings, M. C.; Puddephatt, R. J. *J. Am. Chem. Soc.*, **2005**, *127*, 14196–14197.
(c) Heyduk, A. F.; Driver, T. G.; Labinger, J. A.; Bercaw, J. E. *J. Am. Chem. Soc.* **2004**, *126*, 15034–15035.
(d) Owen, J. S.; Labinger, J. A.; Bercaw, J. E. *J. Am. Chem. Soc.* **2006**, *128*, 2005–2016. (e) Konze, W. V.; Scott, B. L.; Kubas, G. J. *J. Am. Chem. Soc.* **2002**, *124*, 12550–12556.

[63] Garnett, J. L.; Hodges, R. J. *J. Am. Chem. Soc.* **1967**, *89*, 4546–4547.

[64] Fekl, U.; Kaminsky, W.; Goldberg, K. I. *J. Am. Chem. Soc.* **2001**, *123*, 6423–6424.

[65] Fekl, U.; Goldberg, K. I. *J. Am. Chem. Soc.* **2002**, *124*, 6804–6805.

[66] (a) Crumpton, D. M.; Goldberg, K. I. *J. Am. Chem. Soc.* **2000**, *122*, 962–963.
(b) Procelewska, J.; Zahl, A.; Liehr, G.; van Eldik, R.; Smythe, N. A.; Williams, B. S.; Goldberg, K. I. *Inorg, Chem.* **2005**, *44*, 7732–7742.

[67] Reinartz, S. R.; White, P. S.; Brookhart, M.; Templeton, J. L. *Organometallics* **2004**, *23*, 3101–3104.

[68] (a) Reinartz, S. R.; White, P. S.; Brookhart, M.; Templeton, J. L. *J. Am. Chem. Soc.* **2001**, *123*, 12724–12725.
(b) Norris, C. M.; Templeton, J. L. *Organometallics* **2004**, *23*, 3101–3104.

[69] (a) Bartlett, K. L.; Goldberg, K. I.; Borden, W. T. *J. Am. Chem. Soc.* **2000**, *122*, 1456–1465.
(b) Bartlett, K. L.; Goldberg, K. I.; Borden, W. T *Organometallics* **2001**, *20*, 2669–2678.

[70] Wik, B. J.; Ivanovic–Burmazovic, I.; Tilset, M.; van Eldik, R. *Inorg. Chem.* **2006**, *45*, 3613–3621.

[71] Zarić, S.; Hall, M. B. *J. Phys. Chem. A* **1998**, *102*, 1963–1964.

[72] Frisch, M. J.; Trucks, G. W.; Schlegel, H. B.; Scuseria, G. E.; Robb, M. A.; Cheeseman, J. R.; Montgomery, Jr., J. A.; Vreven, T.; Kudin, K. N.; Burant, J. C.; Millam, J. M.; Iyengar, S. S.; Tomasi, J.; Barone, V.; Mennucci, B.; Cossi, M.; Scalmani, G.; Rega, N.; Petersson, G. A.; Nakatsuji, H.; Hada, M.; Ehara, M.; Toyota, K.; Fukuda, R.; Hasegawa, J.; Ishida, M.; Nakajima, T.; Honda, Y.; Kitao, O.; Nakai, H.; Klene, M.; Li, X.; Knox, J. E.; Hratchian, H. P.; Cross, J. B.; Bakken, V.; Adamo, C.; Jaramillo, J.; Gomperts, R.; Stratmann, R. E.; Yazyev, O.; Austin, A. J.; Cammi, R.; Pomelli, C.; Ochterski, J. W.; Ayala, P. Y.; Morokuma, K.; Voth, G. A.; Salvador, P.; Dannenberg, J. J.; Zakrzewski, V. G.; Dapprich, S.; Daniels, A. D.; Strain, M. C.; Farkas, O.; Malick, D. K.; Rabuck, A. D.; Raghavachari, K.; Foresman, J. B.; Ortiz, J. V.; Cui, Q.; Baboul, A. G.; Clifford, S.; Cioslowski, J.; Stefanov, B. B.; Liu, G.; Liashenko, A.; Piskorz, P.; Komaromi, I.; Martin, R. L.; Fox, D. J.; Keith, T.; Al-Laham, M. A.; Peng, C. Y.; Nanayakkara, A.; Challacombe, M.; Gill, P. M. W.; Johnson, B.; Chen, W.; Wong, M. W.; Gonzalez, C.; and Pople, J. A.; Gaussian 03, Revision D.02 Gaussian, Inc., Wallingford CT, 2004.

[73] Hay, P. J.; Wadt, W. R. *J. Chem. Phys.* **1985**, *82*, 270–283.

[74] Couty, M.; Hall, M. B. *J. Comp. Chem.* **1996**, *17*, 1359–1370.

[75] (a) Dunning Jr, T. H. *J. Chem. Phys.* **1989**, *90*, 1007–1023.
(b) Woon, D. E.; Dunning Jr, T. H. *J. Chem. Phys.* **1993**, *98*, 1358–1371.

[76] Dunning Jr, T. H.; Hay, P. J. In *Modern Theoretical Chemistry*; Schaefer III, H. F., Ed.; Plenum: New York; 1996, pp 1–28.

[77] (a) Manson, J.; Webster, C. E.; Perez, L.; Hall, M. B. *JIMP 2 Version 0.091 (built for Windows PC)*; Department of Chemistry, Texas A&M University, College Station, TX, 2006 (available @ http://www.chem.tamu.edu/jimp2/index.html), 2/7/2008
(b) Hall, M. B.; Fenske, R. F. *Inorg. Chem.* **1972**, *11*, 768–779.

[78] Hall, M. B.; Fan, Y. *Adv. Inorg. Chem.* **2003**, *54*, 321–349.

[79] Johansson, L.; Tilset, M.; Labinger, J. A.; Bercaw, J. E. *J. Am. Chem. Soc.* **2000**, *122*, 10846–10855.

[80] Johansson, L.; Tilset, M. *J. Am. Chem. Soc.* **2001**, *123*, 739–740.

[81] Thomas, C. M.; Peters, J. C. *Organometallics* **2005**, *24*, 5858–5867.

[82] (a) Webster, C. E.; Hall, M. B. *Inorg. Chim. Acta.* **2002**, *330*, 268–282.
(b) Webster, C. E.; Hall, M. B. *Inorg. Chim. Acta.* **2002**, *336*, 168.

[83] Feng, Y.; Lail, M.; Foley, N. A.; Gunnoe, T. B.; Barakat, K. A.; Cundari, T. R.; Petersen, J. L. *J. Am. Chem. Soc.* **2006**, *128*, 7982–7997.

[84] (a) Reinartz, S.; Baik, M. H.; White, P. S.; Brookhart, M.; Templeton, J. L. *Inorg. Chem.* **2001**, *40*, 4726–4732.
(b) Davies, M. S.; Hambley, T. W. *Inorg. Chem.* **1998**, *37*, 5408–5409.
(c) Schwartz, D. J.; Andersen, R. A. *J. Am. Chem. Soc.* **1995**, *117*, 4014–4025.

[85] AIM2000 designed by Friedrich Biegler–König, University of Applied Sciences, Bielefeld, Germany (http://www.aim2000.de/), 1/15/2008

[86] Grimme, S. *J. Chem. Phys.* **2006**, *124*, 034108.

[87] Schwabe, T.; Grimme, S. *Phys. Chem. Chem. Phys.* **2006**, *8*, 4398–4401.

[88] The values by which to scale the second order correction were obtained by communication with the authors of refs 86 and 87.

[89] Perdew, J. P. In *Electronic Structures of Solids*; Ziesche, P.; Eschig, H., Eds.; Akademie Verlag: Berlin, 1991; p11.

[90] Perdew, J. P. *Phys. Rev. B* **1986**, *33*, 8822–8824.

[91] Gill, P. M. W. *Mol. Phys.* **1996**, *89*, 433–445.

[92] Hamprecht, F. A.; Cohen, A. J.; Tozer, D. J.; Handy, N. C. *J. Chem. Phys.* **1998**,*109*, 6264–6271.

[93] Adamo, C.; Barone, V. *J. Chem. Phys.* **1998***, 108*, 664–675.

[94] (a) Perdew, J. P.; Burke, K.; Ernzerhof, M. *Phys. Rev. Lett.* **1996**, *77*, 3865–3868.
(b) Perdew, J. P. Burke, K.; Ernzerhof, M. *Phys. Rev. Lett.* **1997**, *78*, 1396.

[95] Lynch, B. J.; Fast, P. L.; Harris, M.; Truhlar, D. G. *J. Phys. Chem. A* **2000**, *104*, 4811–4815.

[96] Becke, A. D. *J. Chem. Phys.* **1993**, *98*, 1372–1377.

[97] Schultz, N. E.; Zhao, Y.; Truhlar, D. G. *J. Phys.Chem. A* **2005**, *109*, 11127–11143.

[98] Becke, A. D. *J. Chem. Phys.***1996**, *104*, 1040–1046.

[99] Krieger, J. B.; Chen, J.; Iafrate, G. J.; Savin, A. In *Electron Correlations and Materials Properties*; Gonis, A.; Koussis, N., Eds.; Plenum, New York, 1999; p 463.

[100] Tao, J.; Perdew, J. P.; Staroverov, V. N.; Scuseria, G. E. *Phys. Rev. Lett.* **2003**, *91*, 146401.

[101] Van Voorhis, T.; Scuseria, G. E. *J. Chem. Phys.***1998**, *109*, 400–410.

[102] Zhao, Y.; González–Garcia, N.; Truhlar, D. G. *J. Phys. Chem. A* **2005**, *109*, 2012–2018.

[103] Zhao, Y.; Lynch, B. J.; Truhlar, D. G. *J. Phys. Chem. A* **2004**, *108*, 2715–2719.

[104] Zhao, Y.; Truhlar, D. G. *J. Phys. Chem. A* **2004**, *108*, 6908–6918.

[105] Tao, J.; Perdew, J. P. *J. Chem. Phys.* **2005**, *122*, 114102.

[106] (a) Truong, T. N.; Duncan, W. *J. Phys. Chem.* **1994**, *101*, 7408–7414.
(b) Durant, J. L. *Chem. Phys. Lett.* **1996**, *256*, 595–602.
(c) Boese, A. D.; Martin, J. M. L. *J. Chem. Phys.* **2004**, *121*, 3405–3416.
(d) Mori–Sanchez, P.; Cohen, A. J.; Yang, W. *J. Chem. Phys.* **2006**, *125*, 201102.
(e) Vydrov, O. A.; Scuseria, G. E. *J. Chem. Phys.* **2006**, *125*, 234109.

[107] Quintal, M. M.; Karton, A.; Iron, M. A.; Boese, A. D.; Martin, J. M. L. *J. Phys. Chem. A* **2006**, *110*, 709–716.

[108] Andrae, D.; Haussermann, U.; Dolg, M.; Stoll, H.; Preuss, H. *Theo. Chim. Acta.* **1990**, *77*, 123–141.

[109] Ross, R. B.; Powers, J. M.; Atashroo, T.; Ermler, W. C.; LaJohn, L. A.; Christiansen, P. A. *J. Chem. Phys.* **1990**, *93*, 6654–6670.

[110] Stevens, W. J.; Krauss, M.; Basch, H.; Jasien, P. G. *Can. J. Chem.* **1992**, *70*, 612–630.

[111] Hay, P. J.; Wadt, W. R. *J. Chem. Phys.* **1985**, *82*, 299–310.

[112] Weigend, F.; Ahlrichs, R. *Phys. Chem. Chem. Phys.* **2005**, *7*, 3297–3305.

[113] (a) Hehre, W. J.; Stewart, R. F.; Pople, J. A. *J. Chem. Phys.* **1969**, *51*, 2657–2664.
(b) Collins, J. B.; Schleyer, P. v. R.; Binkley, J. S.; Pople, J. A. *J. Chem. Phys.* **1976**, *64*, 5142–5151.

[114] 3-21G: Binkley, J. S.; Pople, J. A.; Hehre, W. J. *J. Am. Chem. Soc.* **1980**, *102*, 939–947. 6-31G: Hehre, W. J.; Ditchfield, R.; Pople, J. A. *J. Chem. Phys.* **1972**, *56*, 2257–2261. 6-311G: Krishnan, R.; Binkley, J. S.; Seeger, R; Pople, J. A. *J. Chem. Phys.* **1980**, *72*, 650–654. Diffuse functions (+ & ++): Clark, T.; Chandrasekhar, J.; Sptiznagel, G. W.; Schleyer, P. v. R. *J. Comp. Chem.* **1983**, *4*, 294–301. Polarization functions: Foresman, J. B.; Frisch, Æ. In *Exploring Chemistry with Electronic Structure Methods*, 2nd ed.; Gaussian, Inc.; Pittsburg, PA, 1996; p 110. The 6-31G(d') basis set has the d polarization function for C, N, O, and F taken from the 6-311G basis set, instead of the original arbitrarily assigned value of 0.8 used in the 6-31G(d) basis set.

[115] Dunning Jr. T. H. *J. Chem. Phys.* **1970**, *53*, 2823–2833.

[116] Dunning Jr, T. H.; Hay, P. J. In *Modern Theoretical Chemistry*; Schaefer III, H. F., Ed.; Plenum Press: New York; 1997, Vol. 2; pp 1–462.

[117] Schäfer, A.; Horn, H.; Ahlrich, R. *J. Chem. Phys.* **1992**, *97*, 2571–2577.

[118] (a) Petersson, G. A.; Al–Laham, M. A. *J. Chem. Phys.* **1991**, *94*, 6081–6090.
(b) Petersson, G. A.; Bennett, A.; Tenfeldt, T. G.; Al–Laham, M. A.; Shirley, W. A.; Mantzaris, J. *J. Chem. Phys.* **1988**, *89*, 2193–2218
(c) Montgomery Jr, J. A.; Ochterski, J. W.; Petersson, G. A. *J. Chem. Phys.***1994**, *101*, 5900–5909.

[119] Note in Gaussian03 D.02 (ref 72), the keyword used to retrieve the APNO basis sets appears similar to the keywords for Pople double- and triple-zeta basis sets;

however, APNO basis sets are not Pople basis sets. The 6-311G(d',p') keyword, defined in the current chapter as CBS1, calls for a (14s9p4d,6s3p1d/[6s6p3d,4s2p1d] APNO basis set. The 6-311G(d') keyword, defined in the current chapter as CBS2, calls for an APNO basis set that adds to f polarization functions to first row elements, (14s9p4d2f,6s3p1d)/[6s6p3d2f,4s2p1d].

[120] Oxgaard, J.; Periana, R. A.; Goddard III, W. A. *J. Am. Chem. Soc.* **2004**, *126*, 11658–11665.

[121] For a listing of basis sets used in this study, see Appendix B.

[122] Matsumoto, T.; Taube, D. J.; Periana, R. A.; Taube, H.; Yoshida, H. *J. Am. Chem. Soc.* **2000**, *122*, 7414–7415.

[123] Lail, M.; Arrowood, B. N.; Gunnoe, T. B. *J. Am. Chem. Soc.* **2003**, *125*, 7506–7507.

[124] Oxgaard, J.; Goddard III, W. A. *J. Am. Chem. Soc.* **2004**, *126*, 442–443.

[125] Vastine, B. A.; Hall, M. B. *J. Am. Chem. Soc.* **2007**, *129*, 12068–12069.

[126] Cundari, T. R.; Grimes, T. V.; Gunnoe, T. B. *J. Am. Chem. Soc.* **2007**, *129*, 13172–13182.

[127] Huzinaga, S.; Miguel, B. *J. Chem. Phys. Lett.* **1990**, *175*, 289–291.

[128] Dobbs, K. D.; Hehre, W. J. *J. Comp. Chem.* **1987**, *8*, 861–879.

[129] Rassolov, V. A.; Pople, J. A.; Ratner, M. A.; Windus, T. L. *J. Chem. Phys.* **1998**,*109*, 1223–1229.

[130] Schäfer, A.; Huber, C.; Ahlrichs, R *J. Chem. Phys.* **1994**, *100*, 5829–5835.

[131] Weigand, F.; Haser, M.; Patzelt, H.; Ahlrichs, R. *Chem. Phys.Lett.* **1998**, *294*, 143–152.

[132] Balabanov, N. B.; Peterson, K. A. *J. Chem. Phys.* **2005**, *123*, 064107.

[133] Wachters, A. J. H. *J. Chem. Phys.* **1970**, *52*, 1033–1036. F exponents: Bauschlicher Jr., C. W.; Langhoff, S. R.; Partridge, H.; Barnes, L. A. *J. Chem. Phys.* **1989**, *91*, 2399–2411.

[134] Bauschlicher Jr., C. W. *Theor. Chim. Acta.* **1995**, *92*, 183–198.

[135] Vastine, B. A.; Webster, C. E.; Hall, M. B. *J. Chem. Theory Comp.* **2007**, *3*, 2268–2281.

[136] Hu, X.; Castro–Rodriguez, I.; Meyer, K. *Organometallics* **2003**, *22*, 3016–3018.

[137] (a) Peters, J. C.; Feldman, J. D.; Tilley, T. D. *J. Am. Chem. Soc.* **1999**, *121*, 9871–9872.
(b) Feldman, J. D.; Peters, J. C.; Tilley, T. D. *Organometallics* **2002**, *21*, 4050–4064.
(c) Feldman, J. D.; Peters, J. C.; Tilley, T. D. *Organometallics* **2002**, *21*, 4065–4075.

[138] (a) Chen, Y.; Jonas, D. M.; Kinsey, J. L.; Field, R. W. *J. Chem. Phys.* **1989**, *91*, 3976–3987.
(b) Ervin, K. M.; Ho, J.; Lineberger, W. C. *J. Chem. Phys.* **1989**, *91*, 5974–5992.

[139] Nesmeyanov, A. N.; Aleksandrov, G. G.; Antonova, A. B.; Anisimov, K. N.; Kolobova, N. E.; Struchkov, Yu. T. *J. Organomet. Chem.* **1976**, *110*, C36–C38.

[140] Silvestre, J.; Hoffmann, R. *Helv. Chim. Acta.* **1985**, *68*, 1461–1506.

[141] De Angelis, F.; Fantacci, S.; Sgamellotti, A. *Coord. Chem. Rev.* **2006**, *250*, 1497–1513.

[142] Wolf, J.; Werner, H.; Serhadli, O.; Ziegler, M. L. *Angew. Chem., Int, Ed. Engl.* **1983**, *22*, 414–416.

[143] Grotjahn, D. B.; Zeng, X.; Cooksy, A. L.; Kassel, W. S.; DiPasquale, A. G.; Zakharov, L. N.; Rheingold, A. L. *Organometallics* **2007**, *26*, 3385–3402.

[144] Kaupp, M.; Schleyer, P. v. R.; Stoll, H.; Preuss, H. *J. Chem. Phys.* **1991**, *94*, 1360–1366.

[145] Werner, H. *J. Organomet. Chem.* **1994**, *475*, 45–55.

[146] (a) Gonzalez, C.; Schlegel, H. B. *J. Chem. Phys.* **1989**, *90*, 2154–2161.
(b) Gonzalez, C.; Schlegel, H. B. *J. Chem. Phys.* **1990**, *94*, 5523–5527.

[147] The chloride was assigned the cc-pVDZ basis set. The other atoms were assigned the same basis sets as their bis-alkynyl analogs.

[148] (a) Tellers, D. M.; Bergman, R. G. *Organometallics* **2001**, *20*, 4819–4832.
(b) Tellers, D. M.; Skoog, S. J.; Gunnoe, T. B.; Harman, W. D.; Bergman, R. G. *Organometallics* **2000**, *19*, 2428–2432.

APPENDIX A

SUPPLEMENTAL MATERIAL FOR CHAPTER II

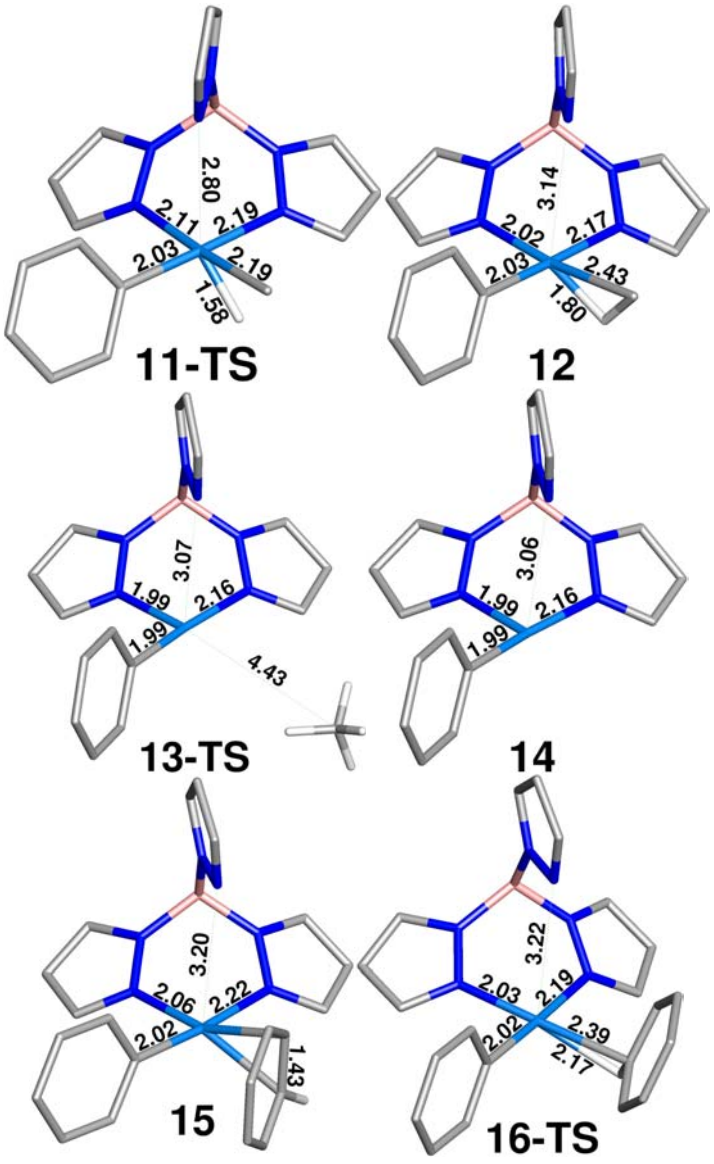

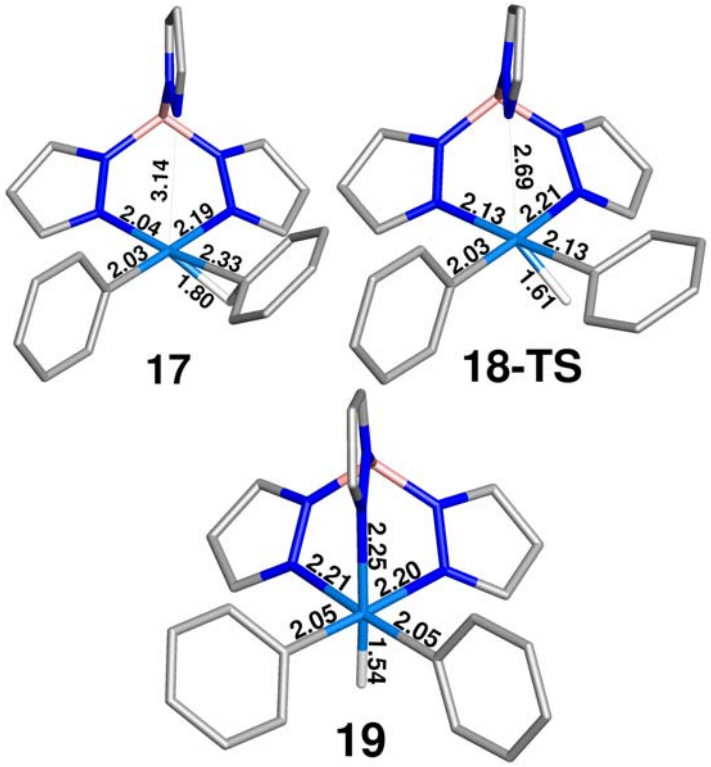

Figure A-1. This figure contains the equilibrium geometries for complexes **11-TS** through **19**. These structures reside along the reaction coordinate involved in the second elimination of methane and the second addition of benzene. Bond lengths are in angstroms.

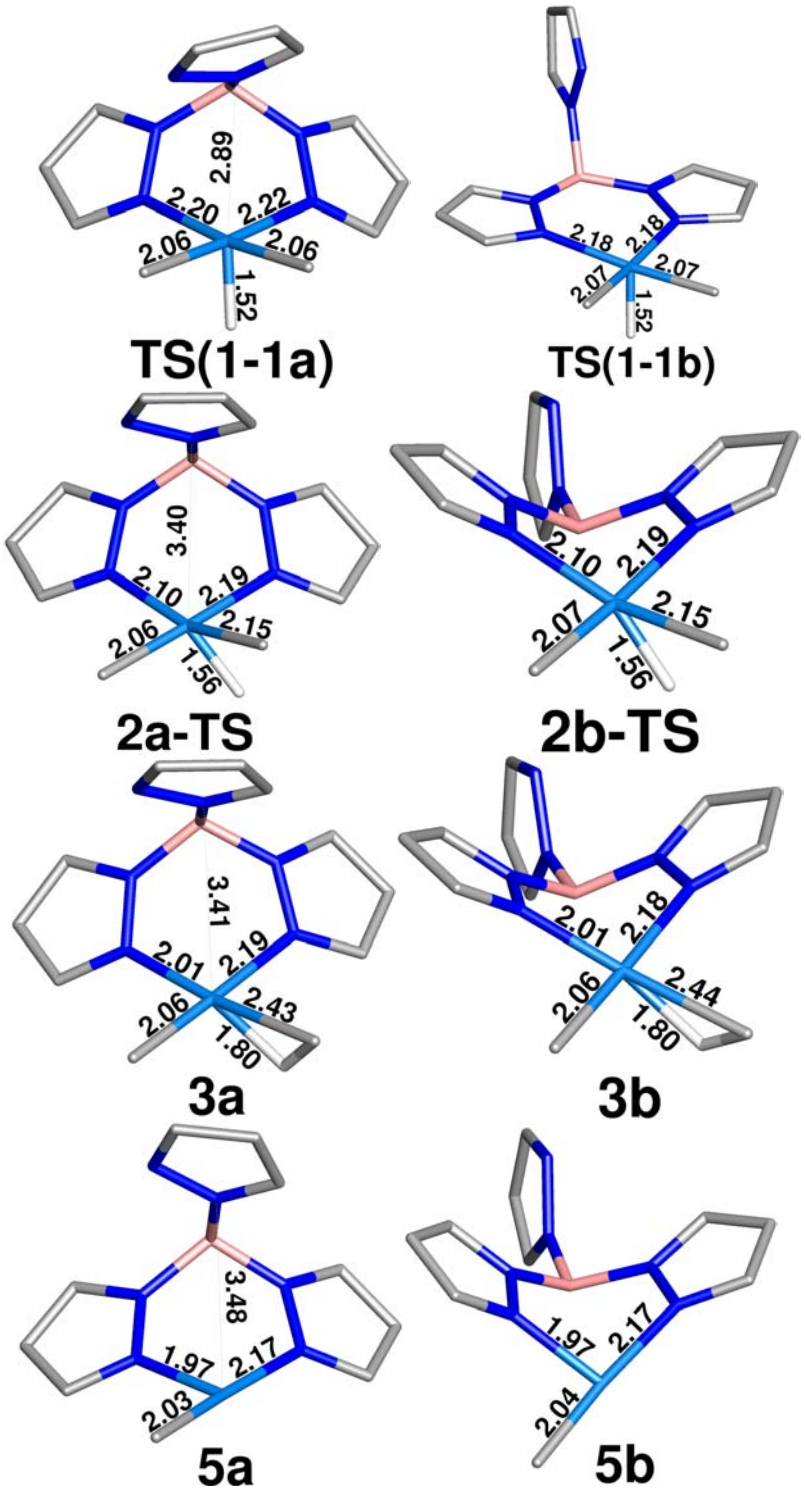

Figure A-2. The equilibrium geometries of the complexes along the *rotation* and *inversion* pathways. Bond lengths are in angstroms.

Table A-1. Calculated barrier values for Ba1 and Ba2.[a]

functional	% HF exc	barrier	basis set	value (kcal/mol)
Pure DFT				
BLYP	0	1	cc-pvDZ	24.00
			cc-pvTZ	23.17
			cc-pvQZ	24.19
		2	cc-pvDZ	33.82
			cc-pvTZ	30.83
			cc-pvQZ	32.71
BPW91	0	1	cc-pvDZ	24.55
			cc-pvTZ	23.95
			cc-pvQZ	25.20
		2	cc-pvDZ	35.38
			cc-pvTZ	34.56
			cc-pvQZ	35.45
BP86	0	1	cc-pvDZ	25.07
			cc-pvTZ	23.83
			cc-pvQZ	24.83
		2	cc-pvDZ	37.52
			cc-pvTZ	66.97
			cc-pvQZ	36.98
HCTH	0	1	cc-pvDZ	20.76
			cc-pvTZ	19.73
			cc-pvQZ	21.42
		2	cc-pvDZ	27.96
			cc-pvTZ	27.16
			cc-pvQZ	28.71
G96LYP	0	1	cc-pvDZ	24.25
			cc-pvTZ	23.15
			cc-pvQZ	25.32
		2	cc-pvDZ	31.50
			cc-pvTZ	28.91
			cc-pvQZ	31.61
G96PW91	0	1	cc-pvDZ	24.98
			cc-pvTZ	24.73
			cc-pvQZ	25.09
	0	2	cc-pvDZ	32.92
			cc-pvTZ	31.56
			cc-pvQZ	32.96

(Table A-1 continued)

mPWPW91	0	1	cc-pvDZ	24.93
			cc-pvTZ	23.72
			cc-pvQZ	24.69
		2	cc-pvDZ	37.84
			cc-pvTZ	35.84
			cc-pvQZ	37.80
PBE	0	1	cc-pvDZ	24.95
			cc-pvTZ	23.72
			cc-pvQZ	24.70
		2	cc-pvDZ	42.26
			cc-pvTZ	40.20
			cc-pvQZ	41.83
		HDFT		
MPWLYP1M	5	1	cc-pvDZ	24.28
			cc-pvTZ	23.51
			cc-pvQZ	24.28
		2	cc-pvDZ	36.05
			cc-pvTZ	33.30
			cc-pvQZ	34.82
B3LYP	20	1	cc-pvDZ	24.33
			cc-pvTZ	23.69
			cc-pvQZ	24.58
		2	cc-pvDZ	33.76
			cc-pvTZ	32.46
			cc-pvQZ	34.33
B3PW91	20	1	cc-pvDZ	24.58
			cc-pvTZ	23.93
			cc-pvQZ	24.86
		2	cc-pvDZ	35.76
			cc-pvTZ	34.75
			cc-pvQZ	36.15
B3P86	20	1	cc-pvDZ	25.25
			cc-pvTZ	24.48
			cc-pvQZ	25.17
		2	cc-pvDZ	38.30
			cc-pvTZ	37.12
			cc-pvQZ	38.53

(Table A-1 continued)

B97-1	21	1	cc-pvDZ	24.87
			cc-pvTZ	24.24
			cc-pvQZ	25.04
		2	cc-pvDZ	37.63
			cc-pvTZ	35.80
			cc-pvQZ	37.57
mPW0	25	1	cc-pvDZ	24.96
			cc-pvTZ	24.22
			cc-pvQZ	25.12
		2	cc-pvDZ	39.10
			cc-pvTZ	37.32
			cc-pvQZ	39.28
PBE0	25	1	cc-pvDZ	25.00
			cc-pvTZ	24.20
			cc-pvQZ	24.97
		2	cc-pvDZ	40.92
			cc-pvTZ	39.19
			cc-pvQZ	41.01
MPW1K	42.8	1	cc-pvDZ	25.07
			cc-pvTZ	24.44
			cc-pvQZ	25.49
		2	cc-pvDZ	37.59
			cc-pvTZ	36.19
			cc-pvQZ	38.34
BH&HLYP	50	1	cc-pvDZ	24.51
			cc-pvTZ	23.42
			cc-pvQZ	25.60
		2	cc-pvDZ	30.18
			cc-pvTZ	28.45
			cc-pvQZ	33.06
B2-PLYP	53	1	cc-pvDZ	27.70
			cc-pvTZ	29.97
			cc-pvQZ	31.09
		2	cc-pvDZ	42.76
			cc-pvTZ	44.32
			cc-pvQZ	51.75

(Table A-1 continued)

mPW2-PLYP	55	1	cc-pvDZ	27.51
			cc-pvTZ	29.60
			cc-pvQZ	30.69
		2	cc-pvDZ	42.70
			cc-pvTZ	44.10
			cc-pvQZ	50.97
		MDFT		
BB95	0	1	cc-pvDZ	24.54
			cc-pvTZ	23.87
			cc-pvQZ	22.60
		2	cc-pvDZ	35.47
			cc-pvTZ	33.95
			cc-pvQZ	32.32
mPWB95	0	1	cc-pvDZ	24.87
			cc-pvTZ	23.51
			cc-pvQZ	24.48
		2	cc-pvDZ	37.97
			cc-pvTZ	35.78
			cc-pvQZ	36.51
mPWKCIS	0	1	cc-pvDZ	23.88
			cc-pvTZ	22.75
			cc-pvQZ	24.42
		2	cc-pvDZ	35.80
			cc-pvTZ	33.33
			cc-pvQZ	34.91
PBEKCIS	0	1	cc-pvDZ	23.72
			cc-pvTZ	22.60
			cc-pvQZ	23.51
		2	cc-pvDZ	35.89
			cc-pvTZ	34.26
			cc-pvQZ	35.52
TPSS	0	1	cc-pvDZ	27.57
			cc-pvTZ	26.66
			cc-pvQZ	27.56
		2	cc-pvDZ	38.46
			cc-pvTZ	37.53
			cc-pvQZ	38.00

(Table A-1 continued)

VSXC	0	1	cc-pvDZ	9.52
			cc-pvTZ	9.03
			cc-pvQZ	9.13
		2	cc-pvDZ	37.78
			cc-pvTZ	36.05
			cc-pvQZ	37.75
HMDFT				
TPSSh	10	1	cc-pvDZ	27.27
			cc-pvTZ	26.51
			cc-pvQZ	27.72
		2	cc-pvDZ	39.46
			cc-pvTZ	39.68
			cc-pvQZ	41.57
B1B95	25	1	cc-pvDZ	24.55
			cc-pvTZ	23.90
			cc-pvQZ	24.86
		2	cc-pvDZ	38.46
			cc-pvTZ	37.23
			cc-pvQZ	39.34
MPW1B95	31	1	cc-pvDZ	24.82
			cc-pvTZ	24.07
			cc-pvQZ	24.88
		2	cc-pvDZ	37.50
			cc-pvTZ	36.06
			cc-pvQZ	37.24
MPWKCIS1K	41	1	cc-pvDZ	24.07
			cc-pvTZ	23.48
			cc-pvQZ	24.45
		2	cc-pvDZ	32.03
			cc-pvTZ	30.51
			cc-pvQZ	32.50
BB1K	42	1	cc-pvDZ	24.71
			cc-pvTZ	31.56
			cc-pvQZ	33.73
		2	cc-pvDZ	37.76
			cc-pvTZ	36.18
			cc-pvQZ	38.17

(Table A-1 continued)

MPWB1K	44	1	cc-pvDZ	24.91
			cc-pvTZ	24.26
			cc-pvQZ	25.27
		2	cc-pvDZ	39.19
			cc-pvTZ	37.67
			cc-pvQZ	39.78

a: The basis set is as follows: platinum was assigned the mLANL2DZ ECP/BS; the nitrogens, boron, and carbons and hydrogen bound to platinum were assigned the basis set listed in the table, while all other atoms were assigned D95.

Table A-2. Calculated values for Ba1 with the 29 all-electron basis sets.

all-electron basis sets	$\Delta H^{\ddagger}$ (kcal•mol^{-1})
STO-3G	35.82
STO-6G	35.18
3-21G	30.27
3-21+G	30.10
6-31G	28.26
6-31+G	28.59
6-31++G	28.51
6-31G(d')	26.37
6-31+G(d')	26.53
6-31++G(d')	26.49
6-31G(d',p')	25.40
6-31+G(d',p')	25.11
6-31++G(d',p')	25.13
6-311G	28.13
6-311+G	28.31
6-311++G	28.33
6-311G*	27.23
6-311+G*	26.60
6-311++G*	26.55
6-311G**	24.81
6-311+G**	25.06
6-311++G**	25.03
CBS1	24.42
CBS2	24.53
VDZ	28.95
VTZ	28.42
DZ	28.19
DZP	25.55
SVP	25.40

APPENDIX B

SUPPLEMENTAL MATERIAL FOR CHAPTER III

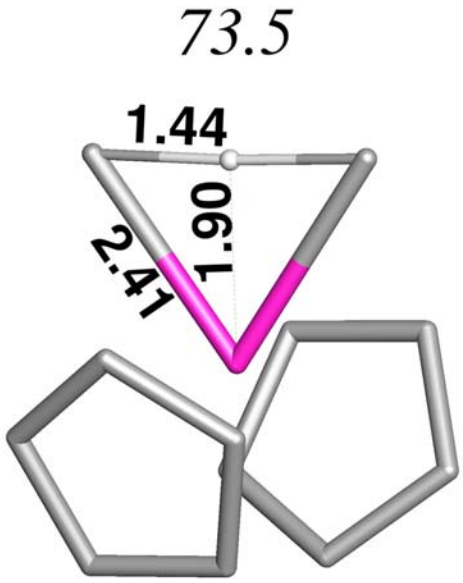

Figure B-1. B3LYP/DZP optimized geometry of **1**. The methyl and cyclopentadienyl hydrogen atoms were removed for clarity. E_{SCF} = -1228.30604309 hartrees

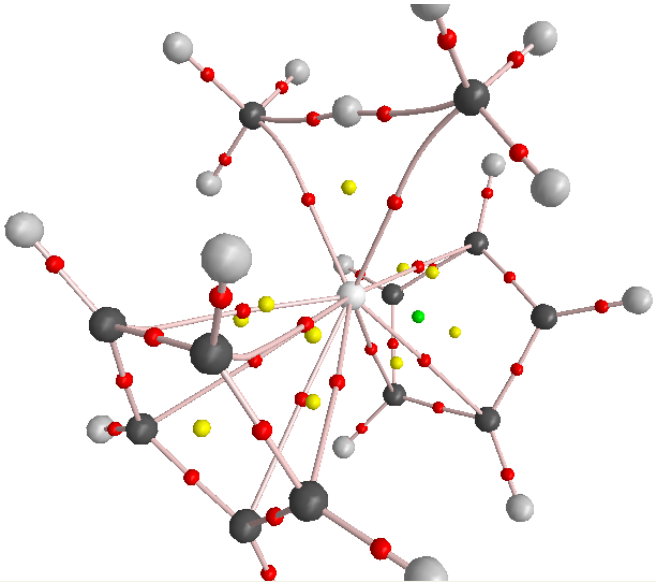

Figure B-2. Representation of the AIM CPs of **1**.

Table B-1. Optimized Cartesian coordinates of **1.**

21	-0.005496	0.186358	-0.026992
6	0.035628	1.895314	-1.722630
6	-0.015396	2.299429	1.127708
1	0.002570	2.065088	-0.293039
6	-1.908742	-0.844553	1.240910
6	-2.431533	0.334754	0.638351
6	-2.414493	0.153491	-0.767404
6	2.515718	0.478025	-0.010971
6	2.215203	-0.436226	-1.054853
6	1.672064	-1.610718	-0.469466
6	-1.583903	-1.758828	0.203840
6	-1.881803	-1.138719	-1.038352
6	2.166203	-0.133078	1.222244
6	1.641925	-1.422778	0.942116
1	-1.793901	-1.021813	2.306848
1	-2.776705	1.219102	1.163320
1	-2.744173	0.874686	-1.507662
1	2.924042	1.475853	-0.135111
1	2.365175	-0.261963	-2.116269
1	1.345936	-2.498207	-1.003003
1	0.966933	2.422146	-1.969876
1	-0.021391	1.019302	-2.395161
1	-0.812146	2.541705	-1.986934
1	-1.165595	-2.751276	0.336772
1	-1.742154	-1.580207	-2.021456
1	2.272344	0.313676	2.206460
1	1.288462	-2.141546	1.674951
1	-0.095320	1.644555	2.015186
1	0.907345	2.882379	1.249045
1	-0.871230	2.986333	1.173805

Basis Sets: Opt and Freq
Sc: LANL2DZ(f)
C: aug-cc-pVDZ
H being transferred: aug-cc-pVDZ
All other H: D95.

Basis Sets: AIM analysis
Sc: WTBS
C: aug-cc-pVDZ
H being transferred: aug-cc-pVDZ
All other H: D95.

Table B-2. AIM CP data for **1**.

	ρ (a.u.)	$\nabla^2(\rho)$	Distance (Å)
Sc-C	0.049837	0.151443	1.157927
C-H_t	0.128339	-0.156703	0.966571
C-H	0.259873	-0.680968	0.685212
Ring	0.046071	0.209364	1.136153

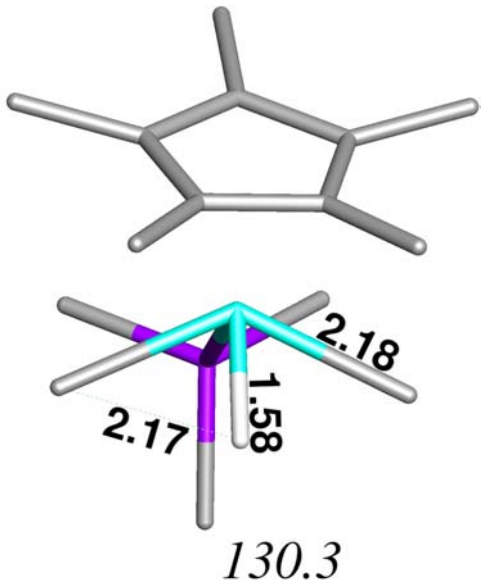

Figure B-3. B3LYP/DZP optimized geometry of **2**. E_{SCF} = -1036.17995683 hartrees

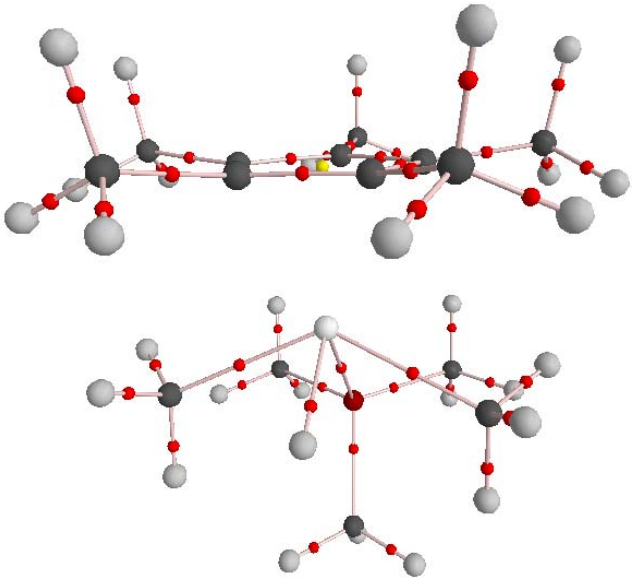

Figure B-4. Representation of the AIM CPs of **2**.

Basis Sets: Opt and Freq	**Basis Sets: AIM analysis**
Ir: LANL2DZ(f)	Ir: WTBS
P: cc-pVDZ	P: cc-pVDZ
Aromatic carbons of Cp* ring: cc-pVDZ	Aromatic carbons of Cp* ring: cc-pVDZ
Carbon atoms of methyl ligands: cc-pVDZ	Carbon atoms of methyl ligands: cc-pVDZ
H being transferred: cc-pVDZ	H being transferred: cc-pVDZ
All other C and H: D95	All other C and H: D95

Table B-3. Optimized Cartesian coordinates of **2**.

77	-0.005728	-0.008154	-0.477058
15	2.299309	-0.000346	0.046256
6	0.489846	-1.996015	-1.222500
6	0.509259	1.960681	-1.259607
1	0.115587	-0.016721	-2.051335
6	-1.413237	1.182475	0.955599
6	-0.978033	0.048624	1.718277
6	-1.389030	-1.136578	1.023657
6	-2.126351	-0.735556	-0.167329
6	-2.140114	0.698722	-0.209876
6	-1.320729	2.617351	1.391861
6	-0.321590	0.096757	3.071083
6	-1.267867	-2.541661	1.542966
6	-2.905797	-1.651269	-1.070499
6	-2.934560	1.545244	-1.166283
6	2.846784	-1.398875	1.135825
6	3.459651	-0.088692	-1.392286
6	2.892520	1.489404	0.981757
1	-0.337099	-2.350229	-1.851989
1	1.391131	-2.007521	-1.839011
1	0.624845	-2.678589	-0.378831
1	-0.351562	-2.693278	2.123899
1	-2.114343	-2.769843	2.207456
1	-1.284217	-3.284091	0.739516
1	0.289402	-0.790227	3.268547
1	0.308682	0.983516	3.197975
1	-1.086571	0.136568	3.860615
1	-0.417719	2.816909	1.979126
1	-1.333622	3.310924	0.545812
1	-2.182056	2.870416	2.027738
1	-3.040202	1.067211	-2.145238
1	-3.947160	1.711412	-0.770439
1	-2.486399	2.531634	-1.321657
1	-2.448848	-2.642060	-1.154466
1	-3.920559	-1.797596	-0.672376
1	-3.006561	-1.241730	-2.080615
1	-0.336684	2.325690	-1.857950
1	0.693552	2.652292	-0.422846
1	1.387320	1.946981	-1.910219
1	3.939997	1.345543	1.294252
1	2.834275	2.391719	0.355156
1	2.274914	1.638082	1.875769
1	3.240381	0.709449	-2.109859

(Table B-3 continued)

1	4.495429	0.023079	-1.045279
1	3.365390	-1.052317	-1.904975
1	2.311692	-1.354047	2.092283
1	2.639630	-2.367543	0.658963
1	3.928309	-1.326256	1.333738

Table B-4. AIM CP data for **2**.

	ρ (a.u.)	∇^2	Distance (Å)
Ir-C	0.104164	0.093511	1.192596
Ir-H	0.162408	0.019232	1.093013

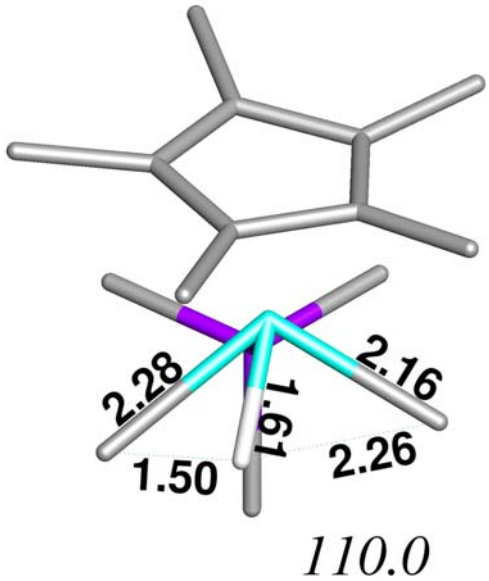

Figure B-5. B3LYP/DZP optimized geometry of **3**. E_{SCF} = -1036.16860046 hartrees

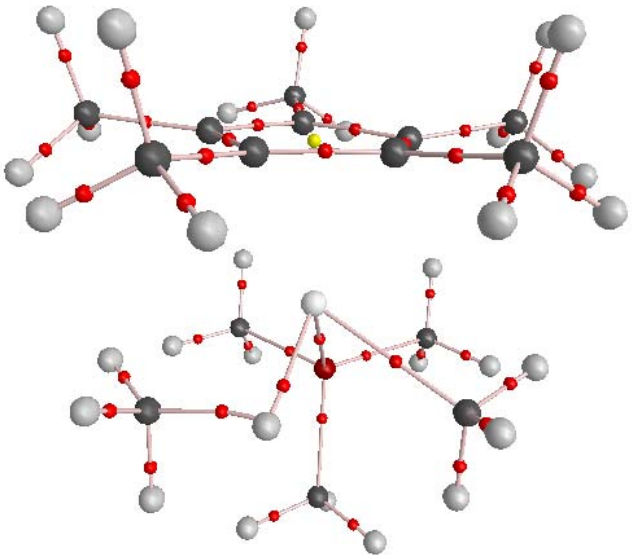

Figure B-6. Representation of the AIM CPs of **3**.

Basis Sets: Opt and Freq	Basis Sets: AIM analysis
Ir: LANL2DZ(f)	Ir: WTBS
P: cc-pVDZ	P: cc-pVDZ
Aromatic carbons of Cp* ring: cc-pVDZ	Aromatic carbons of Cp* ring: cc-pVDZ
Carbon atoms of methyl ligands: cc-pVDZ	Carbon atoms of methyl ligands: cc-pVDZ
H being transferred: cc-pVDZ	H being transferred: cc-pVDZ
All other C and H: D95	All other C and H: D95

Table B-5. Optimized Cartesian coordinates of **3**.

77	0.022537	-0.022930	-0.442191
15	-2.269808	-0.023198	0.070644
6	-0.476372	1.680434	-1.665509
6	-0.406365	-1.951050	-1.579924
1	-0.123072	-0.531550	-1.960322
6	1.543369	-1.133280	0.950578
6	0.909301	-0.122604	1.729569
6	1.146858	1.161177	1.090291
6	2.033353	0.930763	-0.041272
6	2.233490	-0.480912	-0.158541
6	1.607057	-2.602821	1.263634
6	0.222977	-0.317717	3.053634
6	0.819325	2.511359	1.671755
6	2.705514	1.998509	-0.857187
6	3.137782	-1.175462	-1.140357
6	-2.860385	1.503886	0.930880
6	-3.451625	-0.188911	-1.347142
6	-2.813685	-1.393991	1.192620
1	0.354387	1.877360	-2.350253
1	-1.378294	1.562596	-2.273395
1	-0.609056	2.554684	-1.017394
1	-0.045017	2.472719	2.342750
1	1.667135	2.895093	2.257880
1	0.605825	3.252824	0.893858
1	-0.617073	0.370318	3.199555
1	-0.142401	-1.340696	3.186931
1	0.934122	-0.123176	3.869990
1	0.785831	-2.922680	1.913474
1	1.577238	-3.220010	0.358389
1	2.545248	-2.846825	1.782961
1	3.247494	-0.608768	-2.070283
1	4.142751	-1.298747	-0.711093
1	2.777557	-2.177905	-1.397117
1	2.069159	2.878622	-0.992972
1	3.621371	2.334710	-0.349289
1	2.996883	1.638315	-1.849006
1	0.491147	-2.340986	-2.067623
1	-0.646950	-2.585976	-0.723078
1	-1.237938	-1.992558	-2.288949
1	-3.894447	-1.335628	1.370626
1	-2.587008	-2.364477	0.736679
1	-2.296172	-1.329817	2.154255
1	-3.326061	-1.157855	-1.841722

(Table B-5 continued)

1	-4.481984	-0.119773	-0.977910
1	-3.289971	0.603465	-2.083781
1	-2.311115	1.644705	1.867816
1	-2.690080	2.378704	0.294540
1	-3.931284	1.430639	1.155362

Table B-6. AIM data of **3**.

	ρ (a.u.)	∇^2	Distance (Å)
Ir-C'	0.108916	0.111959	1.175042
Ir-H	0.162408	0.019232	1.093013
C-H	0.117912	-0.069848	0.922356

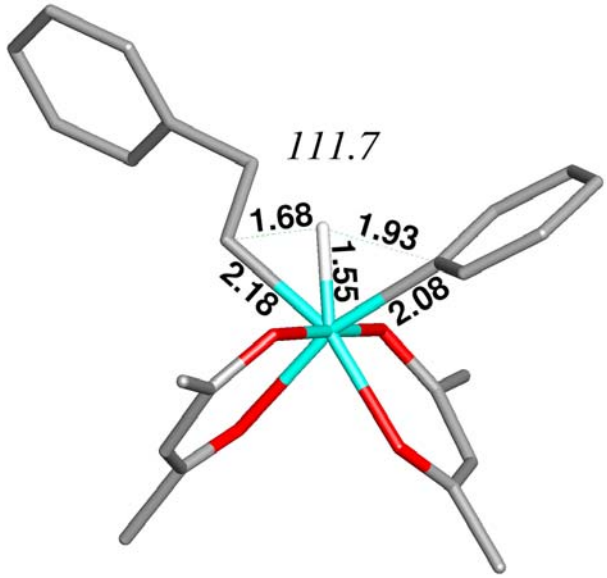

Figure B-7. B3LYP/DZP optimized geometry of **4**. E_{SCF} = -1337.54215904 hartrees

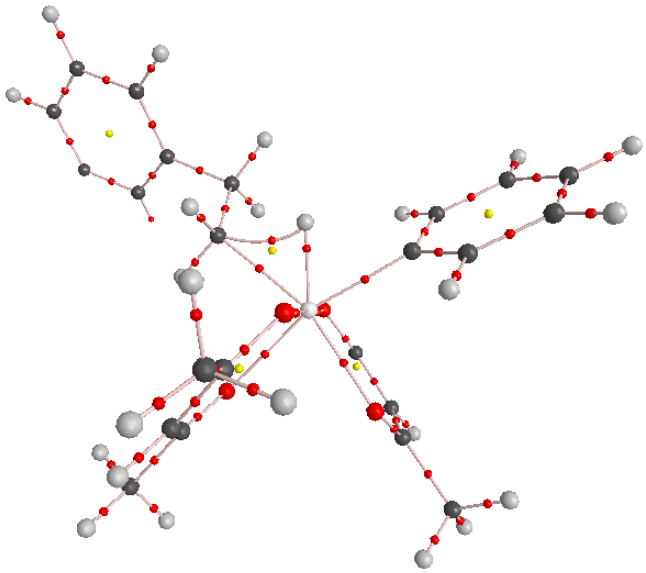

Figure B-8. Representation of the AIM CPs of **4**.

Basis Sets: Opt and Freq	Basis Sets: AIM analysis
Ir: LANL2DZ(f)	Ir: WTBS
O: cc-pVDZ	O: cc-pVDZ
Ligated carbons: cc-pVDZ	Ligated carbons: cc-pVDZ
H being transferred: cc-pVDZ	H being transferred: cc-pVDZ
All other C and H: D95	All other C and H: D95

Table B-7. Optimized Cartesian coordinates of **4**.

77	0.492224	0.128681	-0.112894
8	0.786896	1.072737	-1.906841
8	-0.047066	1.964242	0.865324
8	2.406325	0.816717	0.423952
8	0.172802	-0.759010	1.699934
6	-1.654602	0.016879	-0.489858
6	1.473216	-1.569195	-0.796941
1	-0.341856	-0.917614	-0.903251
6	0.673745	2.351390	-2.067998
6	0.309315	3.316405	-1.102393
6	-0.014251	3.097351	0.261339
6	2.933541	0.555903	1.567925
6	2.328319	-0.154996	2.634221
6	1.041064	-0.733513	2.659705
6	0.994514	2.806512	-3.481530
6	-0.370909	4.291740	1.131433
6	4.348188	1.079793	1.741627
6	0.561153	-1.421778	3.925076
6	-3.942667	-0.965069	-0.015285
6	-4.767912	-1.380199	-1.083683
6	-6.150142	-1.108859	-1.079180
6	-6.730954	-0.414933	-0.000416
6	-5.918553	0.003251	1.072837
6	-4.538701	-0.270338	1.062962
6	-2.442993	-1.231179	-0.030406
6	1.235121	-2.846019	-0.251884
6	2.468563	-1.440253	-1.783696
6	3.227522	-2.554101	-2.196933
6	2.994050	-3.824472	-1.635773
6	1.989507	-3.964921	-0.659486
1	0.345525	2.281033	-4.193117
1	0.866756	3.884978	-3.606208
1	2.029808	2.537303	-3.727118
1	-1.382878	4.160850	1.535355
1	0.315240	4.334996	1.986907
1	-0.322345	5.236974	0.583876
1	5.021937	0.518936	1.080158
1	4.392080	2.131592	1.435074
1	4.703059	0.983537	2.771407
1	0.287244	-2.460036	3.699334
1	1.321613	-1.414649	4.710260
1	-0.341350	-0.919621	4.296588
1	0.278885	4.344070	-1.444924
1	2.919012	-0.263439	3.536251
1	-4.327769	-1.921129	-1.920024
1	-6.769579	-1.439954	-1.909890
1	-7.798404	-0.206439	0.006391
1	-6.359738	0.534876	1.913241
1	-3.918680	0.051273	1.898517
1	-1.948788	0.877906	0.118326
1	-1.861703	0.250585	-1.541483

(Table B-7 continued)

1	-2.228165	-2.079121	-0.696685

1	-2.096061	-1.512282	0.971667
1	0.464003	-2.977733	0.503500
1	1.787175	-4.938658	-0.216962
1	3.578013	-4.685087	-1.954937
1	3.996949	-2.424848	-2.956217
1	2.660305	-0.470606	-2.232133

Table B-8. AIM Data of **4**.

	ρ (a.u.)	∇^2	Distance (Å)
Ir-$C_{sp}2$	0.107763	0.131764	1.228019
Ir-$C_{sp}3$	0.089130	0.127722	1.241145
Ir-H_t	0.167010	0.013086	1.231745
$C_{sp}3$-H_t	0.094083	0.033759	1.043281
Ring	0.092980	0.128984	1.350846

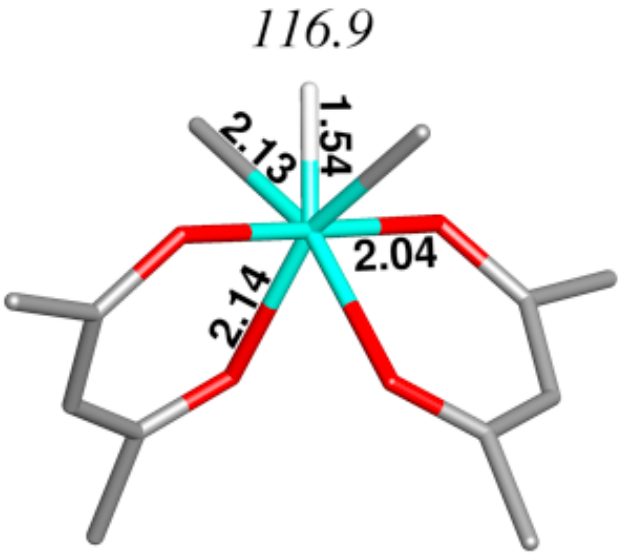

Figure B-9. B3LYP/DZP optimized geometry of **5**. E_{SCF} = -875.509732042 hartrees

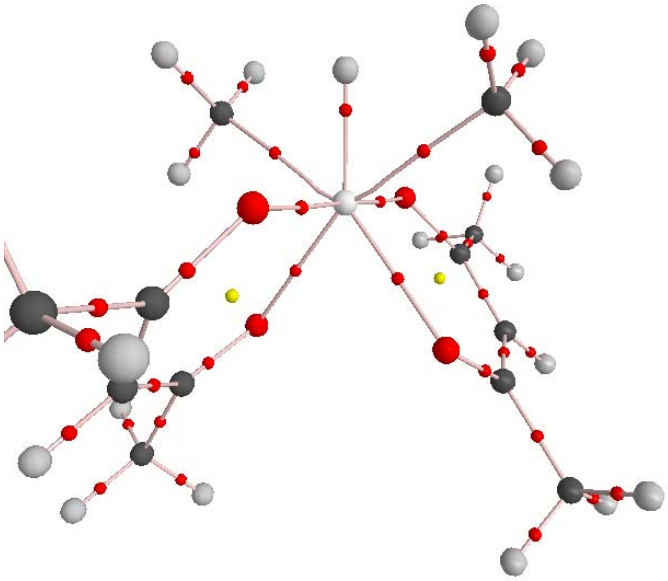

Figure B-10. Representation of the AIM CPs of **5**.

Basis Sets: Opt and Freq	Basis Sets: AIM analysis
Ir: LANL2DZ(f)	Ir: WTBS
O: cc-pVDZ	O: cc-pVDZ
Ligated carbons: cc-pVDZ	Ligated carbons: cc-pVDZ
H being transferred: cc-pVDZ	H being transferred: cc-pVDZ
All other C and H: D95	All other C and H: D95

Table B-9. Optimized geometric coordinates of **5**.

77	0.000000	0.000000	0.710896
8	-0.214629	2.029753	0.721039
8	1.350389	0.035809	-0.945508
8	-1.350389	-0.035809	-0.945508
8	0.214629	-2.029753	0.721039
6	1.808213	0.121364	1.824017
6	-1.808213	-0.121364	1.824017
6	0.355786	2.806787	-0.138095
6	1.234944	2.438410	-1.183433
6	1.669347	1.134849	-1.531847
6	-1.669347	-1.134849	-1.531847
6	-1.234944	-2.438410	-1.183433
6	-0.355786	-2.806787	-0.138095
6	0.000000	4.272342	0.045668
6	2.617727	0.967567	-2.708409
6	-2.617727	-0.967567	-2.708409
6	0.000000	-4.272342	0.045668
1	0.216495	4.578166	1.076643
1	0.546876	4.919187	-0.645532
1	-1.077434	4.408173	-0.114290
1	3.548131	0.498476	-2.363418
1	2.168067	0.288759	-3.444092
1	2.853606	1.918898	-3.193244
1	-3.548131	-0.498476	-2.363418
1	-2.168067	-0.288759	-3.444092
1	-2.853606	-1.918898	-3.193244
1	-0.216495	-4.578166	1.076643
1	-0.546876	-4.919187	-0.645532
1	1.077434	-4.408173	-0.114290
1	1.613014	3.249448	-1.794792
1	-1.613014	-3.249448	-1.794792
1	-1.876749	-1.030175	2.432286
1	-1.964166	0.762594	2.451786
1	-2.578173	-0.138350	1.046094
1	2.578173	0.138350	1.046094
1	1.876749	1.030175	2.432286
1	1.964166	-0.762594	2.451786
1	0.000000	0.000000	2.254810

Table B-10. AIM Data for **5**.

	ρ (a.u.)	∇^2	Distance (Å)
Ir-C	0.115063	0.097341	1.162684
Ir-H_t	0.174558	-0.026269	1.084151

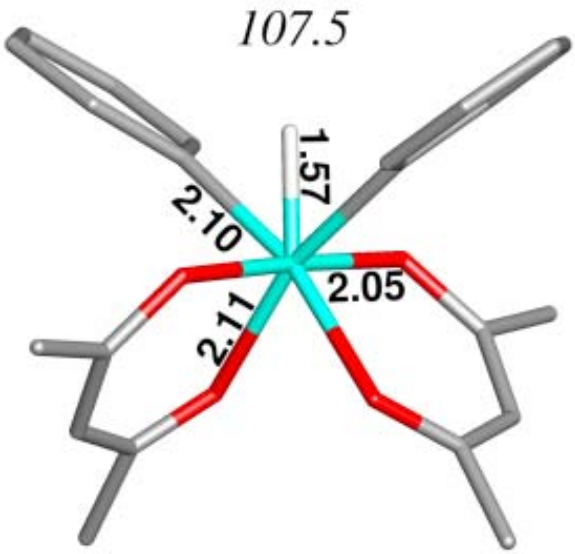

Figure B-11. B3LYP/DZP optimized geometry of **6**. E_{SCF} = -1259.01122033 hartrees

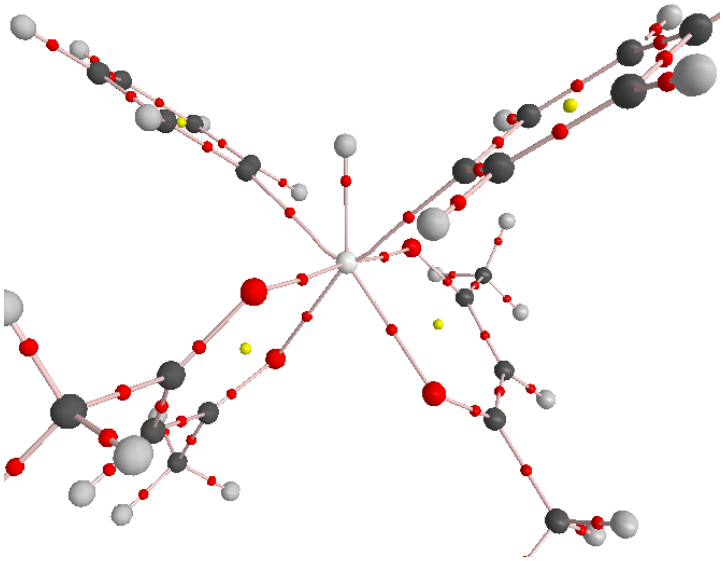

Figure B-12. Representation of the AIM CPs of **6**.

Basis Sets: Opt and Freq	Basis Sets: AIM analysis
Ir: LANL2DZ(f)	Ir: WTBS
O: cc-pVDZ	O: cc-pVDZ
phenyl carbons: cc-pVDZ	phenyl carbons: cc-pVDZ
H being transferred: cc-pVDZ	H being transferred: cc-pVDZ
All other C and H: D95	All other C and H: D95

Table B-11. Optimized geometric coordinates of **6**.

77	0.000000	0.000000	0.010029
8	0.000000	2.047634	-0.039124
8	1.374312	-0.143426	-1.588328
8	-1.374312	0.143426	-1.588328
8	0.000000	-2.047634	-0.039124
6	1.695168	0.008689	1.252015
6	-1.695168	-0.008689	1.252015
6	0.659080	2.732597	-0.919144
6	1.526174	2.242429	-1.918035
6	1.842902	0.887856	-2.194156
6	-1.842902	-0.887856	-2.194156
6	-1.526174	-2.242429	-1.918035
6	-0.659080	-2.732597	-0.919144
6	0.440263	4.230411	-0.797463
6	2.832056	0.572334	-3.302427
6	-2.832056	-0.572334	-3.302427
6	-0.440263	-4.230411	-0.797463
6	2.503640	-1.140533	1.318139
6	3.716825	-1.117773	2.015305
6	4.137643	0.042993	2.674107
6	3.328591	1.182388	2.635448
6	2.115257	1.164033	1.936475
6	-2.503640	1.140533	1.318139
6	-3.716825	1.117773	2.015305
6	-4.137643	-0.042993	2.674107
6	-3.328591	-1.182388	2.635448
6	-2.115257	-1.164033	1.936475
1	0.000000	0.000000	1.582518
1	0.751606	4.569649	0.198872
1	0.995632	4.789942	-1.554665
1	-0.629265	4.454250	-0.897893
1	3.719855	0.095103	-2.867514
1	2.385110	-0.147513	-3.999053
1	3.141419	1.465810	-3.851661
1	-3.719855	-0.095103	-2.867514
1	-2.385110	0.147513	-3.999053
1	-3.141419	-1.465810	-3.851661
1	-0.751606	-4.569649	0.198872
1	-0.995632	-4.789942	-1.554665
1	0.629265	-4.454250	-0.897893
1	2.004785	2.986521	-2.543662
1	-2.004785	-2.986521	-2.543662
1	1.489598	2.053576	1.925888

(Table B-11 continued)

1	3.636413	2.089752	3.153594
1	5.080368	0.055568	3.218423
1	4.335920	-2.013818	2.042988
1	2.184689	-2.048604	0.815328
1	-1.489598	-2.053576	1.925888
1	-3.636413	-2.089752	3.153594
1	-5.080368	-0.055568	3.218423
1	-4.335920	2.013818	2.042988
1	-2.184689	2.048604	0.815328

Table B-12. AIM Data of **6**.

	ρ (a.u.)	∇^2	Distance (Å)
Ir-C	0.120961	0.143555	1.136592
Ir-H_t	0.159288	0.019252	1.104014

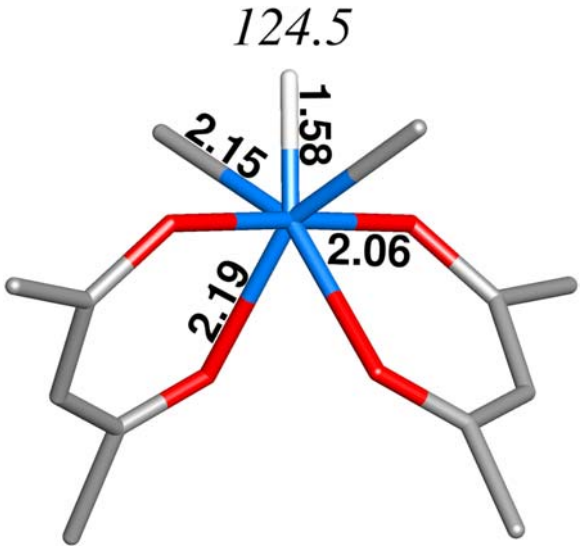

Figure B-13. B3LYP/DZP optimized geometry of **7**. E_{SCF} = -861.903595382 hartrees

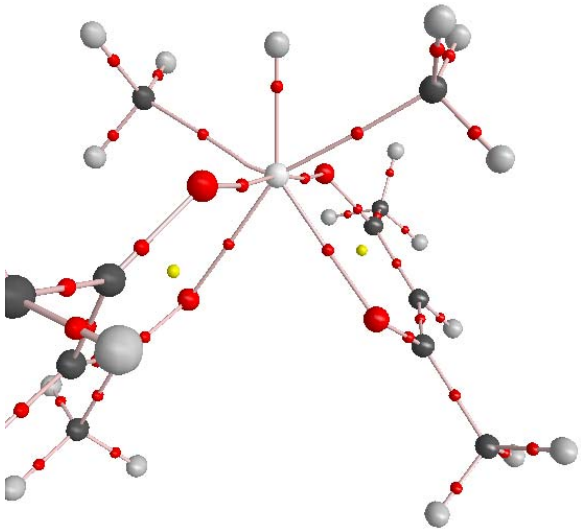

Figure B-14. Representation of the AIM CPs of **7**.

Basis Sets: Opt and Freq	AIM analysis
Os: LANL2DZ(f)	Os: WTBS
O: cc-pVDZ	O: cc-pVDZ
Ligated carbons: cc-pVDZ	Ligated carbons: cc-pVDZ
H being transferred: cc-pVDZ	H being transferred: cc-pVDZ
All other C and H: D95	All other C and H: D95

Table B-13. Optimized geometric coordinates of **7**.

76	0.000000	0.000000	0.758846
8	-0.193255	2.049114	0.719066
8	1.339828	0.039566	-0.967319
8	-1.339828	-0.039566	-0.967319
8	0.193255	-2.049114	0.719066
6	1.892800	0.185030	1.759041
6	-1.892800	-0.185030	1.759041
6	0.362018	2.823638	-0.137140
6	1.241391	2.448599	-1.194338
6	1.655342	1.140865	-1.545857
6	-1.655342	-1.140865	-1.545857
6	-1.241391	-2.448599	-1.194338
6	-0.362018	-2.823638	-0.137140
6	0.000000	4.299044	0.022360
6	2.590216	0.976597	-2.745785
6	-2.590216	-0.976597	-2.745785
6	0.000000	-4.299044	0.022360
1	0.166318	4.609721	1.062299
1	0.585985	4.941339	-0.644904
1	-1.067952	4.442978	-0.195915
1	3.522899	0.497195	-2.417326
1	2.121896	0.306739	-3.479968
1	2.826654	1.931993	-3.228205
1	-3.522899	-0.497195	-2.417326
1	-2.121896	-0.306739	-3.479968
1	-2.826654	-1.931993	-3.228205
1	-0.166318	-4.609721	1.062299
1	-0.585985	-4.941339	-0.644904
1	1.067952	-4.442978	-0.195915
1	1.620110	3.258288	-1.811820
1	-1.620110	-3.258288	-1.811820
1	-1.962616	-1.046915	2.441701
1	-2.154691	0.720710	2.328016
1	-2.654212	-0.311306	0.974793
1	2.654212	0.311306	0.974793
1	1.962616	1.046915	2.441701
1	2.154691	-0.720710	2.328016
1	0.000000	0.000000	2.343047

Table B-14. AIM Data of **7**.

	ρ (a.u.)	∇^2	Distance (Å)
Os-C	0.112665	0.1309667	1.145907
Os-H_t	0.161597	0.0465918	1.086563

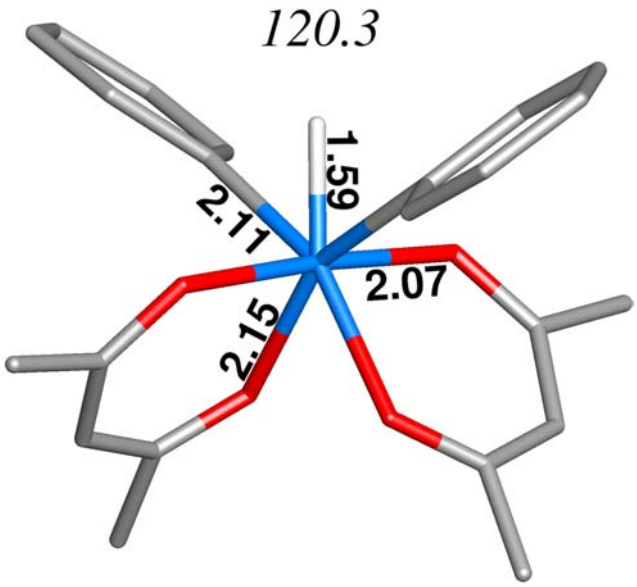

Figure B-15. B3LYP/DZP optimized geometry of **8**. E_{SCF} = -1245.42592031 hartrees

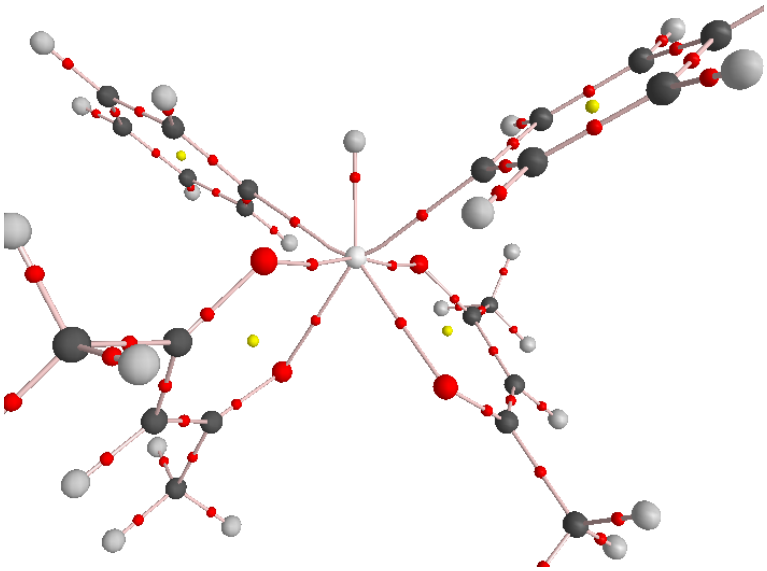

Figure B-16. Representation of the AIM CPs of **8**.

Basis Sets: Opt and Freq	Basis Sets: AIM analysis
Os: LANL2DZ(f)	Os: WTBS
O: cc-pVDZ	O: cc-pVDZ
phenyl carbons: cc-pVDZ	phenyl carbons: cc-pVDZ
H being transferred: cc-pVDZ	H being transferred: cc-pVDZ
All other C and H: D95	All other C and H: D95

Table B-15. Optimized geometric coordinates of **8**.

76	0.000000	0.000000	0.120197
8	0.000000	2.069348	0.041501
8	1.355041	-0.126724	-1.548966
8	-1.355041	0.126724	-1.548966
8	0.000000	-2.069348	0.041501
6	1.827483	0.033214	1.170131
6	-1.827483	-0.033214	1.170131
6	0.644415	2.758690	-0.828321
6	1.507032	2.269250	-1.846748
6	1.808106	0.918018	-2.142675
6	-1.808106	-0.918018	-2.142675
6	-1.507032	-2.269250	-1.846748
6	-0.644415	-2.758690	-0.828321
6	0.434616	4.264952	-0.709015
6	2.779626	0.619828	-3.281217
6	-2.779626	-0.619828	-3.281217
6	-0.434616	-4.264952	-0.709015
6	2.743205	-1.038114	1.042247
6	4.011188	-1.010660	1.638068
6	4.418223	0.092134	2.398704
6	3.529087	1.163386	2.553600
6	2.263849	1.127133	1.955176
6	-2.743205	1.038114	1.042247
6	-4.011188	1.010660	1.638068
6	-4.418223	-0.092134	2.398704
6	-3.529087	-1.163386	2.553600
6	-2.263849	-1.127133	1.955176
1	0.000000	0.000000	1.708323
1	0.760426	4.604868	0.283388
1	0.985996	4.820148	-1.475351
1	-0.635438	4.495541	-0.798521
1	3.669294	0.122858	-2.870918
1	2.310704	-0.078761	-3.986753
1	3.089419	1.524365	-3.815957
1	-3.669294	-0.122858	-2.870918
1	-2.310704	0.078761	-3.986753
1	-3.089419	-1.524365	-3.815957
1	-0.760426	-4.604868	0.283388
1	-0.985996	-4.820148	-1.475351
1	0.635438	-4.495541	-0.798521
1	1.984988	3.018390	-2.470486
1	-1.984988	-3.018390	-2.470486
1	1.587918	1.970246	2.096407

(Table B-15 continued)

1	3.821728	2.032847	3.145192
1	5.403749	0.114635	2.864443
1	4.686223	-1.858798	1.507372
1	2.449093	-1.908513	0.459539
1	-1.587918	-1.970246	2.096407
1	-3.821728	-2.032847	3.145192
1	-5.403749	-0.114635	2.864443
1	-4.686223	1.858798	1.507372
1	-2.449093	1.908513	0.459539

Table B-16. AIM Data of **8**.

	ρ (a.u.)	∇^2	Distance (Å)
Os-C	0.121808	0.174665	1.11952
Os-H_t	0.158264	0.051555	1.09078

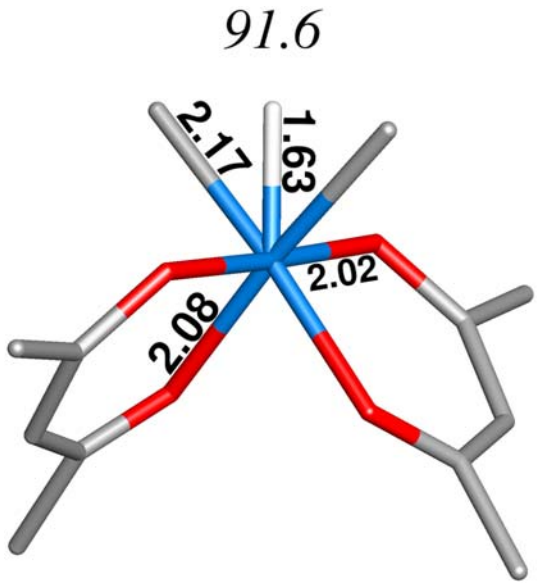

Figure B-17. B3LYP/DZP optimized geometry of **9**. E_{SCF} = -899.676826899 hartrees

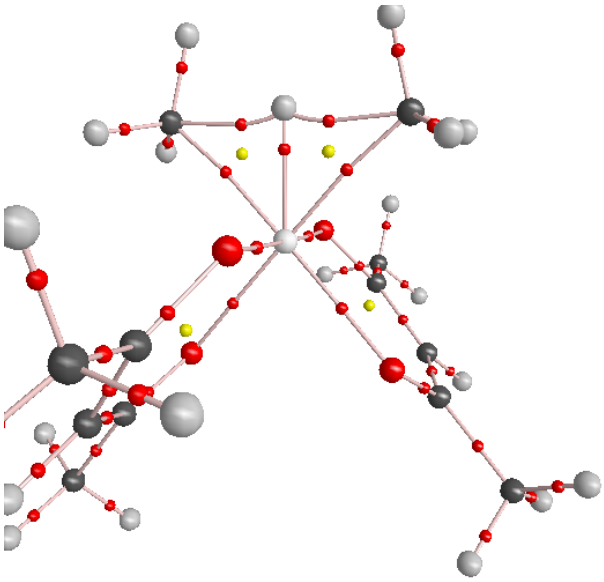

Figure B-18. Representation of the AIM CPs of **9**.

Basis Sets: Opt and Freq	Basis Sets: AIM analysis
Pt: LANL2DZ(f)	Pt: WTBS
O: cc-pVDZ	O: cc-pVDZ
Ligated carbons: cc-pVDZ	Ligated carbons: cc-pVDZ
H being transferred: cc-pVDZ	H being transferred: cc-pVDZ
All other C and H: D95	All other C and H: D95

Table B-16. Optimized geometric coordinates of **9**.

78	0.000000	0.000000	0.628507
8	-0.221818	2.010647	0.662715
8	1.396682	0.008686	-0.913767
8	-1.396682	-0.008686	-0.913767
8	0.221818	-2.010647	0.662715
6	1.555636	0.087818	2.143435
6	-1.555636	-0.087818	2.143435
6	0.384555	2.790009	-0.198561
6	1.303469	2.410346	-1.191539
6	1.762084	1.103683	-1.498243
6	-1.762084	-1.103683	-1.498243
6	-1.303469	-2.410346	-1.191539
6	-0.384555	-2.790009	-0.198561
6	0.000000	4.243493	-0.032605
6	2.778165	0.906129	-2.601155
6	-2.778165	-0.906129	-2.601155
6	0.000000	-4.243493	-0.032605
1	0.127589	4.550194	1.012199
1	0.593332	4.896001	-0.676358
1	-1.061908	4.370982	-0.279790
1	3.668007	0.406769	-2.198212
1	2.361393	0.244472	-3.370884
1	3.074621	1.850120	-3.062816
1	-3.668007	-0.406769	-2.198212
1	-2.361393	-0.244472	-3.370884
1	-3.074621	-1.850120	-3.062816
1	-0.127589	-4.550194	1.012199
1	-0.593332	-4.896001	-0.676358
1	1.061908	-4.370982	-0.279790
1	1.709192	3.212220	-1.794730
1	-1.709192	-3.212220	-1.794730
1	-2.014188	-1.060879	1.964998
1	-1.335832	0.013149	3.217031
1	-2.167220	0.757900	1.827864
1	2.167220	-0.757900	1.827864
1	2.014188	1.060879	1.964998
1	1.335832	-0.013149	3.217031
1	0.000000	0.000000	2.258724

Table B-17. AIM Data of **9**.

	ρ (a.u.)	∇^2	Distance (Å)
Pt-C	0.098688	0.157931	1.179723
Pt-H_t	0.130878	0.160979	1.138435
C-H	0.103731	-0.030184	0.988517
RCP	0.095016	0.147549	1.123083

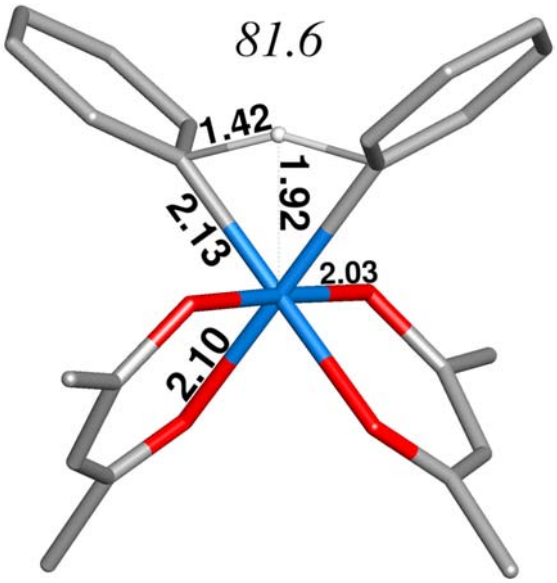

Figure B-17. B3LYP/DZP optimized geometry of **10**. E_{SCF} = -1273.19407755 hartrees

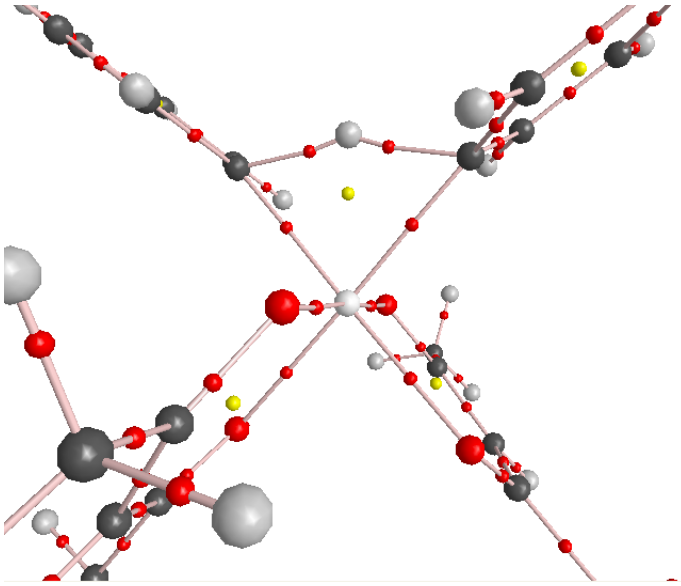

Basis Sets: Opt and Freq	Basis Sets: AIM analysis
Pt: LANL2DZ(f)	Pt: WTBS
O: cc-pVDZ	O: cc-pVDZ
phenyl carbons: cc-pVDZ	phenyl carbons: cc-pVDZ
H being transferred: cc-pVDZ	H being transferred: cc-pVDZ
All other C and H: D95	All other C and H: D95

Table B-18. Optimized geometric coordinates of **10**.

78	-0.000189	-0.150572	-0.000057
8	0.940128	-0.180700	-1.797364
8	1.188246	-1.693337	0.791264
8	-1.191638	-1.690646	-0.792062
8	-0.940493	-0.179639	1.797257
6	1.223998	1.456704	0.659546
6	-1.221285	1.459362	-0.658836
6	1.818640	-1.103778	-2.113033
6	2.359474	-2.091500	-1.280468
6	2.059730	-2.326364	0.090031
6	-2.064242	-2.322344	-0.091032
6	-2.363374	-2.087603	1.279630
6	-1.820582	-1.101329	2.112630
6	2.257864	-1.009012	-3.559367
6	2.819685	-3.398818	0.841994
6	-2.826496	-3.392852	-0.843443
6	-2.259082	-1.006800	3.559196
6	1.217157	1.787814	2.032633
6	2.205300	2.626644	2.547411
6	3.200934	3.142205	1.706571
6	3.207010	2.827191	0.342432
6	2.226303	1.985483	-0.184473
6	-1.213165	1.791728	-2.031605
6	-2.199625	2.632684	-2.546144
6	-3.194851	3.149120	-1.705363
6	-3.202176	2.832853	-0.341522
6	-2.223150	1.989034	0.185142
1	0.001583	1.772387	0.000699
1	2.619850	0.002653	-3.780352
1	3.045704	-1.728534	-3.791783
1	1.399126	-1.198339	-4.216140
1	3.515608	-2.923318	1.546198
1	2.123601	-4.003657	1.433491
1	3.390143	-4.046168	0.171883
1	-3.523525	-2.915495	-1.545313
1	-2.132106	-3.997133	-1.437463
1	-3.396166	-4.040928	-0.173356
1	-2.615754	0.006306	3.782095
1	-3.050478	-1.722758	3.790543
1	-1.401158	-1.201764	4.215417
1	3.098371	-2.743483	-1.728818
1	-3.103425	-2.738441	1.727748
1	2.217357	1.758437	-1.246290

(Table B-18 continued)

1	3.973372	3.239019	-0.310617
1	3.968255	3.797132	2.114430
1	2.202910	2.876464	3.606227
1	0.448608	1.382785	2.683436
1	-2.215185	1.760985	1.246747
1	-3.968209	3.245339	0.311498
1	-3.960870	3.805692	-2.113025
1	-2.196248	2.883466	-3.604730
1	-0.444969	1.385983	-2.682382

Table B-19. AIM Data of **10**.

	ρ (a.u.)	∇^2	Distance (Å)
Pt-C	0.110913	0.149121	1.152977
C-H	0.122552	-0.119840	0.927599
RCP	0.073929	0.226839	1.251005

AIM images for altering geometric parameters of **9**

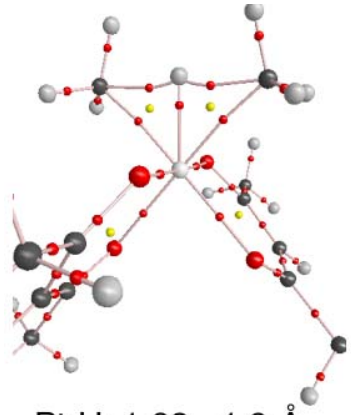

Pt-H: 1.63 - 1.9 Å

C-H: 1.68 Å

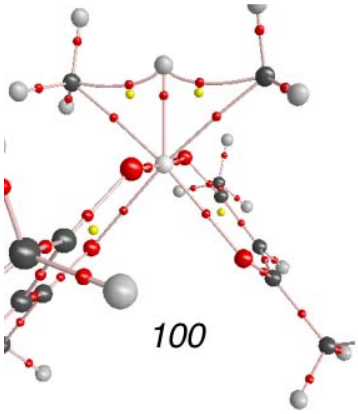

100

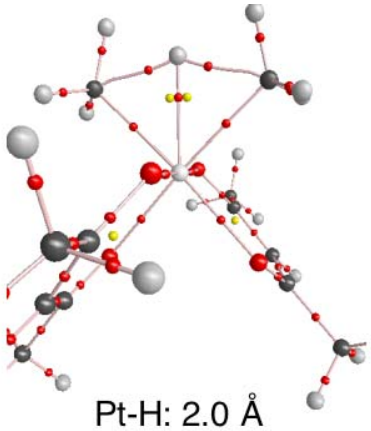

Pt-H: 2.0 Å

C-H: 1.71Å

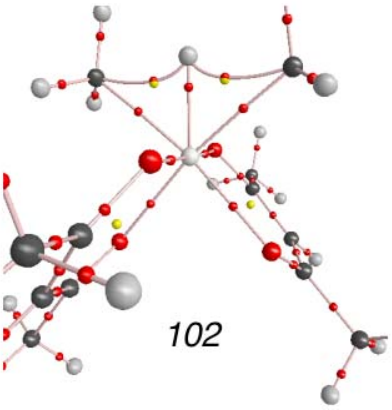

102

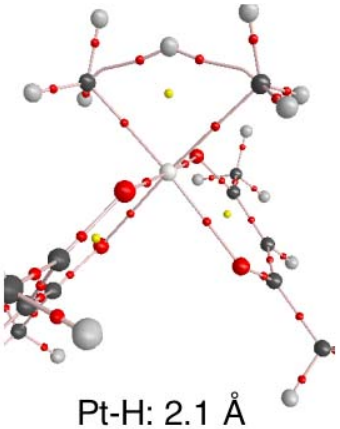

Pt-H: 2.1 Å

C-H: 1.72Å

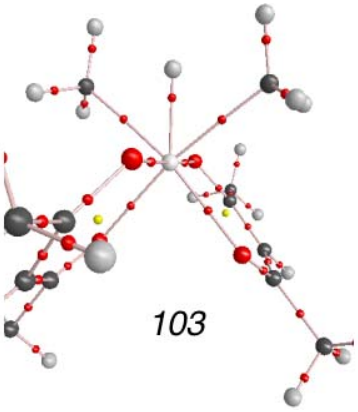

103

APPENDIX C

SUPPLEMENTAL MATERIAL FOR CHAPTER IV

Table C-1. Optimized geometric coordinates of **1**.

1	21	0	-0.002203	0.189637	-0.000199
2	6	0	0.033761	2.120808	-1.440605
3	6	0	0.033330	2.119762	1.441013
4	1	0	0.025073	2.085237	-0.000046
5	6	0	-1.900703	-0.991561	1.142860
6	6	0	-2.417508	0.268311	0.726341
7	6	0	-2.427539	0.291319	-0.691377
8	6	0	2.524137	0.442971	0.009947
9	6	0	2.193468	-0.312817	-1.146225
10	6	0	1.643477	-1.551508	-0.720757
11	6	0	-1.607304	-1.750854	-0.021305
12	6	0	-1.917596	-0.954499	-1.155702
13	6	0	2.186022	-0.330821	1.152196
14	6	0	1.639206	-1.562722	0.703927
15	1	0	-1.768953	-1.321605	2.169635
16	1	0	-2.741664	1.071267	1.379595
17	1	0	-2.760810	1.114951	-1.313537
18	1	0	2.942848	1.444030	0.019073
19	1	0	2.327643	0.006305	-2.175487
20	1	0	1.295703	-2.351429	-1.367057
21	1	0	0.966983	2.669937	-1.623826
22	1	0	-0.041401	1.350617	-2.230558
23	1	0	-0.811134	2.804974	-1.595846
24	1	0	-1.199485	-2.756199	-0.040637
25	1	0	-1.800246	-1.251123	-2.194396
26	1	0	2.314235	-0.027913	2.187132
27	1	0	1.287237	-2.372491	1.335504
28	1	0	-0.033463	1.348142	2.230389
29	1	0	0.963234	2.675051	1.622597
30	1	0	-0.816052	2.797524	1.599758

Basis Sets: Opt and Freq
Sc: LANL2mDZ(f)
C, 4: aug-cc-pVDZ
15 → 30: D95

Basis Sets: AIM Analysis
Sc: WTBS
C, 4: cc-pVDZ
15 → 30: D95

Table C-2. Optimized geometric coordinates of **2**.

1	39	0	-0.001682	0.174934	-0.000162
2	6	0	0.032700	2.271889	-1.454562
3	6	0	0.032374	2.271659	1.454635
4	1	0	0.026409	2.234080	0.000216
5	6	0	-2.080968	-1.074448	1.144616
6	6	0	-2.594557	0.187379	0.727097
7	6	0	-2.604788	0.209357	-0.693096
8	6	0	2.694373	0.369921	0.010610
9	6	0	2.368954	-0.388417	-1.147194
10	6	0	1.829729	-1.635002	-0.721254
11	6	0	-1.782286	-1.834802	-0.020364
12	6	0	-2.097546	-1.038782	-1.156675
13	6	0	2.361522	-0.407599	1.153579
14	6	0	1.825432	-1.646946	0.703514
15	1	0	-1.974592	-1.413550	2.171924
16	1	0	-2.931717	0.986470	1.380310
17	1	0	-2.950600	1.028273	-1.316532
18	1	0	3.127927	1.365370	0.020362
19	1	0	2.522827	-0.076775	-2.176766
20	1	0	1.508036	-2.446960	-1.367349
21	1	0	0.958697	2.832090	-1.644181
22	1	0	-0.031355	1.506439	-2.255760
23	1	0	-0.817241	2.948072	-1.620638
24	1	0	-1.393694	-2.848763	-0.038954
25	1	0	-2.005745	-1.345700	-2.195462
26	1	0	2.509004	-0.113253	2.189191
27	1	0	1.499370	-2.469435	1.333886
28	1	0	-0.027049	1.505872	2.255872
29	1	0	0.956074	2.836003	1.643109
30	1	0	-0.820378	2.944077	1.621665

Basis Sets: Opt and Freq
Y: LANL2mDZ(f)
C, 4: aug-cc-pVDZ
15 → 30: D95

Basis Sets: AIM Analysis
Y: WTBS
C, 4: cc-pVDZ
15 → 30: D95

Table C-3. Optimized geometric coordinates of **3**.

1	71	0	0.000612	0.160210	-0.003656
2	6	0	0.005076	2.482450	1.458069
3	6	0	0.006839	2.493081	-1.449013
4	1	0	0.022696	2.402947	0.004221
5	6	0	2.292577	-1.176312	-1.145846
6	6	0	2.807253	0.080856	-0.717505
7	6	0	2.809632	0.093384	0.703476
8	6	0	2.903774	0.302452	-0.028649
9	6	0	2.592516	-0.441560	1.142341
10	6	0	-2.072364	-1.704254	0.737970
11	6	0	1.980032	-1.942470	0.012281
12	6	0	2.296447	-1.155931	1.155620
13	6	0	-2.576775	-0.497702	-1.157613
14	6	0	-2.062708	-1.738979	-0.685108
15	1	0	2.199405	-1.511571	-2.176138
16	1	0	3.158094	0.880788	-1.363577
17	1	0	3.161756	0.904804	1.334301
18	1	0	-3.330709	1.301067	-0.056203
19	1	0	-2.754660	-0.115226	2.166596
20	1	0	-1.776663	-2.515778	1.397978
21	1	0	-0.953992	2.982314	1.655932
22	1	0	0.157625	1.763542	2.289852
23	1	0	0.804164	3.228945	1.570439
24	1	0	1.602757	-2.961547	0.021942
25	1	0	2.206338	-1.472701	2.192014
26	1	0	-2.726369	-0.222443	-2.198740
27	1	0	-1.759447	-2.581890	-1.300744
28	1	0	0.161358	1.780054	-2.285563
29	1	0	-0.951783	2.994397	-1.645258
30	1	0	0.806241	3.240254	-1.554795

Basis Sets: Opt and Freq
La: LANL2mDZ(f)
C, 4: aug-cc-pVDZ
15 → 30: D95

Basis Sets: AIM Analysis
La: WTBS
C, 4: cc-pVDZ
15 → 30: D95

Table C-4. Optimized geometric coordinates of **4**.

1	77	0	-0.037875	0.081606	0.077989
2	15	0	-1.885223	-1.241262	-0.399939
3	6	0	-0.935751	0.429929	1.966578
4	6	0	-1.539480	2.172602	-0.940602
5	1	0	-0.832171	1.827834	-0.107291
6	6	0	1.955321	-0.151176	0.991300
7	6	0	1.546685	-1.340208	0.269350
8	6	0	1.555671	-1.015812	-1.157571
9	6	0	1.820971	0.357945	-1.280887
10	6	0	2.050631	0.908562	0.053253
11	1	0	-2.824374	-1.477870	0.633837
12	1	0	-1.605918	-2.566776	-0.808679
13	1	0	-2.755570	-0.839888	-1.445182
14	1	0	2.298835	1.939981	0.279091
15	1	0	1.834347	0.925697	-2.205101
16	1	0	1.338603	-1.703227	-1.967469
17	1	0	1.432022	-2.329598	0.698787
18	1	0	2.080006	-0.074181	2.065647
19	1	0	-0.366786	1.205493	2.492330
20	1	0	-1.977642	0.764437	1.882396
21	1	0	-0.918476	-0.483121	2.573370
22	1	0	-1.397696	1.682367	-1.903464
23	1	0	-2.563617	2.062037	-0.578810
24	1	0	-1.271103	3.231059	-1.024043

Basis Sets: Opt and Freq
Ir: LANL2mDZ(f)
P, 3 → 10: cc-pVDZ
11 → 24: D95

Basis Sets: AIM Analysis
Ir: WTBS
P, 3 → 10: cc-pVDZ
11 → 24: D95

Table C-5. Optimized geometric coordinates of **5**.

1	77	0	0.058756	0.060731	-0.155989
2	15	0	2.046804	-0.364695	0.948741
3	6	0	0.935066	-1.287868	-1.597959
4	6	0	0.956544	2.110710	-0.523115
5	1	0	0.601035	0.903291	-1.406075
6	6	0	-1.887498	1.006496	0.670514
7	6	0	-1.443986	0.032763	1.598821
8	6	0	-1.406958	-1.250115	0.919359
9	6	0	-1.890456	-1.046497	-0.416085
10	6	0	-2.141264	0.349366	-0.593573
11	1	0	-1.993765	2.068835	0.862680
12	1	0	-1.176625	0.213278	2.634310
13	1	0	-1.163883	-2.206273	1.368988
14	1	0	-1.993725	-1.811371	-1.177738
15	1	0	-2.517382	0.820775	-1.494537
16	1	0	2.368573	-1.721417	1.190014
17	1	0	3.230126	0.074365	0.308736
18	1	0	2.231723	0.187433	2.240011
19	1	0	0.331014	-1.263022	-2.509094
20	1	0	1.965873	-1.035287	-1.868169
21	1	0	0.911828	-2.299578	-1.179554
22	1	0	0.305399	2.761234	-1.112338
23	1	0	0.974822	2.472464	0.508240
24	1	0	1.970051	2.140304	-0.933196

Basis Sets: Opt and Freq
Ir: LANL2mDZ(f)
P, 3 → 10: cc-pVDZ
11 → 24: D95

Basis Sets: AIM Analysis
Ir: WTBS
P, 3 → 10: cc-pVDZ
11 → 24: D95

Table C-6. Optimized geometric coordinates of **6**.

1	77	0	0.066857	0.000012	-0.211169
2	15	0	2.139327	0.000165	0.825222
3	6	0	0.817144	-1.966123	-0.787710
4	6	0	0.816753	1.966269	-0.787802
5	1	0	0.542596	0.000010	-1.706560
6	6	0	-1.632367	1.153745	0.850712
7	6	0	-1.415939	0.000634	1.661659
8	6	0	-1.631341	-1.153584	0.851950
9	6	0	-2.033620	-0.716610	-0.463626
10	6	0	-2.034226	0.715063	-0.464394
11	1	0	-1.534220	2.184645	1.171737
12	1	0	-1.109941	0.001392	2.702366
13	1	0	-1.532180	-2.184030	1.174102
14	1	0	-2.310989	-1.355087	-1.294501
15	1	0	-2.312105	1.352423	-1.295958
16	1	0	2.438072	-1.094679	1.670395
17	1	0	3.263419	-0.000835	-0.032139
18	1	0	2.438814	1.095952	1.668909
19	1	0	0.121402	-2.380922	-1.519866
20	1	0	1.807925	-1.921168	-1.246736
21	1	0	0.851510	-2.610375	0.096031
22	1	0	0.121090	2.380664	-1.520261
23	1	0	0.850605	2.610629	0.095873
24	1	0	1.807714	1.921576	-1.246473

Basis Sets: Opt and Freq
Ir: LANL2mDZ(f)
P, 3 → 10: cc-pVDZ
11 → 24: D95

Basis Sets: AIM Analysis
Ir: WTBS
P, 3 → 10: cc-pVDZ
11 → 24: D95

Table C-7. Optimized geometric coordinates of **7**.

1	77	0	0.052086	-0.587206	-0.167647
2	8	0	1.859977	-0.759680	0.741922
3	8	0	0.459766	1.143632	-1.065551
4	8	0	-0.646540	0.565039	1.556425
5	8	0	-1.777143	-0.470578	-1.074036
6	6	0	0.770001	-1.600952	-1.829348
7	6	0	-0.497431	-2.561443	1.295641
8	6	0	2.788003	0.123828	0.608011
9	6	0	2.707259	1.302425	-0.174270
10	6	0	1.602410	1.742525	-0.931836
11	6	0	-1.815505	1.081183	1.591744
12	6	0	-2.831991	0.939887	0.604150
13	6	0	-2.768876	0.218946	-0.608414
14	6	0	4.056442	-0.176727	1.384835
15	6	0	1.681240	3.050157	-1.697327
16	6	0	-2.118425	1.918887	2.827838
17	6	0	-3.983187	0.207773	-1.523707
18	1	0	4.463734	-1.144916	1.067239
19	1	0	3.822599	-0.255374	2.454236
20	1	0	4.817699	0.594936	1.242468
21	1	0	3.583365	1.939991	-0.182871
22	1	0	2.652645	3.536939	-1.576422
23	1	0	1.501540	2.864091	-2.763583
24	1	0	0.892921	3.729267	-1.348706
25	1	0	-1.417315	2.762335	2.874963
26	1	0	-1.956808	1.314315	3.729335
27	1	0	-3.141872	2.305082	2.831631
28	1	0	-3.767573	1.449997	0.803600
29	1	0	-3.722469	0.682619	-2.478481
30	1	0	-4.836104	0.732941	-1.085039
31	1	0	-4.269627	-0.827975	-1.744917
32	1	0	1.383410	-0.923981	-2.441619
33	1	0	-0.070782	-1.947229	-2.446727
34	1	0	1.391203	-2.464988	-1.550350
35	1	0	0.468922	-2.464764	1.788428
36	1	0	-1.291082	-2.062430	1.849858
37	1	0	-0.743041	-3.622913	1.160296
38	1	0	-0.480096	-2.289326	0.171514

Basis Sets: Optimization and Frequency
Ir: LANL2mDZ(f)
O, 6, 7, 38: cc-pVDZ
8 → 37: D95

Basis Sets: Bader's Analysis
Ir: WTBS
O, 6, 7, 38: cc-pVDZ
8 → 37: D95

Table C-8. Optimized geometric coordinates of **8**.

1	77	0	0.021039	-0.693724	-0.006304
2	8	0	-1.842198	-0.731863	-0.842650
3	8	0	-0.495911	0.941468	1.315241
4	8	0	0.431746	0.930727	-1.263110
5	8	0	1.881521	-0.685214	0.829109
6	6	0	-0.643453	-1.883614	1.681770
7	6	0	0.700446	-1.866551	-1.618114
8	6	0	-2.775719	0.109129	-0.540925
9	6	0	-2.730945	1.145514	0.419761
10	6	0	-1.647283	1.506138	1.263047
11	6	0	1.570000	1.534873	-1.247812
12	6	0	2.689152	1.212080	-0.443774
13	6	0	2.789214	0.176093	0.515653
14	6	0	-4.047238	-0.092091	-1.348770
15	6	0	-1.827568	2.671568	2.224594
16	6	0	1.665982	2.703857	-2.213438
17	6	0	4.081688	0.010841	1.295886
18	1	0	-4.387721	-1.130110	-1.248325
19	1	0	-4.847529	0.582764	-1.033416
20	1	0	-3.833557	0.078011	-2.411896
21	1	0	-1.652332	2.327972	3.252043
22	1	0	-1.073737	3.439543	2.008687
23	1	0	-2.823673	3.118238	2.159418
24	1	0	1.473638	2.351180	-3.234660
25	1	0	0.886830	3.438701	-1.973952
26	1	0	2.643475	3.192562	-2.179250
27	1	0	4.457968	-1.012386	1.173833
28	1	0	4.850304	0.718368	0.973499
29	1	0	3.884339	0.159711	2.365291
30	1	0	-3.632318	1.739178	0.518675
31	1	0	3.567574	1.834022	-0.569679
32	1	0	1.543737	-2.514481	-1.350015
33	1	0	-0.112264	-2.471654	-2.036638
34	1	0	1.025655	-1.147664	-2.379111
35	1	0	-0.820909	-1.076880	2.399034
36	1	0	-1.575216	-2.428567	1.496122
37	1	0	0.110921	-2.557940	2.102580
38	1	0	-0.052061	-2.231769	0.217202

Basis Sets: Optimization and Frequency
Ir: LANL2mDZ(f)
O, 6, 7, 38: cc-pVDZ
8 → 37: D95

Basis Sets: Bader's Analysis
Ir: WTBS
O, 6, 7, 38: cc-pVDZ
8 → 37: D95

Table C-9. Optimized geometric coordinates of **9**.

1	77	0	0.000000	0.000000	0.710896
2	8	0	-0.214629	2.029753	0.721039
3	8	0	1.350389	0.035809	-0.945508
4	8	0	-1.350389	-0.035809	-0.945508
5	8	0	0.214629	-2.029753	0.721039
6	6	0	1.808213	0.121364	1.824017
7	6	0	-1.808213	-0.121364	1.824017
8	6	0	0.355786	2.806787	-0.138095
9	6	0	1.234944	2.438410	-1.183433
10	6	0	1.669347	1.134849	-1.531847
11	6	0	-1.669347	-1.134849	-1.531847
12	6	0	-1.234944	-2.438410	-1.183433
13	6	0	-0.355786	-2.806787	-0.138095
14	6	0	0.000000	4.272342	0.045668
15	6	0	2.617727	0.967567	-2.708409
16	6	0	-2.617727	-0.967567	-2.708409
17	6	0	0.000000	-4.272342	0.045668
18	1	0	0.216495	4.578166	1.076643
19	1	0	0.546876	4.919187	-0.645532
20	1	0	-1.077434	4.408173	-0.114290
21	1	0	3.548131	0.498476	-2.363418
22	1	0	2.168067	0.288759	-3.444092
23	1	0	2.853606	1.918898	-3.193244
24	1	0	-3.548131	-0.498476	-2.363418
25	1	0	-2.168067	-0.288759	-3.444092
26	1	0	-2.853606	-1.918898	-3.193244
27	1	0	-0.216495	-4.578166	1.076643
28	1	0	-0.546876	-4.919187	-0.645532
29	1	0	1.077434	-4.408173	-0.114290
30	1	0	1.613014	3.249448	-1.794792
31	1	0	-1.613014	-3.249448	-1.794792
32	1	0	-1.876749	-1.030175	2.432286
33	1	0	-1.964166	0.762594	2.451786
34	1	0	-2.578173	-0.138350	1.046094
35	1	0	2.578173	0.138350	1.046094
36	1	0	1.876749	1.030175	2.432286
37	1	0	1.964166	-0.762594	2.451786
38	1	0	0.000000	0.000000	2.254810

Basis Sets: Optimization and Frequency
Ir: LANL2mDZ(f)
O, 6, 7, 38: cc-pVDZ
8 → 37: D95

Basis Sets: Bader's Analysis
Ir: WTBS
O, 6, 7, 38: cc-pVDZ
8 → 37: D95

Table C-10. Optimized geometric coordinates of **10**.

1	26	0	-0.699794	-0.175248	-0.105350
2	8	0	-0.910324	-0.744368	-2.004624
3	8	0	-0.502111	-2.072964	0.528598
4	8	0	-2.677222	-0.445579	0.077823
5	8	0	-0.476620	0.292665	1.819033
6	6	0	1.409572	0.030040	-0.470870
7	6	0	-0.909429	1.836522	-0.647190
8	1	0	0.197812	0.981994	-0.575388
9	6	0	-0.996582	-1.952351	-2.401956
10	6	0	-0.872368	-3.117499	-1.601586
11	6	0	-0.631014	-3.106646	-0.201525
12	6	0	-3.314840	-0.401611	1.175077
13	6	0	-2.760426	-0.130692	2.457566
14	6	0	-1.399457	0.180678	2.695865
15	6	0	-1.256403	-2.124436	-3.899830
16	6	0	-0.504266	-4.446518	0.527012
17	6	0	-4.819201	-0.663088	1.072537
18	6	0	-0.951738	0.429705	4.137455
19	6	0	3.781523	0.449739	0.403986
20	6	0	4.614511	1.368174	-0.278380
21	6	0	5.982601	1.103292	-0.485168
22	6	0	6.553975	-0.092407	-0.006299
23	6	0	5.738463	-1.017490	0.678500
24	6	0	4.372243	-0.746928	0.878792
25	6	0	2.296764	0.717847	0.595194
26	6	0	-0.873761	2.874068	0.312463
27	6	0	-1.385802	2.176786	-1.934047
28	6	0	-1.853792	3.471089	-2.237367
29	6	0	-1.835684	4.482736	-1.254590
30	6	0	-1.336541	4.174982	0.027005
31	1	0	-0.470772	-1.608273	-4.467908
32	1	0	-1.286306	-3.177776	-4.199920
33	1	0	-2.213301	-1.649790	-4.156584
34	1	0	0.482084	-4.509202	1.006552
35	1	0	-1.258105	-4.495155	1.324411
36	1	0	-0.632634	-5.302486	-0.145070
37	1	0	-5.281091	0.125971	0.463374
38	1	0	-4.986630	-1.616996	0.555072
39	1	0	-5.307659	-0.689787	2.053326
40	1	0	-0.483554	1.420918	4.210581
41	1	0	-1.782689	0.369918	4.849140
42	1	0	-0.189643	-0.312492	4.412042
43	1	0	-0.965211	-4.080625	-2.093333
44	1	0	-3.428507	-0.158161	3.312694
45	1	0	4.179878	2.294654	-0.651550
46	1	0	6.600278	1.827292	-1.015147
47	1	0	7.611380	-0.299612	-0.162739
48	1	0	6.167302	-1.945424	1.054607
49	1	0	3.746651	-1.467427	1.403658
50	1	0	1.552086	-1.055933	-0.425960
51	1	0	1.725885	0.343129	-1.480300
52	1	0	2.121905	1.805103	0.573020
53	1	0	1.971233	0.368224	1.582852
54	1	0	-0.489233	2.654637	1.306252
55	1	0	-1.307508	4.941825	0.801855
56	1	0	-2.197638	5.485084	-1.482984
57	1	0	-2.233283	3.687609	-3.236775
58	1	0	-1.407947	1.405255	-2.699188

Basis Sets: Optimization and Frequency
Fe: LANL2mDZ(f)
O, 6, 7, 8: cc-pVDZ
9 → 58: D95

Basis Sets: Bader's Analysis
Fe: WTBS
O, 6, 7, 8: cc-pVDZ
9 → 58: D95

Table C-11. Optimized geometric coordinates of **11**.

1	27	0	-0.700476	-0.180592	-0.094331
2	8	0	-0.857847	-0.640086	-1.953850
3	8	0	-0.514428	-2.053610	0.483693
4	8	0	-2.640376	-0.376906	0.021133
5	8	0	-0.444067	0.220814	1.758059
6	6	0	1.398305	0.054361	-0.431460
7	6	0	-0.815526	1.830696	-0.574493
8	1	0	0.272764	0.986096	-0.528412
9	6	0	-1.038996	-1.833667	-2.403736
10	6	0	-1.011376	-3.024120	-1.649153
11	6	0	-0.733733	-3.071476	-0.260453
12	6	0	-3.290822	-0.373435	1.119978
13	6	0	-2.727342	-0.185504	2.409984
14	6	0	-1.367818	0.089335	2.650459
15	6	0	-1.290703	-1.904918	-3.901206
16	6	0	-0.660270	-4.418324	0.441409
17	6	0	-4.791627	-0.579740	0.986696
18	6	0	-0.883554	0.277431	4.078980
19	6	0	3.765448	0.483618	0.343731
20	6	0	4.628991	1.192054	-0.521353
21	6	0	5.972454	0.801557	-0.682030
22	6	0	6.475637	-0.308267	0.024187
23	6	0	5.624589	-1.021816	0.891906
24	6	0	4.282951	-0.627768	1.048036
25	6	0	2.303461	0.887230	0.495922
26	6	0	-0.759322	2.809060	0.436248
27	6	0	-1.306923	2.185546	-1.844090
28	6	0	-1.766934	3.493483	-2.091567
29	6	0	-1.727018	4.465083	-1.072081
30	6	0	-1.216570	4.119054	0.193758
31	1	0	-0.470510	-1.411542	-4.437882
32	1	0	-1.383308	-2.935546	-4.254671
33	1	0	-2.213383	-1.360129	-4.140276
34	1	0	0.330385	-4.541003	0.897490
35	1	0	-1.396808	-4.444039	1.254710
36	1	0	-0.847326	-5.252408	-0.240878
37	1	0	-5.224079	0.262487	0.430940
38	1	0	-4.985994	-1.488284	0.403619
39	1	0	-5.287784	-0.657173	1.958460
40	1	0	-0.388365	1.251852	4.179387
41	1	0	-1.700768	0.213822	4.802751
42	1	0	-0.136955	-0.492548	4.313025
43	1	0	-1.180804	-3.959003	-2.169002
44	1	0	-3.390689	-0.238308	3.264690
45	1	0	4.248605	2.054105	-1.067330
46	1	0	6.623035	1.361436	-1.350487
47	1	0	7.513566	-0.610137	-0.096543
48	1	0	6.006146	-1.876943	1.445723
49	1	0	3.631932	-1.181442	1.723154
50	1	0	1.474330	-1.008065	-0.192428
51	1	0	1.640800	0.188347	-1.493096
52	1	0	2.194880	1.957290	0.270455
53	1	0	1.973030	0.737796	1.530267
54	1	0	-0.359816	2.555820	1.412826
55	1	0	-1.171816	4.860357	0.988819
56	1	0	-2.084208	5.474945	-1.262157
57	1	0	-2.155681	3.748436	-3.075357
58	1	0	-1.344383	1.441239	-2.631165

Basis Sets: Optimization and Frequency
Co: LANL2mDZ(f)
O, 6, 7, 8: cc-pVDZ
9 → 58: D95

Basis Sets: Bader's Analysis
Co: WTBS
O, 6, 7, 8: cc-pVDZ
9 → 58: D95

Table C-12. Optimized geometric coordinates of **12**.

1	28	0	-0.750540	-0.169326	-0.084767
2	8	0	-0.814042	-0.545081	-1.924585
3	8	0	-0.504262	-2.075550	0.407077
4	8	0	-2.695496	-0.283381	-0.045931
5	8	0	-0.513228	0.149918	1.739742
6	6	0	1.518622	0.185606	-0.378188
7	6	0	-0.697738	1.882028	-0.492707
8	1	0	0.415119	1.000793	-0.435261
9	6	0	-1.120457	-1.712260	-2.424300
10	6	0	-1.166185	-2.926031	-1.728120
11	6	0	-0.800875	-3.058226	-0.362161
12	6	0	-3.362863	-0.349028	1.046472
13	6	0	-2.805129	-0.287034	2.351981
14	6	0	-1.451423	-0.049502	2.623193
15	6	0	-1.413302	-1.669325	-3.911311
16	6	0	-0.695297	-4.436490	0.260247
17	6	0	-4.864395	-0.483481	0.876307
18	6	0	-0.956449	0.016975	4.054795
19	6	0	3.816258	0.485967	0.360642
20	6	0	4.680429	1.011876	-0.628546
21	6	0	5.979138	0.496443	-0.785447
22	6	0	6.423660	-0.559339	0.035786
23	6	0	5.564756	-1.095492	1.017284
24	6	0	4.266551	-0.580574	1.174132
25	6	0	2.403428	1.042791	0.526290
26	6	0	-0.649053	2.782074	0.579938
27	6	0	-1.110891	2.256958	-1.775536
28	6	0	-1.518135	3.591206	-1.981504
29	6	0	-1.496555	4.515821	-0.919139
30	6	0	-1.058780	4.112414	0.357152
31	1	0	-0.582331	-1.193156	-4.445833
32	1	0	-1.575263	-2.669143	-4.320191
33	1	0	-2.310123	-1.061558	-4.088162
34	1	0	0.356537	-4.658425	0.483862
35	1	0	-1.239634	-4.454761	1.211492
36	1	0	-1.085242	-5.215255	-0.399445
37	1	0	-5.265625	0.445968	0.451607
38	1	0	-5.086711	-1.287937	0.166135
39	1	0	-5.366211	-0.683220	1.825964
40	1	0	-0.430949	0.963469	4.231536
41	1	0	-1.776392	-0.075939	4.770219
42	1	0	-0.237181	-0.793564	4.228369
43	1	0	-1.424681	-3.820153	-2.279635
44	1	0	-3.476260	-0.399476	3.193075
45	1	0	4.346396	1.834610	-1.258287
46	1	0	6.642122	0.917145	-1.536581
47	1	0	7.428080	-0.956459	-0.084320
48	1	0	5.909052	-1.903114	1.657620
49	1	0	3.611283	-0.992085	1.940139
50	1	0	1.454206	-0.852543	-0.051200
51	1	0	1.717827	0.250343	-1.452560
52	1	0	2.365951	2.096806	0.230219
53	1	0	2.066569	0.961143	1.564282
54	1	0	-0.304206	2.477627	1.560400
55	1	0	-1.031027	4.820952	1.180516
56	1	0	-1.814963	5.541323	-1.085107
57	1	0	-1.851674	3.895739	-2.969869
58	1	0	-1.135198	1.544476	-2.589503

Basis Sets: Optimization and Frequency
Ni: LANL2mDZ(f)
O, 6, 7, 8: cc-pVDZ
9 → 58: D95

Basis Sets: Bader's Analysis
Ni: WTBS
O, 6, 7, 8: cc-pVDZ
9 → 58: D95

Table C-13. Optimized geometric coordinates of **13**.

1	44	0	0.560734	0.137084	-0.143295
2	8	0	0.866316	1.165248	-1.951257
3	8	0	-0.023644	2.036160	0.836318
4	8	0	2.516251	0.823545	0.474165
5	8	0	0.249350	-0.778053	1.715207
6	6	0	-1.572849	-0.012015	-0.572214
7	6	0	1.546763	-1.558182	-0.838679
8	1	0	-0.229852	-0.908845	-0.973136
9	6	0	0.742259	2.428460	-2.099396
10	6	0	0.340621	3.389080	-1.132055
11	6	0	-0.000264	3.154563	0.229130
12	6	0	2.998358	0.576299	1.627177
13	6	0	2.375788	-0.139601	2.686866
14	6	0	1.090014	-0.738857	2.680338
15	6	0	1.084984	2.929333	-3.504398
16	6	0	-0.391506	4.365335	1.083114
17	6	0	4.405526	1.128229	1.866245
18	6	0	0.614063	-1.438274	3.954111
19	6	0	-3.872291	-0.968670	0.011902
20	6	0	-4.691121	-1.496140	-1.014055
21	6	0	-6.078354	-1.251318	-1.042190
22	6	0	-6.680921	-0.470852	-0.035880
23	6	0	-5.878797	0.061535	0.994860
24	6	0	-4.493868	-0.185686	1.015211
25	6	0	-2.369824	-1.200791	0.026200
26	6	0	1.410016	-2.840667	-0.253821
27	6	0	2.479783	-1.452071	-1.898144
28	6	0	3.246854	-2.550839	-2.337870
29	6	0	3.099550	-3.815355	-1.731010
30	6	0	2.168883	-3.950260	-0.680558
31	1	0	0.500049	2.367384	-4.244129
32	1	0	0.890214	4.000522	-3.624922
33	1	0	2.146568	2.733739	-3.709269
34	1	0	-1.413410	4.226534	1.461356
35	1	0	0.274421	4.418053	1.954863
36	1	0	-0.337663	5.309029	0.528927
37	1	0	5.096348	0.667933	1.147108
38	1	0	4.406898	2.209796	1.676201
39	1	0	4.765513	0.937243	2.883258
40	1	0	0.439549	-2.502400	3.743248
41	1	0	1.337109	-1.350750	4.772201
42	1	0	-0.344151	-1.005317	4.270905
43	1	0	0.297932	4.420014	-1.470091
44	1	0	2.945945	-0.235083	3.605880
45	1	0	-4.232624	-2.100721	-1.795417
46	1	0	-6.685866	-1.668936	-1.843897
47	1	0	-7.752792	-0.280886	-0.053673
48	1	0	-6.332096	0.666277	1.778944
49	1	0	-3.878790	0.231513	1.810895
50	1	0	-1.881026	0.911803	-0.065321
51	1	0	-1.824123	0.105199	-1.637953
52	1	0	-2.135448	-2.120085	-0.532094
53	1	0	-2.019194	-1.354759	1.054759
54	1	0	0.699332	-2.974584	0.560919
55	1	0	2.030876	-4.916380	-0.192422
56	1	0	3.689341	-4.668144	-2.066879
57	1	0	3.958656	-2.416262	-3.154082
58	1	0	2.607796	-0.488320	-2.385969

Basis Sets: Optimization and Frequency
Ru: LANL2mDZ(f)
O, 6, 7, 8: cc-pVDZ
9 → 58: D95

Basis Sets: Bader's Analysis
Ru: WTBS
O, 6, 7, 8: cc-pVDZ
9 → 58: D95

Table C-14. Optimized geometric coordinates of **14**.

1	45	0	-0.663985	-0.145855	-0.101063
2	8	0	-0.875674	-0.731716	-2.053713
3	8	0	-0.514751	-2.148426	0.575291
4	8	0	-2.739978	-0.433705	0.120579
5	8	0	-0.418336	0.373615	1.862473
6	6	0	1.513647	0.017190	-0.454888
7	6	0	-0.810163	1.886714	-0.682345
8	1	0	0.362831	1.007643	-0.613300
9	6	0	-0.979152	-1.968250	-2.414854
10	6	0	-0.895252	-3.116493	-1.599598
11	6	0	-0.668907	-3.155815	-0.196283
12	6	0	-3.335315	-0.320959	1.244075
13	6	0	-2.732678	0.002594	2.492492
14	6	0	-1.377588	0.305763	2.729043
15	6	0	-1.213972	-2.142658	-3.908129
16	6	0	-0.588662	-4.511503	0.492041
17	6	0	-4.838890	-0.556056	1.199741
18	6	0	-0.928175	0.612230	4.150067
19	6	0	3.851907	0.421680	0.416900
20	6	0	4.697765	1.192264	-0.412213
21	6	0	6.053868	0.851959	-0.578247
22	6	0	6.588077	-0.269411	0.086121
23	6	0	5.755147	-1.044912	0.917056
24	6	0	4.400229	-0.700472	1.079095
25	6	0	2.377328	0.772811	0.574257
26	6	0	-0.681899	2.923769	0.262673
27	6	0	-1.275211	2.193110	-1.975704
28	6	0	-1.645066	3.510545	-2.307784
29	6	0	-1.536886	4.541097	-1.352873
30	6	0	-1.050007	4.243212	-0.065600
31	1	0	-0.415079	-1.640608	-4.468192
32	1	0	-1.250358	-3.195779	-4.199537
33	1	0	-2.160780	-1.661398	-4.185253
34	1	0	0.378818	-4.606748	1.001065
35	1	0	-1.367377	-4.571526	1.263164
36	1	0	-0.710633	-5.343351	-0.207313
37	1	0	-5.309669	0.234155	0.600247
38	1	0	-5.044883	-1.510206	0.699811
39	1	0	-5.289724	-0.561928	2.196237
40	1	0	-0.450182	1.599616	4.184318
41	1	0	-1.760372	0.592017	4.858858
42	1	0	-0.176068	-0.124611	4.460193
43	1	0	-1.006643	-4.071243	-2.099835
44	1	0	-3.388846	0.024720	3.354669
45	1	0	4.293925	2.064079	-0.924920
46	1	0	6.690545	1.459612	-1.217703
47	1	0	7.636113	-0.532286	-0.038256
48	1	0	6.160542	-1.909184	1.438771
49	1	0	3.763554	-1.301087	1.727098
50	1	0	1.633000	-1.063616	-0.342596
51	1	0	1.789554	0.269562	-1.488217
52	1	0	2.242954	1.856942	0.454981
53	1	0	2.027987	0.515939	1.580325
54	1	0	-0.301426	2.705143	1.255985
55	1	0	-0.954408	5.029632	0.680122
56	1	0	-1.823951	5.558606	-1.608990
57	1	0	-2.016929	3.727660	-3.307021
58	1	0	-1.364151	1.403154	-2.714146

Basis Sets: Optimization and Frequency
Rh: LANL2mDZ(f)
O, 6, 7, 8: cc-pVDZ
9 → 58: D95

Basis Sets: Bader's Analysis
Rh: WTBS
O, 6, 7, 8: cc-pVDZ
9 → 58: D95

Table C-15. Optimized geometric coordinates of **15**.

1	46	0	-0.701096	-0.126670	-0.093083
2	8	0	-0.845847	-0.622701	-2.051061
3	8	0	-0.609360	-2.158698	0.513418
4	8	0	-2.788333	-0.289946	0.034518
5	8	0	-0.465633	0.307337	1.863299
6	6	0	1.596154	0.099948	-0.408691
7	6	0	-0.591599	1.939651	-0.623130
8	1	0	0.530403	1.038028	-0.542163
9	6	0	-1.073379	-1.847333	-2.453163
10	6	0	-1.099711	-3.018335	-1.684141
11	6	0	-0.848559	-3.131165	-0.286677
12	6	0	-3.401776	-0.227388	1.157841
13	6	0	-2.806150	-0.028444	2.435983
14	6	0	-1.452987	0.207422	2.714699
15	6	0	-1.314177	-1.923867	-3.950422
16	6	0	-0.840237	-4.507747	0.351710
17	6	0	-4.911165	-0.364350	1.063999
18	6	0	-1.000583	0.396215	4.151695
19	6	0	3.894902	0.369059	0.425308
20	6	0	4.792769	0.946614	-0.501297
21	6	0	6.100301	0.444846	-0.634575
22	6	0	6.521400	-0.645961	0.151431
23	6	0	5.630260	-1.230564	1.074028
24	6	0	4.323559	-0.728643	1.206552
25	6	0	2.471042	0.905335	0.560049
26	6	0	-0.482831	2.903098	0.394042
27	6	0	-0.977640	2.279540	-1.929007
28	6	0	-1.269762	3.626291	-2.218859
29	6	0	-1.173670	4.607528	-1.211704
30	6	0	-0.777049	4.246491	0.091123
31	1	0	-0.483070	-1.453105	-4.489118
32	1	0	-1.421898	-2.956416	-4.289361
33	1	0	-2.226627	-1.368343	-4.201833
34	1	0	0.110725	-4.666565	0.874324
35	1	0	-1.635216	-4.561925	1.106460
36	1	0	-0.987219	-5.305398	-0.379749
37	1	0	-5.331615	0.561871	0.649775
38	1	0	-5.169284	-1.176207	0.375846
39	1	0	-5.367158	-0.548428	2.039707
40	1	0	-0.467509	1.348814	4.258092
41	1	0	-1.843075	0.377894	4.846184
42	1	0	-0.298654	-0.403180	4.420456
43	1	0	-1.299357	-3.939115	-2.216708
44	1	0	-3.476235	-0.044786	3.285825
45	1	0	4.478072	1.797358	-1.103535
46	1	0	6.787555	0.903924	-1.340207
47	1	0	7.532350	-1.031845	0.050909
48	1	0	5.955578	-2.065298	1.689254
49	1	0	3.644512	-1.177351	1.930071
50	1	0	1.569042	-0.960559	-0.150412
51	1	0	1.835932	0.211745	-1.472303
52	1	0	2.442128	1.973632	0.316651
53	1	0	2.099923	0.778489	1.582165
54	1	0	-0.171665	2.628357	1.395440
55	1	0	-0.695238	4.999697	0.869844
56	1	0	-1.405763	5.644085	-1.440600
57	1	0	-1.574723	3.900616	-3.224958
58	1	0	-1.062782	1.523443	-2.700419

Basis Sets: Optimization and Frequency
Pd: LANL2mDZ(f)
O, 6, 7, 8: cc-pVDZ
9 → 58: D95

Basis Sets: Bader's Analysis
Pd: WTBS
O, 6, 7, 8: cc-pVDZ
9 →58: D95

Table C-16. Optimized geometric coordinates of **16**.

1	76	0	0.434863	0.119264	-0.182113
2	8	0	0.763489	1.296109	-1.851378
3	8	0	-0.024675	1.871969	1.010630
4	8	0	2.396529	0.780714	0.462733
5	8	0	0.127235	-0.910089	1.586350
6	6	0	-1.697696	0.143870	-0.453986
7	6	0	1.583478	-1.507806	-0.849909
8	1	0	-0.140795	-0.889033	-1.265644
9	6	0	0.712266	2.576621	-1.869290
10	6	0	0.354382	3.437755	-0.794071
11	6	0	0.013842	3.060756	0.526787
12	6	0	2.878512	0.452569	1.605519
13	6	0	2.260733	-0.349780	2.597401
14	6	0	0.972135	-0.945153	2.554813
15	6	0	1.087785	3.200709	-3.210182
16	6	0	-0.362430	4.157072	1.521679
17	6	0	4.271051	1.011994	1.887398
18	6	0	0.486403	-1.725252	3.772628
19	6	0	-3.981800	-0.965673	-0.092267
20	6	0	-4.761013	-1.236294	-1.242660
21	6	0	-6.153230	-1.022823	-1.252379
22	6	0	-6.803798	-0.532080	-0.102496
23	6	0	-6.042911	-0.256791	1.052661
24	6	0	-4.652060	-0.471941	1.053802
25	6	0	-2.473524	-1.155264	-0.096143
26	6	0	1.382015	-2.841689	-0.415714
27	6	0	2.674104	-1.302433	-1.731185
28	6	0	3.524252	-2.351427	-2.137847
29	6	0	3.308199	-3.666853	-1.679080
30	6	0	2.222200	-3.901836	-0.810379
31	1	0	0.548565	2.689389	-4.017505
32	1	0	0.862685	4.272280	-3.243300
33	1	0	2.162673	3.060783	-3.393114
34	1	0	-1.402096	4.012556	1.846088
35	1	0	0.271893	4.067955	2.413588
36	1	0	-0.255938	5.162066	1.098873
37	1	0	4.975563	0.609775	1.146620
38	1	0	4.256672	2.103524	1.766765
39	1	0	4.628117	0.762789	2.892799
40	1	0	0.315424	-2.774645	3.495476
41	1	0	1.204184	-1.689566	4.599075
42	1	0	-0.474259	-1.315481	4.112433
43	1	0	0.343621	4.501072	-1.013493
44	1	0	2.830173	-0.512028	3.507607
45	1	0	-4.264535	-1.614467	-2.135237
46	1	0	-6.728421	-1.239836	-2.151632
47	1	0	-7.880114	-0.367448	-0.105885
48	1	0	-6.533051	0.123084	1.948185
49	1	0	-4.068763	-0.253276	1.946990
50	1	0	-2.051799	0.941762	0.217378
51	1	0	-1.978837	0.444918	-1.477600
52	1	0	-2.204411	-1.941786	-0.817462
53	1	0	-2.134259	-1.495399	0.891161
54	1	0	0.547912	-3.054606	0.251312
55	1	0	2.025951	-4.909254	-0.440223
56	1	0	3.960801	-4.482097	-1.990903
57	1	0	4.353228	-2.138067	-2.814625
58	1	0	2.862274	-0.298165	-2.104451

Basis Sets: Optimization and Frequency
Os: LANL2mDZ(f)
O, 6, 7, 8: cc-pVDZ
9 → 58: D95

Basis Sets: Bader's Analysis
Os: WTBS
O, 6, 7, 8: cc-pVDZ
9 → 58: D95

Table C-17. Optimized geometric coordinates of **17**.

1	77	0	-0.447169	0.161674	-0.411661
2	7	0	0.167864	-1.871935	-0.737044
3	7	0	-0.408700	-2.873275	-0.026743
4	7	0	-2.417014	-0.685959	-0.478812
5	7	0	-2.677085	-1.842387	0.183382
6	7	0	-0.521968	-0.325905	1.637029
7	7	0	-0.999856	-1.541521	2.019507
8	5	0	-1.546344	-2.550327	0.973021
9	6	0	-0.449950	0.534870	-2.259849
10	8	0	-0.463360	0.731603	-3.383783
11	6	0	1.734891	0.717577	-0.392321
12	6	0	-1.260723	2.126142	-0.077092
13	1	0	0.271589	1.506515	0.062959
14	6	0	1.059531	-2.427269	-1.586135
15	6	0	1.063176	-3.827804	-1.415722
16	6	0	0.109988	-4.064135	-0.413710
17	6	0	-3.554524	-0.284927	-1.083744
18	6	0	-4.583069	-1.211013	-0.806955
19	6	0	-3.977014	-2.183793	0.002309
20	6	0	-0.201209	0.362096	2.755472
21	6	0	-0.470686	-0.428416	3.889558
22	6	0	-0.978619	-1.629472	3.370548
23	6	0	4.039426	0.305053	0.480318
24	6	0	4.691054	1.516163	0.805191
25	6	0	6.054801	1.698905	0.511123
26	6	0	6.786281	0.670166	-0.114440
27	6	0	6.146945	-0.542142	-0.439120
28	6	0	4.782404	-0.721261	-0.143899
29	6	0	2.551624	0.122617	0.769631
30	6	0	-2.239309	2.286757	0.924203
31	6	0	-0.925057	3.231460	-0.886389
32	6	0	-1.576439	4.470464	-0.720526
33	6	0	-2.564379	4.620307	0.268386
34	6	0	-2.892295	3.522677	1.088729
35	1	0	1.647502	-1.829674	-2.266338
36	1	0	1.661144	-4.554414	-1.942031
37	1	0	-0.218424	-4.991092	0.031576
38	1	0	-3.594630	0.626733	-1.660259
39	1	0	-5.607122	-1.177395	-1.142646
40	1	0	-4.390329	-3.076395	0.447311
41	1	0	0.180532	1.370121	2.708200
42	1	0	-0.320566	-0.167813	4.924808
43	1	0	-1.319129	-2.518885	3.878739
44	1	0	-1.947554	-3.544350	1.507899
45	1	0	4.138386	2.313205	1.301459
46	1	0	6.546003	2.632308	0.773755
47	1	0	7.840713	0.808596	-0.338348
48	1	0	6.709868	-1.343483	-0.910981
49	1	0	4.299802	-1.667777	-0.383612
50	1	0	2.044176	0.273665	-1.342648
51	1	0	1.946294	1.791470	-0.488631
52	1	0	2.295099	0.619432	1.711535
53	1	0	2.316479	-0.940802	0.889424
54	1	0	-2.525719	1.458696	1.563102
55	1	0	-3.656813	3.621991	1.854888
56	1	0	-3.069003	5.573311	0.399863
57	1	0	-1.305908	5.306771	-1.359376
58	1	0	-0.155549	3.155909	-1.652177

Basis Sets: Optimization and Frequency
Ir: LANL2mDZ(f)
O, 6, 7, 8: cc-pVDZ
9 → 58: D95

Basis Sets: Bader's Analysis
Ir: WTBS
O, 6, 7, 8: cc-pVDZ
9 → 58: D95

Table C-18. Optimized geometric coordinates of **18**.

1	78	0	-0.591785	-0.104757	-0.084983
2	8	0	-0.721694	-0.732580	-2.011319
3	8	0	-0.223331	-2.047178	0.658820
4	8	0	-2.602566	-0.635878	0.098455
5	8	0	-0.429418	0.486821	1.845902
6	6	0	1.596166	0.258226	-0.443491
7	6	0	-0.923518	1.886729	-0.716431
8	1	0	0.404938	1.147248	-0.636099
9	6	0	-0.688081	-2.002510	-2.341218
10	6	0	-0.472923	-3.102044	-1.498308
11	6	0	-0.253153	-3.091401	-0.093436
12	6	0	-3.240383	-0.562307	1.217017
13	6	0	-2.701475	-0.137031	2.458958
14	6	0	-1.402943	0.329439	2.709867
15	6	0	-0.906375	-2.214306	-3.824262
16	6	0	-0.046688	-4.406043	0.628736
17	6	0	-4.696470	-0.966576	1.133359
18	6	0	-1.000784	0.737394	4.111147
19	6	0	3.867884	0.331734	0.563363
20	6	0	4.589916	1.514489	0.287945
21	6	0	5.962664	1.460683	-0.016824
22	6	0	6.629914	0.220525	-0.052702
23	6	0	5.918219	-0.963970	0.221300
24	6	0	4.545535	-0.907296	0.525566
25	6	0	2.372680	0.386015	0.870869
26	6	0	-0.814566	2.948530	0.201851
27	6	0	-1.412209	2.105573	-2.017201
28	6	0	-1.820439	3.399077	-2.391573
29	6	0	-1.728268	4.466791	-1.476270
30	6	0	-1.221605	4.240637	-0.182160
31	1	0	-0.191025	-1.613596	-4.398854
32	1	0	-0.799814	-3.264284	-4.104754
33	1	0	-1.912993	-1.873749	-4.098808
34	1	0	0.652859	-4.274391	1.459923
35	1	0	-1.004293	-4.738003	1.054260
36	1	0	0.316183	-5.189558	-0.041530
37	1	0	-5.254427	-0.196802	0.583402
38	1	0	-4.793559	-1.900730	0.569184
39	1	0	-5.147156	-1.085763	2.121239
40	1	0	-0.672114	1.784172	4.119191
41	1	0	-1.822472	0.617226	4.820036
42	1	0	-0.150346	0.128530	4.442303
43	1	0	-0.470414	-4.074400	-1.974796
44	1	0	-3.371661	-0.167384	3.308540
45	1	0	4.086033	2.479328	0.327749
46	1	0	6.509895	2.378165	-0.217042
47	1	0	7.691046	0.178557	-0.283655
48	1	0	6.431376	-1.922021	0.205624
49	1	0	4.005830	-1.826039	0.751014
50	1	0	1.744175	-0.690376	-0.964645
51	1	0	1.895584	1.042933	-1.159975
52	1	0	2.119454	1.328732	1.368954
53	1	0	2.086800	-0.424560	1.548601
54	1	0	-0.418358	2.784034	1.198110
55	1	0	-1.139514	5.060582	0.526042
56	1	0	-2.044496	5.463956	-1.770094
57	1	0	-2.208378	3.567726	-3.392391
58	1	0	-1.486433	1.287914	-2.724371

Basis Sets: Optimization and Frequency
Pt: LANL2mDZ(f)
O, 6, 7, 8: cc-pVDZ
9 → 58: D95

Basis Sets: Bader's Analysis
Pt: WTBS
O, 6, 7, 8: cc-pVDZ
9 → 58: D95

Table C-19. Optimized geometric coordinates of **19**.

1	25	0	-0.533093	0.153422	-0.565347
2	7	0	-0.485055	-1.922673	-0.912718
3	7	0	-1.304828	-2.762430	-0.237746
4	7	0	-2.613680	-0.078112	-0.522824
5	7	0	-3.189676	-1.143279	0.084969
6	7	0	-0.668906	-0.411449	1.547555
7	7	0	-1.479016	-1.443925	1.886964
8	5	0	-2.292739	-2.180612	0.795891
9	6	0	-0.496558	0.488450	-2.289296
10	8	0	-0.473600	0.684107	-3.447075
11	6	0	1.671653	0.278989	-0.566977
12	6	0	-0.676222	2.207592	-0.158775
13	1	0	0.447252	1.246147	-0.149252
14	6	0	0.217385	-2.678417	-1.774619
15	6	0	-0.149618	-4.045554	-1.652777
16	6	0	-1.132444	-4.046972	-0.654093
17	6	0	-3.607719	0.662699	-1.037570
18	6	0	-4.866980	0.064171	-0.760685
19	6	0	-4.545290	-1.092014	-0.037234
20	6	0	-0.147330	0.055503	2.695489
21	6	0	-0.623191	-0.689804	3.805928
22	6	0	-1.476628	-1.641630	3.232171
23	6	0	4.014016	0.054671	0.442720
24	6	0	4.875301	1.156649	0.225546
25	6	0	6.238182	0.971280	-0.076055
26	6	0	6.775449	-0.328904	-0.163536
27	6	0	5.931319	-1.437534	0.052451
28	6	0	4.569625	-1.244479	0.351904
29	6	0	2.532977	0.254951	0.725262
30	6	0	-1.435805	2.647675	0.961482
31	6	0	-0.209389	3.250600	-1.008201
32	6	0	-0.499050	4.611680	-0.790425
33	6	0	-1.275400	5.005393	0.318759
34	6	0	-1.742191	4.003150	1.194074
35	1	0	0.932680	-2.224798	-2.444094
36	1	0	0.235460	-4.888678	-2.206906
37	1	0	-1.706245	-4.856807	-0.227551
38	1	0	-3.383887	1.578263	-1.563587
39	1	0	-5.847197	0.420315	-1.041207
40	1	0	-5.176651	-1.859409	0.386725
41	1	0	0.522586	0.900931	2.687386
42	1	0	-0.384034	-0.553809	4.849988
43	1	0	-2.068051	-2.424343	3.684257
44	1	0	-2.961296	-3.059254	1.289421
45	1	0	4.466677	2.164309	0.288906
46	1	0	6.878885	1.836528	-0.240519
47	1	0	7.829093	-0.475464	-0.395167
48	1	0	6.333474	-2.447719	-0.010939
49	1	0	3.922139	-2.105181	0.513410
50	1	0	1.836493	-0.668944	-1.093853
51	1	0	2.085254	1.058811	-1.228374
52	1	0	2.400357	1.200509	1.276398
53	1	0	2.175733	-0.551028	1.379493
54	1	0	-1.832026	1.911269	1.656259
55	1	0	-2.352107	4.272478	2.057613
56	1	0	-1.509639	6.055002	0.493518
57	1	0	-0.122128	5.360086	-1.488760
58	1	0	0.392572	2.989641	-1.878991

Basis Sets: Optimization and Frequency
Mn: LANL2mDZ(f)
N, B, O, 9, 11, 12, 13: cc-pVDZ
14 → 58: D95

Basis Sets: Bader's Analysis
Mn: WTBS
N, B, O, 9, 11, 12, 13: cc-pVDZ
14 → 58: D95

Table C-20. Optimized geometric coordinates of **20**.

1	26	0	-0.536303	0.087486	-0.472904
2	7	0	-0.723454	-1.914626	-0.884872
3	7	0	-1.692281	-2.638848	-0.281222
4	7	0	-2.573597	0.210576	-0.519551
5	7	0	-3.324015	-0.770399	0.033520
6	7	0	-0.759507	-0.429178	1.530103
7	7	0	-1.712024	-1.340950	1.850567
8	5	0	-2.613284	-1.944325	0.747294
9	6	0	-0.452116	0.411880	-2.226426
10	8	0	-0.422915	0.576819	-3.361829
11	6	0	1.645014	0.010545	-0.436020
12	6	0	-0.283325	2.152059	-0.077297
13	1	0	0.606237	1.065236	-0.065659
14	6	0	-0.089283	-2.736107	-1.742695
15	6	0	-0.658939	-4.031566	-1.688020
16	6	0	-1.682512	-3.917588	-0.737518
17	6	0	-3.418219	1.116353	-1.042049
18	6	0	-4.758801	0.713261	-0.821252
19	6	0	-4.645488	-0.499502	-0.127773
20	6	0	-0.185268	-0.044835	2.685912
21	6	0	-0.771357	-0.725065	3.779720
22	6	0	-1.744907	-1.543339	3.192082
23	6	0	4.015411	-0.139280	0.468375
24	6	0	4.902234	0.896383	0.097390
25	6	0	6.237591	0.616604	-0.250419
26	6	0	6.710624	-0.710114	-0.231136
27	6	0	5.837190	-1.751603	0.140765
28	6	0	4.503455	-1.465911	0.487337
29	6	0	2.560451	0.159707	0.806951
30	6	0	-1.033874	2.693482	0.989810
31	6	0	0.315711	3.067920	-0.972106
32	6	0	0.156395	4.460913	-0.833988
33	6	0	-0.612489	4.977120	0.225296
34	6	0	-1.207137	4.082927	1.137390
35	1	0	0.727687	-2.384481	-2.355596
36	1	0	-0.371333	-4.905683	-2.250951
37	1	0	-2.383990	-4.650548	-0.368215
38	1	0	-3.045527	2.005089	-1.528606
39	1	0	-5.661223	1.225166	-1.116910
40	1	0	-5.405713	-1.165122	0.252876
41	1	0	0.594422	0.699201	2.700102
42	1	0	-0.524754	-0.632967	4.825752
43	1	0	-2.441576	-2.237961	3.636783
44	1	0	-3.408800	-2.718829	1.211805
45	1	0	4.545434	1.925373	0.084331
46	1	0	6.905990	1.428178	-0.530119
47	1	0	7.742486	-0.928282	-0.496936
48	1	0	6.195152	-2.778698	0.164908
49	1	0	3.835893	-2.276112	0.777799
50	1	0	1.648832	-1.038172	-0.740349
51	1	0	2.085320	0.585143	-1.262968
52	1	0	2.488474	1.179796	1.214725
53	1	0	2.220276	-0.529197	1.588905
54	1	0	-1.518556	2.036803	1.704514
55	1	0	-1.807865	4.462124	1.961774
56	1	0	-0.743507	6.050827	0.339850
57	1	0	0.630667	5.131957	-1.547139
58	1	0	0.931565	2.702100	-1.792793

Basis Sets: Optimization and Frequency
Fe: LANL2mDZ(f)
N, B, O, 9, 11, 12, 13: cc-pVDZ
14 → 58: D95

Basis Sets: Bader's Analysis
Fe: WTBS
N, B, O, 9, 11, 12, 13: cc-pVDZ
14 → 58: D95

Table C-21. Optimized geometric coordinates of **21**.

1	27	0	-0.566032	0.089489	-0.371836
2	7	0	-0.583433	-1.857040	-0.915635
3	7	0	-1.556556	-2.654996	-0.416811
4	7	0	-2.572225	0.163917	-0.482680
5	7	0	-3.286222	-0.890221	-0.022548
6	7	0	-0.735225	-0.523153	1.495959
7	7	0	-1.655889	-1.482000	1.770188
8	5	0	-2.534166	-2.071076	0.632521
9	6	0	-0.557184	0.467277	-2.186940
10	8	0	-0.612044	0.621031	-3.306767
11	6	0	1.609685	0.050728	-0.233115
12	6	0	-0.381460	2.097499	0.064282
13	1	0	0.587660	1.086409	0.071968
14	6	0	0.164718	-2.600543	-1.759300
15	6	0	-0.336962	-3.919824	-1.800200
16	6	0	-1.433862	-3.905458	-0.925497
17	6	0	-3.442840	1.077175	-0.960381
18	6	0	-4.762380	0.598652	-0.801001
19	6	0	-4.611313	-0.658058	-0.195749
20	6	0	-0.080057	-0.245947	2.643804
21	6	0	-0.590805	-1.044934	3.688296
22	6	0	-1.591772	-1.817948	3.081277
23	6	0	4.042805	0.320096	0.262506
24	6	0	4.879145	0.734963	-0.797828
25	6	0	6.139582	0.139457	-0.990575
26	6	0	6.577440	-0.881970	-0.125112
27	6	0	5.749886	-1.301998	0.935286
28	6	0	4.490400	-0.705765	1.125485
29	6	0	2.669599	0.954496	0.458217
30	6	0	-1.103769	2.564083	1.180227
31	6	0	0.114983	3.028953	-0.873671
32	6	0	-0.121656	4.407669	-0.712315
33	6	0	-0.853460	4.867251	0.398027
34	6	0	-1.339548	3.941655	1.343411
35	1	0	1.015655	-2.189011	-2.281912
36	1	0	0.040878	-4.751629	-2.372950
37	1	0	-2.110983	-4.696913	-0.641368
38	1	0	-3.106991	2.018858	-1.368267
39	1	0	-5.680492	1.091365	-1.078690
40	1	0	-5.353743	-1.376701	0.117362
41	1	0	0.695009	0.502260	2.688681
42	1	0	-0.282784	-1.055595	4.721563
43	1	0	-2.245192	-2.568389	3.499959
44	1	0	-3.288638	-2.904803	1.046923
45	1	0	4.555931	1.534961	-1.462430
46	1	0	6.779237	0.475209	-1.802613
47	1	0	7.552798	-1.338882	-0.269866
48	1	0	6.087911	-2.082552	1.611855
49	1	0	3.862994	-1.030537	1.954628
50	1	0	1.581776	-0.933095	0.233745
51	1	0	1.850544	-0.037701	-1.295826
52	1	0	2.659830	1.964133	0.032076
53	1	0	2.449305	1.054168	1.527951
54	1	0	-1.507716	1.875617	1.912600
55	1	0	-1.906109	4.286604	2.204160
56	1	0	-1.037927	5.929947	0.528839
57	1	0	0.271617	5.110411	-1.441710
58	1	0	0.719279	2.706210	-1.719712

Basis Sets: Optimization and Frequency
Co: LANL2mDZ(f)
N, B, O, 9, 11, 12, 13: cc-pVDZ
14 → 58: D95

Basis Sets: Bader's Analysis
Co: WTBS
N, B, O, 9, 11, 12, 13: cc-pVDZ
14 → 58: D95

Table C-22. Optimized geometric coordinates of **22**.

1	43	0	-0.473633	0.253244	-0.582401
2	7	0	0.076534	-1.949869	-0.889159
3	7	0	-0.525347	-2.904401	-0.140363
4	7	0	-2.509934	-0.641725	-0.561782
5	7	0	-2.760213	-1.784417	0.125733
6	7	0	-0.514254	-0.374164	1.623725
7	7	0	-1.034938	-1.580540	1.959962
8	5	0	-1.624846	-2.520877	0.880185
9	6	0	-0.493483	0.696165	-2.378994
10	8	0	-0.499549	0.984126	-3.525324
11	6	0	1.807926	0.596925	-0.635923
12	6	0	-1.433717	2.130640	-0.120771
13	1	0	0.579371	1.432070	-0.236242
14	6	0	0.887856	-2.585332	-1.751347
15	6	0	0.817659	-3.991134	-1.557468
16	6	0	-0.106743	-4.144424	-0.516198
17	6	0	-3.666142	-0.255127	-1.121772
18	6	0	-4.701729	-1.171135	-0.797252
19	6	0	-4.070419	-2.133253	0.002016
20	6	0	-0.160584	0.229803	2.769516
21	6	0	-0.450074	-0.602755	3.882922
22	6	0	-1.011943	-1.751427	3.310353
23	6	0	4.115869	0.580982	0.454970
24	6	0	4.877598	1.760625	0.280618
25	6	0	6.261427	1.705426	0.025557
26	6	0	6.917926	0.461202	-0.057551
27	6	0	6.173070	-0.723389	0.115078
28	6	0	4.789744	-0.660616	0.367913
29	6	0	2.614702	0.642458	0.689343
30	6	0	-2.371612	2.233492	0.944201
31	6	0	-1.232314	3.344677	-0.836615
32	6	0	-1.897860	4.549239	-0.531708
33	6	0	-2.819737	4.605716	0.534855
34	6	0	-3.050301	3.427279	1.271705
35	1	0	1.464023	-2.026909	-2.473956
36	1	0	1.346346	-4.764149	-2.095041
37	1	0	-0.487771	-5.033721	-0.035857
38	1	0	-3.705440	0.650618	-1.706999
39	1	0	-5.738714	-1.132997	-1.095510
40	1	0	-4.460147	-3.021841	0.476732
41	1	0	0.257522	1.224823	2.751089
42	1	0	-0.282664	-0.396283	4.929361
43	1	0	-1.390590	-2.654013	3.767124
44	1	0	-2.061346	-3.518703	1.404926
45	1	0	4.376713	2.725704	0.342830
46	1	0	6.825015	2.627857	-0.105846
47	1	0	7.987849	0.415287	-0.253055
48	1	0	6.668479	-1.691120	0.053578
49	1	0	4.219292	-1.579240	0.496047
50	1	0	2.075999	-0.329357	-1.160014
51	1	0	2.161585	1.413634	-1.282524
52	1	0	2.367792	1.564957	1.237850
53	1	0	2.302194	-0.197525	1.323086
54	1	0	-2.596179	1.349713	1.540761
55	1	0	-3.760344	3.429691	2.100607
56	1	0	-3.339523	5.531993	0.779450
57	1	0	-1.696219	5.440653	-1.128367
58	1	0	-0.532064	3.350316	-1.672619

Basis Sets: Optimization and Frequency
Tc: LANL2mDZ(f)
N, B, O, 9, 11, 12, 13: cc-pVDZ
14 → 58: D95

Basis Sets: Bader's Analysis
Tc: WTBS
N, B, O, 9, 11, 12, 13: cc-pVDZ
14 → 58: D95

Table C-23. Optimized geometric coordinates of **23**.

1	44	0	-0.463752	0.188713	-0.516449
2	7	0	-0.282204	-1.980337	-0.898513
3	7	0	-1.043487	-2.850212	-0.194176
4	7	0	-2.611250	-0.274362	-0.502083
5	7	0	-3.059529	-1.385691	0.129813
6	7	0	-0.583116	-0.415292	1.609741
7	7	0	-1.307739	-1.517331	1.931078
8	5	0	-2.063062	-2.329533	0.848178
9	6	0	-0.437190	0.593167	-2.330304
10	8	0	-0.427645	0.816455	-3.463557
11	6	0	1.768289	0.361436	-0.574103
12	6	0	-0.877386	2.258235	-0.098988
13	1	0	0.494806	1.369953	-0.083916
14	6	0	0.449738	-2.701119	-1.767206
15	6	0	0.161239	-4.079984	-1.619756
16	6	0	-0.801598	-4.123169	-0.602752
17	6	0	-3.678283	0.350877	-1.027451
18	6	0	-4.858544	-0.375325	-0.731507
19	6	0	-4.410290	-1.476699	0.010045
20	6	0	-0.107412	0.094702	2.760746
21	6	0	-0.527262	-0.694001	3.857854
22	6	0	-1.292968	-1.712302	3.274751
23	6	0	4.074114	0.182276	0.461766
24	6	0	4.880652	1.325603	0.261960
25	6	0	6.252759	1.202204	-0.026994
26	6	0	6.843971	-0.073248	-0.119973
27	6	0	6.051469	-1.220920	0.079345
28	6	0	4.679703	-1.091404	0.367826
29	6	0	2.582114	0.317336	0.739910
30	6	0	-1.696066	2.570592	1.010600
31	6	0	-0.480867	3.332960	-0.928140
32	6	0	-0.903108	4.655662	-0.684783
33	6	0	-1.731546	4.942518	0.415397
34	6	0	-2.125521	3.887855	1.262088
35	1	0	1.134096	-2.224083	-2.453014
36	1	0	0.582854	-4.907548	-2.168423
37	1	0	-1.316794	-4.961935	-0.159327
38	1	0	-3.563917	1.276548	-1.570903
39	1	0	-5.871975	-0.134559	-1.012114
40	1	0	-4.958209	-2.297554	0.447973
41	1	0	0.492413	0.991362	2.763154
42	1	0	-0.307763	-0.545325	4.903371
43	1	0	-1.816013	-2.542150	3.725489
44	1	0	-2.649150	-3.250655	1.354783
45	1	0	4.432424	2.315446	0.337519
46	1	0	6.858044	2.094088	-0.174001
47	1	0	7.904645	-0.170928	-0.339901
48	1	0	6.500677	-2.209697	0.015525
49	1	0	4.074518	-1.982886	0.526310
50	1	0	1.977614	-0.547440	-1.147019
51	1	0	2.123560	1.200981	-1.187236
52	1	0	2.403715	1.232491	1.323756
53	1	0	2.241338	-0.526388	1.351459
54	1	0	-2.032957	1.782506	1.676774
55	1	0	-2.770691	4.083860	2.116488
56	1	0	-2.061955	5.960492	0.608822
57	1	0	-0.581448	5.452209	-1.352877
58	1	0	0.166984	3.152928	-1.784376

Basis Sets: Optimization and Frequency
Ru: LANL2mDZ(f)
N, B, O, 9, 11, 12, 13: cc-pVDZ
14 →58: D95

Basis Sets: Bader's Analysis
Ru: WTBS
N, B, O, 9, 11, 12, 13: cc-pVDZ
14 → 58: D95

Table C-24. Optimized geometric coordinates of **24**.

1	45	0	-0.505679	0.127728	-0.443424
2	7	0	-0.801367	-1.969052	-0.869301
3	7	0	-1.800165	-2.629312	-0.239111
4	7	0	-2.644167	0.279589	-0.483557
5	7	0	-3.381936	-0.701342	0.089325
6	7	0	-0.758652	-0.406456	1.583531
7	7	0	-1.738108	-1.298841	1.887132
8	5	0	-2.678381	-1.886737	0.796153
9	6	0	-0.432948	0.481320	-2.314238
10	8	0	-0.442008	0.642119	-3.438775
11	6	0	1.781528	-0.015332	-0.395906
12	6	0	-0.119250	2.216598	-0.037214
13	1	0	0.810110	1.081798	-0.007328
14	6	0	-0.207607	-2.832309	-1.719856
15	6	0	-0.838300	-4.093511	-1.630493
16	6	0	-1.847407	-3.914112	-0.673531
17	6	0	-3.490038	1.201787	-0.983592
18	6	0	-4.822264	0.805942	-0.725470
19	6	0	-4.702027	-0.410569	-0.038373
20	6	0	-0.152897	-0.053777	2.738707
21	6	0	-0.750408	-0.737601	3.816669
22	6	0	-1.754513	-1.517305	3.224286
23	6	0	4.097641	-0.274653	0.493792
24	6	0	5.008873	0.725012	0.086117
25	6	0	6.323849	0.386707	-0.283092
26	6	0	6.742239	-0.958134	-0.251921
27	6	0	5.840385	-1.961420	0.154506
28	6	0	4.526095	-1.620790	0.523596
29	6	0	2.664211	0.089074	0.869654
30	6	0	-0.789026	2.777151	1.069546
31	6	0	0.509286	3.072181	-0.968044
32	6	0	0.463271	4.469956	-0.801677
33	6	0	-0.214236	5.024670	0.299406
34	6	0	-0.840157	4.173493	1.232214
35	1	0	0.621367	-2.536816	-2.346741
36	1	0	-0.598095	-4.991776	-2.176551
37	1	0	-2.575227	-4.611759	-0.287518
38	1	0	-3.127437	2.089443	-1.480093
39	1	0	-5.728437	1.324471	-0.995286
40	1	0	-5.462645	-1.065926	0.358579
41	1	0	0.651350	0.663459	2.761308
42	1	0	-0.492589	-0.673786	4.861597
43	1	0	-2.463794	-2.197624	3.670710
44	1	0	-3.480451	-2.628943	1.288722
45	1	0	4.698103	1.768851	0.072800
46	1	0	7.019747	1.165301	-0.584572
47	1	0	7.759062	-1.219571	-0.532657
48	1	0	6.162357	-2.998885	0.191446
49	1	0	3.839904	-2.401092	0.850394
50	1	0	1.716497	-1.056692	-0.715010
51	1	0	2.202924	0.575014	-1.216776
52	1	0	2.637814	1.104817	1.286801
53	1	0	2.291335	-0.599769	1.634161
54	1	0	-1.298590	2.149512	1.791087
55	1	0	-1.371699	4.591389	2.082898
56	1	0	-0.253791	6.102474	0.430224
57	1	0	0.956574	5.113059	-1.525235
58	1	0	1.062088	2.673632	-1.816118

Basis Sets: Optimization and Frequency
Rh: LANL2mDZ(f)
N, B, O, 9, 11, 12, 13: cc-pVDZ
14 → 58: D95

Basis Sets: Bader's Analysis
Rh: WTBS
N, B, O, 9, 11, 12, 13: cc-pVDZ
14 → 58: D95

Table C-25. Optimized geometric coordinates of **25**.

1	75	0	0.368041	-0.298167	-0.478453
2	7	0	-0.242906	1.846061	-0.894229
3	7	0	0.183093	2.865124	-0.107468
4	7	0	2.317037	0.847234	-0.482899
5	7	0	2.475557	1.979800	0.247142
6	7	0	0.329951	0.355218	1.670206
7	7	0	0.723772	1.605983	2.028023
8	5	0	1.257949	2.602275	0.975952
9	6	0	0.400038	-0.786631	-2.265323
10	8	0	0.403580	-1.091031	-3.412493
11	6	0	-1.852044	-0.542132	-0.590360
12	6	0	1.764982	-1.899678	-0.003706
13	1	0	-0.235415	-1.734635	0.015733
14	6	0	-0.990341	2.388364	-1.870360
15	6	0	-1.057477	3.796697	-1.715602
16	6	0	-0.281782	4.053376	-0.576917
17	6	0	3.489553	0.595791	-1.085821
18	6	0	4.439420	1.593079	-0.746189
19	6	0	3.739827	2.459676	0.105197
20	6	0	0.010116	-0.292046	2.803757
21	6	0	0.192143	0.554594	3.927717
22	6	0	0.651843	1.758516	3.379074
23	6	0	-4.165326	-0.705977	0.496463
24	6	0	-4.804929	-1.956641	0.318017
25	6	0	-6.185752	-2.042525	0.057481
26	6	0	-6.966373	-0.871763	-0.029481
27	6	0	-6.345822	0.381992	0.145178
28	6	0	-4.964241	0.459513	0.405481
29	6	0	-2.666275	-0.616697	0.733804
30	6	0	2.628402	-1.839162	1.122339
31	6	0	1.917793	-3.068121	-0.799277
32	6	0	2.851054	-4.083745	-0.512200
33	6	0	3.692347	-3.985044	0.615987
34	6	0	3.568430	-2.845589	1.433410
35	1	0	-1.431704	1.763179	-2.630860
36	1	0	-1.579671	4.507945	-2.337493
37	1	0	-0.031457	4.983780	-0.088764
38	1	0	3.601722	-0.279453	-1.706472
39	1	0	5.467419	1.665406	-1.067657
40	1	0	4.052781	3.367138	0.600704
41	1	0	-0.316181	-1.319404	2.764889
42	1	0	0.018186	0.323031	4.967635
43	1	0	0.927487	2.689429	3.852249
44	1	0	1.572954	3.638052	1.511393
45	1	0	-4.207796	-2.865342	0.379471
46	1	0	-6.651883	-3.017794	-0.076435
47	1	0	-8.034633	-0.935138	-0.230044
48	1	0	-6.936571	1.294809	0.080247
49	1	0	-4.490886	1.431668	0.536005
50	1	0	-2.253028	0.310757	-1.158187
51	1	0	-2.114314	-1.430230	-1.182340
52	1	0	-2.335739	-1.495984	1.307345
53	1	0	-2.445712	0.266883	1.349488
54	1	0	2.584818	-0.976030	1.784402
55	1	0	4.203273	-2.729983	2.313274
56	1	0	4.415747	-4.766587	0.847364
57	1	0	2.917290	-4.951426	-1.170452
58	1	0	1.282759	-3.191701	-1.674802

Basis Sets: Optimization and Frequency
Re: LANL2mDZ(f)
N, B, O, 9, 11, 12, 13: cc-pVDZ
14 → 58: D95

Basis Sets: Bader's Analysis
Re: WTBS
N, B, O, 9, 11, 12, 13: cc-pVDZ
14 → 58: D95

Table C-26. Optimized geometric coordinates of **26**.

1	76	0	-0.384647	0.249676	-0.443397
2	7	0	0.270204	-1.829811	-0.830298
3	7	0	-0.181392	-2.847972	-0.055244
4	7	0	-2.310419	-0.830987	-0.486691
5	7	0	-2.485731	-1.966535	0.235525
6	7	0	-0.375269	-0.323733	1.656777
7	7	0	-0.775404	-1.565258	2.038320
8	5	0	-1.286630	-2.587281	0.997879
9	6	0	-0.399761	0.707819	-2.244401
10	8	0	-0.394477	0.980507	-3.373554
11	6	0	1.797475	0.612900	-0.549079
12	6	0	-1.665918	1.929708	-0.034985
13	1	0	0.210658	1.634231	0.051998
14	6	0	1.048518	-2.369687	-1.788189
15	6	0	1.110437	-3.773235	-1.627902
16	6	0	0.302452	-4.030594	-0.512215
17	6	0	-3.466324	-0.571078	-1.123343
18	6	0	-4.420693	-1.567880	-0.811954
19	6	0	-3.745783	-2.438122	0.055827
20	6	0	-0.078304	0.362494	2.776282
21	6	0	-0.281781	-0.451945	3.913792
22	6	0	-0.728646	-1.672866	3.390664
23	6	0	4.107113	0.658122	0.495858
24	6	0	4.751519	1.912751	0.401571
25	6	0	6.127381	2.001837	0.117818
26	6	0	6.887033	0.831245	-0.076329
27	6	0	6.257875	-0.425931	0.016586
28	6	0	4.881426	-0.508309	0.300471
29	6	0	2.610654	0.565819	0.766079
30	6	0	-2.583876	1.883418	1.037729
31	6	0	-1.678914	3.100377	-0.827506
32	6	0	-2.577776	4.158557	-0.587014
33	6	0	-3.492632	4.084604	0.480044
34	6	0	-3.485842	2.936353	1.293260
35	1	0	1.518849	-1.755249	-2.540092
36	1	0	1.651663	-4.483924	-2.232190
37	1	0	0.045976	-4.962837	-0.031949
38	1	0	-3.570109	0.305376	-1.743941
39	1	0	-5.438568	-1.639697	-1.161346
40	1	0	-4.079483	-3.343511	0.540298
41	1	0	0.245429	1.389824	2.724583
42	1	0	-0.128982	-0.191194	4.949011
43	1	0	-1.010520	-2.588000	3.889049
44	1	0	-1.608838	-3.611975	1.538259
45	1	0	4.172736	2.822743	0.554022
46	1	0	6.605275	2.977017	0.052438
47	1	0	7.950885	0.897586	-0.292840
48	1	0	6.837150	-1.335714	-0.126557
49	1	0	4.402772	-1.483804	0.375107
50	1	0	2.175261	-0.177081	-1.206767
51	1	0	2.021405	1.557156	-1.059792
52	1	0	2.307457	1.395432	1.420384
53	1	0	2.389639	-0.363346	1.306949
54	1	0	-2.624073	1.013060	1.686074
55	1	0	-4.181695	2.850427	2.126046
56	1	0	-4.187586	4.898650	0.673554
57	1	0	-2.554081	5.036188	-1.230527
58	1	0	-0.976840	3.207565	-1.651709

Basis Sets: Optimization and Frequency
Os: LANL2mDZ(f)
N, B, O, 9, 11, 12, 13: cc-pVDZ
14 → 58: D95

Basis Sets: Bader's Analysis
Os: WTBS
N, B, O, 9, 11, 12, 13: cc-pVDZ
14 → 58: D95

Table C-27. Optimized geometric coordinates of **27**.

1	77	0	-0.447169	0.161674	-0.411661
2	7	0	0.167864	-1.871935	-0.737044
3	7	0	-0.408700	-2.873275	-0.026743
4	7	0	-2.417014	-0.685959	-0.478812
5	7	0	-2.677085	-1.842387	0.183382
6	7	0	-0.521968	-0.325905	1.637029
7	7	0	-0.999856	-1.541521	2.019507
8	5	0	-1.546344	-2.550327	0.973021
9	6	0	-0.449950	0.534870	-2.259849
10	8	0	-0.463360	0.731603	-3.383783
11	6	0	1.734891	0.717577	-0.392321
12	6	0	-1.260723	2.126142	-0.077092
13	1	0	0.271589	1.506515	0.062959
14	6	0	1.059531	-2.427269	-1.586135
15	6	0	1.063176	-3.827804	-1.415722
16	6	0	0.109988	-4.064135	-0.413710
17	6	0	-3.554524	-0.284927	-1.083744
18	6	0	-4.583069	-1.211013	-0.806955
19	6	0	-3.977014	-2.183793	0.002309
20	6	0	-0.201209	0.362096	2.755472
21	6	0	-0.470686	-0.428416	3.889558
22	6	0	-0.978619	-1.629472	3.370548
23	6	0	4.039426	0.305053	0.480318
24	6	0	4.691054	1.516163	0.805191
25	6	0	6.054801	1.698905	0.511123
26	6	0	6.786281	0.670166	-0.114440
27	6	0	6.146945	-0.542142	-0.439120
28	6	0	4.782404	-0.721261	-0.143899
29	6	0	2.551624	0.122617	0.769631
30	6	0	-2.239309	2.286757	0.924203
31	6	0	-0.925057	3.231460	-0.886389
32	6	0	-1.576439	4.470464	-0.720526
33	6	0	-2.564379	4.620307	0.268386
34	6	0	-2.892295	3.522677	1.088729
35	1	0	1.647502	-1.829674	-2.266338
36	1	0	1.661144	-4.554414	-1.942031
37	1	0	-0.218424	-4.991092	0.031576
38	1	0	-3.594630	0.626733	-1.660259
39	1	0	-5.607122	-1.177395	-1.142646
40	1	0	-4.390329	-3.076395	0.447311
41	1	0	0.180532	1.370121	2.708200
42	1	0	-0.320566	-0.167813	4.924808
43	1	0	-1.319129	-2.518885	3.878739
44	1	0	-1.947554	-3.544350	1.507899
45	1	0	4.138386	2.313205	1.301459
46	1	0	6.546003	2.632308	0.773755
47	1	0	7.840713	0.808596	-0.338348
48	1	0	6.709868	-1.343483	-0.910981
49	1	0	4.299802	-1.667777	-0.383612
50	1	0	2.044176	0.273665	-1.342648
51	1	0	1.946294	1.791470	-0.488631
52	1	0	2.295099	0.619432	1.711535
53	1	0	2.316479	-0.940802	0.889424
54	1	0	-2.525719	1.458696	1.563102
55	1	0	-3.656813	3.621991	1.854888
56	1	0	-3.069003	5.573311	0.399863
57	1	0	-1.305908	5.306771	-1.359376
58	1	0	-0.155549	3.155909	-1.652177

Basis Sets: Optimization and Frequency
Ir: LANL2mDZ(f)
N, B, O, 9, 11, 12, 13: cc-pVDZ
14 → 58: D95

Basis Sets: Bader's Analysis
Ir: WTBS
N, B, O, 9, 11, 12, 13: cc-pVDZ
14 → 58: D95

Table C-28. Optimized geometric coordinates of **28**.

1	25	0	0.719274 0.220307 0.135657
2	5	0	-1.262961 -0.100075 0.089566
3	6	0	0.769499 1.304355 2.056129
4	1	0	-0.128620 0.431396 1.405306
5	6	0	0.363926 1.684967 -0.744783
6	8	0	0.163156 2.646950 -1.400609
7	8	0	-1.871310 -1.352516 -0.246218
8	8	0	-2.312116 0.832891 0.355705
9	6	0	1.507879 -1.781135 0.594904
10	6	0	2.553480 -0.822517 0.760370
11	6	0	2.785564 -0.177274 -0.486238
12	6	0	1.859038 -0.732616 -1.435490
13	6	0	1.072481 -1.713955 -0.766373
14	6	0	-3.597220 0.246780 0.051741
15	6	0	-3.310339 -1.266003 -0.106350
16	1	0	1.089368 -2.416858 1.367782
17	1	0	3.054822 -0.587246 1.695183
18	1	0	3.511258 0.606376 -0.679152
19	1	0	1.760508 -0.439465 -2.475769
20	1	0	0.259694 -2.285079 -1.197064
21	1	0	-3.629399 -1.839163 0.780270
22	1	0	-3.795998 -1.698805 -0.993638
23	1	0	-3.992680 0.687635 -0.878113
24	1	0	-4.305528 0.459134 0.866706
25	1	0	1.690229 1.841159 1.803764
26	1	0	0.002446 2.055609 2.291188
27	1	0	0.953187 0.703804 2.959807

Basis Sets: Optimization and Frequency
Mn: LANL2mDZ(f)
O B 3 4 5 9 → 13: cc-pVDZ
14→27: D95

Basis Sets: Bader's Analysis
Mn: WTBS
O B 3 4 5 9 → 13: cc-pVDZ
14→27: D95

Table C-29. Optimized geometric coordinates of **29**.

1	26	0	0.717101	0.188314	0.152297
2	5	0	-1.271323	-0.119099	0.105932
3	6	0	0.736527	1.166884	2.040189
4	1	0	-0.213467	0.277293	1.315032
5	6	0	0.374147	1.718772	-0.634226
6	8	0	0.191623	2.713545	-1.189456
7	8	0	-1.832095	-1.377083	-0.082536
8	8	0	-2.237503	0.875555	0.193999
9	6	0	1.411297	-1.812731	0.453635
10	6	0	2.482679	-0.908830	0.727245
11	6	0	2.751767	-0.154302	-0.445222
12	6	0	1.838165	-0.601877	-1.463001
13	6	0	1.023410	-1.629600	-0.910251
14	6	0	-3.557379	0.280636	-0.013999
15	6	0	-3.291872	-1.245146	-0.118251
16	1	0	0.960762	-2.505911	1.154205
17	1	0	2.967693	-0.777145	1.688544
18	1	0	3.497208	0.625563	-0.552095
19	1	0	1.774366	-0.215815	-2.474567
20	1	0	0.217856	-2.148821	-1.412668
21	1	0	-3.711742	-1.805900	0.725199
22	1	0	-3.660460	-1.678047	-1.054946
23	1	0	-3.987403	0.698938	-0.931608
24	1	0	-4.199022	0.544141	0.834211
25	1	0	1.687614	1.682094	1.883371
26	1	0	-0.038010	1.917142	2.232623
27	1	0	0.827925	0.506820	2.910550

Basis Sets: Optimization and Frequency
Fe: LANL2mDZ(f)
O B 3 4 5 9 → 13: cc-pVDZ
14→27: D95

Basis Sets: Bader's Analysis
Fe: WTBS
O B 3 4 5 9 → 13: cc-pVDZ
14→27: D95

Table C-30. Optimized geometric coordinates of **30**.

1	27	0	0.726647 0.157302 0.174435
2	5	0	-1.325516 -0.130466 0.163374
3	6	0	0.745445 0.898637 2.148735
4	1	0	-0.295137 0.159358 1.254068
5	6	0	0.470670 1.841711 -0.454829
6	8	0	0.340488 2.896249 -0.851252
7	8	0	-1.886147 -1.366514 0.178151
8	8	0	-2.160183 0.920908 -0.040086
9	6	0	1.338425 -1.845057 0.298282
10	6	0	2.483437 -1.023183 0.567498
11	6	0	2.702033 -0.189573 -0.553347
12	6	0	1.711504 -0.532633 -1.555280
13	6	0	0.899573 -1.577370 -1.040340
14	6	0	-3.522647 0.358478 -0.238103
15	6	0	-3.344337 -1.177055 -0.055210
16	1	0	0.900155 -2.572057 0.973112
17	1	0	3.036845 -0.995440 1.500013
18	1	0	3.474508 0.564981 -0.655668
19	1	0	1.616660 -0.075706 -2.535002
20	1	0	0.067405 -2.053899 -1.542988
21	1	0	-3.871845 -1.570968 0.816861
22	1	0	-3.618195 -1.751665 -0.943361
23	1	0	-3.855314 0.638572 -1.240627
24	1	0	-4.179632 0.809693 0.509040
25	1	0	1.731542 1.356605 2.060960
26	1	0	-0.004601 1.660155 2.376885
27	1	0	0.747849 0.106688 2.901151

Basis Sets: Optimization and Frequency
Co: LANL2mDZ(f)
O B 3 4 5 9 → 13: cc-pVDZ
14→27: D95

Basis Sets: Bader's Analysis
Co: WTBS
O B 3 4 5 9 → 13: cc-pVDZ
14→27: D95

Table C-31. Optimized geometric coordinates of **31**.

1	43	0	0.617139	0.261338	0.127846
2	5	0	-1.452558	-0.142931	0.061668
3	6	0	0.664602	1.481026	2.144815
4	1	0	-0.265056	0.696655	1.492526
5	6	0	0.202092	1.803590	-0.817620
6	8	0	-0.013279	2.768737	-1.473503
7	8	0	-1.995702	-1.459576	-0.102714
8	8	0	-2.544685	0.767053	0.172798
9	6	0	1.614500	-1.861390	0.634927
10	6	0	2.677009	-0.900610	0.644271
11	6	0	2.810461	-0.352233	-0.659467
12	6	0	1.790972	-0.943227	-1.485105
13	6	0	1.057893	-1.872884	-0.682413
14	6	0	-3.795621	0.082426	-0.065741
15	6	0	-3.439293	-1.421540	0.008661
16	1	0	1.280220	-2.460112	1.475327
17	1	0	3.277861	-0.629257	1.508064
18	1	0	3.528842	0.399469	-0.969185
19	1	0	1.628019	-0.743594	-2.538729
20	1	0	0.220733	-2.477538	-1.008752
21	1	0	-3.747588	-1.869394	0.968275
22	1	0	-3.890036	-2.005045	-0.807934
23	1	0	-4.185009	0.361897	-1.058434
24	1	0	-4.533408	0.380382	0.694186
25	1	0	1.439881	2.180049	1.818404
26	1	0	-0.152492	2.090789	2.560266
27	1	0	1.057509	0.852175	2.953658

Basis Sets: Optimization and Frequency
Tc: LANL2mDZ(f)
O B 3 4 5 9 → 13: cc-pVDZ
14→27: D95

Basis Sets: Bader's Analysis
Tc: WTBS
O B 3 4 5 9 → 13: cc-pVDZ
14→27: D95

Table C-32. Optimized geometric coordinates of **32**.

1	44	0	0.611988	0.239555	0.134788
2	5	0	-1.447146	-0.171922	0.078421
3	6	0	0.708418	1.452390	2.046606
4	1	0	-0.302252	0.511754	1.437040
5	6	0	0.131611	1.799663	-0.766784
6	8	0	-0.126509	2.756753	-1.364526
7	8	0	-1.939142	-1.470737	-0.006136
8	8	0	-2.464629	0.772021	0.106088
9	6	0	1.648788	-1.781442	0.652655
10	6	0	2.697676	-0.803397	0.556611
11	6	0	2.723284	-0.299652	-0.766693
12	6	0	1.671728	-0.955963	-1.504899
13	6	0	1.038215	-1.893024	-0.631281
14	6	0	-3.748972	0.090380	-0.057163
15	6	0	-3.404640	-1.420400	0.011155
16	1	0	1.390860	-2.358985	1.533027
17	1	0	3.341757	-0.484883	1.369595
18	1	0	3.398465	0.455112	-1.153846
19	1	0	1.443043	-0.809239	-2.554409
20	1	0	0.203659	-2.535468	-0.881545
21	1	0	-3.758113	-1.892519	0.935859
22	1	0	-3.785659	-1.984090	-0.847459
23	1	0	-4.177584	0.381781	-1.023490
24	1	0	-4.422821	0.410950	0.744876
25	1	0	1.592285	2.038504	1.781772
26	1	0	-0.100467	2.150981	2.285288
27	1	0	0.930690	0.839657	2.925885

Basis Sets: Optimization and Frequency
Ru: LANL2mDZ(f)
O B 3 4 5 9 → 13: cc-pVDZ
14→27: D95

Basis Sets: Bader's Analysis
Ru: WTBS
O B 3 4 5 9 → 13: cc-pVDZ
14→27: D95

Table C-33. Optimized geometric coordinates of **33**.

1	45	0	0.620247	0.210410	0.142726
2	5	0	-1.484738	-0.197081	0.125128
3	6	0	0.625448	1.262491	2.127025
4	1	0	-0.428740	0.291475	1.346927
5	6	0	0.153443	1.891864	-0.680834
6	8	0	-0.092956	2.879926	-1.184928
7	8	0	-1.941293	-1.476264	0.122246
8	8	0	-2.412375	0.786902	-0.001490
9	6	0	1.575139	-1.789853	0.541624
10	6	0	2.662825	-0.839338	0.542594
11	6	0	2.719987	-0.238398	-0.733063
12	6	0	1.688189	-0.847940	-1.559035
13	6	0	1.027907	-1.840200	-0.783522
14	6	0	-3.730231	0.119084	-0.162712
15	6	0	-3.419594	-1.400979	-0.039503
16	1	0	1.283692	-2.425107	1.370989
17	1	0	3.289383	-0.595045	1.393789
18	1	0	3.416037	0.529444	-1.053151
19	1	0	1.497351	-0.621004	-2.602549
20	1	0	0.209352	-2.471693	-1.106701
21	1	0	-3.872433	-1.863196	0.841146
22	1	0	-3.687003	-1.968970	-0.933802
23	1	0	-4.127765	0.400022	-1.141126
24	1	0	-4.390392	0.490366	0.624628
25	1	0	1.533641	1.840841	1.951529
26	1	0	-0.217127	1.931992	2.312949
27	1	0	0.760905	0.552930	2.944997

Basis Sets: Optimization and Frequency
Rh: LANL2mDZ(f)
O B 3 4 5 9 → 13: cc-pVDZ
14→27: D95

Basis Sets: Bader's Analysis
Rh: WTBS
O B 3 4 5 9 → 13: cc-pVDZ
14→27: D95

Table C-34. Optimized geometric coordinates of **34**.

1	75	0	0.522516	0.185645	0.082569
2	5	0	-1.579625	-0.148555	0.049604
3	6	0	0.601318	1.474809	2.135175
4	1	0	-0.293514	0.803575	1.497289
5	6	0	0.193787	1.732038	-0.912167
6	8	0	0.038548	2.689247	-1.604137
7	8	0	-2.185609	-1.423171	-0.224931
8	8	0	-2.637946	0.783696	0.285710
9	6	0	1.306932	-1.957101	0.627160
10	6	0	2.422952	-1.061858	0.724566
11	6	0	2.690793	-0.504033	-0.559571
12	6	0	1.685291	-1.005394	-1.465317
13	6	0	0.826359	-1.891325	-0.729457
14	6	0	-3.919821	0.171421	0.021627
15	6	0	-3.619602	-1.344560	-0.061111
16	1	0	0.886810	-2.555861	1.426959
17	1	0	2.981883	-0.845458	1.631206
18	1	0	3.482218	0.196379	-0.802391
19	1	0	1.611388	-0.780518	-2.523616
20	1	0	-0.015277	-2.444595	-1.126851
21	1	0	-3.917570	-1.872070	0.861251
22	1	0	-4.119805	-1.828776	-0.913602
23	1	0	-4.326765	0.559149	-0.926982
24	1	0	-4.625510	0.418753	0.829271
25	1	0	-0.201974	1.963463	2.712042
26	1	0	1.174513	0.854192	2.831484
27	1	0	1.225050	2.268961	1.724702

Basis Sets: Optimization and Frequency
Re: LANL2mDZ(f)
O B 3 4 5 9 → 13: cc-pVDZ
14→27: D95

Basis Sets: Bader's Analysis
Re: WTBS
O B 3 4 5 9 → 13: cc-pVDZ
14→27: D95

Table C-35. Optimized geometric coordinates of **35**.

1	76	0	0.513720	0.184511	0.083098
2	5	0	-1.576017	-0.181669	0.061179
3	6	0	0.667633	1.562717	1.956593
4	1	0	-0.294732	0.726432	1.439039
5	6	0	0.084738	1.681296	-0.942343
6	8	0	-0.148740	2.593919	-1.627145
7	8	0	-2.125383	-1.436945	-0.213278
8	8	0	-2.567982	0.760747	0.320435
9	6	0	1.462070	-1.797767	0.788380
10	6	0	2.544650	-0.865010	0.606149
11	6	0	2.590980	-0.481444	-0.759703
12	6	0	1.508175	-1.153657	-1.441440
13	6	0	0.833512	-1.981711	-0.484040
14	6	0	-3.880444	0.142028	0.149266
15	6	0	-3.581809	-1.360163	-0.097934
16	1	0	1.190973	-2.294575	1.712266
17	1	0	3.204493	-0.500744	1.386515
18	1	0	3.292331	0.213685	-1.206430
19	1	0	1.282609	-1.092030	-2.499419
20	1	0	-0.031981	-2.601509	-0.680246
21	1	0	-3.901434	-1.997240	0.736220
22	1	0	-4.029827	-1.735564	-1.025038
23	1	0	-4.383641	0.616014	-0.702168
24	1	0	-4.474130	0.313180	1.054546
25	1	0	1.348702	2.298851	1.528211
26	1	0	-0.170535	2.120828	2.396133
27	1	0	1.164332	0.998647	2.749389

Basis Sets: Optimization and Frequency
Os: LANL2mDZ(f)
O B 3 4 5 9 → 13: cc-pVDZ
14→27: D95

Basis Sets: Bader's Analysis
Os: WTBS
O B 3 4 5 9 → 13: cc-pVDZ
14→27: D95

Table C-36. Optimized geometric coordinates of **36**.

1	77	0	0.509078	0.175624	0.091958
2	5	0	-1.592763	-0.219966	0.080798
3	6	0	0.757244	1.597297	1.861965
4	1	0	-0.297285	0.562770	1.436145
5	6	0	-0.009370	1.695390	-0.905347
6	8	0	-0.296640	2.606709	-1.530206
7	8	0	-2.087734	-1.478392	-0.098813
8	8	0	-2.519478	0.765550	0.242292
9	6	0	1.593823	-1.678430	0.819054
10	6	0	2.634517	-0.749672	0.429827
11	6	0	2.490856	-0.476338	-0.950951
12	6	0	1.353928	-1.235093	-1.440267
13	6	0	0.848299	-2.021811	-0.351581
14	6	0	-3.858246	0.139205	0.127131
15	6	0	-3.569559	-1.378531	-0.047799
16	1	0	1.453559	-2.100767	1.807861
17	1	0	3.371425	-0.310073	1.093664
18	1	0	3.105062	0.197141	-1.538910
19	1	0	1.005249	-1.270479	-2.466195
20	1	0	-0.004856	-2.688311	-0.391162
21	1	0	-3.915243	-1.982233	0.795502
22	1	0	-3.965314	-1.787915	-0.980519
23	1	0	-4.362720	0.582625	-0.735251
24	1	0	-4.417261	0.368778	1.037546
25	1	0	1.587144	2.180984	1.460678
26	1	0	-0.079643	2.265871	2.080154
27	1	0	1.066574	1.055365	2.757350

Basis Sets: Optimization and Frequency
Ir: LANL2mDZ(f)
O B 3 4 5 9 → 13: cc-pVDZ
14→27: D95

Basis Sets: Bader's Analysis
Ir: WTBS
O B 3 4 5 9 → 13: cc-pVDZ
14→27: D95

Table C-37. Optimized geometric coordinates of **37**.

1	26	0	-0.098128	0.200433	-0.283327
2	15	0	-2.090255	-0.693702	0.050889
3	6	0	-0.870143	2.124985	0.164392
4	1	0	-0.546393	0.388049	-1.734850
5	1	0	-0.611298	1.335294	-1.117469
6	6	0	1.048885	-0.656203	1.313723
7	6	0	1.053967	-1.531072	0.165770
8	6	0	1.644318	-0.832575	-0.919980
9	6	0	1.990414	0.482491	-0.468182
10	6	0	1.632264	0.573427	0.913292
11	1	0	-0.155934	2.935385	-0.027793
12	1	0	-1.854173	2.446155	-0.206502
13	1	0	-0.955496	1.995300	1.248829
14	1	0	-2.611290	-0.917744	1.362996
15	1	0	-3.242298	-0.031795	-0.461227
16	1	0	-2.410938	-1.987634	-0.454507
17	1	0	0.672165	-0.896573	2.301959
18	1	0	0.677947	-2.548408	0.136227
19	1	0	1.769168	-1.213322	-1.927272
20	1	0	2.444542	1.265321	-1.065016
21	1	0	1.730930	1.457924	1.533708

Basis Sets: Optimization and Frequency
Fe: LANL2mDZ(f)
P, 3 → 10: cc-pVDZ
11 → 21: D95

Basis Sets: Bader's Analysis
Fe: WTBS
P, 3 → 10: cc-pVDZ
11 → 21: D95

Table C-38. Optimized geometric coordinates of **37a**.

1	26	0	0.752665	-0.198895	-0.901504
2	15	0	2.951000	0.399908	-0.744408
3	7	0	-1.199376	-0.703982	-1.040720
4	7	0	0.111278	1.617747	-0.225837
5	7	0	0.697586	-0.884581	1.039141
6	6	0	1.303814	-2.108190	-1.713576
7	1	0	0.762744	0.289950	-2.400248
8	1	0	0.989799	-0.715240	-2.314941
9	7	0	-2.034063	-0.404243	-0.017466
10	7	0	-0.854970	1.663397	0.721142
11	7	0	-0.347217	-0.533035	1.824033
12	5	0	-1.476735	0.337059	1.223500
13	6	0	-1.936409	-1.298362	-1.993902
14	6	0	-3.289677	-1.390468	-1.580041
15	6	0	-3.300921	-0.802602	-0.308458
16	6	0	0.394406	2.888580	-0.562282
17	6	0	-0.406601	3.786123	0.188789
18	6	0	-1.193309	2.951331	0.993279
19	6	0	1.489643	-1.687190	1.772457
20	6	0	0.946021	-1.860167	3.071036
21	6	0	-0.232569	-1.102547	3.052417
22	1	0	-1.487220	-1.628908	-2.918056
23	1	0	-4.121169	-1.814665	-2.121140
24	1	0	-4.111710	-0.647624	0.387576
25	1	0	1.129273	3.110339	-1.321854
26	1	0	-0.414581	4.864175	0.145777
27	1	0	-1.955356	3.190461	1.719858
28	1	0	2.390309	-2.111663	1.354523
29	1	0	1.344712	-2.444685	3.885594
30	1	0	-0.977142	-0.942251	3.817781
31	1	0	-2.343260	0.543458	2.033459
32	1	0	0.800806	-2.530619	-2.596736
33	1	0	2.381466	-2.274488	-1.848939
34	1	0	0.955744	-2.684719	-0.852284
35	1	0	3.811314	-0.244786	0.191362
36	1	0	3.801351	0.250000	-1.875457
37	1	0	3.333215	1.732478	-0.418919

Basis Sets: Optimization and Frequency
Fe: LANL2mDZ(f)
P, N, B, 6, 7, 8: cc-pVDZ
13 → 37: D95

Basis Sets: Bader's Analysis
Fe: WTBS
P, N, B, 6, 7, 8: cc-pVDZ
13 → 37: D95

Table C-39. Optimized geometric coordinates of **37b**.

1	26	0	0.738956	-0.186329	-0.874566
2	15	0	2.937955	0.330016	-0.713233
3	6	0	-1.168229	-0.618926	-0.996028
4	6	0	0.149876	1.564462	-0.203423
5	6	0	0.635666	-0.875677	0.976783
6	6	0	1.266012	-2.125772	-1.800602
7	1	0	0.758015	0.327783	-2.395197
8	1	0	0.969944	-0.696669	-2.310224
9	7	0	-2.050358	-0.322960	-0.000268
10	7	0	-0.815258	1.684187	0.752587
11	7	0	-0.379519	-0.528864	1.817342
12	5	0	-1.507062	0.392593	1.271405
13	7	0	-1.924379	-1.227319	-1.953858
14	6	0	-3.270017	-1.319957	-1.578514
15	6	0	-3.333563	-0.738905	-0.331907
16	7	0	0.472093	2.853793	-0.521015
17	6	0	-0.282847	3.780424	0.208990
18	6	0	-1.097878	3.018677	1.015084
19	7	0	1.395535	-1.746686	1.705761
20	6	0	0.870155	-1.958357	2.987031
21	6	0	-0.260618	-1.175135	3.040797
22	1	0	-1.538873	-1.568007	-2.822102
23	1	0	-4.033999	-1.766766	-2.193946
24	1	0	-4.179752	-0.597672	0.322248
25	1	0	1.129175	3.089681	-1.249719
26	1	0	-0.185006	4.848823	0.104175
27	1	0	-1.837386	3.326380	1.737844
28	1	0	2.214696	-2.206453	1.336018
29	1	0	1.317854	-2.611575	3.718462
30	1	0	-0.968051	-1.038199	3.843781
31	1	0	-2.367102	0.616164	2.089014
32	1	0	0.677030	-2.535056	-2.637442
33	1	0	2.323234	-2.273921	-2.064716
34	1	0	1.030406	-2.747461	-0.932045
35	1	0	3.779429	-0.277777	0.273025
36	1	0	3.830316	0.093227	-1.802320
37	1	0	3.395057	1.658794	-0.449785

Basis Sets: Optimization and Frequency
Fe: LANL2mDZ(f)
P, N, B, 3 → 8: cc-pVDZ
14, 15, 17, 18, 20 → 37: D95

Basis Sets: Bader's Analysis
Fe: WTBS
P N B 3 → 8: cc-pVDZ
14, 15, 17, 18, 20 → 37: D95

Table C-40. Optimized geometric coordinates of **37c**.

1	26	0	0.273068	-0.207952	-0.914361
2	15	0	2.404694	-0.517362	-1.607566
3	15	0	-1.965258	-0.076380	-0.378716
4	15	0	0.599083	1.825538	0.109494
5	15	0	0.624782	-1.287295	1.119633
6	6	0	-0.164726	-1.954983	-2.200165
7	1	0	-0.002359	0.589333	-2.243358
8	1	0	-0.146501	-0.432842	-2.374287
9	6	0	-2.374549	0.827690	1.184581
10	6	0	0.043400	1.929988	1.878189
11	6	0	-0.481968	-0.707137	2.497756
12	6	0	2.327727	-1.083687	1.869217
13	6	0	0.518509	-3.154894	1.140805
14	6	0	-3.026571	0.655578	-1.729790
15	6	0	-2.850370	-1.704109	-0.138617
16	6	0	2.320243	2.563094	0.118443
17	6	0	-0.301801	3.238255	-0.714403
18	5	0	-1.125948	0.818752	2.290668
19	1	0	-1.591509	1.159931	3.371941
20	1	0	-1.165260	-2.045227	-2.644242
21	1	0	0.557149	-2.200096	-2.993230
22	1	0	-0.078377	-2.719393	-1.426309
23	1	0	3.554901	0.156190	-1.105353
24	1	0	2.961691	-1.829026	-1.533593
25	1	0	2.703779	-0.314139	-2.985786
26	1	0	-2.636622	1.869430	0.937124
27	1	0	-3.276629	0.368116	1.617546
28	1	0	0.928038	1.792066	2.522825
29	1	0	-0.323946	2.952485	2.060534
30	1	0	-1.299534	-1.437703	2.615818
31	1	0	0.101046	-0.738643	3.431624
32	1	0	3.108622	-1.457179	1.193822
33	1	0	2.518634	-0.025027	2.077882
34	1	0	2.391845	-1.635734	2.815904
35	1	0	1.274852	-3.594958	0.477344
36	1	0	0.675866	-3.530556	2.160194
37	1	0	-0.470090	-3.481007	0.797661
38	1	0	2.679725	2.732023	-0.905411
39	1	0	2.308193	3.522703	0.651644
40	1	0	3.023460	1.893863	0.628793
41	1	0	-0.021632	3.293957	-1.773384
42	1	0	-1.383861	3.085843	-0.647255
43	1	0	-0.056193	4.187960	-0.221021
44	1	0	-2.961074	0.037416	-2.634878
45	1	0	-4.075424	0.715713	-1.410935
46	1	0	-2.672055	1.661848	-1.978875
47	1	0	-2.506369	-2.182355	0.784233
48	1	0	-3.929744	-1.525155	-0.046875
49	1	0	-2.669540	-2.383119	-0.978826

Basis Sets: Optimization and Frequency
Fe: LANL2mDZ(f)
P, 6, 7, 8: cc-pVDZ
9 → 49: D95

Basis Sets: Bader's Analysis
Fe: WTBS
P, 6, 7, 8: cc-pVDZ
9 → 49: D95

Table C-41. Optimized geometric coordinates of **38**.

1	44	0	-0.139033	0.145447	-0.274349
2	15	0	-2.156302	-0.841903	0.151606
3	6	0	-1.142532	2.097096	0.286632
4	1	0	-0.689622	-0.107391	-1.760689
5	1	0	-0.712059	1.447299	-1.015074
6	6	0	1.307363	-0.748150	1.327102
7	6	0	1.387335	-1.500274	0.094756
8	6	0	1.903315	-0.627688	-0.913746
9	6	0	2.091276	0.663179	-0.334343
10	6	0	1.735075	0.573937	1.057739
11	1	0	-0.539829	2.994420	0.105554
12	1	0	-2.161160	2.291910	-0.070275
13	1	0	-1.189941	1.937202	1.369582
14	1	0	-2.602569	-1.130276	1.480096
15	1	0	-3.348494	-0.184935	-0.272250
16	1	0	-2.470232	-2.120869	-0.391827
17	1	0	0.980303	-1.131234	2.287542
18	1	0	1.173382	-2.556238	-0.025720
19	1	0	2.091678	-0.892643	-1.947692
20	1	0	2.475045	1.541318	-0.840883
21	1	0	1.764464	1.391725	1.770071

Basis Sets: Optimization and Frequency
Ru: LANL2mDZ(f)
P, 3 → 10: cc-pVDZ
11 → 21: D95

Basis Sets: Bader's Analysis
Ru: WTBS
P, 3 → 10: cc-pVDZ
11 → 21: D95

Table C-42. Optimized geometric coordinates of **38a**.

1	44	0	0.904296	-0.404882	-0.672512
2	15	0	3.060805	0.364443	-0.444045
3	7	0	-1.106220	-1.094405	-0.933890
4	7	0	0.001112	1.583785	-0.611958
5	7	0	0.400792	-0.371197	1.534118
6	6	0	1.596494	-2.494420	-0.373031
7	1	0	1.070056	-0.150361	-2.244875
8	1	0	1.394078	-1.535544	-1.642442
9	7	0	-2.103883	-0.558490	-0.189639
10	7	0	-1.160805	1.759970	0.061702
11	7	0	-0.824380	0.072746	1.898253
12	5	0	-1.818777	0.578893	0.824300
13	6	0	-1.657975	-2.014874	-1.742783
14	6	0	-3.056363	-2.083963	-1.519334
15	6	0	-3.292436	-1.132451	-0.519371
16	6	0	0.303002	2.754116	-1.200438
17	6	0	-0.686101	3.723117	-0.897475
18	6	0	-1.601133	3.037273	-0.088200
19	6	0	1.050106	-0.708680	2.661558
20	6	0	0.225462	-0.478100	3.792550
21	6	0	-0.964326	0.024234	3.249979
22	1	0	-1.051135	-2.569556	-2.442295
23	1	0	-3.775756	-2.720533	-2.010466
24	1	0	-4.210863	-0.835107	-0.035980
25	1	0	1.183930	2.852055	-1.816599
26	1	0	-0.728625	4.751777	-1.220041
27	1	0	-2.516033	3.372703	0.376623
28	1	0	2.058303	-1.095687	2.628575
29	1	0	0.458587	-0.649799	4.831940
30	1	0	-1.877024	0.340635	3.732395
31	1	0	-2.844310	0.939604	1.342124
32	1	0	0.841871	-3.229216	-0.678759
33	1	0	2.569083	-2.817458	-0.768018
34	1	0	1.653496	-2.512243	0.720263
35	1	0	3.682084	0.450644	0.839279
36	1	0	4.125044	-0.319818	-1.097906
37	1	0	3.413275	1.677212	-0.874971

Basis Sets: Optimization and Frequency
Ru: LANL2mDZ(f)
P, N, B, 6, 7, 8: cc-pVDZ
13 → 37: D95

Basis Sets: Bader's Analysis
Ru: WTBS
P, N, B, 6, 7, 8: cc-pVDZ
13 → 37: D95

Table C-43. Optimized geometric coordinates of **38b**.

1	44	0	0.859186	-0.210609	-0.732756
2	15	0	3.078422	0.496928	-0.350432
3	7	0	-1.091383	-0.788730	-1.074838
4	7	0	-0.020041	1.633725	-0.232149
5	7	0	0.414573	-0.711869	1.308489
6	6	0	1.585751	-2.365548	-1.067260
7	1	0	0.966821	0.424984	-2.261410
8	1	0	1.353011	-1.024435	-2.010440
9	7	0	-2.112880	-0.456972	-0.234134
10	7	0	-1.147686	1.711777	0.526541
11	7	0	-0.772999	-0.364338	1.874463
12	5	0	-1.829686	0.406874	1.030405
13	6	0	-1.676631	-1.523141	-2.062464
14	6	0	-3.054644	-1.661103	-1.861256
15	6	0	-3.316915	-0.978037	-0.695767
16	6	0	0.256577	2.923716	-0.575319
17	6	0	-0.685335	3.816501	-0.052024
18	6	0	-1.571683	3.030344	0.648262
19	6	0	1.068283	-1.407896	2.282657
20	6	0	0.308094	-1.510240	3.453839
21	6	0	-0.861252	-0.838478	3.177945
22	1	0	-1.159155	-1.895342	-2.844945
23	1	0	-3.705052	-2.204175	-2.527415
24	1	0	-4.250899	-0.831043	-0.176567
25	1	0	1.016704	3.171980	-1.191038
26	1	0	-0.652630	4.882292	-0.209486
27	1	0	-2.449921	3.309248	1.209001
28	1	0	1.980309	-1.819446	2.148210
29	1	0	0.640222	-2.023004	4.341974
30	1	0	-1.725604	-0.671730	3.801463
31	1	0	-2.835308	0.633568	1.659315
32	1	0	0.967379	-2.981711	-1.734081
33	1	0	2.630531	-2.493290	-1.381768
34	1	0	1.478758	-2.792958	-0.064094
35	1	0	3.736328	0.345121	0.913174
36	1	0	4.149141	-0.051741	-1.119532
37	1	0	3.481642	1.858790	-0.520274

Basis Sets: Optimization and Frequency
Ru: LANL2mDZ(f)
P, N, B, 3 → 8: cc-pVDZ
14, 15, 17, 18, 20 → 37: D95

Basis Sets: Bader's Analysis
Ru: WTBS
P N B 3 → 8: cc-pVDZ
14, 15, 17, 18, 20 → 37: D95

Table C-44. Optimized geometric coordinates of **38c**.

1	44	0	0.290007 -0.278299 -0.868881
2	15	0	2.556586 -0.642039 -1.440636
3	15	0	-2.034759 0.059395 -0.418495
4	15	0	0.698223 1.855026 0.159176
5	15	0	0.446269 -1.259157 1.362262
6	6	0	-0.225656 -2.229359 -2.029827
7	1	0	0.077695 0.463401 -2.366042
8	1	0	-0.112728 -0.671747 -2.402594
9	6	0	-2.415379 1.072692 1.083181
10	6	0	0.040409 2.047635 1.882325
11	6	0	-0.725207 -0.515727 2.598505
12	6	0	2.091521 -1.121405 2.239086
13	6	0	0.200660 -3.107599 1.486789
14	6	0	-2.981984 0.820937 -1.834099
15	6	0	-3.043957 -1.486803 -0.150376
16	6	0	2.469451 2.449888 0.256191
17	6	0	-0.047952 3.294890 -0.762042
18	5	0	-1.231542 1.038678 2.261365
19	1	0	-1.740472 1.474322 3.287990
20	1	0	-1.144672 -2.273013 -2.630455
21	1	0	0.594754 -2.604785 -2.655059
22	1	0	-0.355631 -2.916558 -1.191910
23	1	0	3.618954 -0.688155 -0.490959
24	1	0	2.899934 -1.855825 -2.109230
25	1	0	3.230508 0.222245 -2.353213
26	1	0	-2.583588 2.114995 0.765859
27	1	0	-3.369095 0.711129 1.498786
28	1	0	0.871645 1.869058 2.585447
29	1	0	-0.261948 3.098919 2.013608
30	1	0	-1.605214 -1.176343 2.675329
31	1	0	-0.231772 -0.539371 3.583074
32	1	0	2.889326 -1.601914 1.659540
33	1	0	2.350267 -0.067148 2.388571
34	1	0	2.031398 -1.602974 3.223876
35	1	0	0.973762 -3.638711 0.916345
36	1	0	0.246588 -3.424694 2.536951
37	1	0	-0.778012 -3.387604 1.080483
38	1	0	2.899446 2.554358 -0.748885
39	1	0	2.516026 3.422729 0.763261
40	1	0	3.076151 1.733929 0.824570
41	1	0	0.310346 3.298774 -1.798440
42	1	0	-1.139327 3.206225 -0.770869
43	1	0	0.219182 4.243089 -0.276578
44	1	0	-2.950105 0.158109 -2.708583
45	1	0	-4.028316 0.995916 -1.550683
46	1	0	-2.521865 1.775055 -2.113754
47	1	0	-2.756226 -1.957319 0.795730
48	1	0	-4.110258 -1.230728 -0.097250
49	1	0	-2.885545 -2.202874 -0.963962

Basis Sets: Optimization and Frequency
Ru: LANL2mDZ(f)
P, 6, 7, 8: cc-pVDZ
9 → 49: D95

Basis Sets: Bader's Analysis
Ru: WTBS
P, 6, 7, 8: cc-pVDZ
9 → 49: D95

Table C-45. Optimized geometric coordinates of **39**.

1	76	0	-0.099618	0.056297	-0.269750
2	15	0	-2.190538	-0.681704	0.308248
3	6	0	-0.958465	1.958324	0.395845
4	1	0	-0.540658	-0.901336	-1.503827
5	1	0	-0.578609	0.861445	-1.586231
6	6	0	1.312156	-0.747496	1.453678
7	6	0	1.486157	-1.478978	0.232902
8	6	0	1.961705	-0.555269	-0.775415
9	6	0	2.043686	0.747056	-0.174915
10	6	0	1.634898	0.611386	1.196747
11	1	0	-0.272856	2.776258	0.143023
12	1	0	-1.921204	2.198879	-0.069454
13	1	0	-1.106874	1.958746	1.485457
14	1	0	-2.875490	-0.083449	1.407747
15	1	0	-3.263439	-0.610028	-0.627403
16	1	0	-2.383539	-2.041202	0.689012
17	1	0	0.966995	-1.151141	2.398739
18	1	0	1.347249	-2.545992	0.104722
19	1	0	2.243086	-0.805979	-1.791081
20	1	0	2.385483	1.655895	-0.655028
21	1	0	1.548077	1.424765	1.908521

Basis Sets: Optimization and Frequency
Os: LANL2mDZ(f)
P, 3 → 10: cc-pVDZ
11 → 21: D95

Basis Sets: Bader's Analysis
Os: WTBS
P, 3 → 10: cc-pVDZ
11 → 21: D95

Table C-46. Optimized geometric coordinates of **39a**.

1	76	0	0.838640	-0.408426	-0.425854
2	15	0	2.898975	0.572946	-0.309957
3	7	0	-1.054149	-1.379252	-0.531739
4	7	0	-0.302398	1.416444	-0.949044
5	7	0	0.192986	0.240265	1.587679
6	6	0	1.637790	-2.129223	0.620533
7	1	0	0.961216	-0.319174	-2.036306
8	1	0	1.403223	-1.538139	-1.410509
9	7	0	-2.169251	-0.791708	-0.026170
10	7	0	-1.536776	1.611099	-0.426031
11	7	0	-1.101873	0.578187	1.803248
12	5	0	-2.098859	0.612018	0.617161
13	6	0	-1.422389	-2.567344	-1.044115
14	6	0	-2.815332	-2.759591	-0.869129
15	6	0	-3.247313	-1.599356	-0.215403
16	6	0	-0.065568	2.429499	-1.801976
17	6	0	-1.173863	3.310964	-1.830838
18	6	0	-2.087801	2.745226	-0.931719
19	6	0	0.840833	0.373065	2.760116
20	6	0	-0.055256	0.811083	3.764314
21	6	0	-1.284129	0.931921	3.100622
22	1	0	-0.694844	-3.214371	-1.508559
23	1	0	-3.409000	-3.607941	-1.171563
24	1	0	-4.231204	-1.306183	0.118525
25	1	0	0.858970	2.478595	-2.356620
26	1	0	-1.289614	4.211481	-2.413439
27	1	0	-3.070245	3.074576	-0.628603
28	1	0	1.892503	0.145770	2.842502
29	1	0	0.157657	1.006236	4.803599
30	1	0	-2.251516	1.241529	3.466519
31	1	0	-3.188503	0.959056	0.991710
32	1	0	1.015507	-3.018412	0.443927
33	1	0	2.668612	-2.404173	0.356414
34	1	0	1.616988	-1.940849	1.702688
35	1	0	4.060339	-0.255861	-0.316523
36	1	0	3.348849	1.502685	-1.296859
37	1	0	3.262462	1.368549	0.821531

Basis Sets: Optimization and Frequency
Os: LANL2mDZ(f)
P, N, B, 6, 7, 8: cc-pVDZ
13 → 37: D95

Basis Sets: Bader's Analysis
Os: WTBS
P, N, B, 6, 7, 8: cc-pVDZ
13 → 37: D95

Table C-47. Optimized geometric coordinates of **39b**.

1	76	0	0.801007	-0.246984	-0.536769
2	15	0	2.954131	0.592243	-0.169657
3	6	0	-1.060656	-1.068603	-0.874042
4	6	0	-0.272127	1.587072	-0.463767
5	6	0	0.193062	-0.275565	1.523780
6	6	0	1.613054	-2.260605	-0.016650
7	1	0	0.836946	0.402012	-2.047518
8	1	0	1.352404	-1.021887	-1.865716
9	7	0	-2.190515	-0.668367	-0.216917
10	7	0	-1.489077	1.705018	0.133654
11	7	0	-1.074042	0.028609	1.911480
12	5	0	-2.116079	0.467601	0.840573
13	7	0	-1.476554	-2.059049	-1.713134
14	6	0	-2.850886	-2.292063	-1.600231
15	6	0	-3.291181	-1.402565	-0.647227
16	7	0	-0.037626	2.812969	-1.014844
17	6	0	-1.090409	3.701304	-0.776959
18	6	0	-2.005524	2.983072	-0.041835
19	7	0	0.837265	-0.613415	2.675363
20	6	0	-0.007638	-0.537388	3.785431
21	6	0	-1.220458	-0.120594	3.284107
22	1	0	-0.842205	-2.544554	-2.330082
23	1	0	-3.380625	-3.033321	-2.176068
24	1	0	-4.283736	-1.244895	-0.255732
25	1	0	0.782937	3.013729	-1.566732
26	1	0	-1.105088	4.719640	-1.129831
27	1	0	-2.961902	3.282637	0.356359
28	1	0	1.791813	-0.941230	2.690929
29	1	0	0.301938	-0.773361	4.790517
30	1	0	-2.151027	0.071450	3.794249
31	1	0	-3.193300	0.714246	1.325476
32	1	0	0.953260	-3.060695	-0.382311
33	1	0	2.605630	-2.454940	-0.447035
34	1	0	1.703957	-2.420532	1.067439
35	1	0	3.459479	0.826216	1.151864
36	1	0	4.084554	-0.157917	-0.616476
37	1	0	3.407308	1.847785	-0.687752

Basis Sets: Optimization and Frequency
Os: LANL2mDZ(f)
P, N, B, 3 → 8: cc-pVDZ
14, 15, 17, 18, 20 → 37: D95

Basis Sets: Bader's Analysis
Os: WTBS
P N B 3 → 8: cc-pVDZ
14, 15, 17, 18, 20 → 37: D95

Table C-48. Optimized geometric coordinates of **39c**.

1	76	0	0.318166	-0.288688	-0.747413
2	15	0	2.592392	-0.634805	-1.193267
3	15	0	-2.037530	0.058026	-0.580659
4	15	0	0.655623	1.907024	0.300387
5	15	0	0.215111	-1.104989	1.603767
6	6	0	0.166533	-2.468872	-1.194575
7	1	0	0.336329	0.876690	-1.887034
8	1	0	0.031205	-0.527716	-2.329044
9	6	0	-2.663828	0.549764	1.097581
10	6	0	-0.711754	2.475359	1.404897
11	6	0	-0.502523	0.111229	2.804467
12	6	0	1.806492	-1.728871	2.355801
13	6	0	-0.867967	-2.594721	1.884720
14	6	0	-2.654637	1.410034	-1.704711
15	6	0	-3.146420	-1.334953	-1.133204
16	6	0	2.186289	2.090085	1.354488
17	6	0	0.959794	3.296977	-0.903014
18	5	0	-1.547978	1.230667	2.134440
19	1	0	-2.181438	1.718443	3.062554
20	1	0	-0.860600	-2.848436	-1.160552
21	1	0	0.552799	-2.703347	-2.194205
22	1	0	0.757959	-3.074134	-0.491705
23	1	0	3.594187	-0.787845	-0.184852
24	1	0	2.951199	-1.792800	-1.944054
25	1	0	3.326545	0.305282	-1.974851
26	1	0	-3.491078	1.261513	0.945645
27	1	0	-3.107223	-0.343281	1.568914
28	1	0	-0.282728	3.147384	2.164902
29	1	0	-1.408006	3.079871	0.799858
30	1	0	-1.022741	-0.469600	3.581535
31	1	0	0.319578	0.641929	3.311004
32	1	0	2.176114	-2.595007	1.791447
33	1	0	2.572812	-0.945361	2.327565
34	1	0	1.645652	-2.026562	3.400265
35	1	0	-0.592302	-3.421330	1.224191
36	1	0	-0.766286	-2.915205	2.929727
37	1	0	-1.915529	-2.331820	1.706422
38	1	0	3.083437	1.846981	0.771346
39	1	0	2.268324	3.123740	1.715391
40	1	0	2.140083	1.426401	2.222898
41	1	0	1.848736	3.085346	-1.511027
42	1	0	0.100338	3.392188	-1.576306
43	1	0	1.100909	4.245634	-0.368458
44	1	0	-2.354197	1.198227	-2.737895
45	1	0	-3.748586	1.487795	-1.650545
46	1	0	-2.221979	2.370864	-1.404872
47	1	0	-2.930469	-1.601465	-2.174969
48	1	0	-2.981910	-2.221087	-0.511027
49	1	0	-4.197650	-1.031347	-1.043195

Basis Sets: Optimization and Frequency
Os: LANL2mDZ(f)
P, 6, 7, 8: cc-pVDZ
9 → 49: D95

Basis Sets: Bader's Analysis
Os: WTBS
P, 6, 7, 8: cc-pVDZ
9 → 49: D95

APPENDIX D

SUPPLEMENTAL MATERIAL FOR CHAPTER V

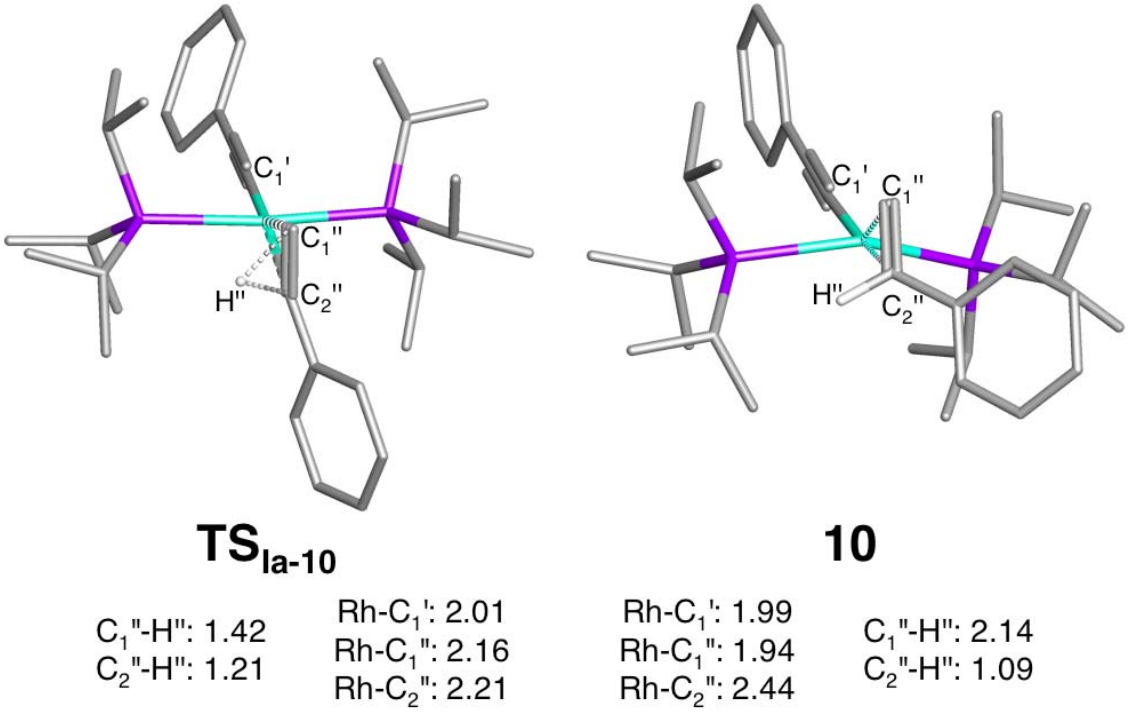

Figure D-1. B3LYP/BS1 optimized geometries of $\mathbf{TS_{Ia–10}}$ and **10**. Select parameters are reported in Angstroms.

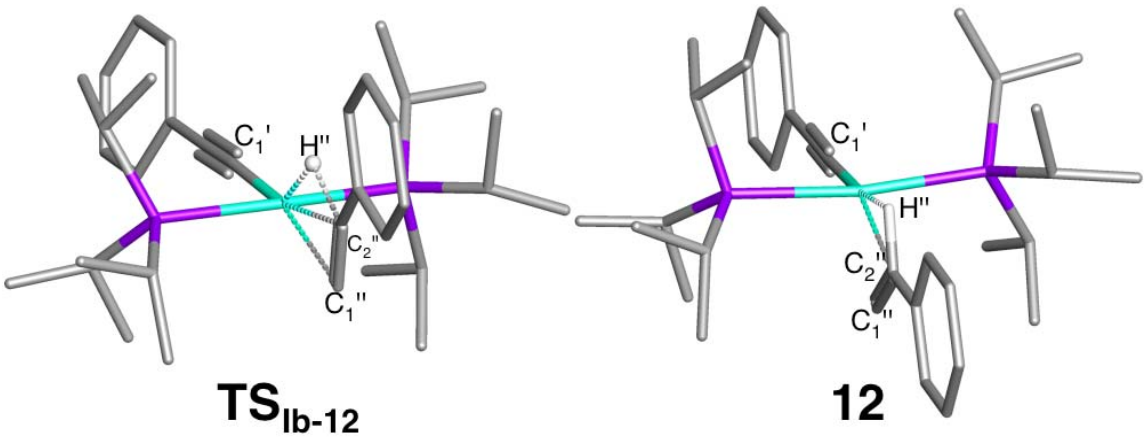

TS$_{Ib-12}$ **12**

Rh-H'': 1.62	Rh-C$_1$': 2.01	Rh-C$_1$': 1.96	Rh-H'': 1.92
C$_2$''-H'': 1.45	Rh-C$_1$'': 2.21	Rh-C$_1$'': 2.73	C$_2$''-H'': 1.17
	Rh-C$_2$'': 2.45	Rh-C$_2$'': 2.11	

Figure D-2. B3LYP/BS1 optimized geometries of **TS$_{Ib-12}$** and **12**. The included parameters are reported in Angstroms.

VITA

Benjamin Alan Vastine graduated from Virginia Polytechnic State Institute and State University in May, 2003, with a Bachelors of Science degree in Chemistry. He received his Doctorate of Philosophy from Texas A&M University in May, 2008. His permanent address is 2109 Chemistry, Texas A&M University, College Station, TX, 77842.